Nanostructured ceramic coatings deposited by High-Power Impulse Magnetron Sputtering in an industrial scale reactor

Neus Sala Bascompte

UNIVERSITAT RAMON LLULL

DOCTORAL THESIS

Title	Nanostructured ceramic coatings deposited by High-power Impulse Magnetron Sputtering in an industrial scale reactor
Presented by	Neus Sala Bascompte
Centre	IQS School of Engineering
Department	Departament d'Enginyeria Química i Ciència dels Materials
Directed by	Dr. Manuel David Abad Roldán Dr. Carles Colominas i Guàrdia

C. Claravall, 1-3 | 08022 Barcelona | Tel. 93 602 22 00 | Fax 93 602 22 49 | info@url.edu | www.url.edu

ABSTRACT

The pressing need to improve industrial manufacturing processes for enhanced productivity, superior end products, and cost-efficiency makes the development of new materials virtually a must. In this context, coatings that improve mechanical, tribological, and even optical properties play a significant role. Such coatings are applied to extend the lifespan and boost the performance of various items, including cutting tools, dies, and moulds.

The PVD-MS technique stands out as one of the most extensively researched methods for generating coatings that are not only homogeneous but also offer precise control over composition and morphology. This makes it an especially valuable tool for tailored surface engineering. However, the need to improve the efficiency of industrial processes has led to the study and development of new coating deposition techniques such as HiPIMS, and new and more sophisticated structures such as the nanocomposites and multilayer systems.

This research involves the design, deposition and characterisation of various nanostructured ceramics coating using the HiPIMS technique in an industrial-scale reactor.

The study of the carbon incorporation into TiB_2/TiBC coatings results in the formation of ternary TiB_xC_y structures, significantly improving the mechanical properties of the coatings.

A comparison between DC-MS and HiPIMS techniques is conducted for NbC/a-C(:H) coatings, highlighting the need for precise HiPIMS parameters adjustment to achieve coatings with superior microstructural and mechanical properties.

The research into nano/multilayer TiN/CrN, TiSiN/CrN and NbN/CrN coatings involve modifying deposition times to produce coatings with different varying bilayer periods, ranging from 460 nm down to 5 nm. The properties of these coatings are described in terms of the deposition parameters, the microstructure, and its composition. Using the optimal parameters identified, the coatings displayed tightly packed, smooth structures characterized by low roughness levels. X-ray diffraction confirmed separate crystalline phases for coatings with bilayer periods of $\Lambda \geq 85$ nm, while epitaxial growth was evident as the period decreased, resulting in a superlattice structure at $\Lambda = 15$ nm for the TiN/CrN coating, with an exceptional hardness value of 32 GPa attributed to nanoscale phenomena.

These findings offer valuable insights into the potential and challenges of using HiPIMS technology in industrial reactors to customize advanced coatings, meeting a diverse range of industrial requirements.

RESUM

La necessitat de millorar els processos de fabricació industrials per aconseguir una productivitat més elevada, l'obtenció de productes finals superiors i una major eficiència de costos, fa que el desenvolupament de nous materials sigui pràcticament imprescindible. En aquest context, els recobriments que milloren les propietats mecàniques, tribològiques i fins i tot òptiques del substrat tenen un paper significatiu. Aquests s'apliquen per prolongar la vida útil i millorar el rendiment de diversos productes, incloent eines de tall, matrius i motlles.

La tècnica PVD-MS destaca com un dels mètodes més estudiats per generar recobriments homogenis amb un control precís sobre la composició i la morfologia. Això la converteix en una eina especialment valuosa per a l'enginyeria de superfícies adaptades. No obstant, la necessitat de millorar els processos industrials ha portat a l'estudi i al desenvolupament de noves tècniques de deposició de recobriments com és el HiPIMS; i de noves i més sofisticades estructures com els *nanocomposites* i els sistemes multicapa.

Aquesta investigació implica el disseny, la deposició i la caracterització de diversos recobriments ceràmics nanoestructurats utilitzant la tècnica HiPIMS en un reactor a escala industrial.

L'estudi de la incorporació de carboni en recobriments de TiB_2/TiBC resulta en la formació d'estructures ternàries TiB_xC_y, millorant significativament les propietats mecàniques dels recobriments.

Es mostra una comparació entre les tècniques DC-MS i HiPIMS per a recobriments de NbC/a-C(:H), destacant la necessitat d'un ajust precís dels paràmetres HiPIMS per aconseguir recobriments amb propietats microestructurals i mecàniques superiors.

La recerca en recobriments nano/multicapa de TiN/CrN, TiSiN/CrN i NbN/CrN implica la modificació dels temps de deposició per produir recobriments amb diferents períodes de bicapa, que van des de 460 nm fins als 5 nm. Les propietats d'aquests recobriments es descriuen en termes dels paràmetres de deposició, la microestructura i la seva composició. Utilitzant els paràmetres òptims identificats, els recobriments mostren estructures denses i compactes amb baixos valors de rugositat. La difracció de raigs X confirma la formació de fases cristal·lines separades per a recobriments amb períodes de bicapa de $\Lambda \geq 85$ nm, mentre que s'evidencia un creixement epitaxial a mesura que el període disminueix, resultant en una estructura tipus *Superlattice* per al recobriment de TiN/CrN amb $\Lambda = 15$ nm que a la vegada mostra un valor excepcional de duresa de 32 GPa atribuït a fenòmens a escala nanomètrica.

Aquests estudis ofereixen perspectives valuoses sobre el potencial i els reptes de l'ús de la tecnologia HiPIMS en reactors industrials per la personalització de recobriments avançats, que puguin respondre a una àmplia gamma de requisits industrials.

RESUMEN

La necesidad de mejorar los procesos de fabricación industriales para una mayor productividad, la obtención de productos finales superiores y una mayor eficiencia en costos convierte el desarrollo de nuevos materiales en algo prácticamente indispensable. En este contexto, los recubrimientos que mejoran las propiedades mecánicas, tribológicas e incluso ópticas del sustrato desempeñan un papel significativo. Estos se aplican para extender la vida útil y mejorar el rendimiento de diversos productos, incluidas herramientas de corte, matrices y moldes.

La técnica PVD-MS destaca como uno de los métodos más investigados para depositar recubrimientos homogéneos con un control preciso sobre la composición y la morfología. Esto la convierte en una herramienta especialmente valiosa para la ingeniería de superficies adaptadas. Sin embargo, la necesidad de mejorar los procesos industriales ha llevado al estudio y desarrollo de nuevas técnicas de deposición de recubrimientos, como el HiPIMS, y de nuevas y más sofisticadas estructuras, como los *nanocomposites* y los sistemas multicapa.

Esta investigación implica el diseño, la deposición y la caracterización de varios recubrimientos cerámicos nanoestructurados utilizando la técnica HiPIMS en un reactor a escala industrial. El estudio de la incorporación de carbono en recubrimientos de TiB_2/TiBC resulta en la formación de estructuras ternarias de TiB_xC_y, mejorando significativamente las propiedades mecánicas de los recubrimientos.

Se realiza una comparación entre las técnicas DC-MS y HiPIMS para recubrimientos de NbC/a-C(:H), destacando la necesidad de un ajuste preciso de los parámetros HiPIMS para lograr recubrimientos con propiedades microestructurales y mecánicas superiores.

La investigación sobre recubrimientos nano/multicapa de TiN/CrN, TiSiN/CrN y NbN/CrN implica modificar los tiempos de deposición para producir recubrimientos con diferentes períodos de bicapa, que varían desde 460 nm hasta 5 nm. Las propiedades de estos recubrimientos se describen en términos de los parámetros de deposición, la microestructura y su composición. Utilizando los parámetros óptimos identificados, los recubrimientos mostraron estructuras densas y compactas con valores bajos de rugosidad. La difracción de rayos-X confirmó fases cristalinas separadas para recubrimientos con períodos de bicapa de $\Lambda \geq 85$ nm, mientras que se evidenció un crecimiento epitaxial a medida que disminuía el período, resultando en una estructura tipo *Superlattice* para el recubrimiento de TiN/CrN con a $\Lambda = 15$ nm que a su vez muestra un valor de dureza excepcional de 32 GPa atribuible a fenómenos a escala nanométrica.

Estos hallazgos ofrecen valiosas perspectivas sobre el potencial y los desafíos de utilizar la tecnología HiPIMS en reactores industriales para personalizar recubrimientos avanzados, satisfaciendo una amplia gama de requisitos industriales.

AGRAÏMENTS

El desenvolupament d'aquesta tesi no hagués estat possible sense la inestimable ajuda i suport de tota la gent que m'ha envoltat en el camí recorregut. Sense voler oblidar-me a ningú hi ha persones que es mereixen una menció especial.

En primer lloc, agrair als meus directors de tesi, Dr. Carles Colominas i Dr. Manuel D. Abad pel seu lideratge, paciència i coneixement. La seva orientació experta y dedicació constant han sigut fonamentals per donar forma a aquest treball i millorar les meves habilitats d'investigació.

A tot l'equip de Flubetech S.L., en especial al Víctor, Francesc i Sandra. Gràcies per la vostre predisposició a ajudar-me sempre en la deposició i caracterització dels recobriments. Aquesta tesi porta una mica del vostre ADN.

Al equipo del Instituto de Ciencia de Materiales de Sevilla (CSIC-US), especialmente al Dr. Juan Carlos y la Dra. Cristina por su inestimable ayuda en la caracterización de los recubrimientos. Transmitís pasión por vuestro trabajo, gracias por vuestra predisposición siempre a ayudar y enseñar.

I would like to extend my heartfelt gratitude to Montanuniversität Leoben team for Marisa, Robert, Chrisi, Aydan, Florian, thank you for your generous guidance and mentorship throughout my stay.

A tots els estudiants i companys de laboratori amb els que en algun moment hem compartit coneixement, discussions tècniques, maldecaps, cerveses... Gràcies per compartir aquest viatge amb mi.

Ana Ramos, la teva influència i exemple han sigut una font d'inspiració constant durant la meva trajectòria acadèmica. Tens un capacitat resolutiva infinita i sempre saps com dir i transmetre de forma efectiva el que penses. Ana, jo de gran vull ser com tu.

A tota la meva família: tietes, tiets, cosines, fillols, el vostre suport, ajuda i motivació ha estat, és i serà sempre impagable. Als meus pares, Josep i Teresa, això si que es amor i suport incondicional. Heu cregut sempre en mi i heu sigut font de força i inspiració. Sou el meu model a seguir a la vida. Roger, tu també has viscut aquesta tesi des del principi. Gràcies per acompanyar-me en els bons moments i ajudar-me a superar els dolents.

Finalment, als meus avis (allà on sigueu), se que estaríeu orgullosos de mi i contents de saber fins a on he arribat. Us estimo molt a tots.

Aquesta tesi ha estat possible amb el suport de la Secretaria d'Universitats i Recerca (SUR) del Departament d'Economia i Coneixement (DEC) de la Generalitat de Catalunya i Fons Socials Europeus [2019FI_B01190], [2020FI_B1_00114], [2021FI_B2_00167], així com també a IQS School of Engineering de la Universitat Ramon Llull.

INDEX

CHAPTER 1

INTRODUCTION

1. INTRODUCTION

A wide variety of manufacturing processes are used to form product elements. These processes use thermal, mechanical, chemical, electrochemical, electromagnetic and even radiation to manipulate materials into product elements with the desired shape, dimensions, material features, and material properties [1–4]. Normally, more than one processing operation is required to transform the starting material into the final form. These operations can be classified into shaping operations, property-enhancing operations, and surface processing operations. Shaping operations such as casting or forging alter the geometry of the starting materials. Property-enhancing operations add value to the material, improving its properties without changing its shape (e.g., heat treatment). And finally, surface processing operations are performed onto the surface of the material; coatings and paintings are included in this group [5,6]. Manufacturing operations are accomplished using machinery, tooling, and people. The extensive use of machinery in manufacturing began with the Industrial Revolution in the 18^{th}-19^{th} century. It was at that time that machines started to be developed and became widely used since nowadays. These machine tools include presses for stamping operations, cutting machines, forge hammers, rolling mills and welding machine among others.

In the realm of manufacturing processes, the role of coatings is particularly prominent, especially within the category of surface processing operations. Coatings are applied to various product elements to impart specific properties, enhance performance, and protect against degradation. These coatings represent a crucial step in the manufacturing chain, adding value to products in numerous industries. They range from simple decorative purposes in architecture and jewellery, to more intricate roles in advanced fields like optoelectronics [7], Micro-electromechanical systems (MEMS) [8], and micro/nanoelectronics [9].

For instance, in the jewellery industry, the deposition of transparent and protective coatings like TiO_2/Al_2O_3 using Atomic Layer Deposition (ALD) can extend the shelf life of silver products [10,11]. Coatings also play a vital role in the tooling industry, where coatings based on transition metal nitrides and carbides are applied to steel tools such as end mill cutters, cutting inserts, and thread mill cutters. Titanium Nitride (TiN) is an example of a hard coating, widely used for cutting tools. It possesses several exceptional characteristics, including a low coefficient of friction, high hardness, and a remarkable wear resistance [9]. These coatings seek to improve the hardness, wear resistance, and tribological properties of tools in order to increase tool durability and enhance overall efficiency.

Another sector in which coatings are widely used is in manufacturing processes involving moulds and matrices, particularly in industries like plastics, composites and metal shaping. These coatings are applied to the surfaces of moulds and dies to enhance their performance and durability. Their primary functions include improving release properties, reducing friction, preventing wear and corrosion, and extending the lifespan of these critical tools. By creating a smooth, low-friction surface, coatings enable easy release of moulded

products, reduce the need for mould release agents, and enhance the precision of manufactured parts. Additionally, coatings can provide thermal insulation to regulate temperature within moulds, ensuring consistent product quality [12–14]. They are essential for maintaining the integrity of moulds and matrices, optimizing manufacturing efficiency, and ensuring the cost-effective production of high-quality components. Ceramic coatings such as CrN, AlCrN or TiCN are industrially used nowadays [15–17].

The research carried out in this thesis focuses on the development of new and specialised nanostructured ceramic coatings using the HiPIMS technique in industrial reactors for processes involving the use of dies and moulds: coatings for the sheet metal forming sector and coatings for plastic injection moulding processes.

1.1. Sheet metal forming

Sheet metal stamping is a process for converting sheet metal into shapes and sizes based on the end-user requirements. Modern continuous rolling mills produce large quantities of thin metal sheet at low cost. It then must be formed in secondary processes to obtain the desired final metal shape for application in automobiles, domestic appliances, building products and beverage cans, among others. Finished products have good quality, are geometrically accurate and parts are ready to be used.

Punches and dies are the basic shaping and cutting tools used in sheet forming. These tools are mounted in presses that provide the necessary forces to accommodate workpieces that must be sheared, simply bent, curved, deeply recessed, or impressed with a pattern in relief (coining). Some examples of sheet metal forming processes are shown in Figure 1.1.

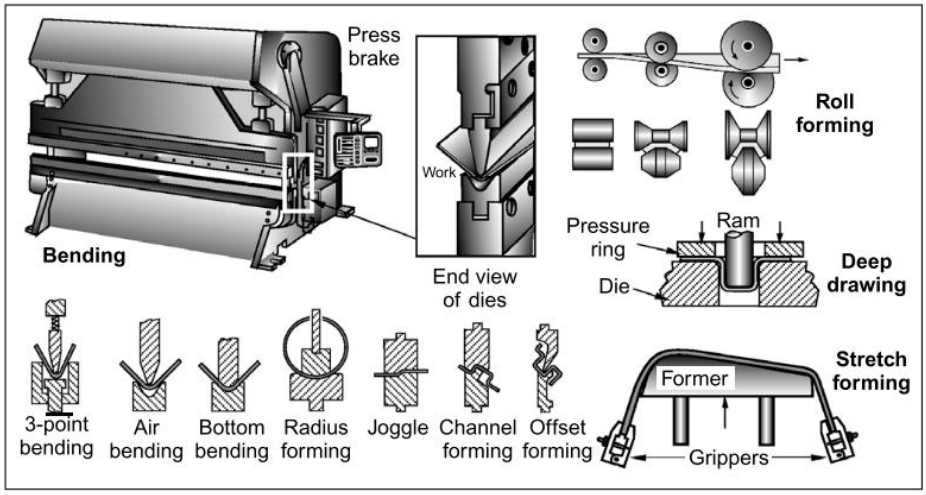

Figure 1.1: Sheet metal forming processes [18].

The most important processes in the sheet metal forming sector are blanking and piercing, bending, and stamping.

Blanking and piercing are two shearing processes in which a punch or a die are used to produce holes from a metal sheet. The basic cutting process is shown in Figure 1.2a. In blanking, the small removed piece is the useful part while the rest of the metal sheet is scrap. In piercing, the cut-out portion is scrap which gets disposed off, while the important part is the large metal sheet with the desired holes. The terminology is different here, though both processes are basically the same. A schematic view of the two processes can be observed in Figure 1.2b. One of the major advantages of these processes is the ability to quickly produce economical metal work pieces in medium or high production processes, although the quality of the ultimate pieces depends on the conditions used. The major drawbacks of the technique are the generation of residual cracks and hardening along the blanked edges, and the creation of excess roll-over and burr if the clearance is excessive [19–21].

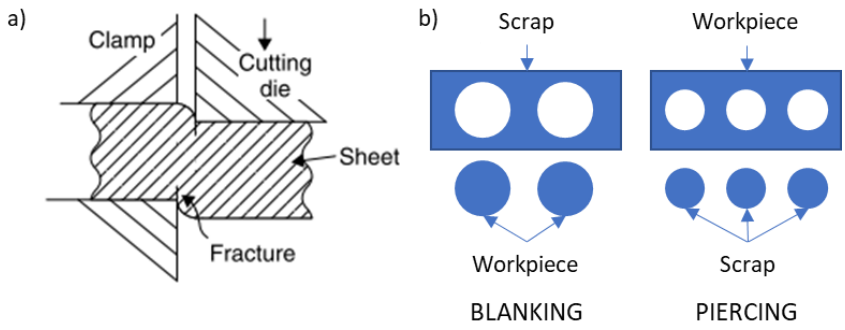

Figure 1.2: a) Basic mechanism of blanking a metal sheet. b) Schematic view of blanking and piercing processes.

Sheet metal bending is an operation that involves using forces to change the shape of a sheet. This force causes stress on the sheet metal beyond its yield strength, causing the material to physically deform without breaking or failing. The simplest forming process is making a straight-line bend; however, metal sheets can be bended in many different ways as shown in Figure 1.1. Plastic deformation occurs only in the bend region and the material away from the bend is not deformed. If the material lacks ductility, cracking may appear on the outside bend surface, but the greatest difficulty is usually to get an accurate and repeatable bend angle. Elastic springback is appreciable in most of the cases. The thickness of the material, size of the bend, sheet metal bend radius and intended purpose determine the bending method used [22,23].

In the stamping process, sheet metal is transformed into complex 3D parts by the use of a stamping tool (or die) and a press. In this process, the die is pushed into the sheet, creating tensile forces at the centre which will cause the deformation of the sheet in the

contact area. Normally, the outer edge or flange is allowed to draw inwards under restraints to supply material for the part shape. It is a complex process that can include a number of metal forming techniques such as blanking, punching, bending and piercing, among others. This process is widely used to form auto-body panels and a variety of appliance parts. However, die design requires the combination of skill and extensive computer-aided engineering systems. [24,25].

All these sheet metal manufacturing processes have some major drawbacks. Especially the punch/die is exposed to high dynamic loads, to sliding motion against work material and high contact temperatures [26], which leads to high friction and wear of the tool [27]. Severe tribological conditions between the punch and the work-piece material in the case of blanking, cause an accumulation of adhered material on the punch, which increases the stamping force and increases the extraction force. The wear of the tools has a direct effect on the quality of the parts obtained, which reduces production and an increase in costs [28,29].

Also, these processes sometimes use heat to increase the formability of some metals. Heating can drastically improve the ductility of ultra-high strength steels, making it possible to be formed at large bending angles and stamp them without springback [30–32]. Every time materials are processed, or heat treated at temperatures different from the use temperature, residual stresses are either produced or relieved. The thermal fatigue cycles to which punches and dies are subjected during these processes can cause excessive and non-uniform cracking and wear of these parts, having a direct effect on the quality and costs of the obtained products [33]. These metals are of great interest nowadays, particularly for automotive applications, where weight reduction is of high importance [34].

To overcome these problems, two main approaches are used industrially. The first one is the use of lubricant oils, which reduce the friction coefficient and wear of the punches and dies and also helps to cool down the temperature generated oh the tool/sheet interphase, preventing the seizure of the pieces [35,36]. However, the use of lubricants is not preferred due to environmental issues and subsequent cleaning requirements [37].

The second and newest approach is the use of coatings as protective materials for punches and dies. These coatings must fulfil the requirements used in these processes such as good adhesion to the base material to withstand high loads and shearing forces without chipping or peeling, high toughness and low friction against stamped material [38,39]. In the last years, attention was focused on the carbon-based nanocomposite coatings because of their great tribological properties, and also multilayer coatings due to their enhanced mechanical properties thanks to their promising structure [40–43].

1.2. Plastic injection moulding

Plastics can be shaped into a wide variety of products, such as moulded parts, extruded sections, films and sheets, insulation coatings on electrical wires, and fibres for

textiles. The commercial and technological importance of these shaping processes derives from the growing importance of the materials being processed. Applications of plastics have increased at a much faster rate than either metals or ceramics during the last 50 years. Indeed, many parts previously made of metals are today being made of plastics and plastic composites.

Plastic-shaping processes can be classified according to the resulting product geometry: continuous extruded products, including sheets, films and fibers, moulded parts that are mostly solid, hollow moulded parts with relatively thin walls and discrete parts made of formed sheets and films. The most important processes commercially are extrusion and injection moulding [44].

Injection moulding is a process in which a polymer is heated to a highly plastic state and forced to flow under high pressure into a mould cavity, where it solidifies. The moulded part, called a moulding, is then removed from the cavity. This process produces discrete components that are almost always neat shape [45]. The main parts of one plastic injection moulding cycle can be observed in Figure 1.3. First, the mould is closed and clamped. Then, a controlled portion of plastic melt, which has been brought to the right temperature and viscosity by heating and the mechanical working of the screw, is injected under high pressure into the mould cavity. The plastic then cools and solidifies when it encounters the cold surface of the mould. After a complete solidification, the mould is opened, and the plastic part is ejected and removed.

The mould is the most special tool in injection moulding; it is custom designed and fabricated for the part to be produced. The two-plate mould (Figure 1.4) is the most widely used industrially. The main parts are a channel through which the polymer melt flows from the nozzle of the injection barrel into the mould cavity. An ejection system with ejector pins, used for pushing the part out of the mould cavity when the mould opens, a cooling system through which water is recirculated to rapidly remove the heat from the hot plastic, and finally air vents to permit evacuation of air from the cavities (but not the polymer).

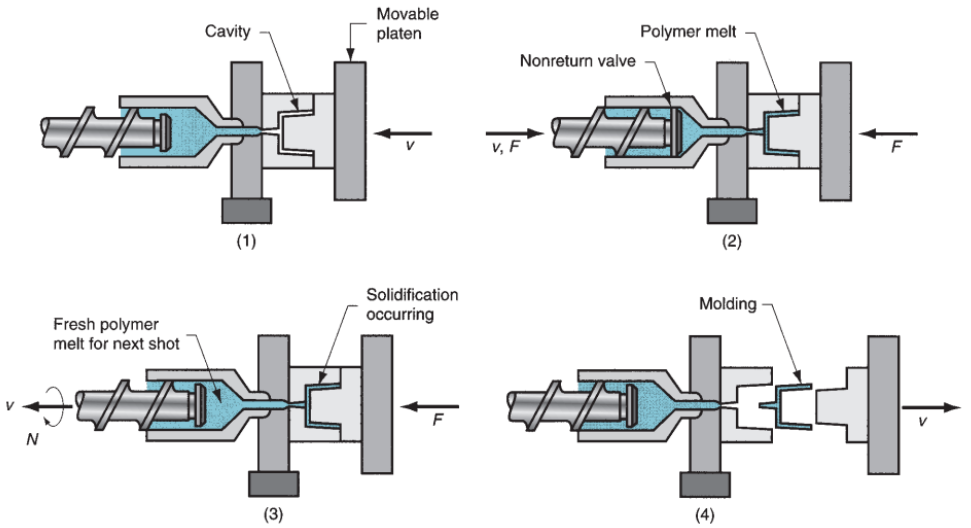

Figure 1.3: Schematic view of an injection moulding cycle [46].

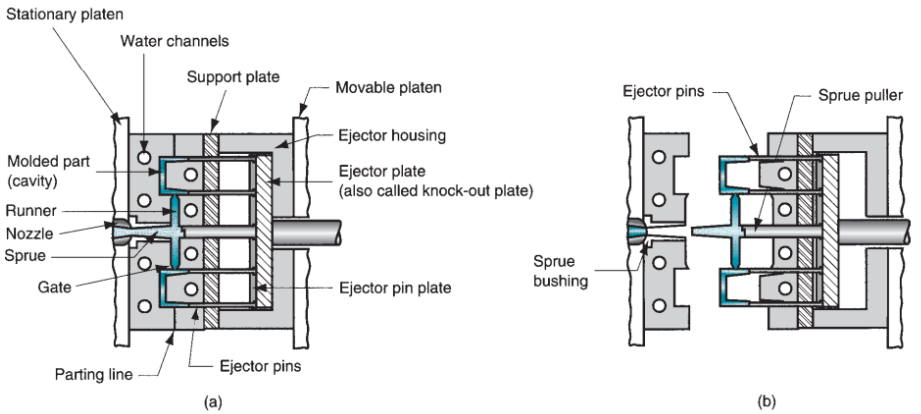

Figure 1.4: Schematic view of a two-plate plastic injection mould, a) closed and b) open [46].

Moulding conditions and process parameters play an important role for the plastic injection moulding. The quality of the moulded part including strength, warpage, and residual stress is greatly influenced by the conditions under which it is processed. Moulding conditions such as melt temperature, mould temperature, filling time, packing time, and packing pressure affect the productivity, cycle time, and energy consumption of the moulding process [47].

The production cycle time is typically between 10 and 30 seconds, although cycles of 1 minute or longer are not uncommon for large parts. Complex and intricate shapes are possible with injection moulding which makes it a suitable technique for large productions with very affordable prices once the process is optimized. The challenge most times is to fabricate a mould whose cavity is the same geometry as the part and that also allows for part removal. Part size can range from about 50 g up to about 25 kg. Once the mould is produced, it is

important to preserve its quality in order to produce as much plastic pieces as possible. However, the mould and ejection pins can be damaged during the process. Specifically, the adhesive and abrasive wear of the mould surface are important failure mechanisms in plastics processing. This problem originates in the prolonged contact with the molten plastics during moulding and the solidified plastics melt during the demoulding of plastic. On the other hand, the corrosion of mould surfaces due to exhaust gases or decomposition products from the plastics plays an important role in plastics processing [48,49].

To overcome the above-mentioned challenges is to modify the surface of the moulds by using innovative surface engineering such as coatings. Compared to an uncoated mould, Physical Vapour Deposition (PVD) coatings reduce release forces, maximize demoulding precision and results in decreased surface roughness after structuring. Furthermore, PVD coatings have improved wear protection due to the contact between the coating and the plastics melt during the moulding process [50,51]. Titanium and chromium-based nitrides hard coatings are the most widely used, although a clear trend is to explore new coatings structures and compositions [52,53].

1.3. Coating deposition techniques

One way of classifying coating deposition techniques is according to the phase in which a new material is deposited on top of the substrate surface, as shown in Figure 1.5.

Among all the techniques, PVD is a very versatile technique that allows the deposition of metallic and ceramic materials. PVD has other advantages over other coating techniques such as electrodeposition, plasma spraying or the more similar Chemical Vapour Deposition (CVD): very high purity deposits, excellent bonding to the substrate is possible, excellent surface finish can be achieved and droplet-free coatings can be deposited among others [54].

All the coatings deposited in this thesis were produced by the PVD technique. Some of them by the traditional PVD-Magnetron Sputtering (PVD-MS) technique and some others by the newest variation PVD-High Power Impulse Magnetron Sputtering (PVD-HIPIMS). The fundamental characteristics of these techniques are detailed below.

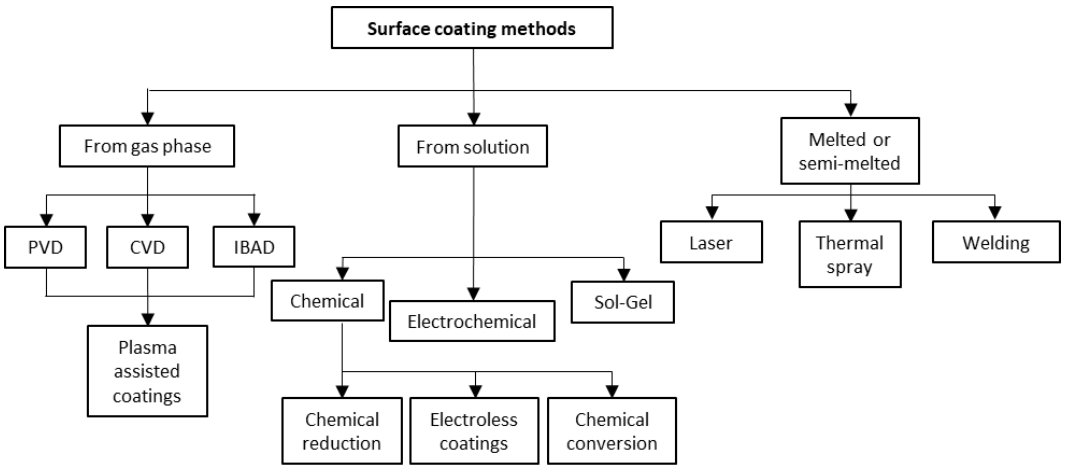

Figure 1.5: Coatings classification techniques based on the phase of the material to be deposited. Adapted from [54].

1.3.1. PVD

Sputter deposition is a plasma-based PVD technique commonly employed in thin film growth. In the basic sputtering process, a potential difference is applied between the negative cathode and a grounded anode causing ionization of the process gas, most commonly Ar, yielding a glow discharge according to Paschen's law [55,56]. Positive ionized gas atoms or molecules are accelerated towards the negatively biased cathode, which causes the removal (sputtering) of target material as atoms. The ejected material travels to the substrate in the gas phase and condenses into a film [57]. Secondary electrons are also emitted from the target surface as a result of the ion bombardment, and these electrons play an important role in maintaining the stability of the plasma. The grounded chamber walls and the substrate table can act as an anode, though usually a negative bias voltage is applied to the substrate table to exceed the floating potential and to achieve reproducible deposition conditions [58].The basic sputtering process that can be observed in Figure 1.6 has been known for many years and many materials have been successfully deposited using this technique. However, the process is limited by low deposition rates, low ionization efficiencies in the plasma and high substrate heating effects [59]. Some of these limitations have been overcome by the development of magnetron sputtering (MS).

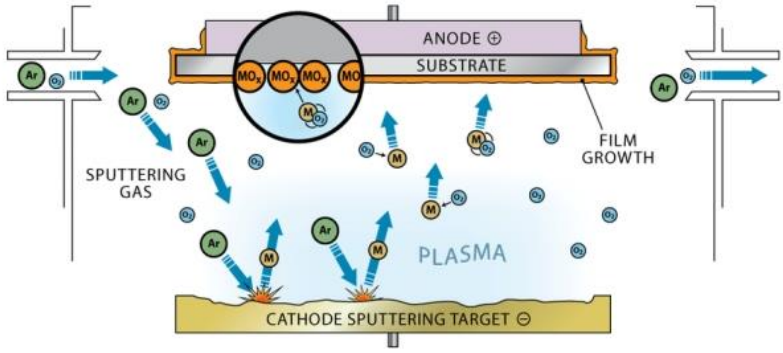

Figure 1.6: Schematic view of a PVD sputtering process [60].

1.3.1.1. PVD-MS

In a magnetron sputtering setup, electrons are confined into a magnetic field near the target surface. Increased number of electrons near the target surface enhances the level of ionization of the working gas and results in greater plasma density in the target vicinity. The working pressure can be decreased because of the increased plasma density, resulting in decreased collisional energy loss of the target bombarding ions in the gas phase, and thus enhanced sputtering rates [61]. Usually, the magnets are arranged in a ring-like pattern, with one pole in the center and the opposite pole circling it. Figure 1.7 shows a balanced magnetron configuration, i.e., closed-loop magnetic field lines, which results in a dense plasma in the target vicinity. Enhanced sputtering over a certain area of the target may cause a so-called racetrack target erosion pattern. The applied magnetic field configurations affect the ion-to-metal flux ratio arriving at the substrate, and can be used to tailor the morphology and properties of the growing film [58].

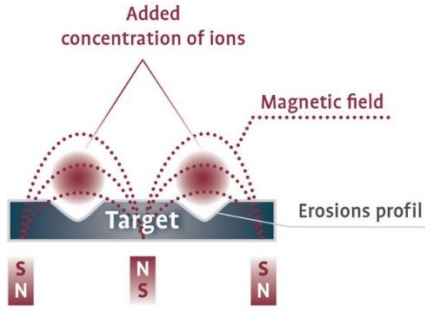

Figure 1.7: MS cross-section schematic view [62].

Magnetrons can be powered by a variety of methods, but the two main ones are radio frequency (RF) and direct current (DC). RF sputtering is used to sputter electrically insulating materials, although the sputtering rate is low. The RF field alternately opens and closes the trap, allowing electrons to escape when the trap is open and forcing electrons to cross magnetic field lines, and hence drop power in the discharge, which decreases the available

power at the target. Since most of the bombarding energy produces heat, large thermal gradients can be generated that result in fracturing the target if high power levels are used [63]. DC sputtering is the simplest and least expensive way to operate the magnetron. By using a direct current voltage to the magnetrons, the electrons can be deflected to stay near the target surface and, by an appropriate arrangement of the magnets, the electrons can be made to circulate on a closed path on the target surface, thus increasing the plasma density and increasing the sputtering rate of the target material [64]. Its primary limitation is that insulating materials take on a charge over time which can cause quality issues like arcing, or the poisoning of the target material with a charge that can result in the complete cessation of sputtering [63].

In magnetron sputtering processes, the degree of ionization of the plasma particles is relatively low, typically less than 1%, resulting in a low total ion flux towards the growing film [65]. The high bias voltages used in combination with a majority of Ar+ ions during the bombardment, can lead to Ar atoms subplantation in the coatings [66], which in turn can generate lattice defects, high residual stresses and poor film adhesion [67,68]. The increase of the fraction of the ionized sputtered species has been an aim of much research works during the recent decades. Among all the studies, the technique that has been most widely used is the so-called High Power Impulse Magnetron Sputtering (HiPIMS).

1.3.2. Reactive sputtering

Using an electrically conductive target makes powering the magnetron much easier, however, it limits the choice in the materials that can be deposited with this technique. To mitigate this problem, a reactive gas can be added to the plasma. The reactive gas, e.g., nitrogen, oxygen, or acetylene, can react with the sputtered material to form a compound on the substrate. However, the addition of the reactive gas to the discharge influences the deposition process in several ways, while increasing the complexity of the overall process. Some aspects of the reactive sputter deposition processes are discussed in this section.

Reactive sputter deposition from an elemental target relies on: (1) the reaction of the depositing species with a gaseous species; (2) reaction with an adsorbed species; or (3) reaction with a co-depositing species to form a compound [69]. The reactive gas may be in the molecular state (e.g. N_2, O_2) or may be “activated” to form a more chemically reactive or more easily adsorbed species (e.g. N, O, N^+, O^+, etc.). Typically, the reactive gases have low atomic masses and are thus not effective in sputtering. It is therefore desirable to have a heavier inert gas, such as argon, to aid in sputtering. Mixing argon with the reactive gas also aids in activating the reactive gas by the Penning ionization/excitation processes [70,71].

The addition of a reactive gas into the sputtering atmosphere leads to target poisoning, i.e. target coverage/chemisorption [72], and/or implantation [73] of reactive gas species at the target surface and the sub-surface layers, respectively. This surface target poisoning greatly reduces the sputtering rate and efficiency of the process [74,75]. Reactive

sputtering processes often show hysteresis in relation to the reactive gas flow and the change in target surface conditions. This means that once the poisoned surface conditions have been achieved, the reactive gas flow has to be lowered significantly to reach metallic surface conditions again. The magnitude of hysteresis depends on the sputter yields of the clean target material and the compound, and also on the pumping speed of the system [63,76,77]. It has been reported that the high peak powers used in HiPIMS technology allow better control over the onset of target poisoning by efficiently removing the poisoned surface layer during the pulse [78,79]. Moreover, target poisoning by reactive gas ion implantation between the pulses is limited, reducing the compound formation on the target [80,81].

In this thesis, two different reactive gases were used to develop coatings: nitrogen and acetylene. Nitrogen is commonly used in reactive magnetron sputtering of metal nitrides, especially in the hard coating industry to deposit coatings such as TiN [82], CrN [83] and TiAlN [84]. Hydrocarbon gases such as acetylene and methane are normally used to synthesise amorphous carbon thin films and metal carbides such as TiC/a-C:H [85] and CrC/a-C:H [86] coatings.

1.3.3. PVD-HiPIMS

High power pulsed magnetron sputtering (HPPMS or HIPPMS), otherwise called high power impulse magnetron sputtering (HiPIMS), uses high peak voltages and very high peak powers (typically in the range of a few kW/cm^2) at very low duration (in the order of microseconds) to give a low average power densities similar to those during the DC-MS technique [80,87]. Typical waveforms obtained for the HiPIMS discharge voltage and current for a 10 µs pulse lengths can be observed in Figure 1.8. The low average target power density is necessary to prevent overheating of the cathode and damage of the magnets and the target. A schematic view of the pulsed discharges based on the peak power density at the target, combined with the duty cycle, can be observed in Figure 1.9. Pulse frequencies used in HiPIMS can range from a few tens of Hz to a few kHz, and the pulse on-time from a few microseconds to several hundreds of microseconds. Power on/off ratios during the cycle (duty cycle) vary from a few percent to a few tens of percent. The experimental realization of HiPIMS requires power supplies different to those used in conventional magnetron sputtering processes based on the technology requirements. The high energy delivered per pulse results in increased plasma densities in front of the target, which leads to elevated amounts of ionized sputtered material due to electron impact ionization. In HiPIMS discharges, the plasma density can reach values up to 10^{19} ions/cm^3 [88,89]. This high-ionized plasma leads to better control of the film growth through the application of the substrate bias which can control the ion arrival energy and guide the deposition material to the substrate [77]. Thus, it has been reported that the use of high-energetic plasma can significantly influence the structure and properties of the coatings. This includes changes in the film orientation (coatings texture), grain size, film stress and more important an increase in the coating density [77,90–92].

One drawback of this technique is that, by using a sharply peaked voltage pulse, the HiPIMS magnetron sputtering rate is lower than would normally be attained with the same power input using DC-MS [93]. Some explanations for the lowered deposition rates include back-attraction of charged metal ions [94], magnetic confinement of the sputtered species [95] and non-linear energetic dependence of the sputtering yield [96]. Another concern is the existence of multiply charged target metal ions, which are accelerated into higher kinetic energies by the substrate bias and can cause undesirable effects, such as ion implantation and higher residual stresses in the coatings [97].

In this word, HiPIMS and reactive HiPIMS techniques are used for depositing different nanostructured coatings in industrial-scale reactors. The influence of the deposition parameters on the final properties of the coatings are studied.

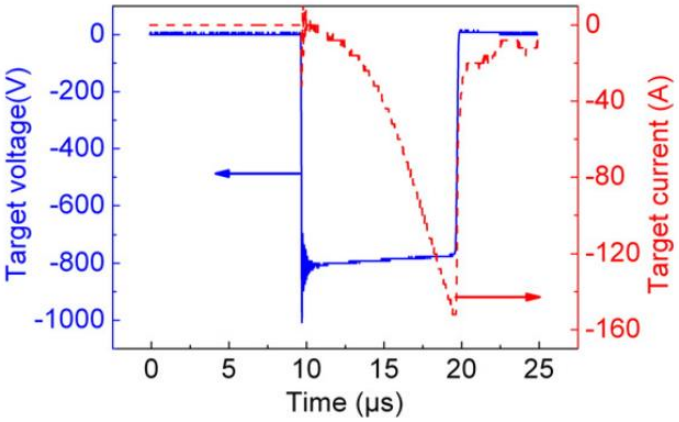

Figure 1.8: Evolution of the magnetron target voltage and current during HiPIMS sputtering for a 10 μs pulse length [80].

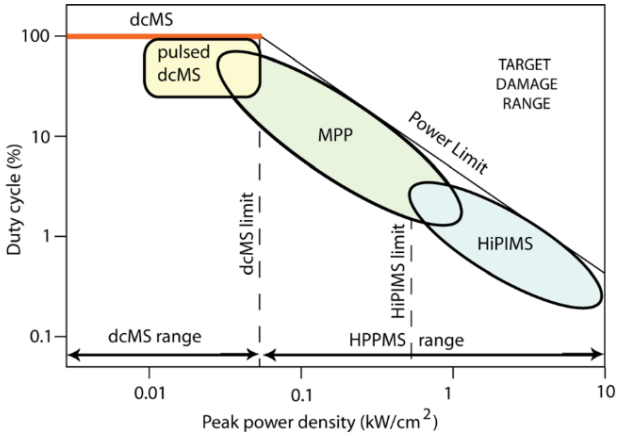

Figure 1.9: Nomenclature for pulsed discharges based on the peak power density at the target, combined with the duty cycle [77].

1.3.4. Coating morphology

The production of coatings by vapor deposition technique is a classic case of heterogeneous nucleation [98]. It is well known that the growth of thin films proceeds through consecutive stages characterised by specific processes of structure evolution: nucleation, coalescence and thickness growth [99].

First, the atoms impacting on the substrate transfer kinetic energy to the crystalline lattice and become adsorbed on the substrate surface. Next, these adsorbed atoms, called adatoms, diffuse over the surface, which has multiple adsorption sites of different stability and chemical potential determined by the atomic structure of the crystalline lattice. They can then be desorbed, either by evaporation or sputtering or, more commonly, trapped in low-energy lattice sites that depend, among others, on the density of adatoms, the deformation state of the surface or the curvature of the surface. Finally, the incorporated atoms readjust their positions within the lattice by bulk diffusion processes [100].

From the initially deposited atoms, and depending on the interaction between the atoms of the substrate and the coating, three modes of growth can occur:

- Layer by layer: If interaction between substrate and film atoms is greater than between adjacent film atoms, layers of material grow one on top of the other (Frank–van der Merwe mode).
- Island: If interaction between film atoms is greater than between adjacent film and substrate atoms, separate three-dimensional islands form on the substrate (Volmer–Weber mode)
- Layer plus Island: One or two monolayers form first and are followed by individual islands (Stranski–Krastanov mode).

The growth mode is controlled not only by interface energies, but also by supersaturation. Growth tends to shift from island to layer as supersaturation increases [101].

The next step of the three-dimensional film formation is the coalescence of islands to form a continuous network. This stage includes the island growth followed by a coalescence of islands, the formation of polycrystalline islands and channels, and finally the development of a continuous structure.

Once the first nanometres of the coating (1-20nm) have been produced, the coating growth (i.e. the final structure of the coatings) is determined by shadowing, surface diffusion, bulk diffusion and recrystallisation processes [100].

Several authors have attempted to summarize the influence of deposition parameters on film morphology and microstructure in a single diagram. These diagrams are known as structure zone models (SZMs). The SZM best known in the sputter deposition community is the one published by Thornton [102], which shows the coating microstructure and morphology as a function of the deposition pressure and the substrate temperature. These two parameters

are the most important ones affecting the coating growth. The first one has a direct impact on the amount of plasma particles that reaches the coatings surface and are able to transfer its energy to the adatoms [103]. The second one, is related with the energy transferred to the adatoms that allow its diffusion throughout the substrate surface [80]. Thornston's SZM can be observed in Figure 1.10.

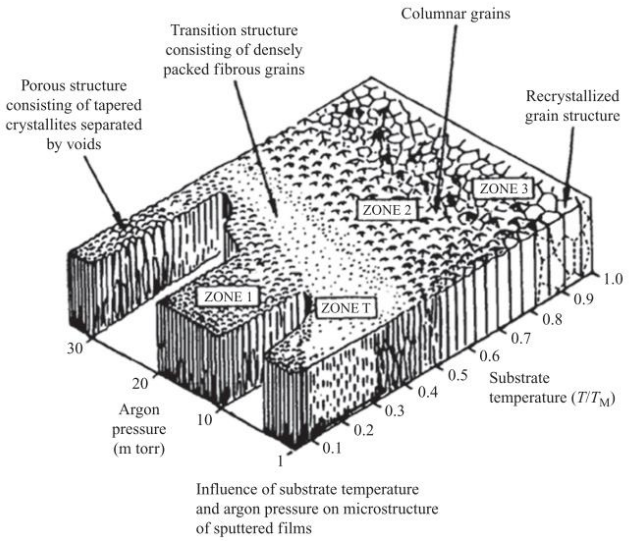

Figure 1.10: Thornton's model of thin coating structure [104].

Four zones exist in Thornton's model, in which different structures are obtained [63,102].

In zone I, the film is composed of fibres of small diameter (1–10 nm) determined by the nucleation density and statistical fluctuation. The crystalline fibres grow out of the primary nuclei and proceed to the top of the film. This is a rather homogeneous structure along the thickness of the film with increasing diameter of fibres by increasing T/T_m where T is the substrate temperature and T_m is the melting point of the film material. The crystals contain probably high density of defects, and the grain boundaries are porous. This structure belongs to the temperature interval of $0 < T/T_m < 0.2$ where neither the bulk diffusion nor the self-surface diffusion has remarkable value.

In zone T, the structure is inhomogeneous along the film thickness in the form of fine crystallite grains at the substrate but columnar in the upper part of the coating. This zone belongs to the temperature interval of $0.2 < T/T_m < 0.4$. The diffusion is remarkable; however, the grain boundary migration is strongly limited in this region.

Zone II represents a homogeneous structure along the film thickness composed of columns penetrating from the bottom to the top of the film. This zone is characteristic for high substrate temperatures $T/T_m > 0.4$.

In zone III, the structure is characterised by globular three-dimensional grains, which is a direct sign that the crystal growth has been blocked periodically. This kind of structure is generally attributed to the highest substrate temperature range.

The model proposed by Thornton can be used to ideally predict the coating microstructure for magnetron sputtering technique, however, Anders [105] describes a new SZM which includes structures obtained by the use of high-energy ions, as in the case HiPIMS (Figure 1.11).

This diagram represents the morphology of the coatings as a function of the generalised temperature T^* (on a logarithmic scale) which includes the substrate temperature and any changes caused by the potential energy of particles reaching the surface, together with a normalised energy E^* (also on a logarithmic scale) which describes the displacement and heating by the kinetic energy of particle bombardment. In addition, an effective thickness t^* is presented on the third axis, which includes the consequences of densification and sputtering, even up to ionic attack effects.

With increasing substrate temperature, a transition from a porous phase (zone 1) to densely packed fibrous grains (zone T) is observed, followed by a zone of columnar growth (zone 2) and finally a recrystallised grain structure (zone 3) or a zone of single crystals. Because of ion bombardment, thermal energy is replaced by kinetic energy, allowing similar morphology at different combinations of energy and temperature [106].

Most PVD coatings are deposited under conditions that allow obtaining coatings with columnar grains oriented approximately parallel to the direction of growth. However, not all columnar grains extend the coating thickness, showing that some grains are nucleated during the coating growth. This indicates that real coatings present some impurities and defects that limit the grains growth and re-nucleation. The most common impurity is oxygen, while the most common defect is microdroplets. The number and size of microdroplets depends on the deposition parameters [104].

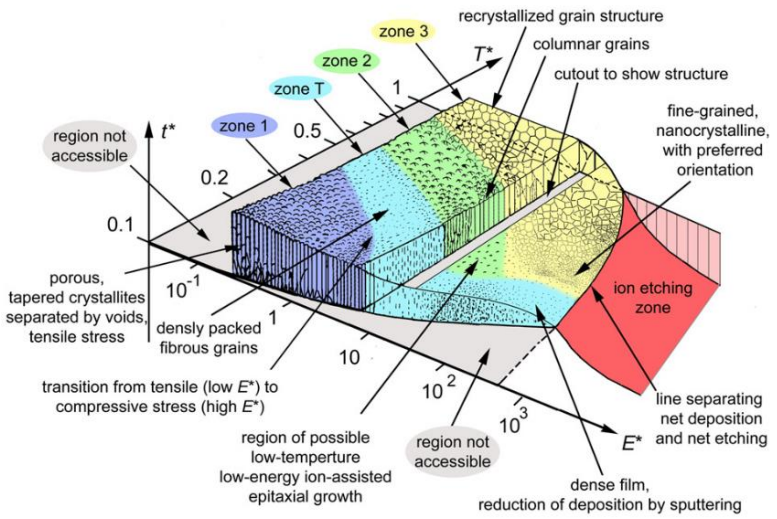

Figure 1.11: SZM model proposed by Anders as a function of generalized temperature T, normalised energy flux E*, and the net thickness t** [105].

1.4. Coatings classification

One way of minimizing wear and increase the lifetime of both the moulds, dies and the moving components that comprise the systems explained earlier, is by surface modifications. Functional surface treatments such as coatings can improve the mechanical [107], tribological [108] and even optical properties of the substrate [109].

Coatings can be classified according to their internal structure as shown in Figure 1.12. The emergence of nanotechnology and the possibilities it offers for manipulation at the nanoscale range, has enabled the design of coatings to fulfil ever more demanding tailor-made properties. This allows the development of coatings in which a second phase or component is added. This second element can be diluted within the coating matrix to form a single-phase solid solution, or it can form a second phase within the matrix to form a two-phase coating. The way these two phases are combined can lead to a gradient, nanocomposite or multilayer design.

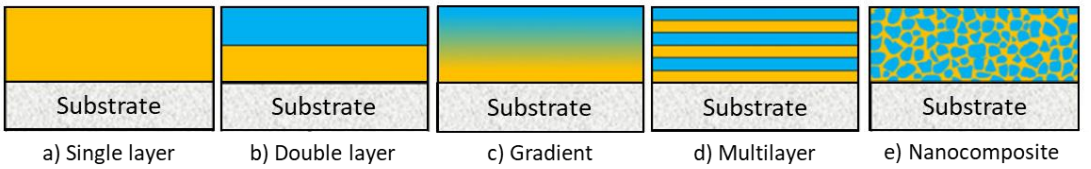

Figure 1.12: Schematic representation of different types of coatings based on its structure. Adapted from [110].

1.4.1. Single layer coatings

Figure 1.12a shows a typical schematic view of a single layer coating. As the name suggests, these coatings are homogeneous throughout their structure and are usually synthesised in a single deposition process. They are the simplest coatings structurally speaking. Examples of such coatings are high-quality synthetic diamond deposited by chemical vapour deposition (CVD) which is known for its high hardness similar to natural diamond [111], some polymers such as ultra-high molecular-weight polyethylene (UHMWPE) which is widely used to improve the lifetime of prostheses and implants [112], and TiB_2 which is well known for its good chemical stability and excellent mechanical properties [113,114].

Sometimes, double layer coating is recommended to be used (Figure 1.12b). Thus, we can combine, for instance, the bottom layer having a high hardness (high wear resistance) and the relatively soft top layer with a low friction coefficient [115]. If the chemical nature of the elements of the two different layers are too different, some adhesion problems may occur in the interphase, leading to delamination of the coatings. Therefore, to overcome this problem, a gradient-type structure is usually desirable.

1.4.2. Alloyed and gradient coatings

Adding different elements to an existing coating is one possibility to adapt some of its properties to a value desired for specific applications. Different elements in the coating can be mixed throughout its structure (usually by co-depositing two materials) or the composition can be varied according to the depth of the coating regarding the substrate, thus gradually varying its properties (Figure 1.12c).

For example, Ni and Cr are added into the whole CrC coatings to enhance their mechanical properties and increase lifetime of piston rings [116], and C is added to TiB_2 and to WC coatings for its feasibility to form a lubricant phase while preserving the hardness of the coatings and therefore can be used for advanced cutting tools for lubricant-free machining [117,118].

1.4.3. Multilayer coatings

Although single-layer coatings have been used in many engineering fields, their performance still has many drawbacks. They offer only one set of properties, which can limit their adaptability to some performance requirements. In addition, achieving high adhesion and uniformity on various substrates can be a real challenge for this type of coating. But the main limitation of monolayer coatings is that they do not withstand the extreme conditions used in some industrial processes. The advent of new materials makes manufacturing processes more and more demanding, which leads to a real need to develop new coatings with the ability to resist these conditions.

One possible solution to overcome these limitations is to use a multilayer coating that combines different components with varied physical and chemical properties. In addition, multilayer coating with alternating layers only containing two components can lead to improved performance compared to a coating with only two different layers. Properties of multilayer coatings strongly depend on several factors [104] as can be observed in Figure 1.13 but are mainly attributed to phenomena occurring at the nano-scale range [119].

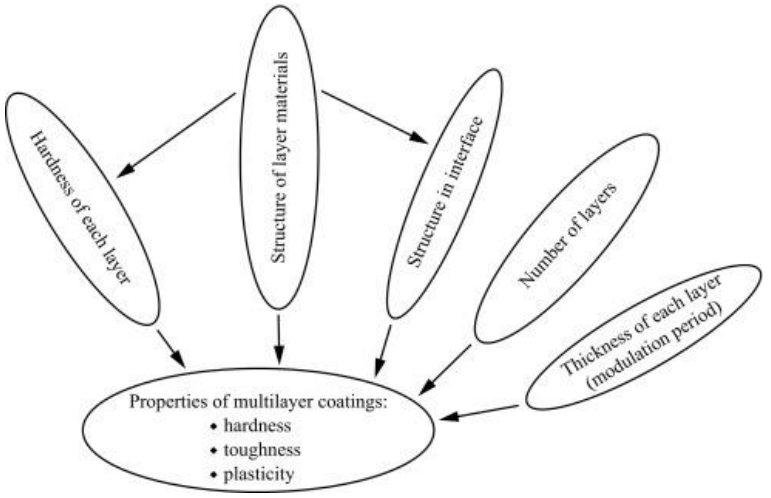

Figure 1.13: Different factor affecting the properties of a multilayer coating based on the properties of the single layers [104].

Research into multilayer PVD coatings started in the 1970s, following Koehler's proposed models [120]. Koehler's model suggested that materials with higher yield strength could be achieved by alternating thin layers with differing shear moduli, thus inhibiting dislocation formation and mobility. This was studied with Al/AlxOy coatings which also revealed a Hall–Petch effect between yield stress and layer spacing [121]. Multilayer coatings have better wear resistance, resistance to fracture (higher critical load) and hardness than monolayer coatings. The linear correlation between hardness and period thickness was then reported by Lehoczky [122] with Al-Cu laminates but it is also based on Koehler's model.

Layers of TiN and TiCN, each several microns thick, made up the earliest multilayer coatings for cutting tool applications. It has been demonstrated that these multilayer coatings can extend the cutting tool's life over that of a single TiN or TiC coating [123]. The combination of a nitride or carbide material and an oxide, such as TiN or TiC and Al_2O_3, is the basis for other successful multilayer coatings for industrial applications. Its strength and finer grain size from the nitride/carbide layer combined with the oxide layer's chemical resistance made this coating ideal for some applications.

Over the past years, a new class of multilayer coatings emerged with excellent properties such as high hardness and wear resistance. These multilayers are based on very thin layers (2-10nm) of transition metal nitrides, normally deposited by PVD-MS, and are commonly named nanoscale multilayer coatings or Superlattices. The fundamental argument for realising this concept is the interruption of the columnar grain growth with the several repetitions of two different layers.

They have been the subject of many recent studies to determine the mechanisms that give rise to such high hardness. This was found to be mainly associated with the hindering of dislocation movements arising from the lattice mismatch at the interfaces [124,125]. In addition, the decrease in the crystallite size by reducing the bilayer period (Λ, which corresponds to the thickness of two of the alternating monolayers) influence the hardness of the films because of the Hall-Petch effect [126,127].

Properties of multilayer coating also depend on the number of layers and the thickness of each layer. According to Holleck and Schier [128], the thickness of interfaces is between 1 and 3 nm depending on the kind of materials meeting together. Therefore, with increasing layer number and decreasing layer thickness the interfaces which can be coherent, incoherent or semi-coherent, play dominant role in the properties of a multilayer coating. Thus, it is important to select materials with similar crystallographic structure and lattice parameter to minimize the interfacial stress, and the risk of crack initiation and layer delamination [129].

Among the years, various multilayer coatings have been designed, and the inherent functional mechanisms were elucidated. One way of classifying them is by the chemical nature of the inner layers which give rise to different coating properties.

1. Metal-metal multilayer coatings

   This type of multilayer coating is based on the superposition of layers of metallic nature. In general, they have low hardness values and are commonly used for tribological purposes, [130,131] or corrosion resistance applications [132].

   Anand et. al. [131] reported an increase in the tribological performance of Sn-Ni multilayer coatings with respect the monolithic ones by the formation of hard intermetallic sublayers with an overall rise in the coating hardness.

   Stoudt et. al. [133] developed a nanoscale multilayer coating with two ductile metals (Cu-Ni) to improve fatigue resistance in a high stacking fault energy FCC metal. Testing revealed that this coating effectively prevented fatigue crack initiation, outperforming monolithic layers of the same metals. This demonstrates the potential of nanoscale multilayer coatings in enhancing material fatigue resistance.

2. Metal-ceramic multilayer coatings

To increase the coating's toughness and reduce internal stress, it is advantageous to design multilayer coatings that combine transition metal nitride layers and metallic layers.

In metal-ceramic multilayer coatings, such as Cr-CrN (see Figure 1.14) [134,135], cracks are initiated at interfaces and developed in hard and brittle ceramic layers but then block at the next interface thus increasing the fracture toughness of these coatings.

The impact of Ti layer thickness on the internal stress and crystalline structure of multilayer TiN/Ti coatings was studied by Cheng et al. [136]. It was discovered that increasing the layer thickness of Ti can reduce the internal stress between Ti layers and TiN layers as well as the internal stress of the TiN/Ti coating. Additionally, by increasing the layer thickness of Ti, it is possible to enhance the crystallinity of the Ti and TiN phases and reduce lattice strain.

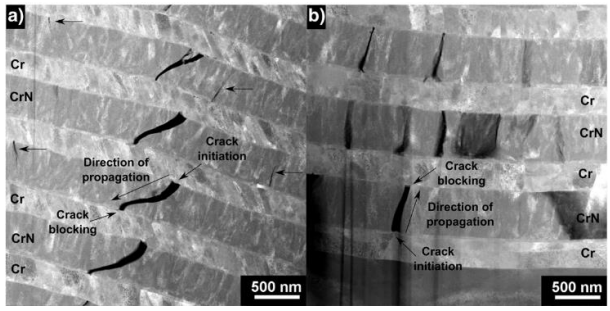

Figure 1.14: Crack propagation behaviour of a multilayer coating [135].

3. Ceramic-ceramic multilayer coatings.

They are based on the combination of two different transition metal nitrides, for example TiN/CrN [137], CrN/NbN [138] and ZrN/TiN [139]. They are well known for their outstanding hardness values, good mechanical properties, and high wear resistance. Recently, nanoscale multilayer coatings have attracted a lot of interest in industry and scientific circles. Most researchers focus on the nanoscale structure and mechanical properties; however, their industrial deposition and functional application is still under exploration.

Depositing multilayer and superlattice coatings is difficult using laboratory scale reactors; producing them in a large industrial scale system is a real hard challenge for several reasons. First, the deposition process must be sufficiently stable to deposit nm-thick layers over a long enough time to make a coating that is generally a few microns thick. Second, two

different materials must be deposited simultaneously to make the layered structure. The substrates are mounted on a planetary rotating table in which cross contamination of the sputtered fluxes can occur. Normally, reactive sputtering is preferred over sputtering from a compound target to achieve higher deposition rates. However, this poses the challenging problem of depositing two materials simultaneously that require different partial pressures of a reactive gas. Also, multilayer coatings are more difficult to characterize than homogeneous films. It is important to characterize the grain structure and crystallographic orientation of each layer, as well as any epitaxial relationships between the layers and the magnitude of the composition modulation. Moreover, very specific high-resolution characterization techniques are required for the characterization of superlattice coatings, which are also very expensive and difficult to implement in a company.

1.4.4. Nanocomposite coatings

Nanocomposite material consists out of several phases which at least one, two or three dimensions are in the nanometer range. Taking material dimensions down to nanometer level creates phase interfaces which are very important for enhancement of materials properties. The ratio between surface area and volume of the materials used during nanocomposites preparation is directly involved in understanding of structure-property relationship. Nanocomposites incorporate materials such as carbon nanotubes (CNTs) or mineral, metal or other nanoparticles which can enhance significantly a composite's properties [140–143]. They are attracting great interest; some are already commercially available, and they have the potential to offer all manner of unique capabilities.

Among them, nanocomposite coatings are a new generation of materials consisting of at least two different phases. Their development can be traced back to the latter half of the 20th century with the incorporation of nanoparticles into various matrices to enhance material properties, giving rise to nanoscale-reinforced materials [144–146]. The 21st century brought about a more systematic exploration of nanocomposite coatings, particularly in the context of improving mechanical and tribological properties. Research papers began to discuss nanocomposite coatings for wear-resistant applications in industries like automotive and aerospace [147–149].

In this context, two different materials, normally named the crystalline and the amorphous phase, are deposited simultaneously and the nanocomposite material forms by a phase separation. A prerequisite for the phase separation is a complete immiscibility of the two phases. Normally, crystallites are embedded in an amorphous matrix, with grain sizes in the nanometer range [150].

The nanocomposite materials exhibit unique functional properties due to (1) composition of very small grains (<10 nm), (2) boundary regions surrounded by individual grains of the same and different phase, and (3) different behaviour of the grains in nanocomposite coatings compared with bulk materials. The main property of nanocomposite

coatings is an increased hardness [151]. The main reasons of the hardness increase are the dislocation-induced plastic deformation, the nanostructure of materials, and cohesive forces between atoms of neighbouring grains [150].

According to Musil and Vleck [152], nanocomposites can be classified depending on the nature of the amorphous phase. If this second phase is hard, these nanocomposites show super- and ultra-hardness. Some examples of these nanocomposites are TiN/Si_3N_4 [153,154], CrN/SiNx [155] and CrAlN/SiNx [156] coatings. The other kind of nanocomposites consists of those formed by crystals of a hard phase embedded in a soft phase. These soft phases usually have self-lubricant properties and consist of transition metal carbides dispersed in amorphous carbon (a-C) matrix namely as MeC/a-C, for example TiC/a-C [157,158], WC/a-C [159], TiBC/a-C [160,161] and NbC/a-C [162].

This last group of nanocomposite coatings attracted especial interest industrially in many areas like cutting, forming and casting tools, mechanical components in general and even biomedical prostheses. The desire to increase component life and performance drives the development of enhanced mechanical and thermal surface qualities via hard and lubricant coatings. One of the problems associated with coatings based on amorphous a-C(:H) matrixes is that they do not allow working at temperatures above 350°C, leading to degradation of the coating [10,11]. The introduction of refractory metal nitrides into amorphous a-C(:H) coatings could improve the thermal resistance of these coatings enabling higher working temperatures while maintaining tribological properties.

Coatings can be also classified into two big groups depending on their final applicability: hard coatings and lubricant coatings.

1.4.5. Hard coatings

As the name suggests, these are coatings that have a high hardness. When applied to rigid and relatively hard substrates, they are highly beneficial in reducing tool wear [163]. In general, materials that provide characteristics of high hardness, high mechanical strength, and good chemical stability at high or moderate temperatures are of a ceramic nature. The final properties are determined by the type of bond and their microstructure.

A mixture of metallic, covalent and ionic components prevail in the bonding of these transition metal components [18]. Due to the overlap between atomic orbitals, very specific properties, such as electrical conductivity, metallic lustre, ductility and high hardness are obtained. The adhesion of these layers is usually high due to the similarity of properties with the most commonly used metal substrate. This group of coatings includes nitrides, carbides and oxides of transition metals such as TiN, CrN, TiC, NbN, WC, Al_2O_3, etc.

1.4.6. Lubricant coatings

Lubricating materials are considered as soft materials. They are used to facilitate the relative motion of solid bodies by minimising friction and wear between interacting surfaces. They can be classified into three categories:

- Soft metals: These include lead, silver, gold and indium and are characterised by a small shear modulus. These metals can provide effective isolation on the surfaces of materials, reducing friction, providing a lubrication effect [164]. The thickness of the coatings is a critical parameter in this case. Very thin layers are penetrated by the micro asperities generated during working processes increasing the friction coefficient and contrary, very thick layers result in larger contact areas thus increasing the friction coefficient according to the model proposed by Bowden-Tabor [165].

- Polymers: Polymers are a very versatile group of materials. These materials are characterised by high corrosion resistance, moderate wear resistance and self-lubricating capability. The most commonly used lubricating polymers are polytetrafluoride ethylene (PTFE), polyimides and elastomers. Low friction coefficient arises from a weak intermolecular bond that allows the alignment of molecules in the contact zone [166].

- Lamellar compounds: This group includes molybdenum sulphide (MoS_2) and graphite. They both have a lamellar structure in which the atoms are strongly bonded forming a plane. However, weak bonds between different layers allow sliding between planes acting as solid lubricants [167].

In recent years, considerable attention has been devoted to carbon-based solid lubricant films, such as diamond-like-carbon (DLC) coatings. DLC is a generic term used to describe a range of metastable amorphous carbon films with varying portions of sp^2 carbon, sp^3 carbon and hydrogen.

The carbon atoms in the allotropic structure of C diamond have tetrahedral coordination with very short bond distances. This gives the system high rigidity, high hardness, and insulating properties. On the other hand, graphitic carbon has a triangular configuration of atoms forming a plane and the bond distance is also small due to conjugated double bonds within the hexagonal ring. In this case, the Van der Waals-type interactions (electrons in the unhybridized p_z orbital) are weak, allowing easy exfoliation and easy sliding in between the layers, proving the lubricating nature [168]. The mixture of these two structures provides a great versatility of mechanical and tribological properties, depending on the ratio between sp^2 and sp^3 bonds. In general, amorphous carbon can have a mixture of sp^3, sp^2 and even sp^1 bonds with the possible presence of up to 60 at.% of hydrogen [169]. DLCs with very high C-C sp^3 fractions are called tetrahedral amorphous carbon (ta-C) or (ta-C:H for the hydrogenated form). By contrast, DLCs with a low C-C sp^3 fraction are named a-C(:H).

Figure 1.15a shows the ternary phase diagram of the amorphous carbon family with the above phases present [170]. Figure 1.15b shows a typical DLC structure [169].

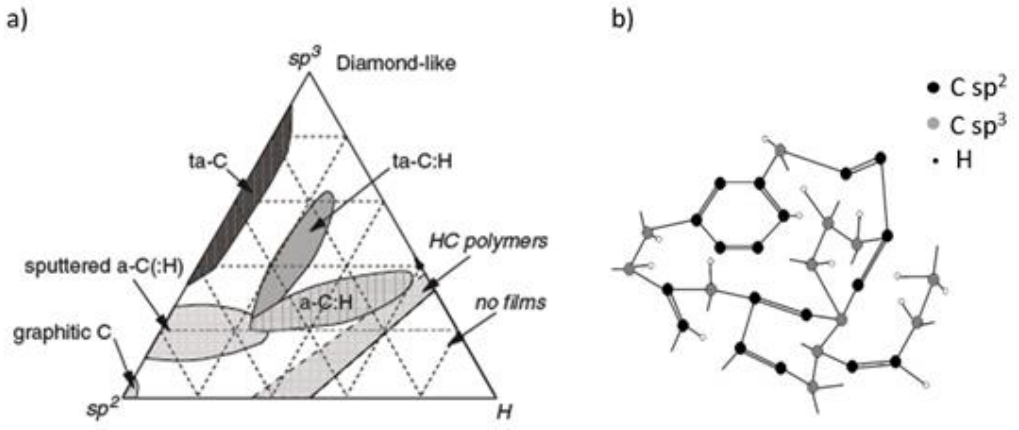

Figure 1.15: a) Ternary phase diagram of the DLC family; b) Binding structure of a DLC, including C-sp^3, C-sp^2 and H.

High hardness values (up to 90 GPa), low friction coefficients ($0.005<\mu<0.1$) and low wear coefficients ($10^{-9}<k<10^{-7}$ mm^3/Nm), together with good chemical resistance, qualify these coatings as good candidates for tribological and anti-wear applications for mechanical, optical or electronic applications [171,172].

The final application of the coating, the desired properties, the thickness of the coating and the temperature limitations of the substrate, among others, determine the choice of the coating deposition technique and parameters.

1.4.7. Parameters affecting PVD coatings

The composition of the coatings, the deposition technique and the parameters used for its deposition highly influence the structural and mechanical properties of the coatings [173–175]. Substrate temperature, gas pressure, bias voltage and target power, among others, influence the coating morphology, crystalline size, coating density, hardness, adhesion, fracture toughness, etc. Some of these parameters are related to the coating properties according to Figure 1.16.

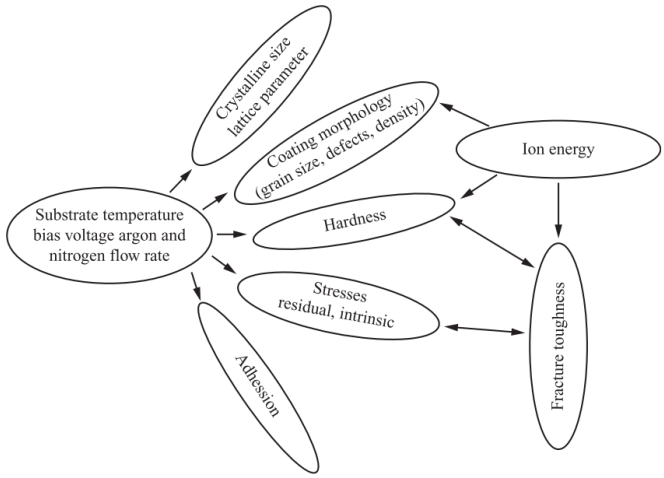

Figure 1.16: Influence of the deposition parameters on PVD coating properties [104].

However, it is difficult to obtain a generic relation between these parameters and the final properties of the coatings, since they highly depend on the material being deposited and on the complete set of deposition parameters being used. Many scientific studies have been done on the effect of one of these parameters on the final properties of the coatings.

To give some examples, Lewin *et. al.* reported an increase of metal ions and dissociated nitrogen in the plasma, resulting in a denser, more textured crystalline phase of Al-Si-N HiPIMS coatings compared to those deposited by DC-MS. Also, an increase in the coating hardness was observed without an addition of residual stress for the HiPIMS deposited coatings [176].

Chen *et. al.* compared Ti-Al-N coatings deposited by both arc evaporation and DC-MS techniques. Denser structures with higher adhesive strengths with the substrate were obtained by arc evaporation due to the higher adatom mobility arising from higher ion to neutral ratio. However, evaporated Ti–Al–N coating exhibited the typical growth defects originating from incorporated macro-particles, while the sputter deposited coating was rather homogeneous [177].

Gautier *et. al.* and Bielawski *et. al.* observed a decrease of the intrinsic residual stress caused by a decrease of the bias voltage for magnetron-sputtered CrN and TiN coatings respectively [178,179]. Bias voltage also has an influence on the mass density [180], adhesion [181] and hardness of coatings [182].

The substrate temperature also has an effect in the coating properties. Helmersson *et. al.* reported an increase in the adhesion of the coating to the substrate with increasing substrate temperature for TiN coatings deposited by reactive DC-MS on high-speed steels [183]. Aditionally, Pelleg *et. al.* described the preferred orientation of TiN coatings in the (200)

direction in case of low substrate temperatures and/or low layer thicknesses and (111) preferred orientation in case of higher layer thicknesses or high temperatures [184].

The HiPIMS pulse length has also been reported to influence the properties of the coatings. Wang *et. al*. demonstrated that varying the HiPIMS pulse length from 50 to 200 µs it is possible to change the morphology, chemical composition, grain size and hardness of WC-DLC coatings although it does not have a lineal trend [118].

Microstructure and properties of coatings are strongly influenced by the deposition technique and parameters used. Thus, the study of the deposition parameters will allow us to develop coatings with the desired properties. In general terms, the HiPIMS deposition technique is much more complicated than conventional PVD-MS, mainly because of the substantial increase in parameters affecting the deposition of coatings. In addition, developing and depositing nanostructured coatings in industrial-scale reactors is even more challenging. Having a precise control over parameters like target-substrate distance, gas flow, and pulse frequency is crucial for ensuring the coating quality and uniformity.

CHAPTER 2

OBJECTIVES

2. OBJECTIVES

The use of coatings to modify the mechanical, tribological and even optical properties of the substrate is widely described, and they are frequently used to increase the lifetime and improve the performance of cutting tools, dies and moulds.

Even though PVD-MS method has been the most studied technique due to the possibility of evaporating non-conductive ceramic materials for obtaining very homogeneous coatings with controlled composition and morphology, the continuous need to improve the efficiency of industrial processes has led to develop a new coating deposition technique like HiPIMS. This technique is still under investigation, and its implementation in industry still has some drawbacks.

The main objective of this thesis is to design and deposit nanostructured ceramic coatings employing the HiPIMS technique within an industrial-scale reactor. These coatings find utility in diverse industrial applications, notably in the operations involving dies and moulds. This general objective is developed through the following specific objectives:

1. To study titanium diboride (TiB_2) coatings deposited by HiPIMS. This is a simple single-layer system which can be directly sputtered from cathodes of the same material, leading to non-reactive HiPIMS deposition. The incorporation of carbon in these structures is also studied with the aim of achieving nanostructured coatings, either with the formation of bilayer structures or nanocomposite coatings.
2. To study the formation of lubricant carbon-based nanocomposite structures doped with refractory metals. In this case, niobium (Nb) is used as the metal part, and graphite and acetylene as carbon sources, which makes it a reactive sputtering process. The difference between the deposition method, either by DC-MS or HiPIMS, on the final properties of the coatings is studied.
3. To study the formation of multilayer-type nanostructured coatings deposited by HiPIMS. For this purpose, reactive HiPIMS will be used to deposit titanium nitride/chromium nitride (TiN/CrN) based coatings. First, the effect of deposition time and the number of monolayers on the formation of multilayer structures are studied (i.e., effect of the bilayer period). Afterwards, the effect of the bias used during the deposition of the coatings is investigated. A first analysis of the effect of the application mode, either in continuous or pulsed mode, is carried out, followed by a study of the synchronisation effect of the bias pulse with respect to the HiPIMS cathode pulse.
4. To study the effect of the composition of the multilayer coatings by developing titanium silicon nitride and chromium nitride (TiSiN/CrN) coatings, as well as niobium nitride and chromium nitride (NbN/CrN) coatings.

CHAPTER 3

MATERIALS AND METHODS

3. MATERIALS AND METHODS

This thesis focuses on the development and characterisation of new ceramic coatings deposited by PVD-MS and PVD-HiPIMS. This chapter describes the substrates used for the deposition of the coatings, the deposition techniques employed, and the techniques used for the characterisation of the microstructure, chemical bonding, mechanical and tribological properties of the coatings.

The specific conditions used for the deposition of each coating and its subsequent characterisation are detailed in each corresponding chapter.

3.1. Substrates of use

As mentioned above, the purpose of the coatings designed and produced in this research is for the metal sheet forming and plastic injection moulding industry.

One of the substrates used for depositing the PVD coatings was AISI D2 steel, also called DIN 1.2379. This is a steel alloyed with chromium, molybdenum and vanadium belonging to the family of cold work tool steels. It is characterized by good fracture toughness, hard hardness, and excellent resistance to both abrasive and adhesive wear. It is most frequently used in the metal and mechanical industry, in particular in the cold forming and cutting industry.

The other substrate used is AISI 420, also called DIN 1.2083. This is a low chromium stainless steel of the family of hot work tool steels. Some of its primary features include excellent resistance to atmospheric corrosion, high wear resistance, and outstanding polishability. It is normally used to manufacture moulds for the hot processing industry.

The typical composition of this two steels is presented in Table 3-1 [185,186].

Monocrystalline silicon wafers with orientation (100) from PhotonExport were also used as substrate. The characteristics of this material enable easier characterisation of the coatings in certain techniques.

The AISI D2 steel samples were cut from a 15 mm diameter rod without heat treatment into 3 mm thick discs. These were face-faced to ensure planoparallel faces. They were then heat treated by quenching and tempering to ensure a hardness of 58-60HRC. The 1.2083 steel samples were cut from a 30 mm diameter rod into 6 mm thick discs. After ensuring planoparallel faces, they are heat treated up to 50HRC.

All the steel discs were mirror-like polished on a BUEHLER MetaServ250 automatic polishing machine using silicon carbide abrasive papers of decreasing grit size, P240, P600 and P1200, for 2 minutes with water as a lubricant. Subsequently, diamond suspensions were

used on fabric cloth, first 9 μm and finally 3 μm, for 5 min. During all stages of polishing, a force of 25N is applied.

Adhesion of a coating to an underlying material depends on the surface condition of the base material. The presence of surface oxidation prevents proper adhesion for some coatings. The presence of surface contamination, such as dirt or oil, causes poor adhesion. The texture of the substrate surface is important for the adhesion of coatings that depend on mechanical bonding to the surface [18]. For all these reasons, it is crucial to ensure a good surface preparation of the substrates to be used.

Table 3-1: Chemical composition of AISI D2 and 420 steels used as substrates.

Element	D2 Content (%)	420 Content (%)
Chromium, Cr	4.75-5.50	12.0-14-0
Molybdenum, Mo	1.10-1.75	-
Silicon, Si	0.80-1.20	1.0
Vanadium, V	0.80-1.20	-
Carbon, C	0.32-0.45	0.15
Nickel, Ni	0.3	-
Copper, Cu	0.25	-
Manganese, Mn	0.20-0.50	1.0
Phosporous, P	0.03	0.04
Sulfur, S	0.03	0.03

3.2. Coating deposition process

Coatings of study were deposited by using the PVD technique. The first approach was by using the traditional PVD-magnetron sputtering (PVD-MS) technique and the second one, a newer and promising variation named HiPIMS. The equipment used for the deposition of the coatings is described below. The specific details of the deposition conditions for each coating are explained in the corresponding chapter.

All the coatings of this thesis were deposited in a CemeCon CC800/9 ML HiPIMS equipment. The equipment comprises 6 cathodes. Two of them can work in either DC (Direct Current) or HiPIMS mode and the remaining four in DC mode.

The equipment has a chamber with a useful space of 400mm diameter x 400mm height equipped with a planetary system of 6 columns in which the pieces to be coated are supported. Inside the reactor, the workpieces can have up to 3 rotations. The first rotation corresponds to the rotation of the table, the second rotates each of the columns in the opposite direction to the rotation of the table, and the third rotation is specific to the pieces supported on the columns. The growth rate of the layer is a function of the position of the sample inside the chamber, the rotation speed of the table and the number of rotations of the sample [187]. A schematic view of the chamber used is shown in Figure 3.1a.

The samples are supported inside the chamber by the use of magnets, as shown in Figure 3.2 and coated with the disposition showed in Figure 3.1b.

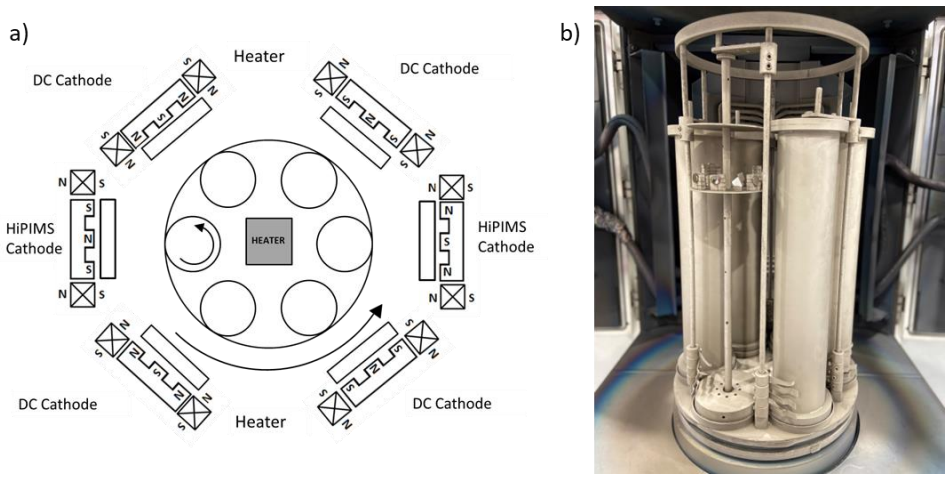

Figure 3.1: CemeCon CC800/9 ML equipment. a) Schematic view of the reactor, b) Image of the inside the chamber.

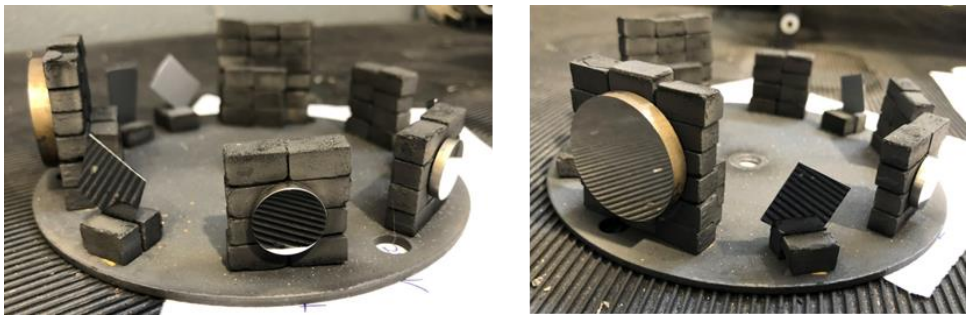

Figure 3.2: Steel disks supported by magnets.

For both the PVD-MS and the HiPIMS processes, the deposition steps are as follows:

- Chamber conditioning: First, the reactor chamber must be conditioned to avoid possible failures during the process. Sandblasting consists of removing adhered material both in the chamber and on all mounting elements to prevent detachment of fragments of previous coatings. The presence of particles and/or dust during the coating process can create defects in the coating (i.e. uncoated areas) and even generate electrical arcing that could stop the process. Subsequently, everything must be vacuumed to remove all this loose material.

- Loading of the substrates into the chamber: The samples are loaded inside the chamber distributed in columns. Afterwards, all the chamber is vacuumed again.
- High-vacuum and heating: Once the samples are loaded, a high vacuum (around 10^{-7} mbar) is required inside the chamber, usually produced by a turbomolecular pump. This high vacuum is used to avoid coating contamination and interferences in the trajectory of the sputtered atoms. The chamber is heated up to reach the optimal temperature for deposition and to eliminate possible organic impurities.
- Pre surface cleaning (Etching): Once the temperature is defined in the program, a plasma made of argon is used for cleaning the substrates. This process activates the surface of the samples for enhanced adhesion and removal of impurities. This is followed by the coating deposition stage.
- Coating: In the coating deposition step, a target plate, also referred as cathode, is bombarded by energetic ions generated in a glow discharge plasma generated in front of the target. The bombardment results in sputtering (removal) of the target atoms which are transferred to a vapor phase and are subsequently condensed on a substrate as a thin film. Different power sources can be applied to the cathode, mainly direct current (DC) or pulsed current as is the case of (HiPIMS) technique. The reactive gases are introduced into the chamber if applicable also in this step for the production of nitrides- and carbides-based coatings.
- Cool down: After the deposition of the coatings, the samples must be cooled down under vacuum below 180ºC to avoid the formation of oxides. The vacuum is then released, the reactor chamber is opened, and the samples can be extracted.

Detailed information on the cathodes used, gases and deposition parameters of each coating system are explained in each corresponding chapter.

3.3. Characterization techniques

In this section, the theoretical principles and equipment used for the characterisation of the coatings are explained.

3.3.1. Chemical and structural characterization

3.3.1.1. Optical microscopy

An optical microscope was used to observe the surface of the coatings and for the evaluation of the results obtained from some characterization techniques, such as calotest, scratch test, etc. The microscope used was a Leica DM750 M inverted binocular microscope in which the sample is observed from the underneath. This type of microscope is mainly used for metallographic samples.

3.3.1.2. Calotest

The thickness of the coatings was evaluated by calotest technique. It consists of creating a wear crater in the coating down to the substrate by using a rotating hard metal ball and a diamond suspension used as an abrasive agent (Figure 3.3a) [188]. The crater produced is analysed with an optical microscope and the thickness of the layer is determined by the equation 3.1, as shown in the Figure 3.3b.

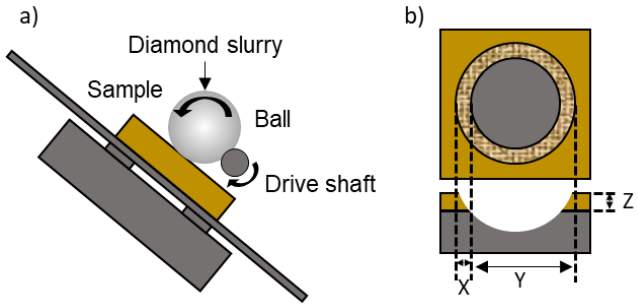

Figure 3.3: Schematics of calotest technique, b) Projection of the crater formed. Adapted from [188].

$$Z = \frac{X * Y}{\emptyset\ ball} \tag{3.1}$$

The tests were carried out with a Kallotchen/L equipment produced by CemeCon with a 20 mm diameter hard metal ball and 0.25 µm size diamond suspension. The time for the crater formation was adjusted according to the characteristics of the sample until the substrate was revealed. The crater was then attacked with Heyn reagent to increase the contrast between the substrate and the coating, thus improving the evaluation of the print.

3.3.1.3. X-ray fluorescence (XRF)

The X-ray fluorescence (XRF) is a rapid and non-destructive analytical technique to determine the chemical elements present in the sample. In this process, the atoms within the sample are excited with X-rays with energy high enough to induce the ejection of core electrons. The generated inner vacancy is filled with an outer electron and the excess energy is released (photon emission). The energy of the generated X-ray photon (fluorescence) is determined by the energy of the electronic levels involved, which in turn depends on the characteristics of the nucleus (see Figure 3.4). The main problem with this technique is that only the detection of Z > 11 elements is permitted if the detector is not cooled down [189,190]. In this thesis, a Fischeroscope X-Ray XDAL was used to determine the presence of some elements in the coatings and to make an indirect density measurement of the coatings.

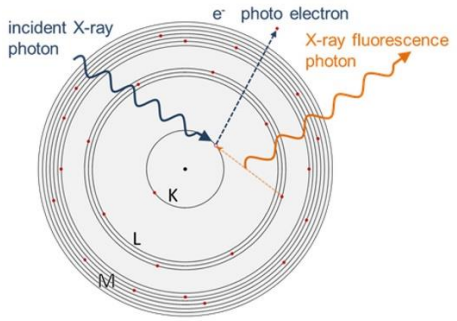

Figure 3.4: XRF principle [190].

3.3.1.4. Electron probe microanalysis (EPMA)

Electron Probe MicroAnalysis (EPMA) is a non-destructive technique to determine the chemical composition of solid materials. The method uses bombardment of the specimen by keV electrons to excite characteristic X-rays from the sample following the same principle that XRF, which are then detected by using wavelength-dispersive spectrometers. Quantitative analysis is performed by measuring the ratio of the characteristic X-ray intensity emitted by an element in the specimen to that emitted by the same element in a reference material (standard) [191]. For this technique, a JEOL JXA-8200 SuperProbe equipment was used for the quantification of each element present in the coatings.

3.3.1.5. Glow discharge optical emission spectroscopy (GD-OES)

Glow Discharge Optical Emission Spectroscopy (GD-OES) is an analytical technique that provides both the surface/depth profile and the bulk elemental composition of solid materials and layers quickly, and with high sensitivity to all elements.

The emission spectrum of the sample is obtained after bombarding the surface with argon gas ions that will cause a sputtering of the surface atoms. These sputtered atoms will migrate into the plasma and will emit light after atomic excitation-deexcitation processes induced by the plasma. Passing through the entrance slit, the emitted light reaches a concave grating, where it is dispersed into its spectral components as observed in Figure 3.5. Each element present in each removed layer emits a series of photons whose wavelength is unique for each element, so that elemental identification of the surface can be made as a function of depth. Unlike other spectroscopy techniques, there are no limitations in detecting elements, as long as there is an open channel for the element in question. This technique allows the quantification of each element by comparing the intensities of the different wavelengths detected with the amount of material present in the area analysed after performing a calibration curve with the appropriate standards [192].

The equipment used to evaluate the composition of the coatings throughout their structure was a Horiba Jobin-Yvon RF10000 equipment.

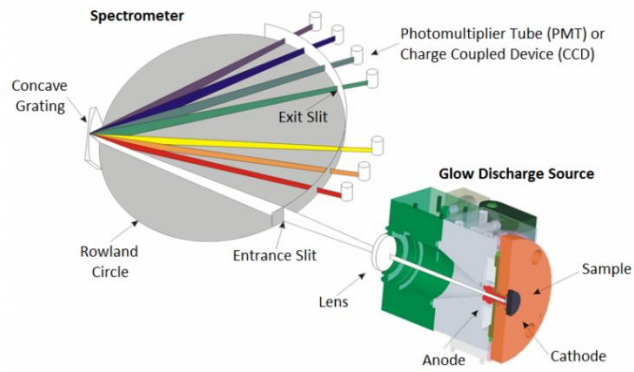

Figure 3.5: GD-OES principle [193].

3.3.1.6. Scanning electron microscopy (SEM)

Scanning Electron Microscopy (SEM) uses a beam of electrons to scan the surface of a sample to build a three-dimensional image of the specimen. When the electron beam hits the sample, the interaction of the electrons from the filament and the sample atoms generates a variety of signals. Depending on the sample, these can include secondary electrons (SE, electrons from the sample itself), backscattered electrons (BSE, beam electrons from the filament that bounce off nuclei of atoms in the sample), X-rays, light, heat, and even transmitted electrons (beam electrons that pass through the sample) as shown in Figure 3.6 [194].

All these different signals provide useful information about the sample. Secondary electrons originate from the surface regions of the sample and therefore provide more detailed information about the sample surface. Backscattered electrons, in contrast, originate from deeper regions of the sample, thus showing a high sensitivity to differences in atomic number. The higher the atomic number, the brighter the material will appear in the SEM image [195].

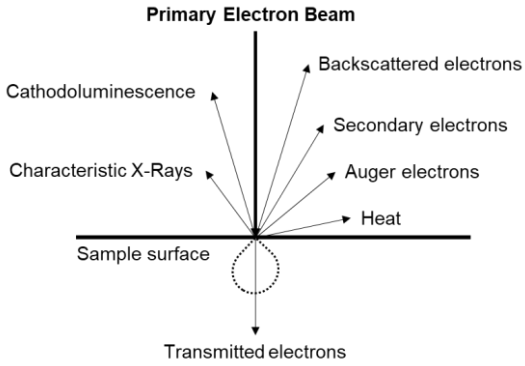

Figure 3.6: Schematic illustration of signals available in a SEM due to electron beam interaction. Adapted from [194].

There are different types of electrons guns. The first SEM systems generally used tungsten or lanthanum hexaboride (LaB_6) filaments as cathodes and are used especially for low magnification imaging and X-ray microanalysis. However, the modern SEMs, use field emission sources, which provide enhanced current and lower energy dispersion. In a field emission gun (FEG), a single crystal tungsten wire with a very sharp tip is used as the electron source. This provides enhanced electron brightness, typically 100× greater than that for a typical tungsten filament source, very low energy dispersion and lower aberration, which provides much higher resolution for SEM images.

A conventional JEOL 6460 SEM operating at 20kV was used to observe the surface of the coatings. However, for observing the structure of the coatings, a FE-SEM equipment was required. Two different instruments were used depending on their availability: a FEG Hitachi S4800 and FEG Hitachi S5200 operating at 5kV.

3.3.1.7. Transmission electron microscopy (TEM) and high-resolution TEM (HRTEM)

In transmission electron microscopy (TEM) a beam of electrons is accelerated towards a thin sample. Due to a small sample thickness of ~ 100 nm, part of the electron beam is transmitted through the sample unaffected while some of the beam is scattered by the atoms, either elastically or inelastically. The acceleration voltages used in materials science TEM imaging are usually around 200 kV. Magnetic lenses and apertures are used to focus the beam on a desired spot on the sample [196].

The most straightforward TEM imaging mode is the bright field (BF) mode, where only the directly transmitted beam is used to construct the image. In a BF image, the sample areas that are thick, have high mass and density appear darker as they scatter more electrons, which are filtered away from the image. The inverse imaging mode to BF is dark field (DF) imaging, where the directly transmitted beam is filtered away and the scattered parts are selected, thus the areas with higher scattering probability appearing brighter in the image. Both signals can be selected to obtain a phase contrast image. Phase contrast imaging is used in high resolution TEM (HRTEM) to achieve atomic resolution.

A multistep preparation procedure needs to be carried out to obtain electron transparent cross-sectional TEM samples. For ceramic materials, focused ion beam (FIB) sample preparation is required to reach lamellas with thicknesses between 100 and 200 nm.

Transmission electron microscopy (TEM) was used to obtain dark field images using a JEOL 2100 microscope operating at 200 kV. Low angle annular dark field images (LAADF) imaging together with energy dispersive X.ray (EDX) spectroscopy were simultaneously performed in scanning transmission electron microscopy (STEM) mode in a double aberration corrected FEI Titan3 Cubed Themis operated at 200 kV. EDX mapping was carried out with

four embedded Bruker SDD detectors using ChemiSTEM technology and processed with the Bruker's ESPRIT software.

3.3.1.8. Energy-dispersive X-ray spectroscopy (EDS)

Energy-dispersive X-ray spectroscopy (EDS) refers to the analytical technique used in conjunction with a TEM or SEM microscope used to identify composition and provide chemical characterization of a specimen. When an electron beam is focused onto the sample, some of its electrons are ejected, forcing them to release some of their energy, causing the X-rays. The amount of energy released is based upon the starting and ending shell of the electron. The resulting X-ray can be converted into an EDX spectrum plot [197].

3.3.1.9. Electron Energy-Loss Spectroscopy (EELS)

Electron Energy-Loss Spectroscopy (EELS) consists in the analysis of the energy distribution of initially monoenergetic electrons after their inelastic interaction with the atomic electrons of the sample. EELS is usually installed in a TEM along with a spectrometer, which consists of a magnetic prism that performs the filtering of the electron energies. Because in TEM observations sample thickness is thin enough to permit almost the total transmission of the electron beam, the energy loss spectrum of the electrons is intense enough to provide information about the chemical and structural properties of the specimen [198].

An EEL spectrum comprises three different signals, as can be observed in Figure 3.7 [199]:

I. The Zero loss (ZL) peak: This peak appears at an energy loss of zero and contains all the electrons that have passed the specimen with no interaction or with elastic interactions. If the sample is thin, the ZL peak is by far the most intense signal.

II. The valence EELS (also called low-loss EELS): This region includes the energy losses between the ZL peak and about 100 eV. Here, the plasmon peaks are the predominant feature.

III. The ionization edges (or core-loss EELS): they arise from the excitation of core electrons into unoccupied electron states. The EEL signal originates from the initial ionization event and the subsequent relaxation of the atoms via X-ray emission. The ionization energy is determined by the element type and so the ionization edges appear at energies in the spectrum specific to each element. This allows the presence, local chemistry, bonding, and electronic structure of those elements to be determined. The intensity in the ionization edges will be proportional to the concentration of those elements in the sample and so mapping of compositional distributions is readily achieved [200].

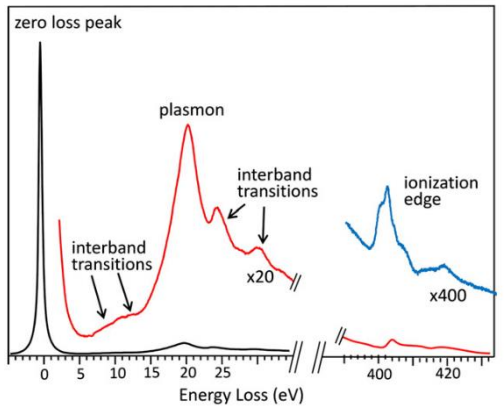

Figure 3.7: Schematic view of an EEL spectrum [199].

3.3.1.10. Atomic force microscopy (AFM)

The Atomic Force Microscopy (AFM) is a mechano-optical technique used to create 3D images of the surface of samples. It uses a micro-cantilever with a tip at the end that moves across the sample controlled by piezoelectric positioning which scans the surface of the sample. A laser is directed on the cantilever, so every time the tip moves up or down due to the interaction with the sample, the laser path is deflected and reaches a photodetector, which is interpreted by software for the image generation (Figure 3.8). There are two main AFM operating modes: contact and tapping. In the contact mode, the AFM tip is in continuous contact with the surface. The optical feedback loop controls and maintains constant the AFM cantilever deflection while operating. In contrast, in the tapping mode, the AFM cantilever is vibrated above the surface of the sample with a constant resonance amplitude in a way that the tip is only in intermittent contact with the surface. In this case, the optical feedback loop controls and maintains constant the AFM cantilever oscillation amplitude while the AFM tip scans de surface of the sample [201,202].

Not only AFM can be used to obtain topographic information of the surface, but it can also be sensitive to a variety of surface properties, such as conductivity, dielectric constant or magnetisation through the use of appropriately chosen proves and signal processing.

From the topography images, it is possible to calculate the roughness of the samples. The two most widely used parameters are Ra and RMS. The first one is defined as the arithmetic average of the absolute values of the profile height deviations from the mean line, within a line (Ra - 2D linear roughness, and Sa - 3D surface roughness), and the second one is defined as the root mean square average of the profile height deviations from the mean line within a line. They are both described and calculated following the ASME B46.1-2019 standard.

The topography and roughness of the samples were measured with a CSI Instruments Nano-Observer AFM microscope (analysed surface 10x10 µm) with silicon N-type tips (µmasch) in contact mode with the coatings prepared on silicon substrates. Data obtained was analysed with the Gwyddion software.

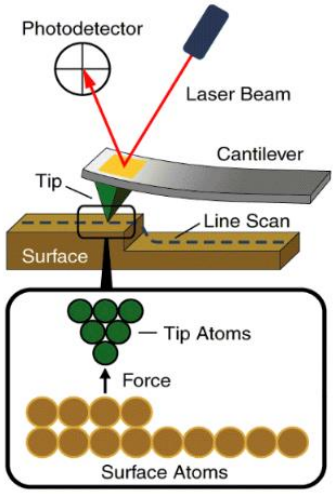

Figure 3.8: Operating scheme of an AFM equipment.

3.3.1.11. X-Ray diffraction (XRD)

X-Ray diffraction (XRD) technique is used to determine the crystalline structure of a crystalline sample. It provides information on structures, phases, preferred crystal orientations (texture), and other structural parameters, such as average grain size, crystallinity, strain, and crystal defects. X-ray diffraction is based on constructive interference of monochromatic X-rays produced in a cathode tube and a crystalline sample when the Bragg's law is fulfilled (eq.3.2) [203]. The geometrical condition for plane diffraction is shown in Figure 3.9.

$$n\lambda = 2\mathrm{d}_{hkl} * \sin\theta \qquad (3.2)$$

Where *n* is the order of diffraction, λ is the wavelength of the incident beam in nm, d_{hkl} the lattice spacing in nm and θ the angle of the diffracted beam in degree.

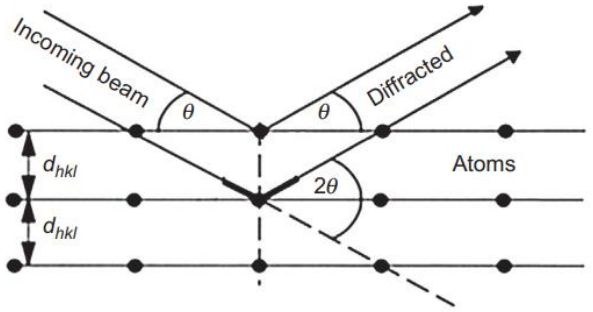

Figure 3.9: Geometrical condition for diffraction from lattice planes [203].

The position of the different peaks in the diffractogram allows the determination of the different spacings of the crystal lattice planes. By comparison with those in a database, it is possible to identify the phases present in a sample. Also, the peak parameters of the different signals shown in Figure 3.10 allow the determination of the crystal size and texture of the sample.

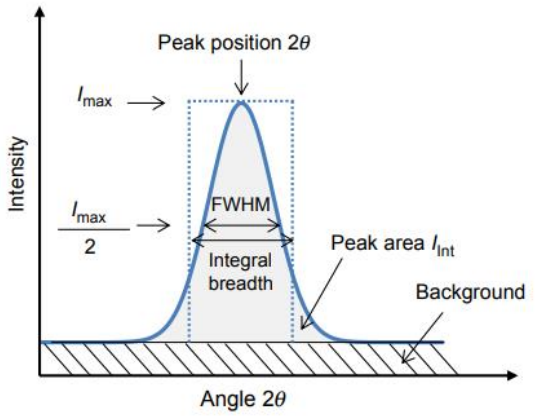

Figure 3.10: Parameters that can be extracted from a peak in a diffractogram.

The crystallite size was determined by the Scherrer equation with a Gaussian peak fit (eq.3.3) [204].

$$D = \frac{K\lambda}{\beta cos\theta} \tag{3.3}$$

Where K is a constant shape factor (K=0.9), D is the mean crystalline size, λ is the X-ray wavelength, β in radian is the peak width at half-maximum height, and θ is the Bragg's angle.

The texture coefficient was calculated from their respective XRD peaks with the following formula (eq 3.4) [205].

$$T(hkl) = \frac{I(hkl)}{I(001) + I(100) + I(101)} \quad (3.4)$$

where T refers to the orientation parameter and (hkl) refers to the corresponding diffracting lattice planes (or crystallographic lattice directions).

In most thin film investigations, the thickness of the deposited coatings is substantially low causing a large fraction of the diffractogram to stem from the substrate. To significantly increase the signals coming from the coating, a variant of the XRD technique was developed called grazing incident X-ray diffraction (GI-XRD). In this technique, the incident angle is fixed at values small enough to limit the penetration of the X-ray beam into the bulk material. Therefore, the signals obtained in the diffractogram mainly stem to the coating [206].

The crystal structure of the films was determined by XRD analysis in Bragg-Brentano and GI-XRD geometries using Cu K_α radiation with a diffractometer Empyrean coupled with a PIXcel Medipix 3 detector manufactured by Malvern Panalytical GmbH. GI-XRD scans were collected at a constant incident angle of 0.5º,1º and 2º depending on the coating-substrate pair, in order to avoid intense signals from the substrate and obtain stronger signals from the coatings. The crystalline phases and Rietveld refinement were performed with an X'Pert Highscore software with the ICDD PDF4+ database.

3.3.1.12. X-Ray photoelectron spectroscopy (XPS)

X-ray Photoelectron Spectroscopy (XPS) is used to determine both the elemental composition and chemical bonding in the coatings. The operational principle of XPS is based on the photoelectric effect caused by soft X-rays. XPS is a surface sensitive technique, as the inelastic mean free path of photoelectrons is in the order of ~ 5-10 nm. The measurements have to be performed under ultra-high vacuum conditions to suppress adsorption of residual gas during the analysis [207].

Binding energies (Eb) of the emitted photoelectrons can be determined according to equation (3.5), as their kinetic energies (Ek) are measured, and the photon energy (hν) is known:

$$Eb = h\nu - Ek - \varphi \quad (3.5)$$

Where φ is the spectrometer work function.

Both the elemental composition, oxidation state and chemical bonding structure of the sample can be determined by the core level electron binding energies.

XPS spectra were measured using a SPECS Phoibos 150 MCD instrument using non-monochromatic Cu K_α radiation (1253.6 eV) as X-ray excitation source. The measurements were performed in constant analyser energy mode with a 35 eV pass energy for high resolution spectra of the detected elements. Samples were previously subjected to

Ar^+ ion bombardment at ≈ 6×10^{-5} mbar (2.70 KeV y 10 mA) for 15 minutes to partially remove the contaminant layer.

3.3.1.13. Raman spectroscopy

Raman spectroscopy is a vibrational spectroscopy method commonly used for determining the molecular and lattice vibrations in materials. It is based on the inelastic scattering of monochromatic light, usually from a laser, by the target material, which can be solid, liquid, or even gaseous. When a sample is excited, most of the signal consist of light that scatters elastically from the sample called Rayleigh radiation. However, a small fraction of the light (about 1 in 10^7 photons) is optically scattered at different, mostly lower, frequencies than the frequency of the incident photons. The Stokes line corresponds to light with a lower frequency than the incident light, as the target molecule or lattice is excited to a higher vibrational state. In anti-Stokes scattering, the sample is on an excited vibrational state and the interaction with the light results in a return to the ground state, and a photon with a larger energy is emitted [208,209]. These tree types of radiation can be observed in Figure 3.11.

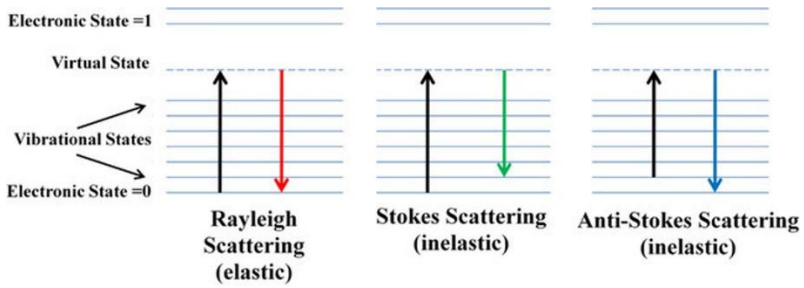

Figure 3.11: Energy diagrams of Rayleigh, Stokes and anti-Stokes Raman scattering. Adapted from [208].

Raman spectroscopy is one of the techniques that allows us to determine the presence of amorphous carbon in a coating and to analyse its structure. Amorphous carbon is observed in the spectrum as two bands (or peaks) called D-G that appear at values of 1300-1600 cm^{-1}. Both bands have their origin in vibrations of sp^2-hybridised carbon-carbon bonds and gives an idea of the disorder of the system. Both the ratio between the intensities of the D-G bands (I_D/I_G) and the peak positions are used to determine the degree of disorder in the system by means of sp^2/sp^3 C-C bonds ratio. This technique also allows us to determine the formation of by-products of the oxidation of the coating or substrate after the tribological test, as long as they present vibrational modes allowed in Raman spectroscopy [168].

Raman measurements (200–1200 cm^{-1}) of the carbon-based coatings were performed using a LabRAM Horiba Jobin Yvon spectrometer equipped with a charge-coupled device (CCD) detector and a diode-pumped solid-state laser (532 nm) operating at 5 mW. All

measurements were recorded using a 50× magnification objective and a 100 µm pinhole with a laser exposure of 150 s. The fitting of the D and G Raman bands was performed using Lorentzian functions.

For the multilayer coatings, Raman spectroscopy was performed with a high-resolution Alpha300R from Witec with a 532 nm laser wavelength and 10 mW of laser power.

3.3.2. Mechanical characterization

3.3.2.1. Mercedes/Daimler-Benz test

The Mercedes or Daimler-Benz adhesion test is a test that allows to determine qualitatively whether the adhesion of the coating to the substrate is acceptable on not. It consists of performing an indentation by using a Rockwell-C hardness essay (120º conic diamond indenter with a load of 150 Kgf) and optically evaluating the indentation left on the sample. By observing the indentation marks shown in Figure 3.12, adhesion properties can be classified into two groups: H1–H4 acceptable, H5–H6 not suitable [210,211].

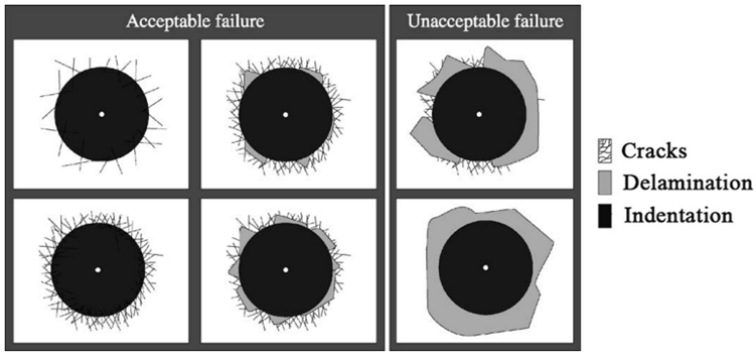

Figure 3.12: Adhesion scale for the Daimler-Benz test indentation marks. Adapted from [210].

It should also be noted that this test has several limitations. Besides adhesion, this test is influenced by two other parameters: substrate hardness and coating thickness. Therefore, the substrate must have a hardness of at least 54 HRC to yield a favourable result, otherwise the phenomena observed would be the collapse of a hard coating while being pressed into a soft, deformable substrate. The coating thickness cannot exceed 5 µm, otherwise the indenter only tests the coating.

In this work, a CV-600A Metrotec durometer equipped with a 120º conic diamond indenter was used.

3.3.2.2. Scratch test

Scratch test is a simple and rapid technique used to determine the adhesion strength of a coating-substrate system. It consists of moving a diamond tip along the surface of the material under increasing normal load, either stepwise or continuously until a well-defined coating failure occurs. The load at which the coating fails is called the critical load (L_C). This force is then taken as a measure of adhesion [212]. Three different critical loads can be defined corresponding to different failure modes [213]:

- L_{C1}: The first cohesion-related failure event; the first appearance of micro cracking, surface flaking inside/outside the track without any exposure of the substrate.
- L_{C2}: The first adhesion-related failure event: the first appearance of cracking, chipping, spallation, and delamination inside/outside the track with the exposure of the substrate.
- L_{C3}: The first exposure of the substrate in the scratch track resulting from wear.

The type of failure observed by scratch-tests for a coating-substrate system depends on the test load, the coating thickness, the residual stress and the properties of the substrate (e.g. hardness), as well as on test parameters such as indenter radius and sliding speed. According to Bull, scratch test results for brittle coatings are classified according to the stresses (compressive or tensile), according to the substrate (ductile or brittle; Figure 3.13) and according to the adhesion between coatings and substrate (poor or good) [214,215].

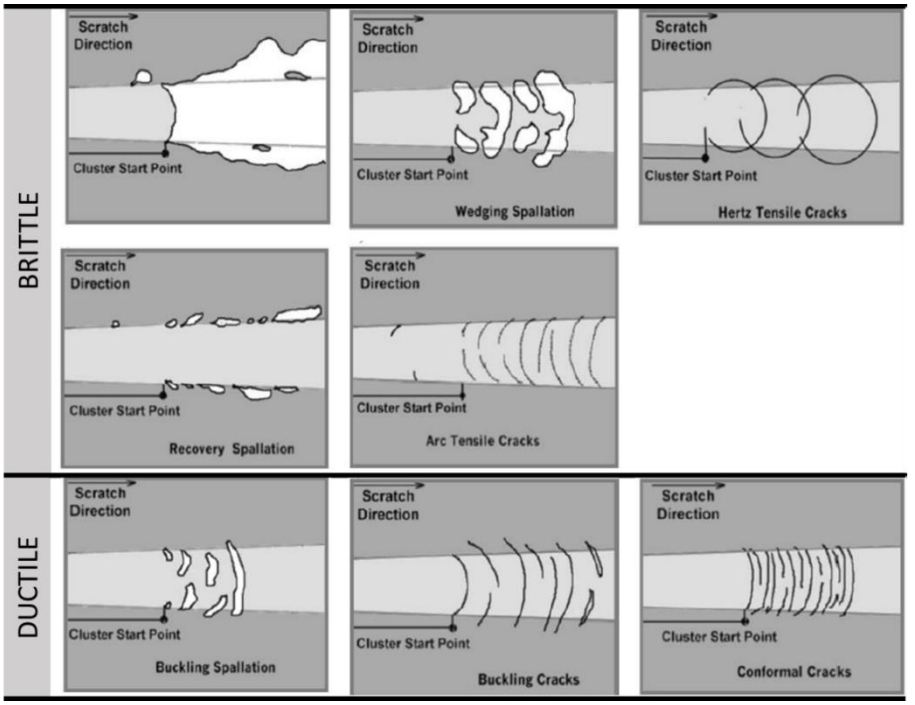

Figure 3.13: Coating fracture morphology according to substrate type in scratch tests.

For the TiB_2/TiBC samples, the scratch tests were carried out using a TRIBOtechnic Millenium 200 scratch-tester. A Rockwell C diamond tip (200 μm radius) was drawn over the coated surface for 8 mm-length as the applied normal load increased continuously up to 30 N. The diamond tip was cleaned after each scratch and the test was repeated twice on each sample. For the multi-layered TiN/CrN coatings, 3 scratch tests were performed in each coating with an increasing normal load value up to 100 N in a 10 mm-length line. Acoustic emissions were recorded during the scratching, but optical microscopy was applied to assess the critical normal load values and to show the coating fracture and delamination modes.

3.3.2.3. Intrinsic residual stress

The residual stress of the coatings was evaluated by the XRD-$\sin^2\psi$ technique [216–218]. A schematic diagram of the method is shown in Figure 3.14. When an X-ray beam hits the sample surface at an incident angle Ω, those grains, with their (hkl) lattice planes fulfilling the Bragg diffraction condition and having an off-axis angle ψ with respect to the sample surface normal, emit a diffraction X-ray beam at a diffraction angle 2θ. Then, the d-spacing $d_{\phi\psi}$ of the (hkl) lattice plane can be measured. The principal formula for the XRD-$\sin^2\psi$ stress measurement can be written as:

$$\frac{d_{\phi\psi} - d_0}{d_0} = \left(\frac{1+\nu}{E}\right) \cdot \sigma_\phi \cdot \sin^2(\psi) - \left(\frac{\nu}{E}\right) \cdot (\sigma_1 + \sigma_2) \tag{3.6}$$

Where E and v stand for the Young's modulus and the Poisson's ratio normal to the (hkl) orientation of the material respectively, and d_0 the lattice spacing at stress-free condition.

Assuming $\sigma_\phi=\sigma_1=\sigma_2$ when the in-plane stress σ_ϕ is independent of the orientation, Eq. (3.6) can be re-written as:

$$d_{\phi\psi} = \left(\frac{1+\nu}{E}\right) \cdot \sin^2(\psi) - \left(\frac{2\nu}{E}\right) \cdot \sigma \cdot d_0 + d_0 \tag{3.7}$$

Then Eq. (3.7) can be treated as a linear function Y=a·X+b by letting:

$$Y = d_{\phi\psi} = \frac{\lambda}{2 \cdot \sin(\theta)}; X = \left(\frac{1+\nu}{E}\right) \cdot \sin^2(\psi) - \left(\frac{2\nu}{E}\right) \tag{3.8}$$

Therefore, a series of XRD scans covering a known Bragg 2θ at fixed glancing angles Ω_i (for i=1, 2, 3, etc.) are performed. The half angle θ_i can be measured in each diffraction peak and the associated off-axis angle ψ_i is calculated according to the relation $\psi_i=\theta_i - \Omega_i$. The obtained θ_i and ψ_i are subsequently used to calculate the data group $\{X_i,Y_i\}$ according to Eq. (3.8). Then, a linear regression of this plotted data group is used to get constants a and b and finally the in-plane stress σ, as well as the strain- free lattice d-spacing d_0, can be obtained from the relations $d_0=b$ and $\sigma=a/d_0$, respectively.

In the conventional $\sin^2\psi$ measurement, a crystal plane, usually having a high diffraction angle (2θ > 125º), is selected. However, for coatings, the measurement at such a

large diffraction angle always comes with an extremely weak diffraction peak and strong peak broadening. Consequently, crystalline planes of low diffraction angles have also been used.

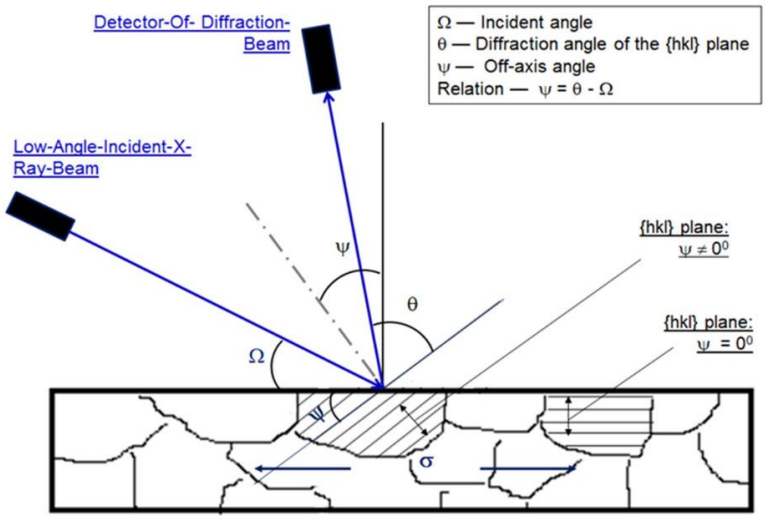

Figure 3.14: Schematic diagram of the XRD - sin²ψ technique [216].

The stress of the coatings was evaluated by this method using a Bruker-AXS D8 Advance in Bragg-Brentano coupled configuration. Samples were tilted in the range between 0 and 0.9 $\sin^2\psi$. The data obtained from the XRD experiments were analysed using the Highscore Plus software.

3.3.2.4. Nanoindentation technique

Many techniques can be employed for measuring the mechanical properties of the materials but nanoindentation technique is the appropriate one for determining the hardness (H) and Young's modulus (E) of the coatings. The application of small loads in the range between 0.001-0.2 N allows measuring the hardness down to a maximum depth of 10% of the coating thickness, in which the influence of the substrate is supposed to be negligible [219].

In nanoindentation, a sharp diamond tip of known geometry is pressed against the sample surface with a steadily increasing load which is afterwards released. The applied load and indentation depth are monitored to construct a load–displacement curve, as the one observed in Figure 3.15. Typically, a Berkovich tip is used for these measurements. Its geometry consists of a three-sided pyramid with a total included angle of 142.3º and a half angle of 65.27º, measured from the axis to one of the pyramid flats [220]. The most used method for the analysis the nanoindentation data was suggested by Oliver and Pharr [221]. In the model, the load deformation is assumed to be both elastic and plastic, and the unload deformation being only elastic.

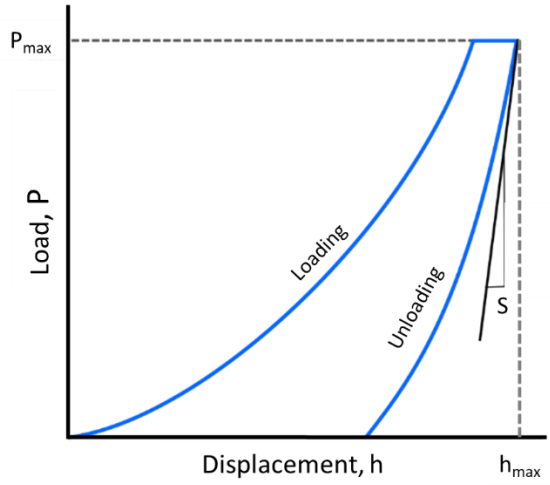

Figure 3.15: Schematic load-displacement curve obtained for a nanoindentation measurement.

The hardness (H) of the films can be calculated from the effective contact area of the tip (A) and maximum applied load (P_{max}) according to equation (3.9):

$$H = \frac{P_{max}}{A} \tag{3.9}$$

The contact area, however, depends on the depth of penetration and the indenter geometry. The cross-sectional area of the indenter tip is estimated as a function of the distance from the tip vertex.

The elastic unloading stiffness dP/dh, which can be determined from the tangent of the first part of the unloading curve (S) and the effective contact area can be connected to the reduced elastic modulus Er by using the equation 3.10:

$$\frac{dP}{dh} = \beta \cdot \frac{2E_r\sqrt{A}}{\sqrt{\pi}} \tag{3.10}$$

Where β is a tip specific constant (1.034 for a Berkovich tip) and E_r is the reduced elastic modulus. E_r is defined as:

$$\frac{1}{E_r} = \frac{1-v^2}{E} - \frac{1-v_i^2}{E_i} \tag{3.11}$$

Here, v is the Poisson ratio and of the specimen, E is the elastic modulus of the specimen, v_i is the Poisson ratio of the indenter, and E_i is the elastic modulus of the indenter.

Nanoindentation technique was used for determining the hardness and Young's modulus of all the coatings developed in this thesis.

For the TiB_2/TiBC and NbC/a-C(:H) coatings, the H and Er were measured using a nanoindententer tester (Nanoindenter XP MTS) with a Berkovich diamond indenter. Data was evaluated following the Oliver and Phar method [221].

For the multilayer coatings, measurements were performed in continuous stiffness mode on a G200 nanoindenter from KLA, equipped with a Berkovich tip. Ten tests were performed for each sample at a maximum penetration depth of 150 nm and the data were evaluated according to the Oliver and Pharr method [221].

3.3.3. Tribological properties

Tribology is the science that studies the interaction between two bodies in contact and relative motion, including wear, lubrication, and surface roughness. The two most important parameters that determine tribological properties are friction and wear.

- Friction

Friction is defined as the force which acts as resistance to movement of a body in contact with another. It can be quantified with the friction coefficient (μ), a dimensionless magnitude which is the ratio of the force of friction that opposes the movement between two bodies and the force pressing them together. Friction coefficient greatly depends on factors such as temperature, humidity and velocity (or rather the heat build-up and heat dissipation capacity of the system) among others, so it is often referred as a system property rather than a material property [222].

There are two different friction coefficients: the static friction coefficient (μ_s) and the kinetic friction coefficient (μ_k). Both depend on the nature of the materials, and for a given pair, the static coefficient tends to be larger than the kinetic one. Static friction refers to the friction between two static surfaces. However, the instant sliding occurs, static friction is no longer applicable. The static friction coefficient greatly depends on surface roughness while kinetic friction depends mainly on a chemical interaction between surfaces, although in some cases, kinetic friction can also be governed by roughness effects [223]. In the case of the pin-on-disk measurements, the relevant parameter is the kinetic friction coefficient, because the result value is the average of the measured coefficient during thousands of rotation cycles.

- Wear

Wear can be defined as the damaging, deformation or removal of material at solid surfaces caused either by erosion (mechanical effect) or corrosion (chemical effect). Normally, when referring to wear in tribology the effect considered to have the most relevance is the removal of material due to a continuous interaction between two surfaces. These particles generated from this process are known as debris and play an important role in friction and wear processes depending on their nature [224].

Just considering the mechanical component of wear, there are several wear mechanisms: adhesive, abrasive and fatigue, all of which can take place in a real contact. It should be remarked that the effect of friction on wear is not proportional and, in several cases, far from obvious. However, continuous and high-intensity friction can produce a raise in temperature, which may lead to new phenomena such as phase transformation, increase in reactivity, oxidation, etc.

The specific wear rate (K) of a material can be quantified, as shown in the following equation (3.12).

$$K\left(\frac{m^3}{Nm}\right) = \frac{V(m^3)}{L(N)\cdot D(m)} \tag{3.12}$$

Where V is the total volume loss, L is the load applied during the test and D is the distance travelled by the ball during the pin-on-disk assay.

3.3.3.1. Evaluation of friction coefficient and wear rate

Tribometers are used to measure the tribological properties for a substrate-counterpart pair by recording the variation of the friction coefficient as a function of time or number of cycles for each test. There is a wide variety of tribometers that simulate different types of real contacts, such as sliding, rolling, or vibrating under different motion configurations, mainly lineal and rotational. Environmental conditions such as humidity and temperature can also be adapted in order to simulate the desired conditions. The equipment used in this thesis is a ball-on-disk tribometer.

The pin-on-disk equipment as shown in Figure 3.16a consists of a speed-controlled turntable on which the sample to be analysed is placed. Above the sample, there is an arm with a cylinder at the end (off-centre from the sample) to which a ball of a specific material (steel, alumina, polymer, etc.) is fixed. A constant, controlled load is applied to the ball. The rotation speed, radius and number of laps are also fixed for each test.

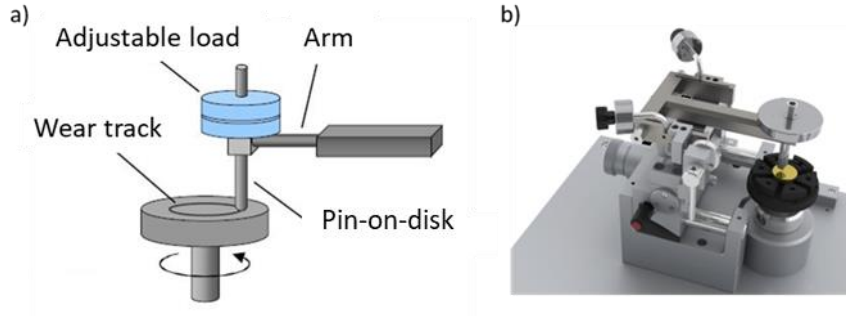

Figure 3.16: a) Schematic view of a pin-on-disk tribometer. b) CSM tribometer.

For the NbC/a-C(:H) coatings, a CSM pin-on-disk tribometer was used in the rotary mode to perform all measurements on the coated D2 steels, and a 100Cr6 steel ball with a diameter of 6 mm was used. The testing conditions were a linear velocity of 10 cm/s, an applied load of 5 N, 10000 laps, a circumference radius of 3 or 4 mm, a temperature between 20 and 25 °C, and a relative humidity of 40% to 50% in ambient air.

For the multilayer coatings, a CSM pin-on-disk tribometer in rotary mode was also used. The sliding wear tests were performed for 2000 laps with an applied normal load of 2N. The linear speed was adjusted to keep the angular velocity constant at 14.3 rad/s for the different wear track radii that varied from 2 to 8.5 mm. The ball used was made of Al_2O_3 (HV 1250-1700) with a diameter of 6 mm. Tests were performed at room temperature (RT), at 300ºC, at RT after heating at 300ºC, at 500ºC and RT after heating at 500ºC.

While the friction coefficient value is obtained directly from the test, the wear rates for both the ball and the sample require further analysis.

- Wear ball (K_{ball})

Wear rates of the balls used as counterparts were evaluated after examination of the balls and calculation of the worn volume using the spherical cap equation. A spherical cap is the region of a sphere which lies above (or below) a given plane (see Figure 3.17). Let the sphere have radius *R*, then the volume of a spherical cap of height *h* and base radius *a* is given by the equation of a spherical segment (eq.3.13):

$$V_{cap} = \frac{\pi \cdot h}{6}(3 \cdot a^2 + h^2) \tag{3.13}$$

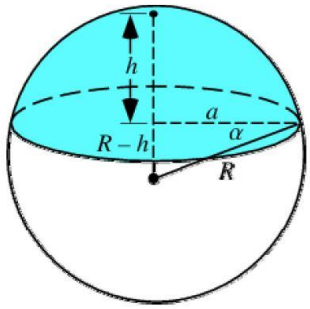

Figure 3.17: Scheme of the spherical cap calculation.

So, the K_{ball} using the eq. 3.12 and substituting the volume (V) for V_{cap} is calculated as:

$$K_{cap} = \frac{V_{cap}(m^3)}{L(N) \cdot D(m)} \tag{3.14}$$

- Wear disk (K_{disk})

Two different methods were used to analyse the track on the coatings after the tribological tests according to the availability of each technique at that moment.

For the carbon-based coatings, profilometry was used to calculate the total worn volume of the track whereas for the multilayer coatings, a confocal laser scanning microscopy (CLSM) was used.

For the profilometry assays, four cross-section profiles were taken across the disk-track according to Figure 3.18a.

The worn area under the baseline in Figure 3.18b is calculated by numerical integration and the worn volume is estimated as the average of the 4 areas obtained multiplied by the perimeter of the wear circle with the following formula:

$$V_{disk} = \acute{A}rea \cdot 2 \cdot \pi \cdot r \tag{3.15}$$

Where *r* is the radius of the track. Now, using the eq. 3.12 and substituting the volume (V) for $V_{disk,}$ the wear disk is calculated as:

$$K_{disk} = \frac{V_{disk}(m^3)}{L(N) \cdot D(m)} \tag{3.16}$$

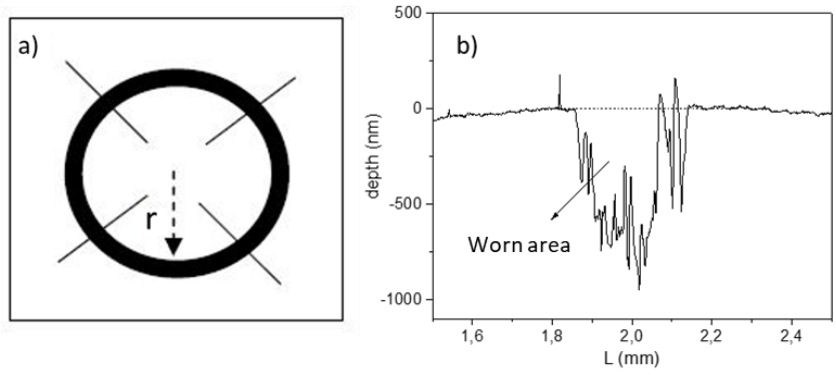

Figure 3.18: a) Distribution of the profiles taken, b) Representative cross-section profile of the disk-track.

For the CLSM measurements, a Keyence VK-X1100 microscope was used for taking the images that were subsequently analysed by MultiFileAnalyzer software. For these coatings, six images were performed for each tribological test, and the total worn volume was obtained by numerical integration. The K_{disk} was then calculated following the 3.16 equation.

CHAPTER 4

TiB_2/TiBC coatings

The results of this chapter gave place to some scientific communications:

Contributions to communications:

1. Advances in Surfaces, Interfaces and Interphases Conference, online conference. "*Influence of the carbon incorporation on the mechanical properties of TiB_2 thin films prepared by HiPIMS*". **N. Sala**, M.D. Abad, J.C. Sánchez-López, F. Crugeira, A. Ramos-Masana, C. Colominas. Poster presentation. 15-18 May 2022.

Contributions to publications:

1. Part of this chapter was published in the International Journal of Refractory Metals and Hard Materials entitled: "*Influence of the carbon incorporation on the mechanical properties of TiB_2 thin films prepared by HiPIMS*".
   N. Sala, M.D. Abad, J.C. Sánchez-López, F. Crugeira, A. Ramos-masana, C. Colominas, Influence of the carbon incorporation on the mechanical properties of TiB_2 thin films prepared by HiPIMS, Int. J. Refract. Met. Hard Mater. 107 (2022). https://doi.org/10.1016/j.ijrmhm.2022.105884.

4. TiB_2 -TiBC coatings

Surface engineering has introduced a great number of improvements in the use of materials for industrial applications. There is a growing interest in the development of advanced coatings as they allow the improvement of surface performances, whose lifetime is very limited under specific conditions. Ceramic coatings such as diamond-like carbon (DLC), borides and nitrides prepared by different deposition techniques present high hardness, good chemical resistance and high thermal stability [157,225–228]. One of the newest and promising techniques for depositing these coatings is high power impulse magnetron sputtering (HiPIMS) [113].

TiB_2 has been widely studied for its good properties such as high hardness between 25-35 GPa, good chemical stability and high melting point (>3000ºC) [113,226,229–232]. which make it an excellent candidate as protective coating. The main problem of these coatings is the high internal tensions that can cause fracture of the film and also high friction coefficient [231]. The introduction of carbon in these structures is a good approach to reduce friction and wear, extending the lifetime of these coatings [108,161,233,234]. These Ti-B-C systems, also called TiB_xC_y, have been deposited and studied by several techniques such as high pressure spark plasma sintering [235], thermo reactive diffusion [236], ion beam deposition [237], pulsed laser ablation [238], chemical vapor deposition [239] and magnetron sputtering [161,233,234,240–242]. HiPIMS technology has been applied to produce TiB_2 thin films, but the study of the incorporation of the carbon over TiB_2 prepared by HiPIMS has not been described yet [113,205].

In this chapter, the influence of the addition of carbon on TiB_2 films sputtered via HiPIMS is studied. Coatings were prepared by multi-target magnetron sputtering using two graphite targets and two TiB_2 targets. The TiB_2 targets were used in HiPIMS and the graphite targets in DC mode. The power densities applied to the graphite and TiB_2 targets were fixed, while the carbon content was controlled by the graphite sputtering time. Very high harnesses are reached due to the formation of nanocrystalline hard TiB_2 phase and the inclusion of C in the TiB_2 forming additional hard TiB_xC_y phases. Accordingly, the microstructural evolution and the variation of the mechanical properties of the TiBC thin films were systematically investigated.

4.1. Coating deposition parameters

TiB_2-TiBC coatings in this study were prepared using a CemeCon CC800/9 ML equipment. The coatings were grown onto silicon wafer and mirror polished AISI D2 steel by argon sputtering of TiB_2 and graphite targets (CemeCon 99.965% purity). The magnetrons were connected to HiPIMS (TiB_2) and DC power sources (graphite), at sputtering powers of

4.5 kW and 1 kW, respectively. HiPIMS pulse parameters were the following: a duty cycle of 5.5 %, a duration of 70 µs and a repetition frequency of 800 Hz. The potential of the substrate holder was operated at 70 V. The background pressure was 3×10^{-3} Pa and the working pressure was set in a range of 0.3 to 0.45 Pa. sputtering times are summarized in Table 4-1. Sample C1 was prepared by sputtering the TiB_2 target. In sample C2, after sputtering the TiB_2 target for 3 hours, the introduction of carbon was carried out during the last 30 minutes of the deposition by switching on the graphite target leading to a co-deposition of C and TiB_2. In sample C3, the TiB_2 and graphite targets were co-sputtered during the whole process.

4.2. Results and discussion

4.2.1. Elemental composition and structural characterization

The elemental compositions of the coatings obtained by EPMA are summarized in Table 4-1. The carbon content varied from 0 to 11 at. %. The carbon content in the sample C2 is relatively low (~ 3 at. %), as carbon was added only in the last step of the coating deposition. In C3 sample, carbon was added from the beginning of the synthesis and a value of 11 at. % is reached. The oxygen content ranged from 2 to 8 at. % in the coatings, in agreement with the reported bibliography of other authors preparing TiB_2 by HiPIMS [113,205].

Table 4-1: Summary of the deposition parameters and properties of the coatings.

Films	Sputtering time (h)		Elemental composition (at.%)			Thickness (µm)	Roughness (nm)
	TiB_2	C	Ti	B	C		
C1-TiB_2	3.5	-	31	69	-	3.03	5.6
C2-TiB_2/TiBC	3.0	0.5	30	67	3	2.27	2.3
C3-TiBC	2	2	27	62	11	1.07	1.5

Figure 4.1 shows SEM micrographs of the cross-sections (left) and AFM surface images (right) of the samples deposited. The three samples were characterized by a dense structure and fine columns, with no significant differences among them. Despite the carbon addition during the last step of the deposition process, no bilayer structure (or multilayer) could be identified in sample C2. Similar morphologies on TiB_2 coatings prepared by HiPIMS were reported by Zhang *et al.* [205]. The AFM top surface images (scanning area = 10 µm x 10 µm) shown in Figure 4.1 reveal very smooth surfaces. The RMS roughness of the prepared coatings is shown in Table 4-1. The highest value (5.6 nm) corresponds to the pure TiB_2 film while the incorporation of carbon leads to a progressive decrease on the roughness (from 5.6 to 2.3 and 1.5 nm). These roughness values are similar to those found by Zhang *et al.* [205]

for TiB_2 coatings and lower than those reported by Contreras *et.al.* for TiBC films deposited by DC-MS [242].

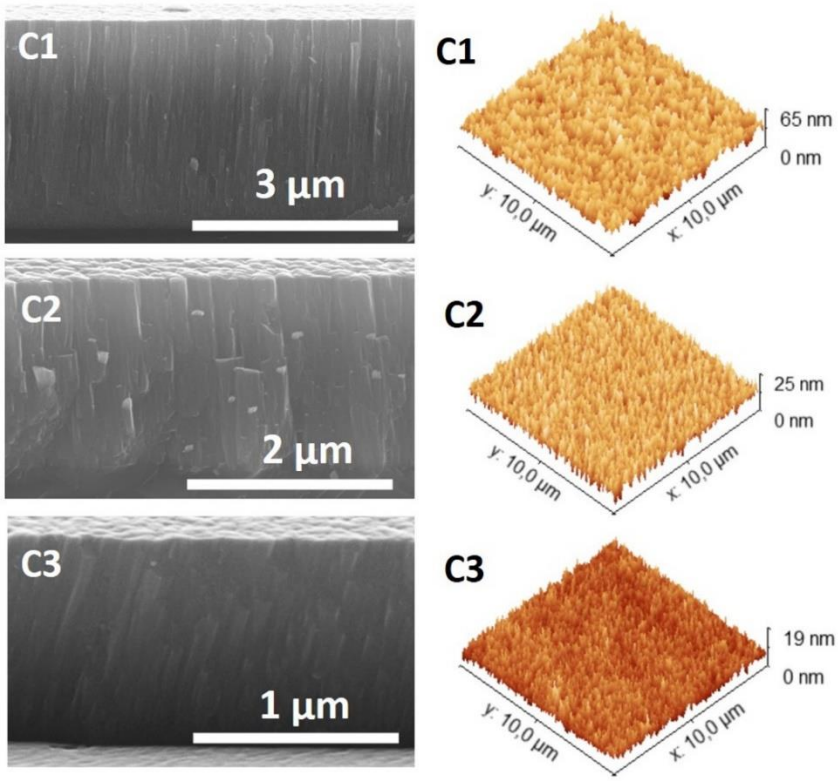

Figure 4.1:SEM cross-section images (left) and AFM top-view images (right) of the studied thin films.

The XPS spectroscopy analysis allow us to investigate the chemical bonding structure. Figure 4.2a shows the B 1s photoelectron spectra for the three coatings. The chemical bonding located at 188.0 eV is assigned to the B-Ti bonds in C1 sample (as there is no carbon on the sample). Interestingly, the spectrum of sample C3 shows a shift of 0.2 eV to higher binding energies which agrees with the incorporation of a more electronegative element, such as carbon, and therefore it is assigned to the B-C bonds. [241]. This displacement of the B 1s peak position was also observed by Baker in TiBC thin films with growing C contents [243].

Figure 4.2b displays the three main component peaks considered in the fitting analysis of C 1s XPS peak for sample C3 (as representative of coating C2 and C3) at 283.0, 284.6 and 286.0 eV. The peak at 283.0 eV can be assigned to a carbon atom bonded to both Ti and B forming a titanium boride-carbide phase (TiB_xC_y) as previously reported by other authors [233,234]. The components at 284.6 and 286.0 eV can be ascribed to carbon bonded

to carbon (C-C) and hydroxide groups (C-OH), respectively, from the hydrocarbon contamination layer formed by the air exposure. The absence of a segregated amorphous C-C phase was proved by micro-Raman analysis (results not shown), in agreement with the low carbon concentration inside the samples. Based on these results, carbon atoms in Ti-B-C

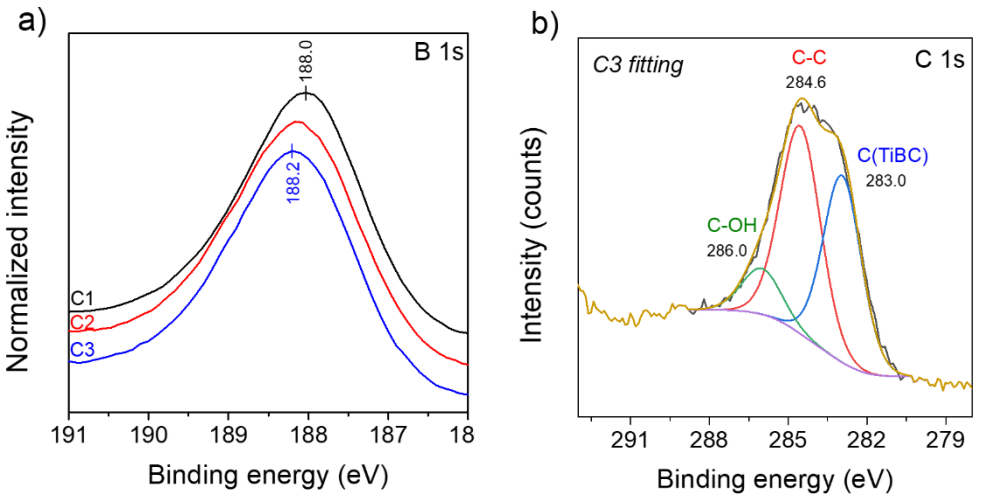

Figure 4.2: (a) XPS spectra of the B1s photoelectron peak for the coatings and (b) a representative example of the XPS fitting of the C 1s for the coating C3.

coatings, are whether occupying interstitial sites within the hexagonal structure of the TiB_2 or forming bonds with titanium and boron atoms, but not in a free state in form of amorphous carbon.

Figure 4.3 depicts the diffractograms in the Bragg-Bentano and grazing incidence geometry at 0.5º, 1º and 2θ degrees. The analysis of the diffractograms allowed the identification of the following phases: TiB_2 (JCPDS card nº 075-0967), and the substrate AISI D2 steel (JCPDS card 006-4192). The three coatings show well-defined peaks, centred at 27.8, 34.1 and 44.6 º that correspond respectively to the crystallographic planes (001), (100) and (101) of the TiB_2 hexagonal phase. The peak corresponding to the plane (101) overlaps with the plane (011) of Fe originating from the D2 substrate [242], this effect can be minimized with the 1 and 0.5º GIXRD measurements, as the signals corresponding to the substrate are removed. The (001) diffraction peaks from the samples with carbon, specially C3, shift towards lower 2θ angles in comparison to the standard pattern and C1. This can be due to the intrinsic residual stress of the thin film and/or the C incorporation in the interstitial spaces in the atomic cell [234]. If the carbon is introduced occupying the interstices of the cell, the cell size increases so the displacement of the peaks is observed at smaller angles [242]. No carbon-rich phases in the form of metal carbides are detected in the diffractograms, which again suggest that the carbon incorporated in the coating is found as a solid solution or

occupying interstices within the crystalline lattice of TiB_2. These results are consistent with those obtained for the XPS spectra.

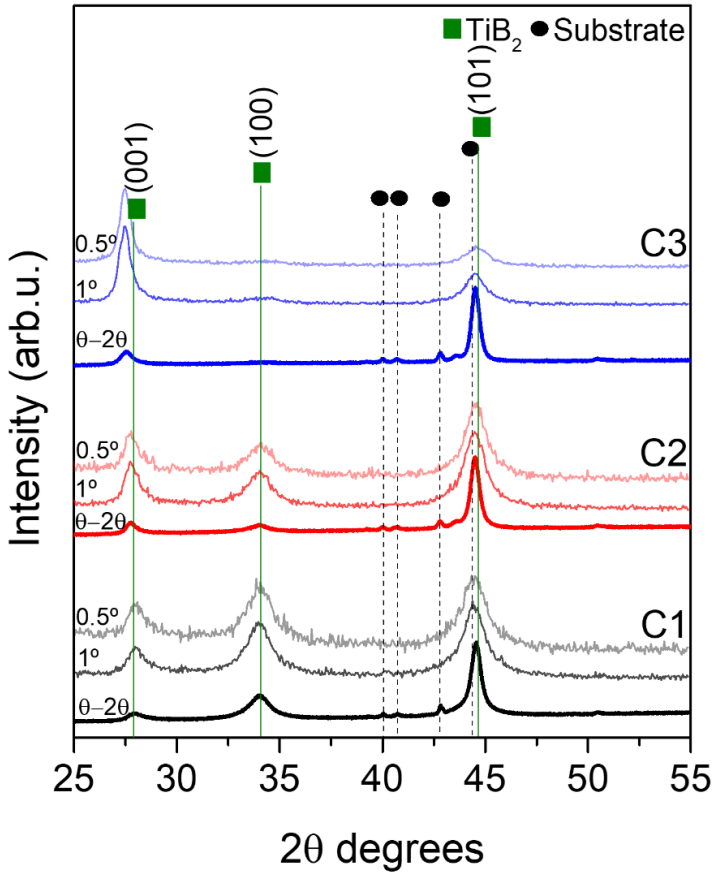

Figure 4.3: XRD and GIXRD diffractograms at Bragg-Bentano and 0.5 and 1 º configurations for the studied coatings.

GIXRD diffractograms show a clear change in the relative intensities of the different peaks as a function of the deposition process. The texture coefficient has been calculated as explained in materials and methods section and the values are shown in Table 4-2 and represented in Figure 4.4a. In the sample prepared without carbon, a combination of different texture components (preferred crystallite orientation) of the lattice planes (001), (100) and (101) parallel to the substrate surface is observed. In C2, where the carbon was added just for 30 minutes, the most significant change is the decrease of the (100). Finally C3, where the carbon was added from the beginning of the deposition process, the (100) orientation almost disappears and the (001), which is the most densely packed plane and thus possesses the lowest surface energy, becomes preferential [205,244].

In addition, the crystallite size was estimated using the Scherrer equation for the different crystallographic planes as shown in Table 4-2 and Figure 4.4b. The comparison of the values obtained from the (100) and (101) planes show minor variations in the crystallite size for the different coatings (varying from 3 to 5 nm and 6 to 7 nm respectively). In contrast, the (001)-oriented crystallites grow from 8 to 14 nm as the carbon content increased from 3 to 11 at. %. Similar crystallite sizes have been reported for TiBC thin films with carbon contents around 5-8 at. % [241]. The results obtained for the texture development and crystallite size are consistent with the changes observed during the modification of the bias voltage reported by Zhang *et al.* [205]. In addition, the low carbon concentrations attained in these coatings reduce the trend towards amorphization of the TiB_2 phase as observed in TiBC coatings with higher carbon contents [234].

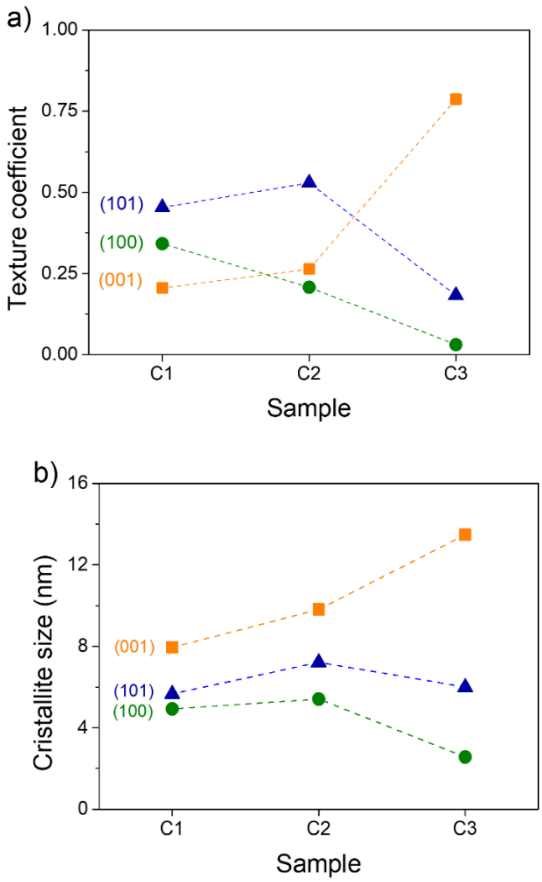

Figure 4.4:Texture coefficient development (a) and crystallite size (b) of the prepared coatings.

4.2.2. Mechanical characterization

The Daimler–Benz Rockwell-C (HRC-DB) adhesion test is a commercially adopted method to evaluate film/substrate adhesion quality, which has grown relevance during the last years [211,245,246]. By observing the indentation marks, adhesion properties can be classified into two groups: H1-H4 acceptable, H5-H6 not suitable [211]. The inspection of the indentations in the coatings (Figure 4.5a) allows to determine H1, H2 and H3 adhesion quality for the samples C1, C2 and C3 respectively. The adhesion is acceptable for all the samples and no delamination is observed. Samples C1 and C2 show radial cracks around the crater, indicating high hardness and brittleness for both coatings. In C3 sample, the adhesion is not so good as inferred from the presence of branched cracks, but still acceptable.

Ball cratering measurements were performed with the aim of determining the resultant thickness of the coatings, and studying the abrasion resistance [114], as can be appreciated in Figure 4.5b. The values of the thickness match with the ones obtained by cross-section SEM (Table 4-2). Visual assessment of the craters in Fig. 5b does not show any perceptible difference in the wear behaviour in the whole section of the coating which confirms that the thin films are homogeneous, even the sample C2 which had a two-step deposition process.

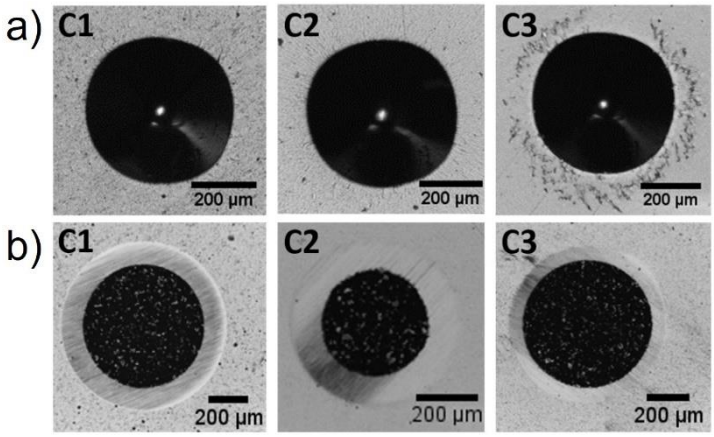

Figure 4.5: a) Photomicrographs of the pits in the coatings surface after a Daimler-Benz test on the samples. b) Images of craters grided by ball crater micro-abrasion method (Calotest) of the different coatings.

The type of failure which is observed by scratch-tests for a given coating-substrate system depends on the test load, the coating thickness, the residual stress and the properties of the substrate (e.g. hardness), as well as on test parameters such as indenter radius and sliding speed [215]. The scratch test marks have been etched with Heyn's reagent to reveal the presence of the substrate and thus detect the failure of the coating (Figure 4.6). Different coating damages can be observed according to [214,215]. L_{c1} and L_{c2} are respectively defined as the load at which the first cracking occurs, and the load at which catastrophic failure begins.

In C1 sample, gross spallation (brittle fracture) is observed and *the* catastrophic failure (L_{c2}) is determined to be at 11.0±0.5 N. This can denote poor adhesion and/or high residual stress of the coatings. C2 and C3 samples however, present a different failure mechanism associated to buckling and spallation. The composition of these coatings (TiB_2 and TiB_xC_y phases) allows the stress generated by the moving indenter to be released by buckling the coating. In C2 where the TiB_xC_y phase was formed only in the last step on deposition process, the buckling spreads laterally by the propagation of an interfacial crack results in spallation. The higher carbon content, and therefore, TiB_xC_y formation across the entire thickness in C3, led to restricted crack propagation and no clear signs of buckle spallation are observed.

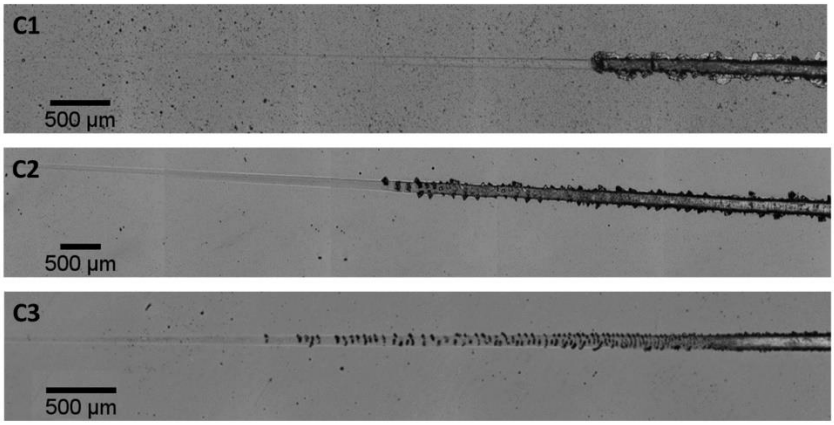

Figure 4.6: Optical images show scratch tracks and the failure of the coatings.

The critical loads for C2 are L_{c1} 12.8 ± 1.2 N and L_{c2} 16.1 ± 0.3 N, and for C3 are L_{c1} 6.31 ± 0.1 N and L_{c2} 18.2 ± 0.8 N. Figure 4.7 displays the L_{c1} and L_{c2} results for the coatings. Similar L_c values varying from 8 to 17 N were found by Contreras *et al.* for TiBC thin films [242]. The TiB_2 coating (C1) exhibit the lowest critical load, attributed to the hard and brittle character of TiB_2. The incorporation of carbon has led a significant increase of the interfacial adhesion, up to 50 % with respect to the TiB_2 coating. The carbon incorporation in the films changes the failure mechanism, as the crack formation appears at lower loads, but the final breakage occurs at higher loads. These values are still low compared to other coatings reported in the literature [159], which could be enhanced by previous deposition of an anchoring layer, such as Ti or TiN.

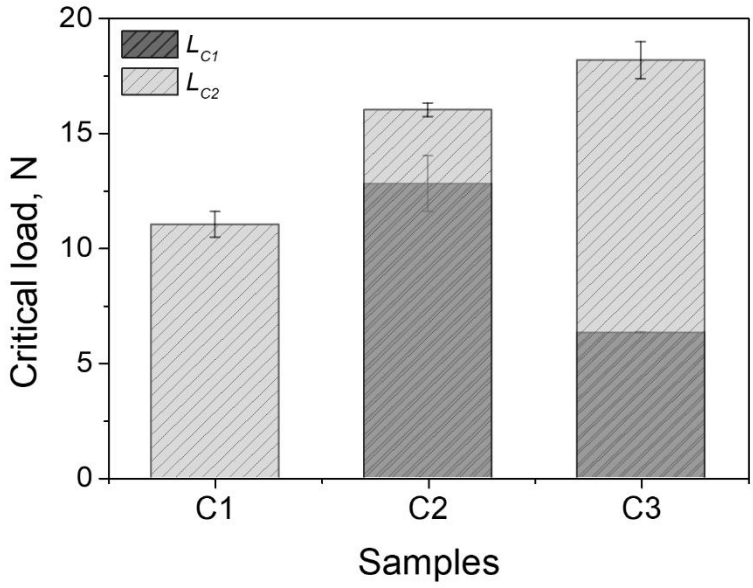

Figure 4.7: LC_1 and LC_2 for the prepared coatings

Hardness and reduced Young modulus of the coatings were measured by nanoindentation. Hardness values vary between 26 and 37 GPa and reduced Young modulus between 365 and 447 GPa depending on the sample and the carbon concentration (Table 4-2). Both C2 and C3 present higher hardness than C1, which shows that the addition of carbon in the structure improve the mechanical properties (Figure 4.8). Contreras *et al.* [242] reported a similar trend with low carbon incorporations and concomitant shift of the (001) TiB_2 diffraction peak. Higher carbon concentrations lead to a decrease of the hardness values because of the favoured formation of an amorphous C (a-C) phase although it results in an enhancement of the tribological properties. Abad *et al*. showed a correlation of the hardness with the formation of a ternary TiB_xC_y phase and the reduction of coefficient of friction by increasing the a-C fraction [161]. In the present research, we show that a small addition of carbon is assimilated into the crystal structure of TiB_2 leading to the formation of the phase TiB_xC_y which correlates with the hardness increment. The reduced Young modulus decreases slightly, but it is still quite high. The consequence increase in the H/E ratio (Table 4-2) helps to increase fracture toughness [152,247], as showed by enhanced resistance to crack propagation in parallel to TiB_xC_y formation.

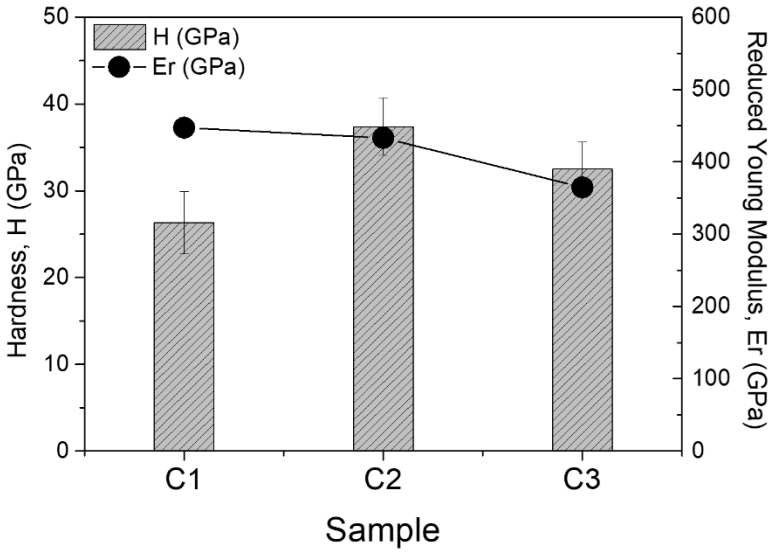

Figure 4.8: Hardness (H) and reduced Young modulus (Er) of the prepared samples.

Table 4-2: Summary of microstructural and mechanical properties of the coatings.

Films	Texture coefficient	Grain size (nm)			Critical load (N)		H(GPa)	Er (GPa)	H/Er
	(001):(100):(101)	(001)	(100)	(101)	L_{c1}	L_{c2}			
C1-TiB_2	0.21:0.34:0.45	8	5	6	-	11±0.5	26.3±3.6	447±9	0.059
C2-TiB_2/TiBC	0.26:0.21:0.53	10	5	7	13±1.2	16±1.3	37.4±3.3	433±10	0.086
C3-TiBC	0.79:0.03:0.18	14	3	6	6.3±0.1	18±0.8	32.5±3.1	365±8	0.089

4.3. Conclusions

TiBC coatings have been successfully deposited using the HiPIMS technique with the introduction of up to 11 at. % carbon in the structure. Thanks to the additional ion bombardment provided by this technique, the coatings appear to be very smooth and compact. The microstructure is formed by very fine columns and the average roughness parameters are in the range of 1-6 nm. The B 1s and C 1s XPS peaks confirm the formation of a mixed TiB_xC_y phase where carbon is bonded to boron and titanium. The displacement of the XRD peaks to smaller angles with the carbon incorporation matches with the expansion of the unit cell due to carbon incorporation in the TiB_2 lattice. In addition, a preferential orientation to the most densely packed plane (001) and increased crystallization is denoted in parallel to the TiB_xC_y formation. The addition of carbon in the structure changes the fracture mechanism and improves the adhesion to the substrate. While in pure TiB_2 a catastrophic failure is observed around 11 N load value, in TiB_2/TiBC and TiBC films, restricted crack propagation and no clear signs of buckle spallation are observed. The benefits of small addition of carbon (up to 11 at. %) is also manifested in a hardness increment with values ranging between 32 and 37 GPa.

CHAPTER 5

NbC/a-C(:H) nanocomposite coatings

The results of this chapter gave place to different scientific contributions:

Contributions to communications:

1. I Jornada de doctorands IQS. Barcelona, Spain. "*Characterization of niobium carbide films deposited by two different techniques: DC and HiPIMS*". **N. Sala**, C. Colominas, M.D. Abad. Poster presentation. 16-17 May 2019.
2. 11a trobada de joves investigadors de la Societat catalana de química. Vilanova i la Geltru, Spain "*Recobriments ceràmics nanoestructurats preparats per plasma d'alta energía*". **N. Sala**, C. Colominas, M.D. Abad. Oral presentation. 28-30 January 2020.
3. ICMCTF 2021. Online conference. *"Nb-C Thin Films Prepared by DC-MS and HiPIMS: Synthesis, Structure and Tribo-mechanical Properties"*. **N. Sala**, M.D. Abad, J.C. Sánchez-López, J. Caro, C. Colominas. Poster presentation. 26-30 April 2021.
4. ÖGV Seminar 2021. Vienna, Austria. "*Ceramic nanostructured coatings prepared by high energy plasma Technology"*. **N. Sala**, M.D. Abad, C. Colominas, J.C. Sánchez-López. Oral presentation. 24th September 2021.

Contribution to publications:

1. Part of this chapter was published in the Materials Letters journal with an article entitled: "*Tribological performance of Nb-C thin films prepared by DC and HiPIMS"*.
   N. Sala, M.D. Abad, J.C. Sánchez-López, M. Cruz, J. Caro, C. Colominas, Tribological performance of Nb-C thin films prepared by DC and HiPIMS, Mater. Lett. 277 (2020) 128334. https://doi.org/10.1016/j.matlet.2020.128334.
2. A second article based on these results was published in the Surface & Coatings Technology journal, entitled: "*Nb–C thin films prepared by DC-MS and HiPIMS: Synthesis, structure, and tribomechanical properties"*.
   N. Sala, M.D. Abad, J.C. Sánchez-López, J. Caro, C. Colominas, Nb–C thin films prepared by DC-MS and HiPIMS: Synthesis, structure, and tribomechanical properties, Surf. Coatings Technol. 422 (2021). https://doi.org/10.1016/j.surfcoat.2021.127569.

5. NbC/a-C(:H) nanocomposite coatings

Diamond-like carbon (DLC) is a form of amorphous carbon with a certain quantity of sp^3-hybridized bonds [248,249]. DLC films are well known for their excellent properties, including high hardness, high wear resistance, chemical inertness, and biocompatibility [250]. Some drawbacks of DLC films are their high residual internal stress, poor thermal stability, and low adherence to metallic substrates [251]. Accepted methods for improving these properties include metal doping (Ti, W, Nb, Cr, etc.) [108,172,252,253] and incorporation in multilayer films or nanocomposites.

Among the various nanocomposite systems, many studies have focused on TiN, WC, and CrC crystals embedded in amorphous and hydrogenated amorphous carbon films [85,108,161,254] for tribological applications and electrical contacts. Niobium carbide (NbC) exhibits a high melting point, high conductivity, and excellent chemical stability [255,256], making it suitable for electrical components [257], high-temperature environments [15], and biomedical applications [259,260]. NbC thin films have been deposited by plasma-assisted physical vapor deposition (PVD) techniques, including filtered cathodic vacuum arc deposition [261], plasma ion implantation [262], non-reactive magnetron sputtering of Nb and C targets [257], and reactive magnetron sputtering using a hydrocarbon gas as a carbon precursor (CH_4 [252,259,263–265] and C_2H_2 [162,266]). However, NbC thin films obtained using high-energy PVD techniques have been less studied. Most recently, Nb–DLC systems were deposited using hybrid DC-MS and HiPIMS.

In this chapter, the chemical composition, microstructure, morphology, thermal stability, and tribomechanical properties of NbC coatings deposited by DC-MS and HiPIMS were studied to reveal the interrelations between them.

5.1. Coating deposition parameters

Nb–C coatings were deposited using an industrial CemeCon CC800/9 ML magnetron sputtering machine in DC-MS or HiPIMS mode. The coatings were labeled #DC or #Hi according to the sputtering technique employed (DC-MS or HiPIMS, respectively). Graphite and Nb targets from CemeCon (99.95% purity) were used to deposit the NbC coatings on single-crystalline silicon wafers (100) and mirror-polished cold-worked AISI D2 and SS316 steel substrates. Argon was used for plasma formation, and acetylene was used as a reactive gas to increase the carbon content in specific samples. The background pressure was 3×10^{-3} Pa, and the working pressure was 0.3–0.45 Pa. A DC bias of 120 V was applied to the substrates during the entire deposition process. The sputtering powers were 3.5–3.6 kW and 1.1–1.2 kW for the Nb and C targets, respectively. The HiPIMS pulse parameters were: duty cycle of 28%, duration of 70 µs, and repetition frequency of 4000 Hz. To improve coating

adhesion, a thin layer of pure Nb was initially deposited. Subsequently, the graphite target was switched on for the deposition of the NbC layers according to the deposition parameters summarized in Table 5-1. A third layer was deposited in samples #2DC, #3Hi, and #4Hi by introducing acetylene at a flow rate of 35 sccm as the reactive gas for the sputtering process of the Nb and C targets. For sample #4Hi, an extra layer of carbon was added by reducing the power applied to the Nb target to 0.3 kW during the last 75 minutes of the process. Further details about the synthesis procedure and characteristics of the films can be found elsewhere [115].

Table 5-1: Deposition conditions, growth rate, and coating thickness for each layer of the various samples.

Film	Sputtering time (min)				Cathode power (kW)		Thickness (nm)				Total Thickness (μm)	Growth rate (nm/min)			
	Nb	Nb+C	Nb+C+ C_2H_2	C+C_2H_2	Nb	C	Nb	Nb+C	Nb+C +C_2H_2	C+C_2H_2		Nb	Nb+C	Nb+C +C_2H_2	C+C_2H_2
#1DC	50	35	-	-	3.5	1.1	538	362	-	-	0.90	11	10		-
#2DC	50	45	50	-	3.5	1.1	530	505	694	-	1.73	11	11	14	-
#3Hi	45	40	40	-	3.6	1.2	398	574	654	-	1.63	9	14	16	-
#4Hi	35	35	35	75	3.6	1.2	264	435	495	180	1.37	8	12	14	2

5.2. Results and discussion

5.2.1. Chemical composition

The elemental chemical compositions of the NbC coatings obtained by EPMA are shown in Figure 5.1a and Table 5-2. Depending on the synthesis conditions, the carbon content varied from 12 to 66 at.%, and the niobium content varied from 29 to 83 at.%. The number of oxygen impurities was relatively low (≤ 5 at.%), except in coating #3Hi (~10 at.%). Similar oxygen contents (2–11 at.%) can be found in earlier studies [259,260]. The amount of oxygen can be attributed to the oxygen absorbed by the coating during synthesis (residual gases) and exposure to an open atmosphere [267]. Figure 5.1b shows the C/Nb ratios of the prepared coatings. In the #1DC sample, the amount of carbon was very low compared to that of niobium because of the synthesis conditions (non-reactive mode). After the acetylene precursor was introduced in the process, the carbon content increased considerably, up to ~1.1 in samples #2DC and #3Hi. The sample with the highest percentage of carbon was #4Hi (C/Nb > 2) because an extra hydrocarbon layer was deposited on top of the third layer.

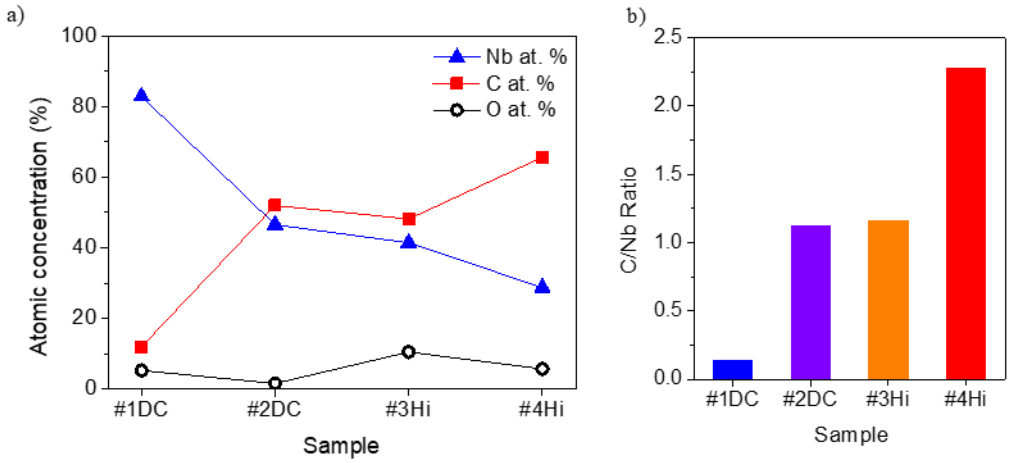

Figure 5.1: (a) Atomic elemental composition and (b) C/Nb ratio of the prepared Nb–C thin films.

Table 5-2: Summary of the properties of the coatings

Film	Elemental composition (at. %)			Roughness		Crystalline phases detected by XRD	H (GPa)	μ
	Nb	C	O	Ra	RMS			
#1DC	83	12	5	0.91	1.02	Nb, Nb_2C	20±2.3	0.85±0.01
#2DC	47	52	1	1.67	2.12	Nb, NbC, Nb_2C	18±0.8	0.27±0.02
#3Hi	42	48	10	1.86	3.58	Nb, NbC	11±0.6	0.24±0.01
#4Hi	29	66	5	2.92	3.69	Nb, NbC	12±1.3	0.25±0.02

5.2.2. Microstructure

Figure 5.2 shows secondary electron (SE, left) and backscattered electron (BSE, middle) SEM images of the cross sections of the deposited coatings and as well as top-view (right) images of the samples. Several microstructures were observed corresponding to different sequences of stacked layers. Table 5-1 shows the coating thickness for each layer measured using SEM and the calculated growth rate. The first layer of coating #1DC (Nb adhesion layer) was approximately 500 nm thick, which changed into a denser structure when carbon was incorporated in the second stage. Coating #2DC exhibited a three-layer structure, in which the additional top layer was generated by introducing acetylene as a carbon precursor. The top layer had a more columnar structure. It is worth noting that the HiPIMS samples developed a clear columnar morphology from the substrate interface to the top surface. Samples #3Hi and #4Hi had very similar microstructures, but sample #4Hi had an extra carbon-rich top layer, which can be clearly observed in the BSE-SEM images. From the top view, samples #1DC and #2DC present considerably more compact structures than those

of the HiPIMS samples. The degree of definition of the columnar boundaries increases in the sequence #1DC < #2DC < #3Hi < #4Hi.

Figure 5.3 displays AFM topographic images (5 × 5 μm^2) of the Nb–C coatings. The columnar growth of the coatings resulted in an increase in the surface roughness. The estimated mean average (Ra) and root mean square (RMS) roughness values of the coatings are shown in Figure 5.4 and Table 5-2. In good agreement with the SEM observations, the DC-MS samples had smoother surfaces than those of the HiPIMS samples. The selected HiPIMS conditions appear to favor more columnar and less compact structures with increased roughness.

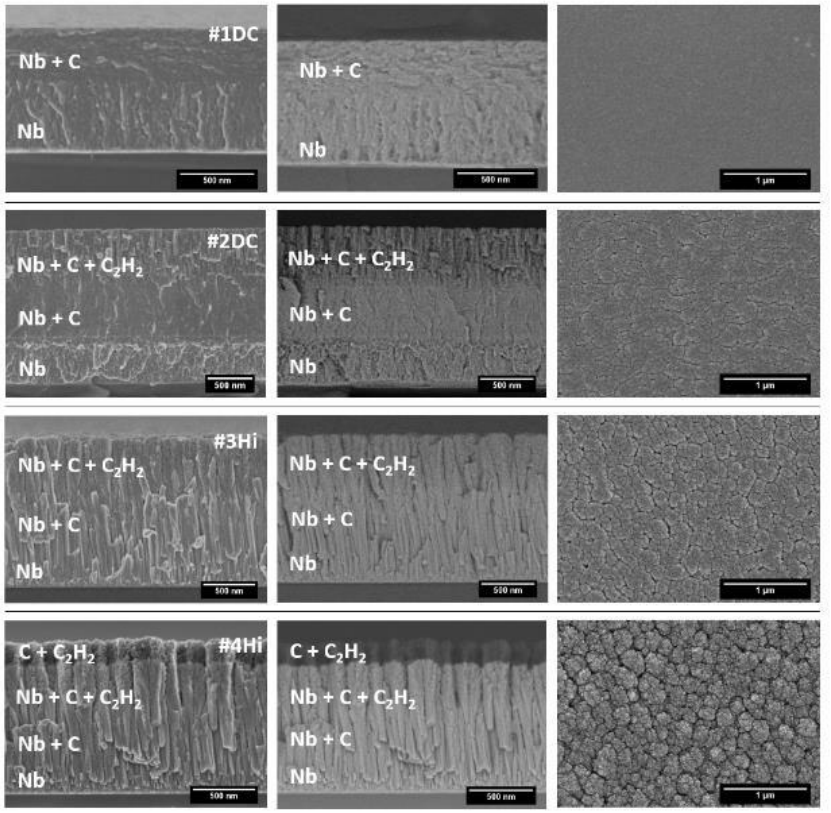

Figure 5.2: Cross-sectional (left, SE; middle, BSE) and top-view (right) SEM images of the Nb–C films.

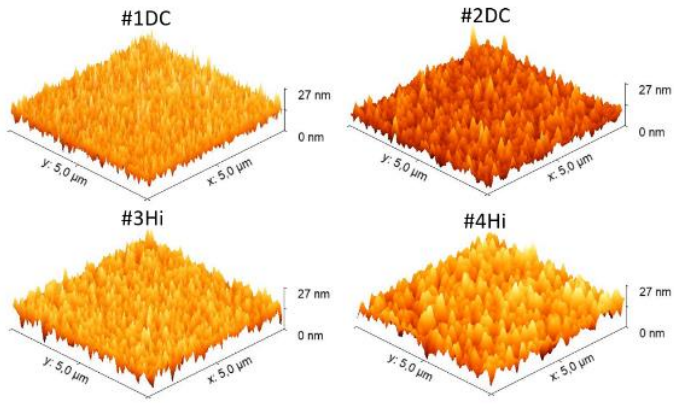

Figure 5.3: AFM images of the Nb–C coatings.

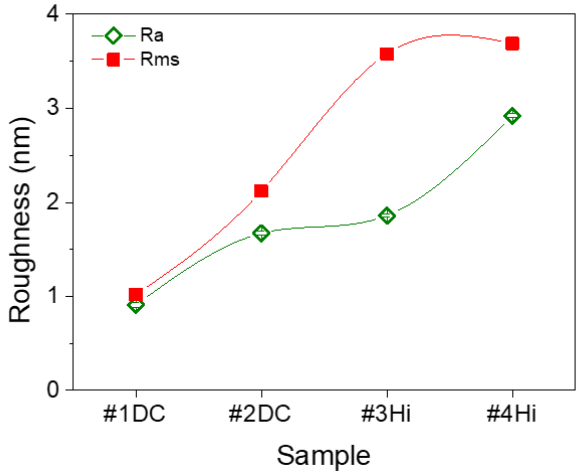

Figure 5.4: Surface roughness values (Ra and RMS) obtained by AFM measurements of the Nb–C coatings.

5.2.3. Phase composition

The crystallographic structure of the coatings was previously analyzed by XRD in a conventional coupled Bragg–Brentano configuration [115]. The crystalline phases obtained by XRD are shown in Table 5-2 for each coating. Asymmetric and broad peaks were observed, indicating nanocrystallinity and lattice defects. In this study, GIXRD diffractograms were analyzed to minimize the substrate effect and to gain more information about the top layer. The following JCPDS diffraction charts were used to identify the crystalline phases present in the samples: 34-0370 (Nb), 71-4649 (Fe), 38-1364 (NbC), and 19-0870 (Nb_2C). Figure 5.5a shows the diffractograms measured under the conventional (θ–2θ) and grazing incidence angle (1°) configurations. The dominant peaks in the coupled θ–2θ diffractograms

are the Fe and Nb peaks, which were due to the steel substrate and the Nb adhesion layer, respectively. Different phases (either Nb_2C or NbC) were formed in the films, depending on the carbon content and sputtering process.

Figure 5.5b shows a magnified view of the region of the diffractograms where the main peaks were detected (31°–43°). The diffractogram of #1DC was primarily due to the Nb adhesion layer and the top layer of Nb_2C, which was promoted by the incorporation of carbon. Sample #2DC, where acetylene was used as an extra source of carbon, showed very similar phases to those in #1DC, with an additional top layer that was richer in carbon and identified as crystalline NbC. However, sample #3Hi, which was prepared following the same stacking sequence as that of #2DC but via HiPIMS, showed a very different result from the DC-MS samples. In the coupled configuration, the cubic form of niobium carbide (NbC) was identified instead of hexagonal Nb_2C. It has been reported that with the HiPIMS technique, the density of the plasma and the number of ionized species are higher than those in the conventional DC-MS [77,268]. This could favor the incorporation of carbon into the films because of the increased population of C^+ and the assistance of Ar^+ ions present in the high-density plasma. The resulting increase in the C/Nb ratio could lead to the formation of NbC instead of Nb_2C. The #Hi4 sample did not exhibit significant crystallographic differences from #3Hi, showing that the additional a-C:H top layer was essentially amorphous. The crystal size decreased from 14 nm (sample #2D) to 8 and 9 nm for the HiPIMS samples (#3Hi and #4Hi, respectively).

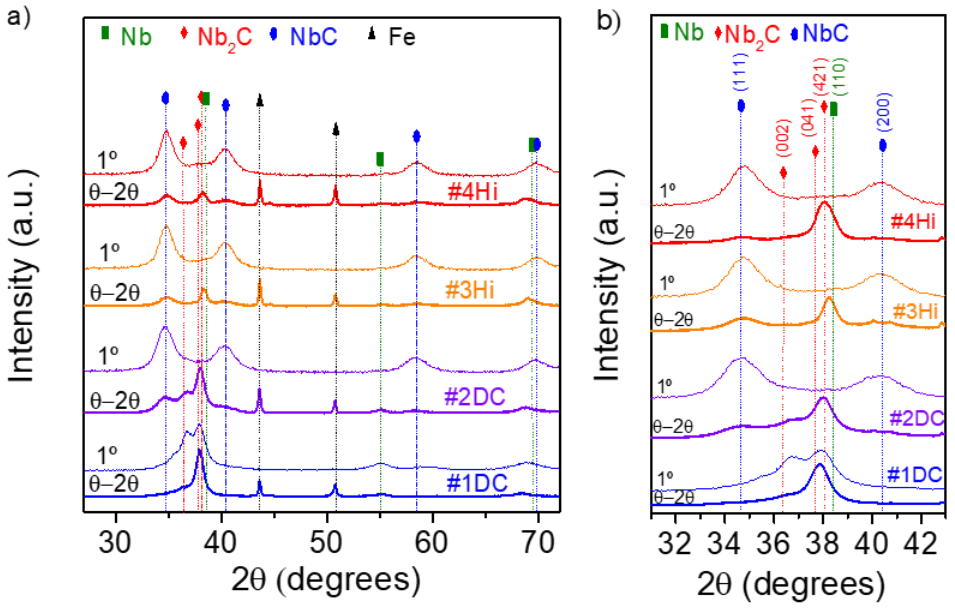

Figure 5.5: (a) XRD patterns of the Nb–C coatings deposited under different conditions measured under Bragg–Brentano and grazing incidence angle (1°) configurations; (b) detail of the region of interest.

Figure 5.6a shows the Raman spectra of the as-deposited coatings. The spectra were measured under identical conditions to allow a direct comparison of their intensities. Disordered graphite can be observed in the Raman spectra with two bands at approximately 1580–1600 cm^{-1} (G) and 1350 cm^{-1} (D), which can be attributed to the stretching of sp^2 C–C bonds and the breathing mode of sp^2 C–C aromatic rings, respectively [168]. The Nb–C coating with the lowest carbon content (#1DC) did not present the characteristic D–G bands, showing the absence of segregated a-C. The presence of disordered carbon was confirmed in the remaining coatings, for which the D and G peaks were clearly observed. Significant peak narrowing and an increase in intensity were observed for sample #4Hi owing to the top carbon-rich layer. Comparing samples #2DC and #3Hi, which had similar carbon contents (approximately 45 at.%), HiPIMS promoted the formation of a-C(:H) more than DC-MS.

To obtain complementary information about the carbon structure and chemical bonding, the G-band position, intensity ratio between the D and G peaks (I_D/I_G), and G-peak width (G_{FWHM}) were determined by deconvolution of the Raman bands using Lorenzian functions as shown in Figure 5.6b. The values can be seen in Figure 5.7. According to Ferrari and Robertson [168], the features of these Raman peaks allow the classification of samples in transition between nanocrystalline graphite and disordered carbon, with a predominance of sp^2 bonding. Samples #2DC and #3Hi had very similar Raman spectra, exhibiting broad D and G bands typically observed in a-C films. Similar I_D/I_G ratios (1.2 to 1.5) were found for NbC-based nanocomposites prepared by reactive magnetron sputtering [162,266]. Sample #4Hi, with a G peak at 1600 cm^{-1}, a small G_{FWHM} value, and an I_D/I_G ratio of ~0.9, is in agreement with region 1 of the three-stage model, representing the transition from bulk to nanocrystalline graphite [248]. This may be attributed to the final top C-rich layer that was grown only on this sample, which generated a more ordered graphitic structure. Figure 5.8 schematically summarizes the different structures and compositions of the prepared coatings based on the XRD, GIXRD, SEM, AFM, and Raman spectroscopy characterization results.

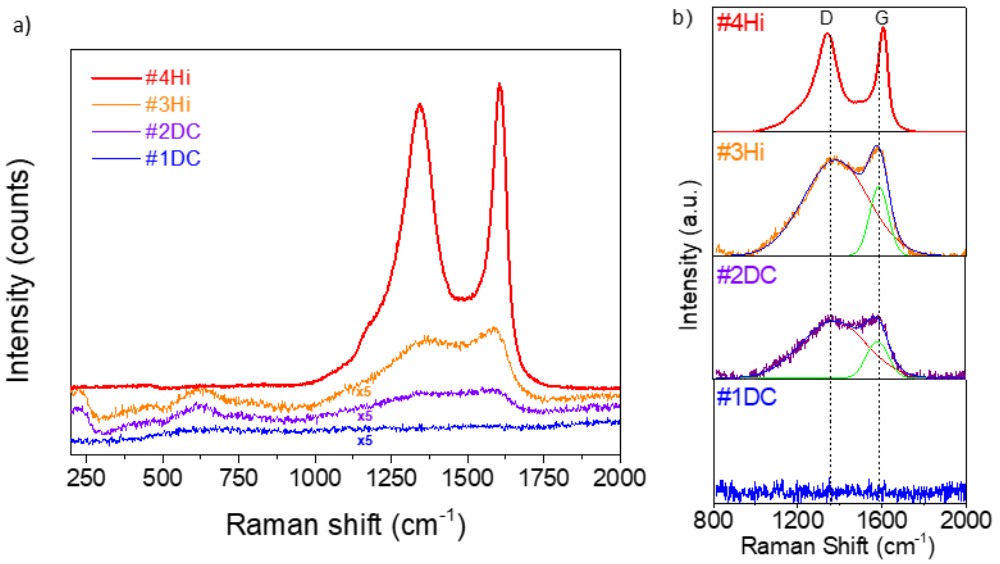

Figure 5.6: a) Raman spectra of the different coatings. Note that the spectra are plotted in counts (not in arbitrary units); thus, the changes in band intensity are significant; b) deconvolution of the Raman bands using Lorentzian functions.

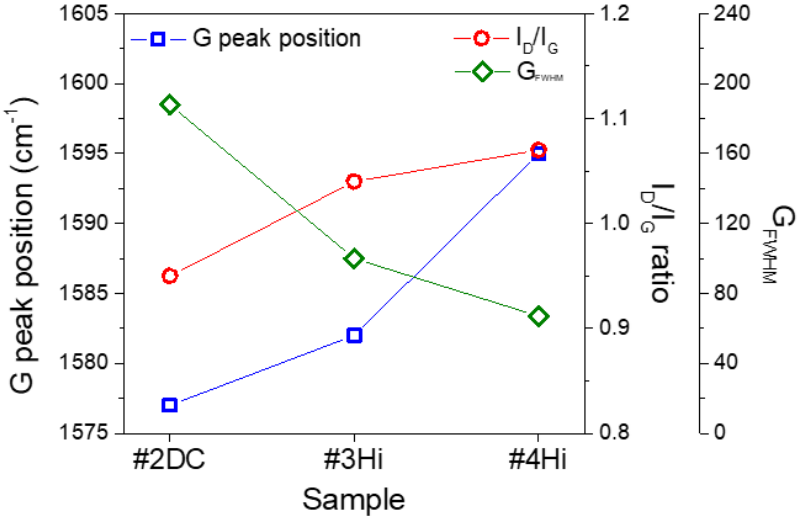

Figure 5.7: G-peak position, ID/IG ratio, and G-FWHM for the samples containing disordered carbon.

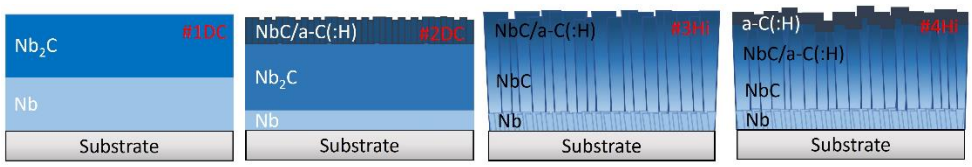

Figure 5.8: Schematics of the Nb–C coatings based on the XRD, GIXRD, SEM, AFM and Raman spectroscopy characterization results.

5.2.4. Mechanical properties

Film hardness and reduced Young's modulus values are presented in Figure 5.9. and in Table 5-2. The hardness varied between 11 and 20 GPa, in good agreement with the values presented by Nedfors *et al.* for NbC_x-based coatings (16–23 GPa) [266]. The reduced Young's modulus did not vary significantly among the samples (~220 GPa). Samples prepared by DC-MS had higher hardness values (18–20 GPa) than those of the samples prepared by HiPIMS (11–12 GPa). Comparing #2DC and #3Hi, which had similar carbon contents (~50 at.%) and stacking layer sequence, the sample prepared by HiPIMS had a lower hardness. This can be attributed to the higher fraction of amorphous carbon, as shown in the Raman spectra, and less crystalline structure, as determined by the decrease in crystalline size estimated by Scherrer's equation. A similar decrease in hardness was observed for NbC_x thin films prepared by reactive and non-reactive PVD as a function of the C/Nb ratio [266].

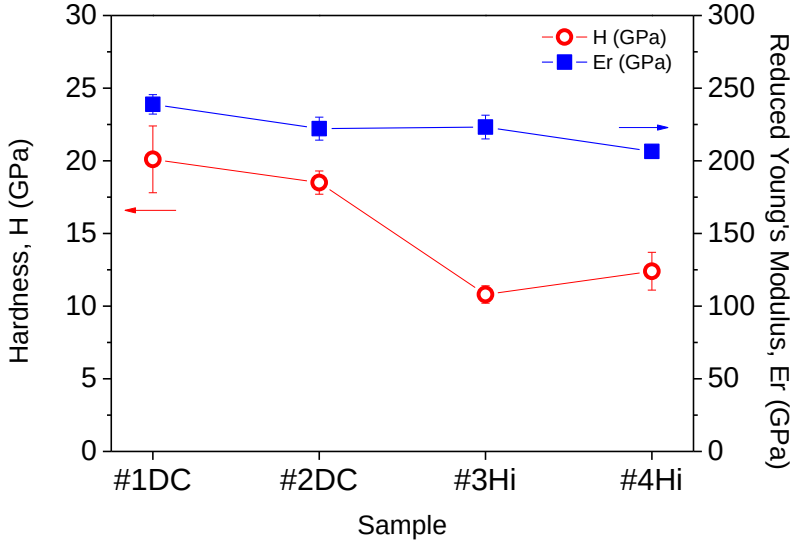

Figure 5.9: Hardness and reduced Young's modulus measurements.

5.2.5. Tribological properties

Figure 5.10 displays representative friction curves for the four different coatings. Except for #1DC, the Nb–C samples exhibited low and steady friction coefficient (μ) values of approximately 0.25 (the exact values can be found in Table 5-2). For sample #1DC, the friction coefficient curve increased suddenly to 1 after a short initial running-in period. Subsequent tests on this sample always led to the same behavior, which is consistent with strong adhesive ball–film interactions, film delamination, or cracking failure. As determined by Raman spectroscopy, this coating did not have amorphous carbon phase. Therefore, the top surface was essentially a layer of a hard metal carbide. The use of a metal ball for the tribological test resulted in strong metal-to-metal bonding, which increased the adhesion forces at the film interface and caused the sudden rise in the coefficient of friction [269]. The variation at the beginning of the test could be due to polishing of the sample because it had some initial roughness. Figure 5.11 summarizes the average measured friction coefficients and estimated ball and coating wear rates. No significant variations were observed in the tribological properties ($\mu \approx 0.25$, and $k \approx 10^{-6}$ mm^3/Nm) except for sample #1DC, which failed prematurely. A deeper investigation of the friction mechanism was conducted through Raman spectroscopy of the ball scars and coating wear tracks.

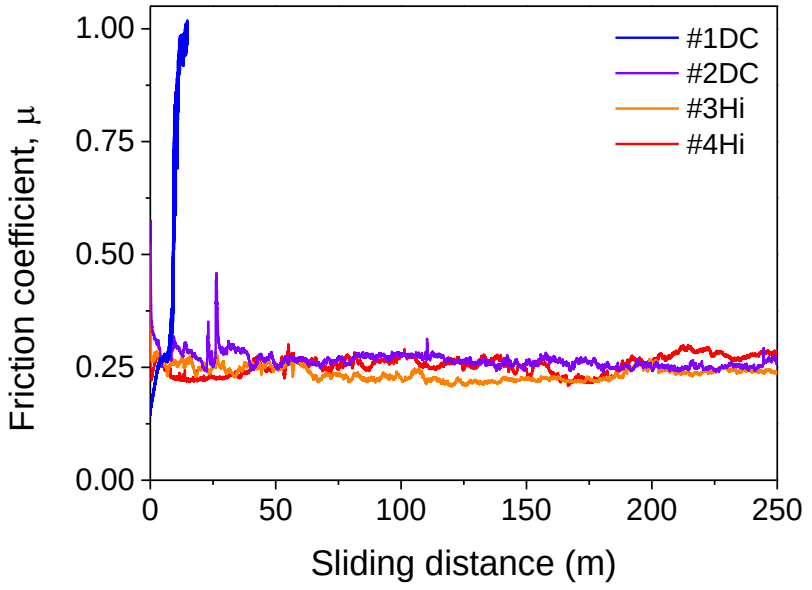

Figure 5.10: Friction coefficient vs. sliding distance for the various coatings.

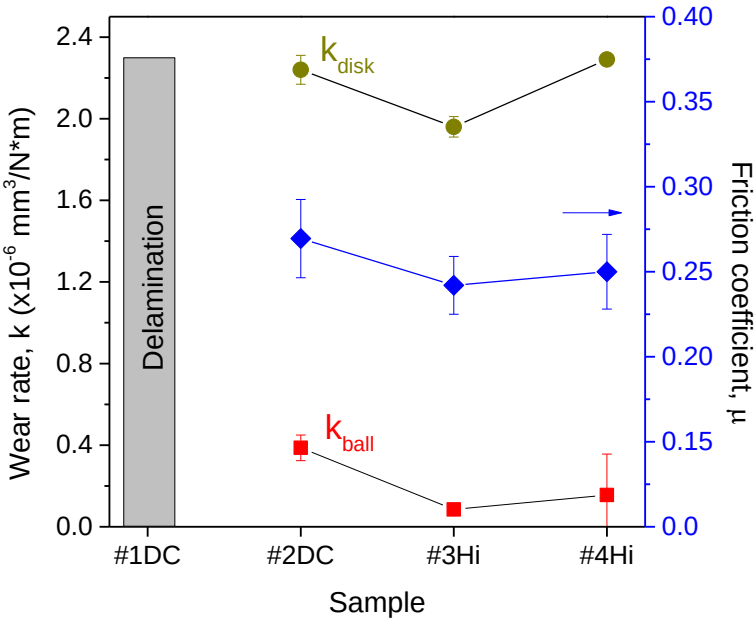

Figure 5.11: Friction coefficients and wear rates (ball and disk) for the various coatings.

5.2.6. Raman analysis of the friction contact regions

Figure 5.12 shows the worn ball surface and wear track of sample #1DC together with the corresponding Raman spectra. The wear was relatively small because the test was stopped after a sudden increase in the friction coefficient. The Raman spectra of the material adhered to the ball had two broad bands between 650 and 850 cm^{-1} associated with Nb and Fe oxides from the coating [270] and the ball, respectively. The presence of free amorphous carbon in metal carbide/a-C nanocomposites allows the formation of a lubricant layer between the ball and the coating, decreasing friction and excessive wear [108,271]. The absence of a free amorphous carbon in this sample, as evidenced by Raman spectroscopy, explains the sudden increase in the friction coefficient and the failure of the film.

The Raman spectra of various positions on the wear track of the #2DC sample were similar to those of the as-deposited state (Track P1) and other colored zones, indicating the presence of oxides (Track P2). On the ball scar, (Ball P1), analysis of debris outside the worn area provided evidence of graphitization of the original disordered carbon phase of the coating. The D and G bands could be clearly identified and were even more pronounced than those of the original sample. In the center of the ball (Ball P2), no transfer material was identified, showing that it was not present or that it was too thin to be detected (Figure 5.13).

The black spots observed on the wear track of the #3Hi sample (Figure 5.14) appear to indicate that some local delamination occurred during the test. However, the corresponding Raman spectra were consistent with the presence of amorphous carbon at all positions. On the ball scar, an increase in the carbon content was observed together with some poorly formed FeO_x/NbO_x oxides at approximately 650 and 850 cm^{-1} [234,272,273].

The Raman spectra of the wear track of sample #4Hi and the ball scar (Figure 5.15) indicate that the nanocrystalline graphite initially present in the film transformed into more disordered carbon during the test. This sp^2-rich layer on both counterfaces lubricated the contact, which reduced the friction coefficient and wear rates of the ball and track. Oxides were observed only in small regions on the top of the ball.

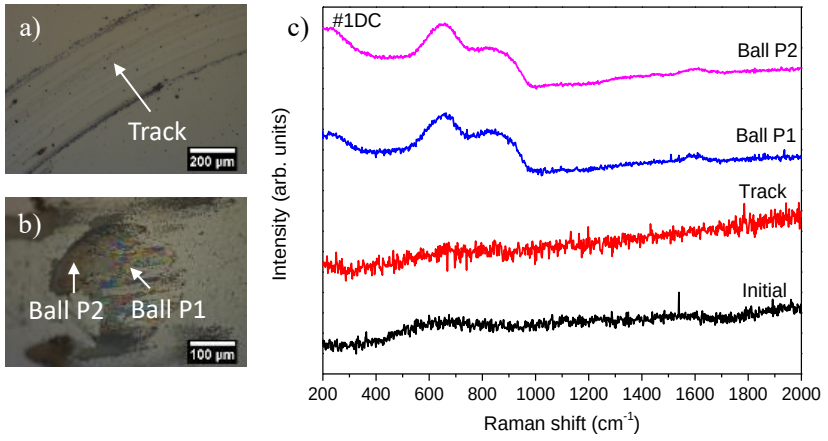

Figure 5.12: Optical micrographs of the (a) wear track of coating #1DC and (b) ball wear scar; (c) corresponding Raman analysis of the specified zones.

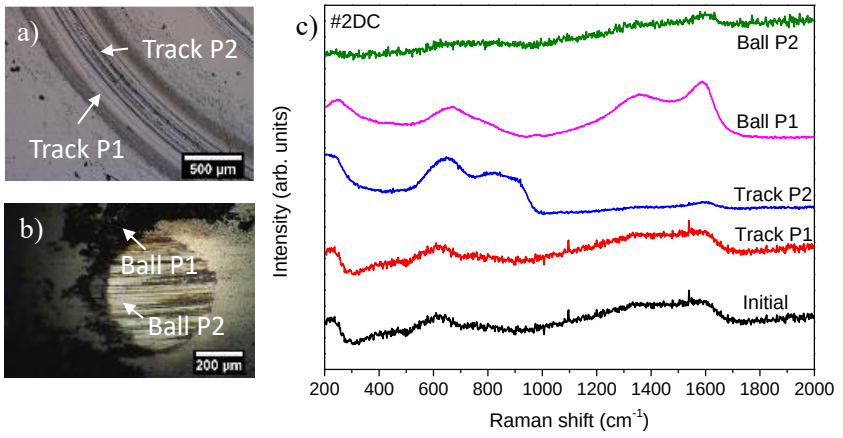

Figure 5.13: Optical micrographs of the (a) wear track of coating #2DC and (b) ball wear scar; (c) corresponding Raman analysis of the specified zones.

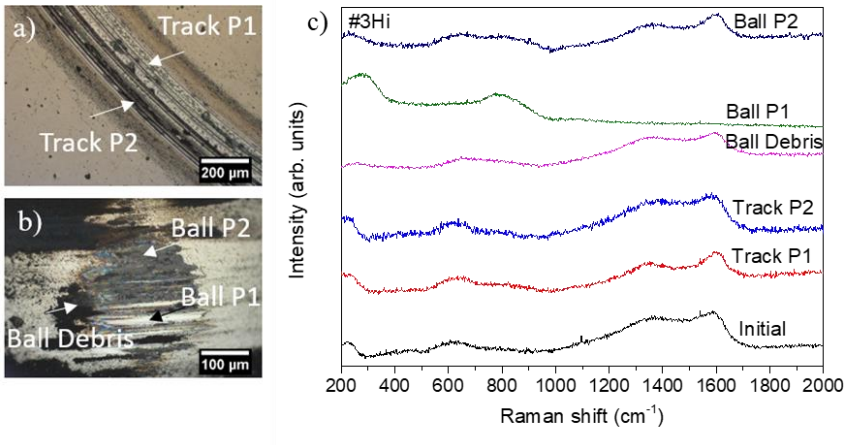

Figure 5.14: Optical micrographs of the (a) wear track on coating #3Hi and (b) ball wear scar; (c) corresponding Raman analysis of the specified zones.

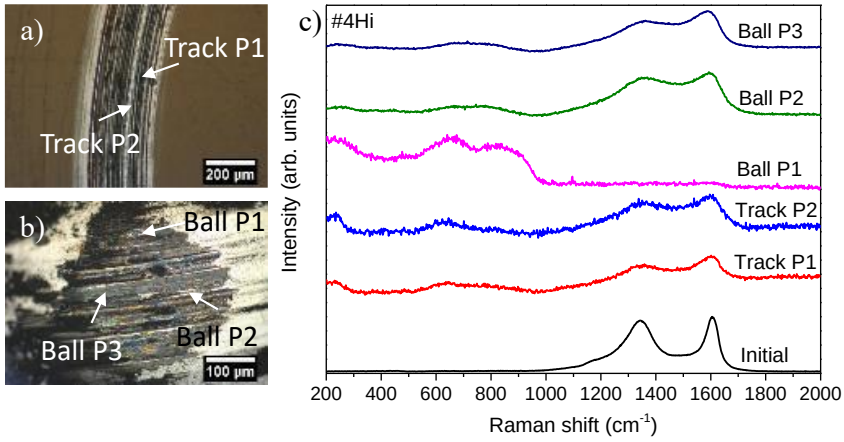

Figure 5.15: Optical micrographs of the (a) wear track of coating #4Hi and (b) ball wear scar; (c) corresponding Raman analysis of the specified zones.

5.2.7. Thermal stability and oxidation resistance

To obtain further insight into the two types of coatings with similar carbon contents but prepared by different methods, samples #2DC and #3Hi underwent further thermal behavior and oxidation resistance analysis. Figure 5.16 a and b shows the Raman spectra of both samples after thermal treatment at 500, 750, and 1000°C in an argon atmosphere. Niobium oxides and carbon were the main phases identified during the successive annealing treatments. NbO_2 and Nb_2O_5 are denoted by the presence of two double bands at approximately 280 and 650 cm^{-1} and a narrow peak at 920 cm^{-1}, as shown by Cao *et al.* and

Kreissl *et al.* [273,274]. The formation of amorphous carbon was confirmed by the presence of the two characteristic D and G peaks of sp^2 bonds of disordered carbon at 1350 and 1585 cm^{-1}, respectively. The D and G bands became more intense and defined, and the G-peak position shifted toward higher wavenumbers as the temperature increased to 750°C. These transformations indicate an increased presence of free carbon and increased clustering of the sp^2 carbon phase. At 500°C, none of the coatings showed clear signs of oxidation, but at 750 °C, the spectra diverged owing to their different thermal stabilities. Coating #2DC developed a smooth band at 670 cm^{-1}, which is associated with the formation of Nb–O bonds, while maintaining the D and G doublet. An optical micrograph of the surface did not reveal significant surface modifications. However, the #3Hi sample had a heterogeneous surface (as shown in the optical micrograph), on which various spots were detected. Analysis of these different areas indicated that they had a different degree of oxidation compared with that of the surrounding areas. The spectrum obtained from these spots showed the carbonaceous phase disappeared, while the niobium oxide bands centered at 280 and 650 cm^{-1} were enhanced. Furthermore, the spectrum of the surrounding areas was very similar to that of #2DC, indicating that oxidation progressed to a minor extent. When the samples were subjected to thermal annealing at 1000°C, the peaks originating from the niobium oxides (NbO_2 and/or Nb_2O_5) and the silicon substrate at 520 cm^{-1} were clearly identified, revealing the total oxidation of the coating [273,275,276]. The total disappearance of the carbon bands at 1000°C can be explained by the formation of volatile CO_2. Oxidation of the samples could originate from oxygen and water impurities in the tubular furnace or the film composition. The #3Hi sample had the lowest threshold temperature for the onset of oxidation, and the localized oxidation (pitting) can be correlated with the columnar microstructure, which allowed inward diffusion of oxygen through the open intercolumnar boundaries.

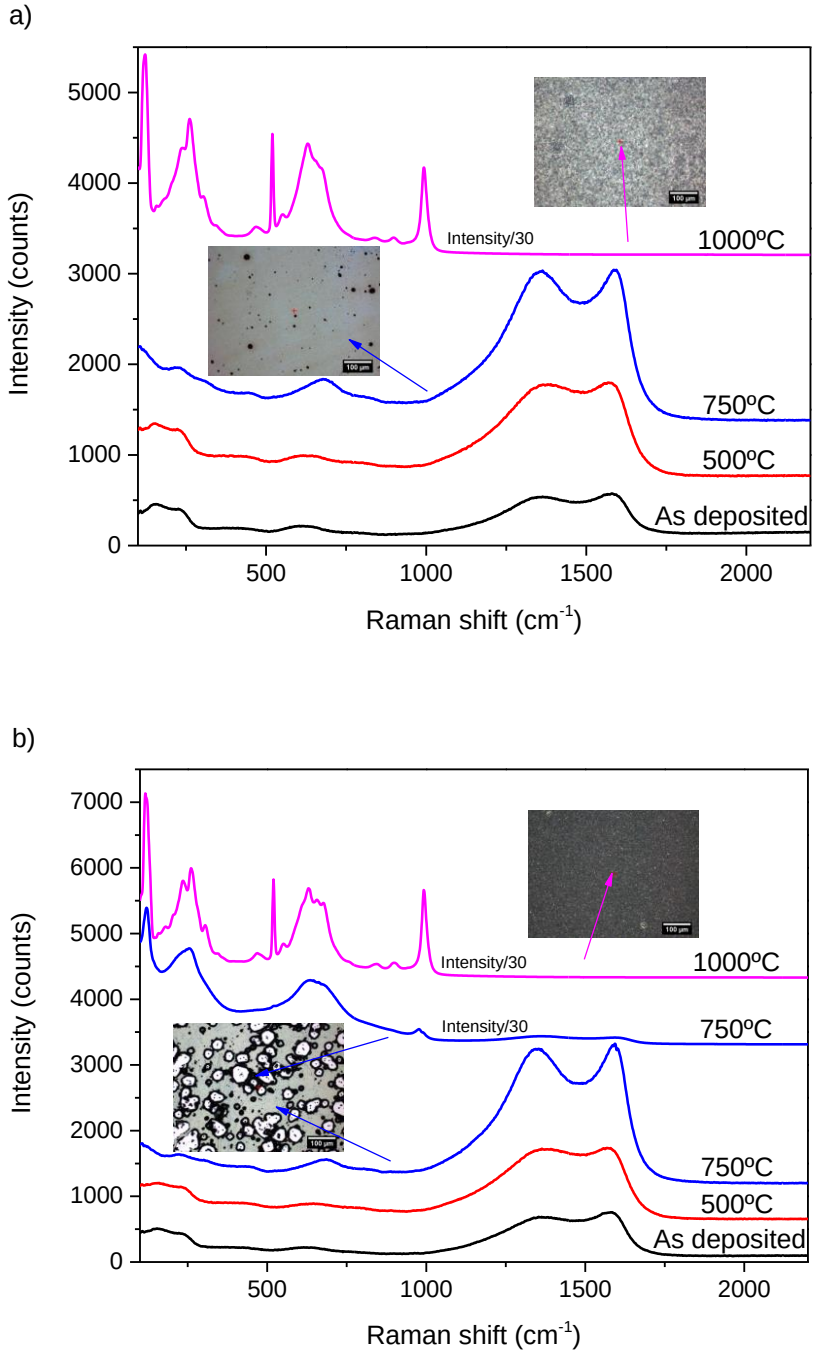

Figure 5.16: Raman spectra of the (a) #2DC and (b) #3Hi coatings at temperatures up to 1000°C. Optical micrographs corresponding to some investigated zones are included as examples. Note that the spectra are plotted in counts (not in arbitrary units); thus, the changes in the band intensity are significant.

Figure 5.17a shows the evolution of the diffractograms with increasing thermal annealing treatment temperature (500, 700, and 1000°C) for the #2DC sample in argon. The main crystalline phases identified for the pristine sample were Nb, Nb_2C, and NbC (as shown in detail in Figure 5.5 a and b). The diffractogram at 500°C shows the presence of the NbC phase and a growing Nb_2C phase, which could be formed by partial decomposition of the cubic NbC phase. Differences in thermal stability and oxidation resistance can be observed at 750 °C. At this temperature, the initial NbC coating of #2DC began to transform into one of the multiple Nb_2O_5 polymorphic forms, specifically the TT phase (JCPDS #28-0317) [277]. It is believed that the high relative intensity of this new phase made it difficult to distinguish the remaining NbC nanocrystals. At 1000°C, the niobium atoms were completely oxidized, and H-Nb_2O_5 (JCPDS #32-0711), which is the most thermodynamically stable niobium oxide phase at atmospheric pressure, became the predominant phase [277].

Figure 5.17b shows the diffractograms of sample #3Hi after thermal treatment at the same temperatures (500, 750, and 1000°C) in argon. The main phases identified for the pristine sample were Nb and NbC (as shown in detail in Figure 5.5 a and b). When the sample was heated to 500°C, a new phase, Nb_2C, was detected, which was probably due to the loss of carbon in the sample (as shown by Raman spectroscopy). The diffractograms of the sample annealed at 750°C indicate the presence of the TT-Nb_2O_5 phase and a new NbO_2 phase not detected in sample #2DC. It is believed that this NbO_2 phase transformed into the most stable high-temperature and oxidized phase (H-Nb_2O_5) when the sample was heated to 1000°C. Similar phase transformations have been found in WC/a-C and TiBC/a-C nanocomposite coatings, where the samples did not show significant signs of degradation and maintained an almost unaltered structure [278,279]. At 750°C, the degradation of the TiB_xC_y and WC phases proceeded by the formation of an additional a-C phase and metal oxides.

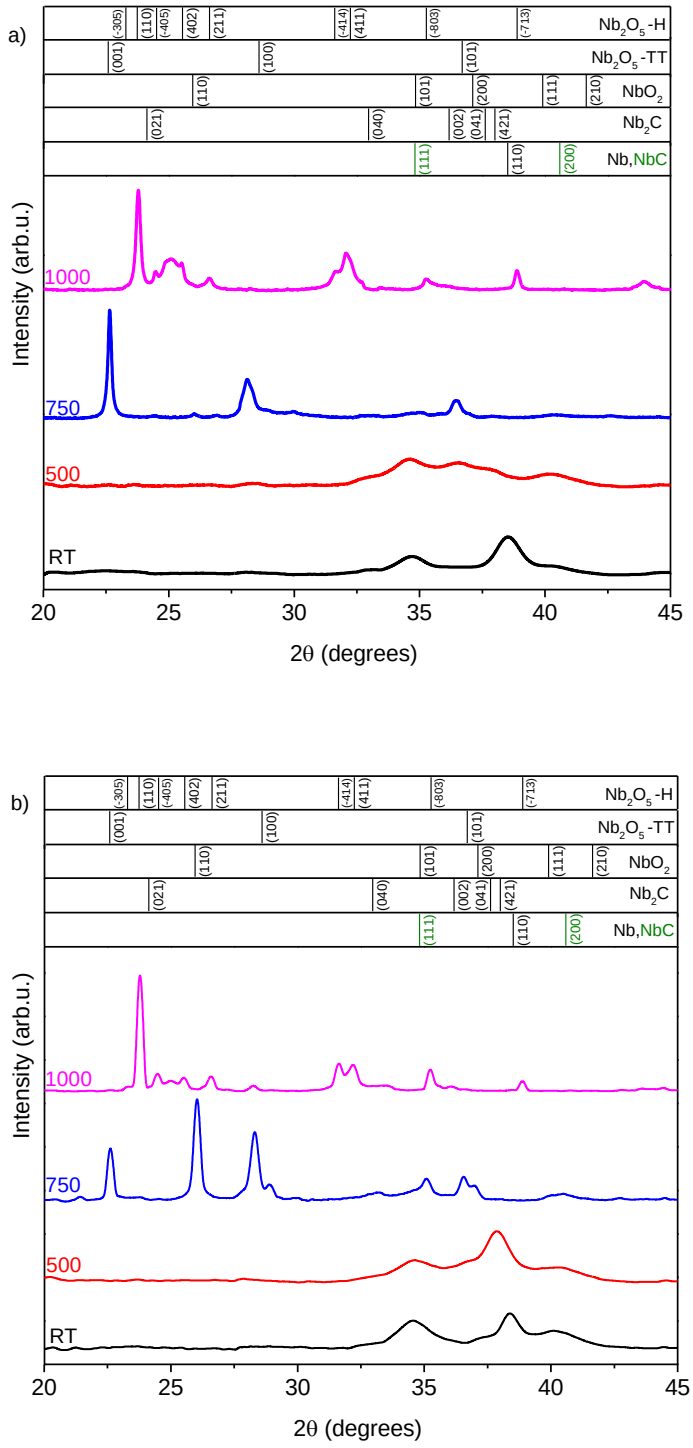

Figure 5.17: XRD patterns of the (a) #2DC and (b) #3Hi coatings at temperatures up to 1000°C.

5.3. Conclusions

Nanostructured Nb–C coatings with various contents of nanocrystalline niobium, niobium carbides, and amorphous hydrogenated carbon phases were prepared with a controlled architecture and phase composition via DC-MS and HiPIMS. The obtained coatings exhibited significant differences in their structure, chemical bonding, and tribomechanical properties as a function of the carbon content. The coatings deposited by HiPIMS developed a considerably more columnar structure comprising nanocrystalline Nb and NbC (vs. Nb_2C that formed under DC-MS) with a higher amount of a-C(:H). These features could be related to the higher carbon and argon ionization under the high-power impulse conditions, which favors a higher incorporation of carbon atoms. Nevertheless, these changes did not necessarily improve the mechanical properties (approximately 11–12 GPa), thermal stability, and oxidation resistance (< 750 °C) owing to the marked columnar growth and open porosity. Regarding the tribological properties, both sets of coatings (DC-MS and HiPIMS) demonstrated protective behavior ($\mu \approx 0.25$, and $k \approx 10^{-7}$ mm^3/Nm) when the carbon content was above 50 at.%, which allowed the formation of a lubricating sp^2-rich C tribofilm in the contact area. Thermal stability was improved by a more compact structure, which helped to stabilize the niobium carbide phases and increased the oxidation resistance. In summary, these results highlight the importance of film compactness, disrupting the columnar growth, and/or decreasing the intercolumnar distance for enhancing the mechanical properties and oxidation resistance of Nb–C coatings. Employing HiPIMS technology doesn't always enhance the film's microstructure and functionality. Rather, the plasma conditions must be optimized to select an appropriate ion bombardment (type, energy, and flux) to guarantee film densification.

CHAPTER 6

TiN/CrN multilayer coatings

The results of this chapter gave place to different scientific communications:

Contributions to communications:

1. 11a trobada de joves investigadors de la Societat catalana de química. Vilanova i la Geltru, Spain "*Recobriments ceràmics nanoestructurats preparats per plasma d'alta energía*". **N. Sala**, C. Colominas, M.D. Abad. Oral presentation. 28-30 January 2020.
2. ÖGV Seminar 2021. Vienna, Austria. "*Ceramic nanostructured coatings prepared by high energy plasma Technology"*. **N. Sala**, M.D. Abad, C. Colominas, J.C. Sánchez-López. Oral presentation. 24th September 2021.
3. Advances in Surfaces, Interfaces and Interphases Conference, online conference. "*Microstructure and mechanical properties of TiN/CrN multilayer coatings deposited in an industrial scale HiPIMS system*". **N. Sala**, M.D. Abad, M. R. de Figueiredo, R. Franz, C. Kainz, C. Colominas. Poster presentation. 15-18 May 2022.

Contributions to publications:

1. Part of this chapter will be submitted to Surface&Coatings Technology journal.

6. TiN/CrN multilayer coatings

Multilayer architectures are widely used to improve the performance of industrial relevant coatings by combining the advantages of different constituent layers [120,280]. The enhancement of the coating properties can be attributed to differences in the intrinsic properties of the materials used and the phenomena occurring at the nano-scale range [119]. In recent years, HiPIMS technique has gained a lot of interest for the synthesis of coatings with exceptional properties.

TiN/CrN multilayer systems have been extensively studied for their microstructure, good mechanical and tribological properties, and beneficial thermal stability making them suitable candidates for applications in the industry of metal machining. Ou *et al.* investigated CrN/TiN superlattice coatings deposited by pulsed direct current magnetron sputtering (DCMS) and by a combination of deep oscillation magnetron sputtering (DOMS) with pulsed DCMS [281–284]. Several authors reported TiN/CrN multilayer coatings deposited by unbalanced reactive magnetron sputtering (UBRMS) [285–288]. Paulitsch *et al.* investigated multilayers deposited by a combination of modulated pulsed power sputtering (MPPS)/DCMS [289], hybrid HiPIMS/DCMS [187,290] and by HiPIMS/unbalanced magnetron sputtering (UBMS) [291]; Nordin *et al*. by reactive electron beam deposition [292,293]; Rabadzhiyska *et al*. by low temperature UBMS [294]; Du *et al*. by cathodic arc evaporation [295]; Huang *et al.* by arc ion plating [296]; Jin *et al.* by radio-frequency sputtering [137] and Major *et al.* by pulsed laser deposition [297]. Despite the many techniques used to produce this multilayer system, the reactive HiPIMS technology has not been used yet to prepare both sublayers of the TiN/CrN multilayer coatings.

This chapter is divided in two sections. In the first one, different TiN/CrN multilayer coatings were deposited by reactive HiPIMS by directly sputtering chromium and titanium targets in a nitrogen-containing atmosphere. The power of the targets was fixed, and Λ was controlled by changing the on-time of each cathode. The chemical composition, crystalline phases and mechanical properties were investigated and compared as a function of Λ.

In the second part of the study, the influence of the bias application mode during the coating deposition step on the final properties of the coatings is studied. First, the effect of the application of the bias in either in continuous (DC) or pulsed (Hi) form is described and, second, the effect of the synchronization of the bias pulse with respect of the cathode pulse is explained with one selected multilayer TiN/CrN coating.

6.1. Coating deposition parameters

TiN/CrN coatings have been deposited using an industrial-scale CemeCon CC800/9 ML magnetron sputtering reactor in reactive HiPIMS mode. One titanium and one chromium target from CemeCon (99.95% purity) were used to deposit the TiN/CrN multilayer coatings

on single-crystalline silicon wafers (100) and mirror-polished cold-worked 1.2379 steel. Argon was used for plasma formation and nitrogen was used as a reactive gas at 170 sccm. The background pressure was 3×10^{-3} Pa, whereas the working pressure amounted to 0.65 Pa. The sputtering powers were 4 kW and 4.2 kW for the titanium and chromium targets, respectively. HiPIMS pulse parameters were: a duty cycle of 5.6 %, a pulse duration of 70 μs, and a repetition frequency of 800 Hz for Ti; a duty cycle of 2.5 %, a pulse duration of 50 μs, and a repetition frequency of 500 Hz for Cr. The multilayer structure was obtained by switching on/off the titanium and chromium targets sequentially and the different Λ were obtained by changing the deposition time of each TiN as well as CrN single layer.

In the first section, five different TiN/CrN multilayered coatings were deposited with different Λ and number of single TiN and CrN layers to obtain thicknesses between 1.4 and 2.3 μm. All coatings consist of a chromium base layer, followed by a CrN layer and subsequently alternating layers of TiN and CrN. On top, a thin TiN top layer was deposited. Single layer TiN and CrN coatings were deposited as a reference using the same deposition parameters. A DC substrate bias of -100 V was applied during the entire deposition processes with an applied table rotation speed of 3 rpm. The specific details of the deposition process for each coating are summarized in Table 6-1.

In the second section, four multilayer TiN/CrN coatings with different Λ, were deposited by using the same process conditions but changing the bias voltage to a pulsed form. In the last part, one selected multilayer TiN/CrN coating was deposited with different time delays in the bias pulse with respect the cathode pulse.

6.2. Influence of the deposition time (bilayer period)

In this first part of the chapter, five different coatings with different bilayer periods were deposited and characterized. The specific details of the deposition process for each coating are summarized in Table 6-1.

6.2.1. Elemental composition and microstructural characterization

The chemical composition of the multilayers was determined by EPMA and is summarized in Table 6-1. No pronounced influence of Λ on the composition is apparent. The N content of about 50 at. % Indicates stoichiometric sublayers. The O content was below 1 at. % for all coatings. Regarding the metal ratio Cr/(Cr+Ti), a value of about 0.6 was observed regardless of the variation in Λ. A possible explanation for this value is the presence of the Cr base layer contribution to the measured composition.

The disposition of the sublayers was observed by the GD-OES technique, and the results are shown in Figure 6.1. For all the coatings with Λ between 460 and 85 nm, it is possible to observe the sublayers with different composition, as well as the Cr anchoring layer. This indicates a well-formed and coherent structure. The loss of resolution with depth has

been previously reported and can be attributed mostly to the surface roughening produced by the ion bombardment and a subsequent change in the crater geometry resulting in a mixing of consecutive layers especially when they are in the nanometre range [298,299].

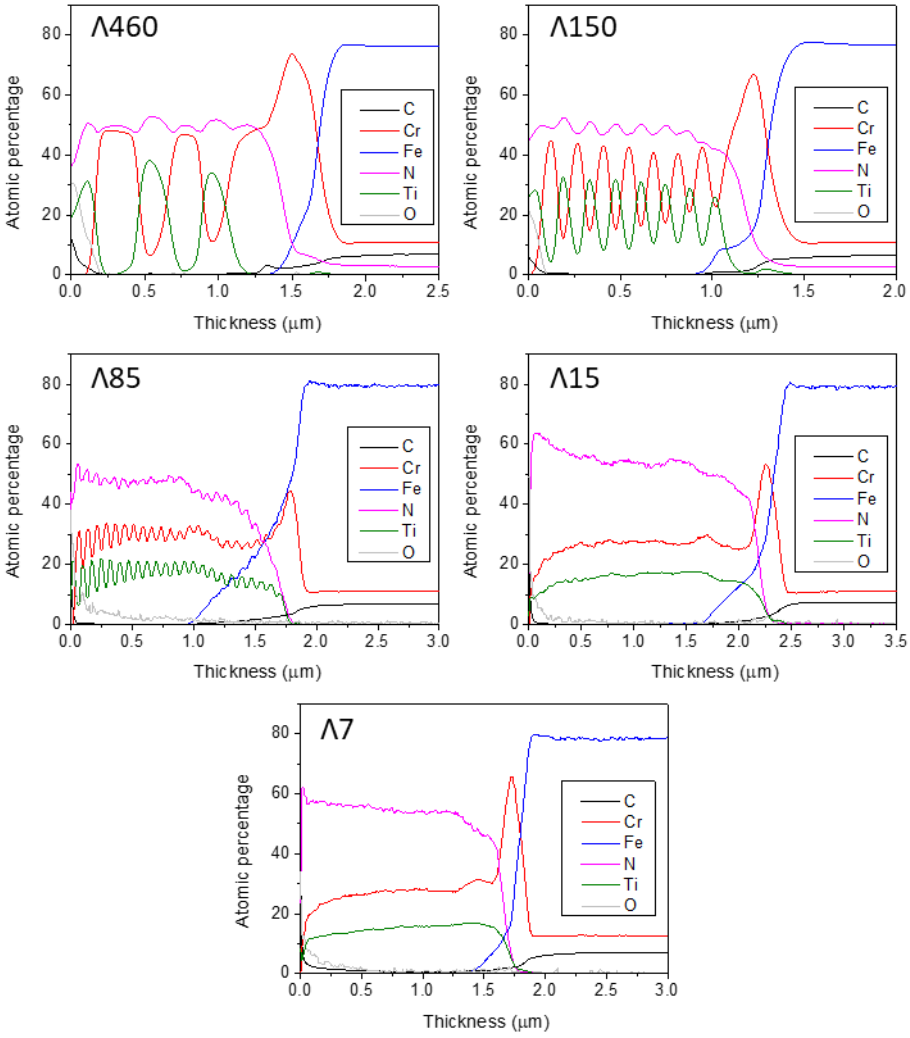

Figure 6.1: GD-OES obtained for the coatings with different Λ.

Figure 6.2 shows SEM (left) and AFM (right) images of the investigated coatings. For coatings with Λ ≥ 150 nm, backscattered electron (BSE) SEM images are also shown. All coatings display a compact featureless structure. Within the BSE images, the composition and distribution of the layers can be observed. The lighter colored layers correspond to CrN and the darker ones to TiN. Below Λ = 150 nm, the resolution is insufficient to distinguish the individual TiN and CrN layers. Due to the higher sputter yield of Cr as compared to Ti [300], the deposition time was adjusted in order to get similar layer thicknesses of TiN and CrN, in

particular for Λ ≤ 150 nm. This fact points towards an influence of the Cr base layer on the measured metal ratio Cr/(Cr+Ti) ratio in the coatings.

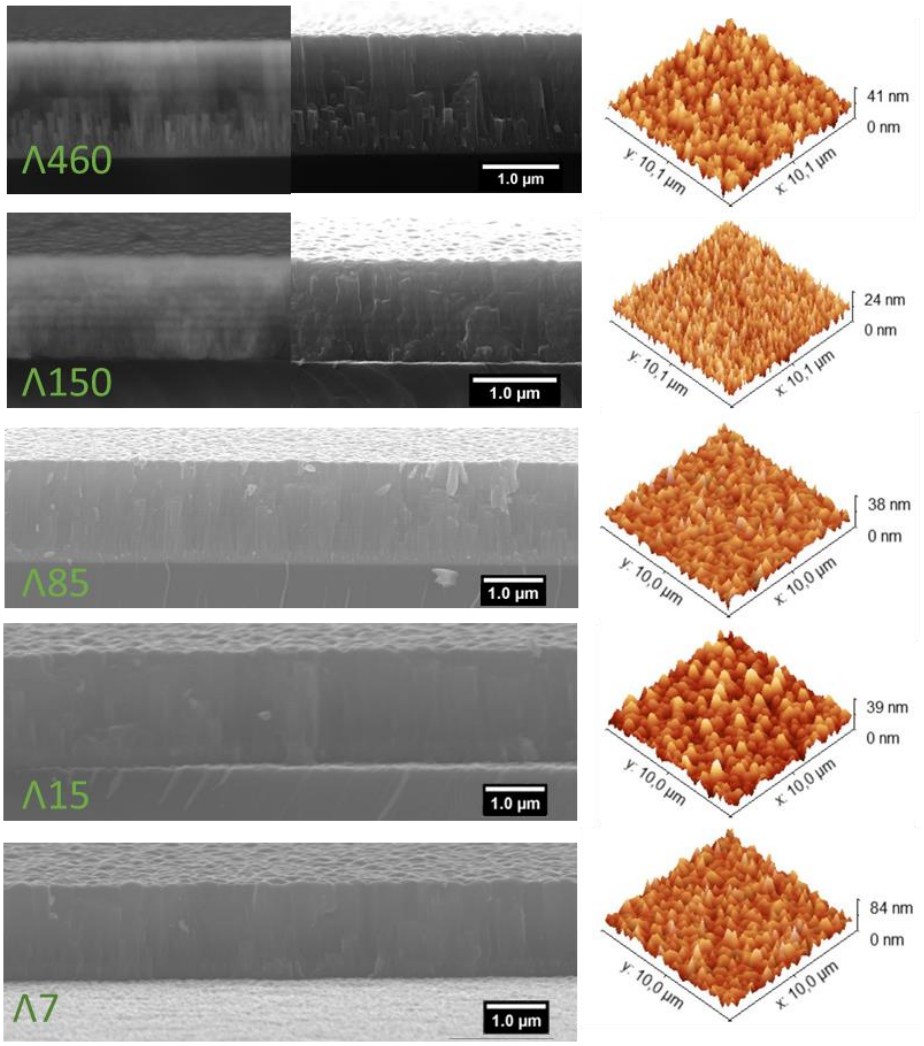

Figure 6.2: SEM (left) and AFM (right) images of the TiN/CrN multilayer coatings. For Λ ≥ 150 nm backscattered (left) and secondary (right) electron SEM images are shown.

Table 6-1: Summary of the sputtering conditions and properties of the coatings.

Sample	Sputtering time (s)		Nº sublayers	Λ (nm)	Thickness (μm)	Chemical composition (at. %)		
	Cr	Ti				Cr	Ti	N
Λ460	1200	2000	6	460	1.8	30	20	50
Λ150	300	900	16	150	1.4	25	19	56
Λ85	200	600	50	85	2.3	26	18	56
Λ15	50	150	176	15	2.2	28	18	54
Λ7	20	60	320	7	2.0	27	18	55

The AFM top surface images (scanning area = 10 × 10 μm^2) shown in Figure 6.2 reveal smooth surfaces. S_a roughness values are represented in Figure 6.3 together with the water contact angle (WCA). The contact angle is normally used to calculate the surface tension by a given substrate-liquid pair and hence the wettability [301]. By increasing the contact angle, the wettability decreases and vice versa. This parameter has a direct effect on the corrosion resistance and the tribological properties of the coatings among others [290,302,303]. In this case, both the surface composition of the coatings and the used liquid were the same, so the parameter that can influence the WCA value is the roughness of the coating. If the roughness changes, the area of the phases in contact also changes, which in turn changes the surface tension [304]. The lowest wettability is found for the sample with the highest roughness value (9.7 nm) corresponding to the sample with the lowest bilayer period and the highest WCA value. The increase in the WCA with increasing roughness can be explained by the Cassie-Baxter model, in which the droplet partially wets the substrate due to the trapped air in the microstructure [305,306]. The roughness values and the contact angle of the multilayers are in between the values obtained for the corresponding TiN and CrN monolayers. These roughness values are lower to those found by Paulitsch *et al.* [290] for CrN/TiN coatings prepared by a hybrid DC-HiPIMS system and also lower than those reported by Rabadzhiyska *et al.* for CrN/TiN layers deposited by UBM [294].

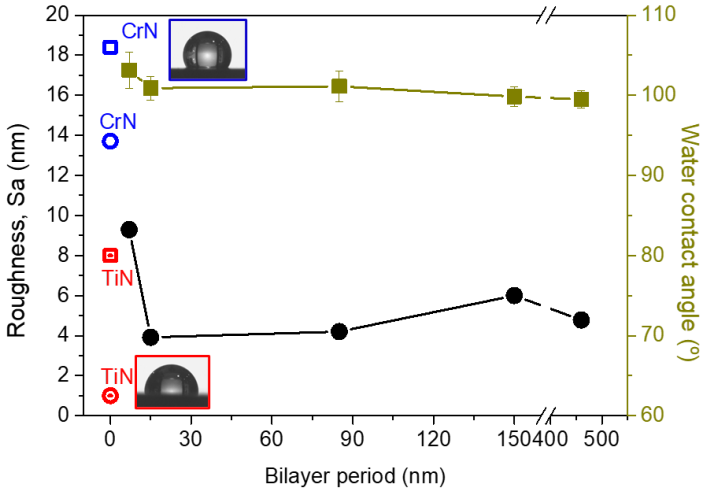

Figure 6.3: Roughness Ra and water contact angle of the investigated coatings as a function of the bilayer period. The top image corresponds to the single CrN coating, and the bottom image corresponds to the single TiN coating.

For the samples with the lowest bilayer period, TEM measurements were carried out to have further information at the nanoscale. For this purpose, samples were prepared by FIB and afterwards analysed by (S)TEM microscopy.

- **Λ15 coating**

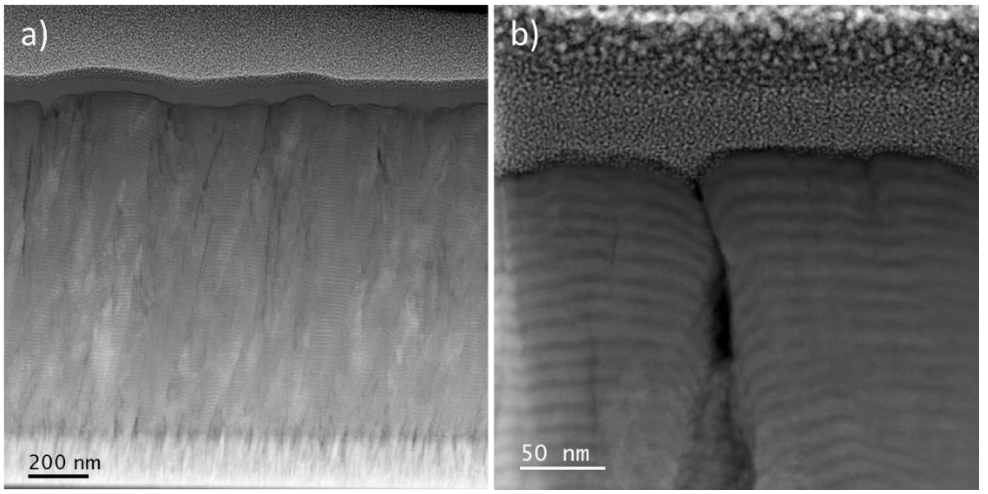

Figure 6.4: a) and b) HAADF-STEM images obtained for Λ15 coating.

In Figure 6.4a-b, the cross-section images of the Λ15 coating can be observed, showing dense and compact structure. In the Cr anchor layer region, a more columnar

structure is observed, however, the formation of the multilayer structure interrupts this tendency of growth thus densifying the coating. Even though the coating appears to be compact, when taking a closer look at the top of the coatings (Figure 6.4b), some columns with significative intercolumnar spacing can be observed.

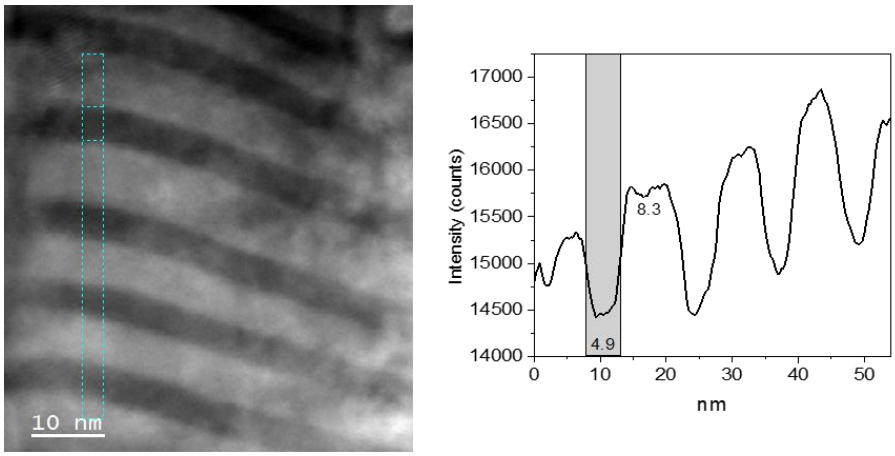

Figure 6.5: HAADF-STEM image of the coating and the corresponding HAADF intensity profile in the highlighted zone.

In Figure 6.5 an abrupt separation of TiN (bright) and CrN (dark) layers can be noted. The thickness of the individual layers was obtained by the HAADF profiles such as the one shown in Figure 6.5. The bilayer period obtained is not constant throuhout the hole coating. TiN layers have a thickness in between 4.4 and 5 nm, and CrN layers of 5.5 – 6 nm. At some point, some CrN show higher values of thickness of about 9 nm. This makes a bilayer period of around 15 nm.

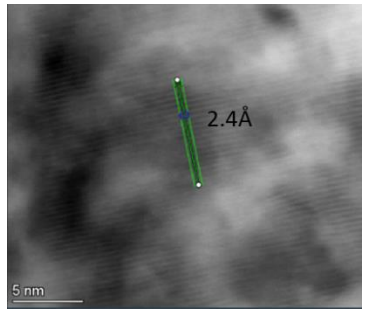

Figure 6.6: HRTEM image

In Figure 6.6, a coherent crystalline growth of the planes from TiN and CrN can be clearly observed. The d spacing calculated over the image corresponds to 2.4 Å.

In this region, both TiN and CrN have an epitaxial growth although they have a lattice parameter mismatch of around 2%. This behavior was previously reported by several authors [307–309] and can be explained in terms of energy. Epitaxial growth of the coating means

coherent interfaces between TiN and CrN. The energy of a coherent interface is smaller than the one from an incoherent interface, therefore, the growth in the same crystallographic structure is favorable. Additionally, the (111) planes of the NaCl-type structure correspond to the highest packed planes and therefore the energy need for growth in this direction is smaller. Both the texture and calculated d spacing match the values obtained by XRD.

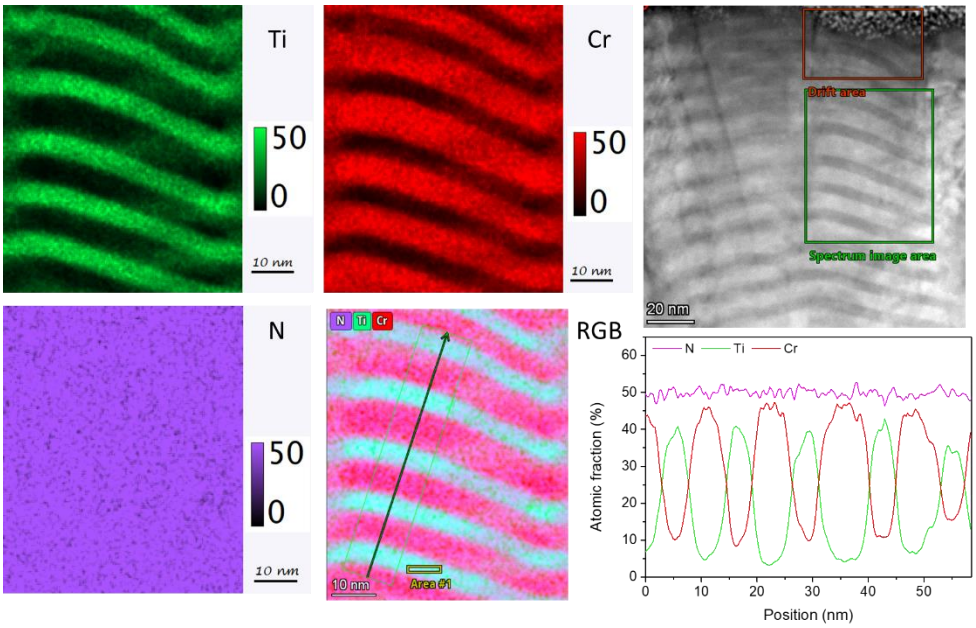

Figure 6.7: EDX elemental maps (Ti, Cr and N), chemical map (RGB Comp) and EDX profiles for the Λ15 coating in the marked area.

Figure 6.7 shows the chemical composition obtained by nanoprobe EDS analysis in STEM mode. The Ti, Cr, N elemental maps and the chemical map (RGB composition) are shown. The % at. composition within the area marked in the STEM image is shown in the graph on the right. A clear alternation of Ti and Cr is observed in the different layers, together with a practically constant amount of N around 50% at. This indicates the formation of separate TiN and CrN layers. A small variation of the thickness of the individual layers can also be observed. The formation of a TiCrN ternary in the interlayers cannot be dismissed with the EDS analysis.

- **Λ7 coating**

HAADF-STEM images obtained for the Λ7 coating can be observed in Figure 6.8. In Figure 6.8a, a cross-section image of the whole sample is shown, whereas in Figure 6.8b, one of the regions of interest is zoomed in. The first remarkable thing is the double periodicity of the sample. In the image on the left, it can be seen that approximately every 50 nm, there is a repetition of a darker layer. However, when looking at the coating more closely, it is

possible to notice different single layers corresponding to TiN (dark) and CrN (bright) phases. It can also be observed that the darker region is not a monolayer, but actually corresponds to a grouping of TiN and CrN thinner layers. It has been proved by contrast intensity profile (Figure 6.9) that there are 6 bilayer periods of 8 nm each, and then, 3 bilayer periods of 4,5 nm each.

This phenomenon has been previously reported in multilayer coatings deposited using a planetary rotation of the table and is therefore consistent with the partial periodic shadowing of the substrate relative to the deposition fluxes during 3 fold substrate rotation [310,311].

In these images, a dense and compact structure is also observed. In the Cr anchor layer region, the structure is more columnar, yet the multilayer structure interrupts this tendency of growth thus densifying the coating.

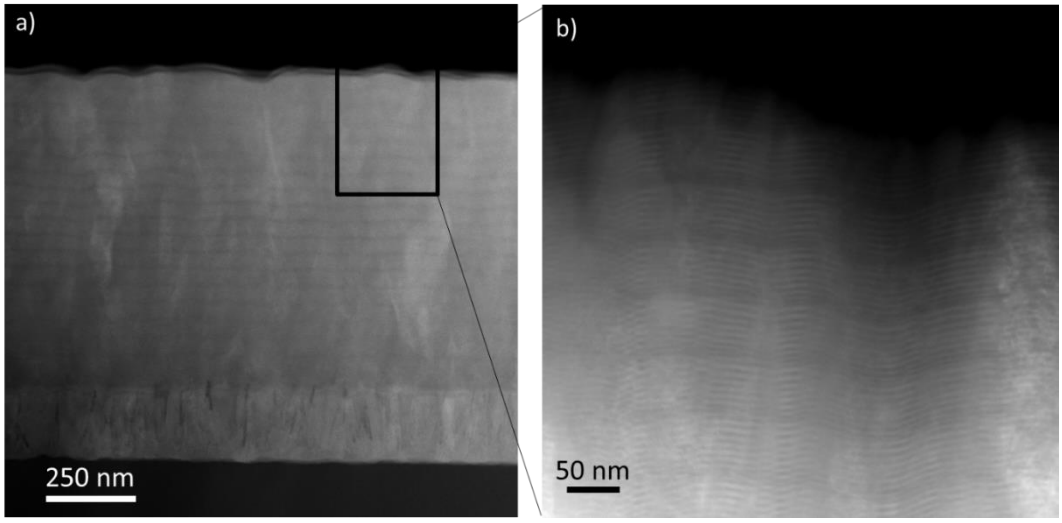

Figure 6.8: HAADF-STEM images of the TΛ7 coating. a) complete cross-section of the samples and b) zoom-in of the zone marked in a.

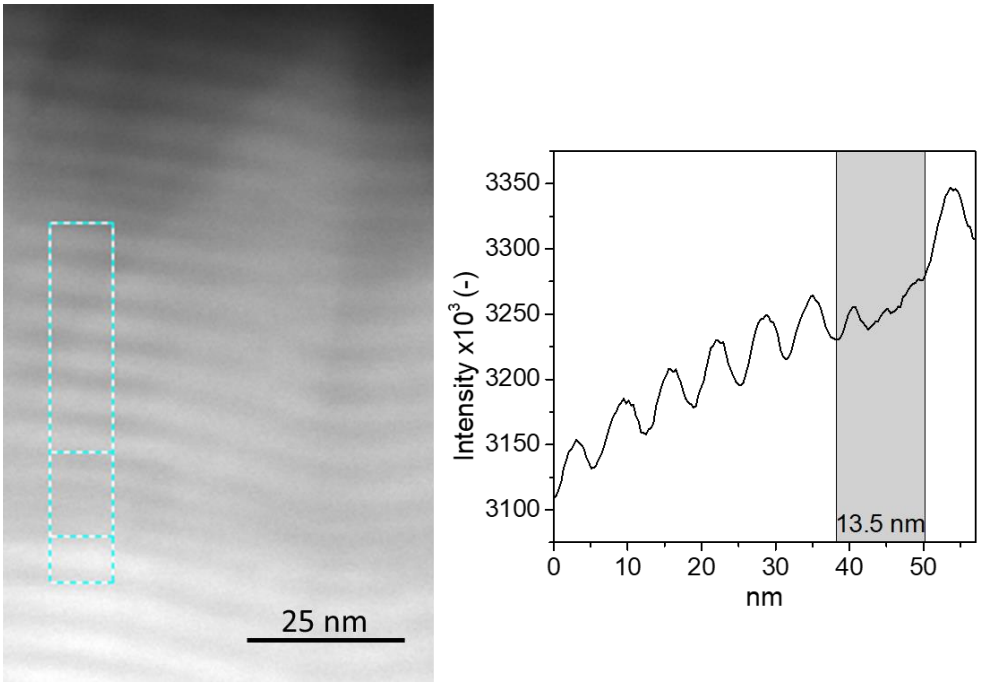

Figure 6.9: HAADF-STEM image of the sample and the corresponding HAADF intensity profile in the highlighted zone.

A ~ 7 nm bilayer period of the multilayer structure was measured directly from the HRSTEM images (Figure 6.10). This value corresponds to a single TiN layer of approximately 3.2 nm and a single CrN layer in between 3.2-4.2 nm. This result is in good agreement with the value determined from the satellite peak positions of the XRD diffractograms. A coherent crystalline growth of the crystalline planes can also be observed in the HRSTEM image.

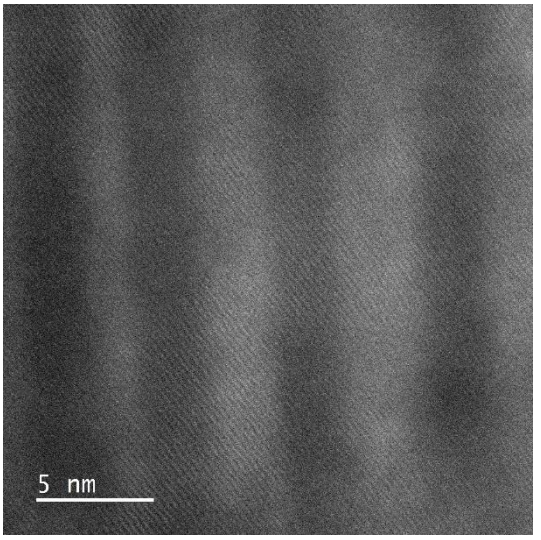

Figure 6.10: HRSTEM image

Figure 6.11a shows an HRTEM images of the sample with the corresponding digital diffraction pattern (DDP) as insert. It is shown the monocrystalline nature of the columns and the coherent growth of the different layers, that form the multilayer structure. D´spacing of 2.4 Å and 2.1 Å have been measured corresponding to (111) and (200) planes respectively. The indexed DDPs correspond to the [110] zone axis of the c-Ti(Cr)N structure.

In Figure 6.11b, in the HAADF-HRSTEM image, it can be clearly observed the coherent crystalline growth of the planes from TiN and CrN.

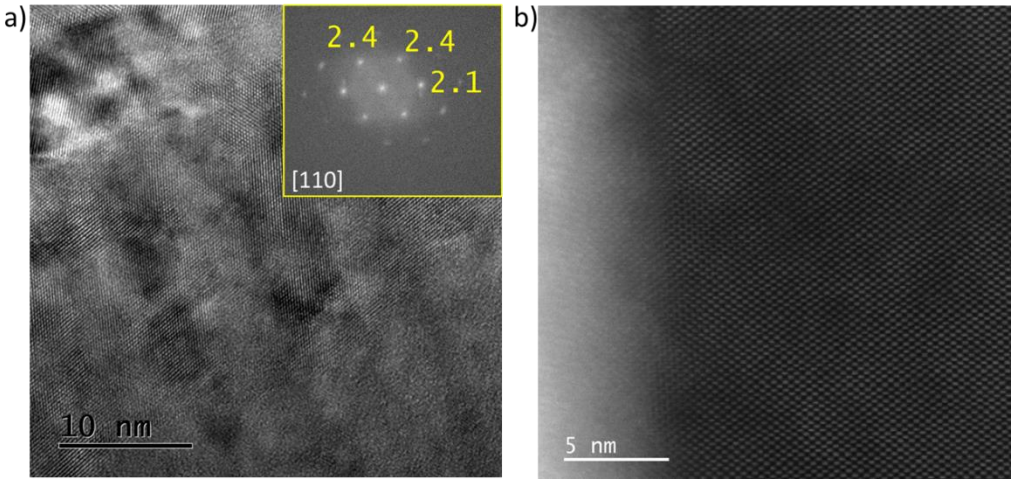

Figure 6.11: a) HRTEM image and its consequent DDP pattern. b) HAADF-HRSTEM image.

Figure 6.12 shows the chemical composition values from nanoprobe EDS analysis in STEM mode. The Ti, Cr, N elemental maps and the chemical map (RGB composition) are shown. The % at. composition within the area marked in the RGB image is shown in the graph on the right. Similarly to Λ15 coating, a clear alternation of Ti and Cr is observed in the different layers, together with a practically constant amount of N around 50% at. This shows the formation of separate TiN and CrN phases. A small variation of the thickness of the individual layers can also be observed, which may be due to the rotating system used during the deposition of the coating and the use of industrial scale-size chambers. The formation of a TiCrN ternary in the interlayers cannot be dismissed with EDS analysis because elemental lines does not reach 0 value.

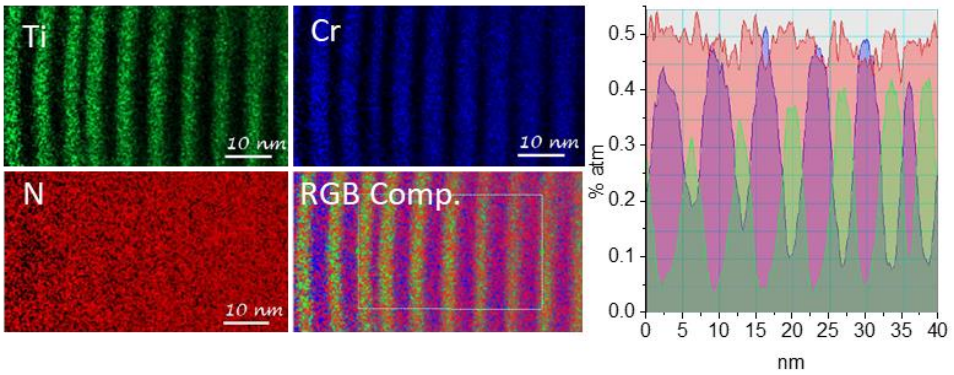

Figure 6.12: EDX elemental maps (Ti, Cr and N), chemical map (RGB Comp) and EDX profiles of the Λ7 coating.

The chemical composition of the sample through the thickness was more precisely obtained by EELS. Figure 6.13 shows the elemental map by recording the N-*K*, Ti-$L_{2,3}$ and Cr-$L_{2,3}$ edges and the corresponding composition maps. The result is similar to that obtained in the EDS-HAADF images. Alternation of TiN and CrN single nano layers with a small variation in the periodicity, but in this analysis the lateral resolution is around the probe size (1nm), much higher that the obtained by EDX. In the line profile obtained across the multilayers, we can see that the intensity of the Ti and Cr signals does not reach 0 at.% (Ti decrease to 5 at.%, and Cr to 7-8 at.%), this could be due to the lateral resolution of the analyses, so for this reason, the formation of ternary compound (TiCrN) in interfaces regions of less than 1 nm cannot be discarded.

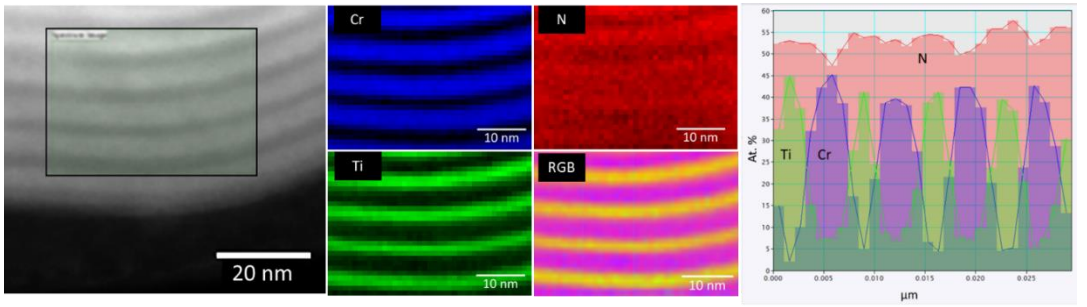

Figure 6.13: HAAD-STEM image and Cr, Ti and N elemental maps of the coating and the corresponding composition obtained by EELS technique.

Figure 6.14 depicts the results obtained from the XRD measurements measured in Bragg-Brentano configuration. The analysis of the diffractograms allowed the identification of the following phases: fcc-TiN (ICDD card nº 38-1420), fcc-CrN (ICDD card nº 11-0065) and the substrate 1.2379 steel. Separate TiN and CrN phases are observed in the diffractograms from the coatings with higher Λ suggesting semi-coherent or incoherent interfaces. However,

upon reduction of Λ, the peaks of CrN and TiN approach each other, which indicates a change in the structure of the coatings showing potential coherent stress due to the low lattice parameter mismatch of around 2 % between the TiN and CrN. The presence of satellite peaks around the respective main peak indicates the formation of a superlattice structure in the sample with Λ = 15 nm (Figure 6.15). In the case of Λ7 coating, the peaks corresponding to CrN and TiN have entirely merged into a single peak, confirming the coherent crystalline growth observed in the TEM analysis. Several authors have reported this very similar correlation between the bilayer period and the formation of different crystalline structures for TiN/CrN systems [124,286,295].

The crystallite size calculated by the Scherrer equation for the (111) and (200) crystalline planes is between 10 to 20 nm for all the samples. No clear trend can be observed depending on the crystalline plane or the bilayer period. The XRD peak positions of the coatings (Figure 6.14) are shifted towards lower 2θ angles compared to the standard patterns. There is a correlation between the shifts of the planes and the compressive residual stress of the films, as discussed in the following section.

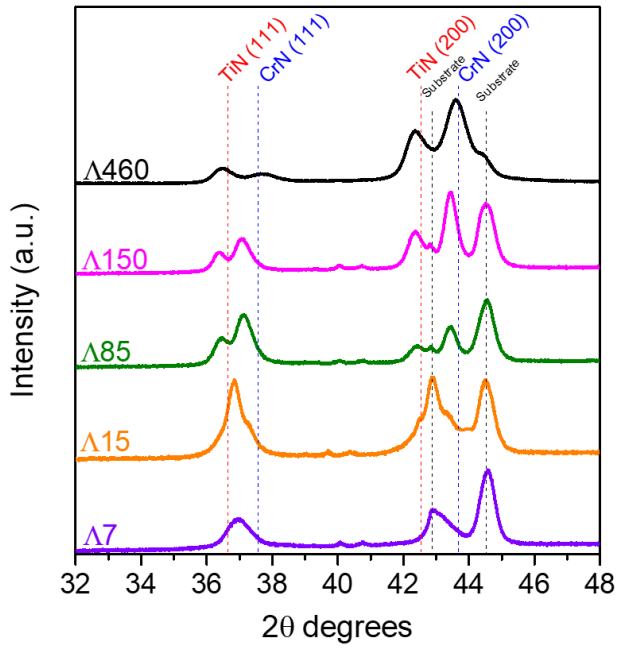

Figure 6.14: X-ray diffractograms measured in Bragg-Brentano configuration.

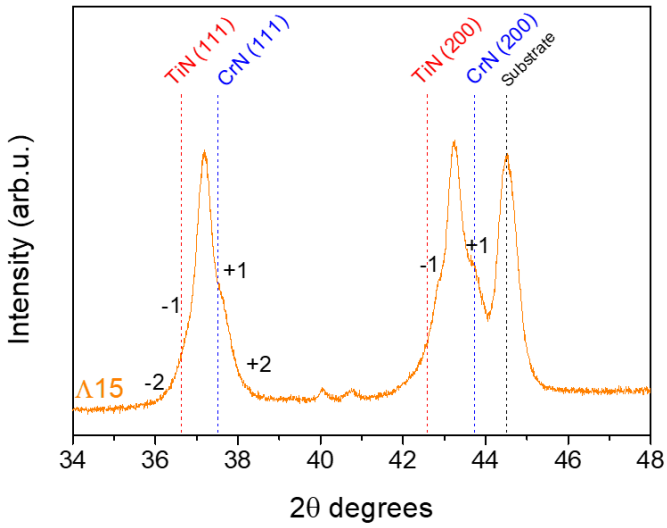

Figure 6.15: X-ray diffractogram from the sample Λ15. The numbers show the position of the superlattice satellite peaks.

6.2.2. Mechanical properties

Figure 6.16 shows the results of the residual stress as determined by the $\sin^2\psi$ method from the (111) peak [217]. Increasing the tilt angle induces a shift of the peak position to higher 2θ angles, which signifies compressive residual stress in the coatings. Very high compressive stress levels can lead to the formation of buckles and film delamination, which is detrimental for the application of the coatings in cutting operations. However, a certain extent of compressive residual stress can be beneficial for the coating performance during service, as it increases the fatigue life, adhesion and hardness [312–314]. The residual stress values obtained for the multilayer coatings of about -2.5 GPa are between the values corresponding to the single layered TiN and CrN coatings, that is -3.6 and -1.1 GPa, respectively. The residual stress becomes slightly more pronounced as Λ decreases, which can be attributed to the higher number of interfaces [315,316]. Similar values were reported by Tillmann *et al.* [317] for CrN/TiN nanocomposites, by Ou *et al*. [281] for pulsed DCMS CrN/TiN multilayer coatings whereas higher values were reported by Ou *et al.* [284] for CrN/TiN coatings deposited by DOMS and pulsed DCMS method.

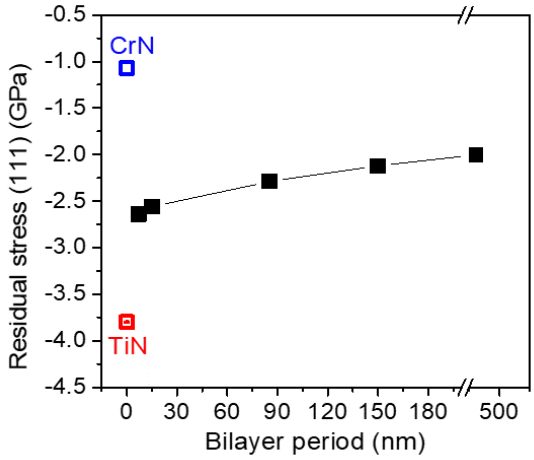

Figure 6.16: Residual stress calculated from the (111) peak of the coatings.

Hardness (H) and Young's modulus (E) of the coatings were measured by nanoindentation and the values are presented in Figure 6.17. H and E of the coatings vary between 23.7-32.1 GPa and 330-394 GPa, respectively. The coating with Λ = 15 nm, that was revealed as superlattice structure by XRD, exhibits both the highest hardness (32.1 GPa) and the highest Young's modulus (394 GPa). Thus, this coating allows for a hardness twice as high as compared to the CrN single layer coating. This increase in hardness and Young's modulus for the multilayer systems with respect to the single layered ones is mainly associated with the hindering of dislocation movements arising from the lattice mismatch at the interfaces. [124,318]. In addition, the decrease in the crystallite size by reducing the bilayer period can influence the hardness of the films because of the Hall-Petch effect [126,127]. Similar hardness values were reported by Yasar *et al.* [285] for CrN/TiN multilayer coatings deposited by UBRMS, by Du *et al*. [295] for TiN/CrN multilayer coatings deposited by cathodic arc evaporation, and by Paulitsch *et al*. [291] for CrN/TiN multilayers deposited by a HiPIMS/UBMS deposition technique.

H/E and H^3/E^2 values can be used to estimate the material elastic strain to failure and the material resistance to plastic deformation, respectively. Higher values of these parameters indicate better properties [284,319]. In Figure 6.18, an increase of these values can be observed when reducing Λ, with a maximum value for the coating with Λ = 7 nm. The improvement of H/E and H^3/E^2 upon reduction of Λ can be related to a more effective blocking of dislocation movement as the number of interfaces between the different TiN and CrN layers increase, well-defined interfaces, optimization of the bilayer period, and denser microstructures [281,291]. All H/E and H^3/E^2 values obtained for the multilayer coatings are superior in comparison to the single layered CrN coating and partly to the single layered TiN coating.

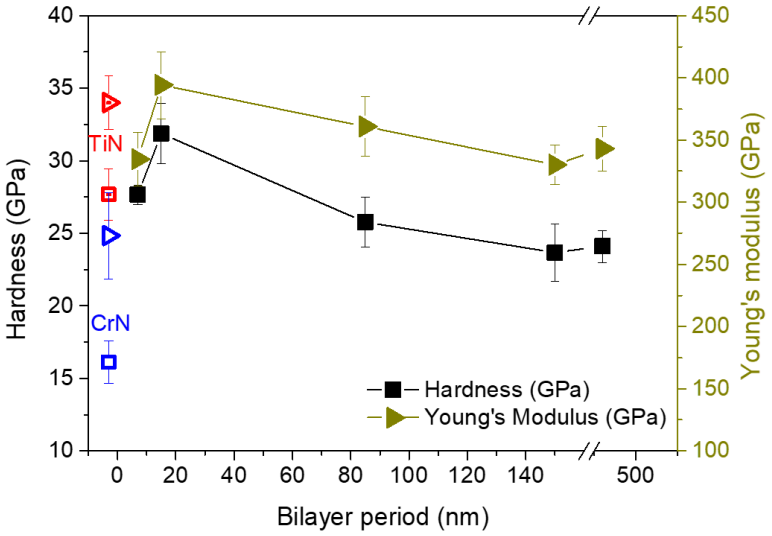

Figure 6.17: Hardness (H) and Young Modulus (E) vs the bilayer period of the coatings.

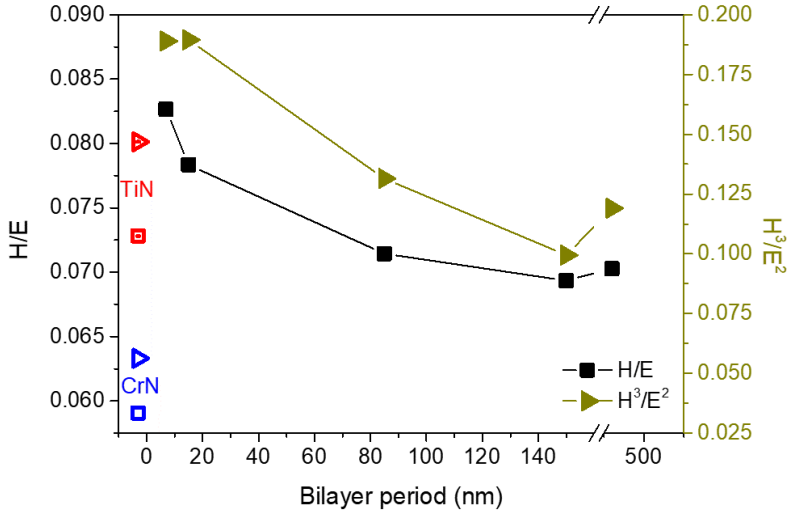

Figure 6.18:H/E and H^3/E^2 ratios of the coatings.

6.3. Bias effect on the properties of the coatings

In the previous section, the effect of the bilayer period on the final properties of the coatings was studied. As Λ decreases, interactions in the nanoscale range increase, leading to substantial changes in the properties of the coatings.

There are multitude of parameters that can be modified during a deposition process using the HiPIMS technique. Among them, the most significant are the frequency and length of the HiPIMS pulses and the bias applied during the process.

The importance of the substrate bias voltage in the film deposition process stems from the fact that high-energy ion bombardment can improve atom movement, encourage the desorption of physically adsorbed atoms and shallow ion implantation, as well as capture impacting atoms [320]. It has been reported that applying negative bias voltage to a substrate causes considerable changes in the film's grain size, deposition rate, hardness, and residual stress [321,322].

This chapter focuses on studying the effect of the way the bias is applied during the deposition process of the coatings. This chapter will be divided in two sections. In the first one, the effect of the application of the bias in either in continuous (DC) or pulsed (Hi) form is described. In the second one, the effect of the synchronization of the bias pulse with respect to the cathode pulse is explained with one selected multilayer TiN/CrN coating.

6.3.1. Effect of the bias application mode: DC or pulsed HiPIMS.

In this section, the effect of applying the bias voltage in either direct current form or pulsed HiPIMS form during the coating deposition step is studied. For this purpose, four coatings with the lower bilayer period from the previous section were selected because of their potential from an industrial point of view and were deposited by changing the bias mode. These four pairs of coatings (8 in total) were deposited by using the same conditions but only by changing the bias mode. The main characteristics of these coatings are described below.

6.3.1.1. Elemental composition and microstructural characterization

The elemental composition of the coatings was determined by EPMA. For all the coatings, the metal ratio Cr/(Cr+Ti) has a value of about 0.6 regardless of the bilayer period and the bias mode applied. The N content of about 50 at.% Indicates stochiometric sublayers [282]. Regarding the oxygen content, all the coatings deposited by using a DC bias, have less that 1 at.%. However, coatings with HiPIMS bias, show between 1-2 at. % of oxygen content. This increase of residual oxygen in HiPIMS coatings can be explained by a larger available adsorption area due to a much more columnar and rougher structure, as discussed below [267,323].

An indirect measurement of the density of the coatings was performed by X-ray fluorescence. The amount of Cr and Ti was obtained for each sample deposited on silicon substrate and then divided by the total thickness of the sample obtained from cross-sectional SEM images. Thus, a value of Cr % and Ti % per micrometre of coating could be obtained. Comparing the 4 samples deposited with each type of bias, an increase in densification of between 25 and 30 % was obtained using a DC bias mode. This densification effect can also

be related to the much more columnar growth of the coatings deposited by using a HiPIMS bias. The increase in the film thickness because of columnar grain growth reduces the amount of metal/µm coating. This is also accompanied with an increase in the deposition rate for the coatings deposited by HiPIMS bias, by approximately a 15% with respect to the samples deposited by DC bias.

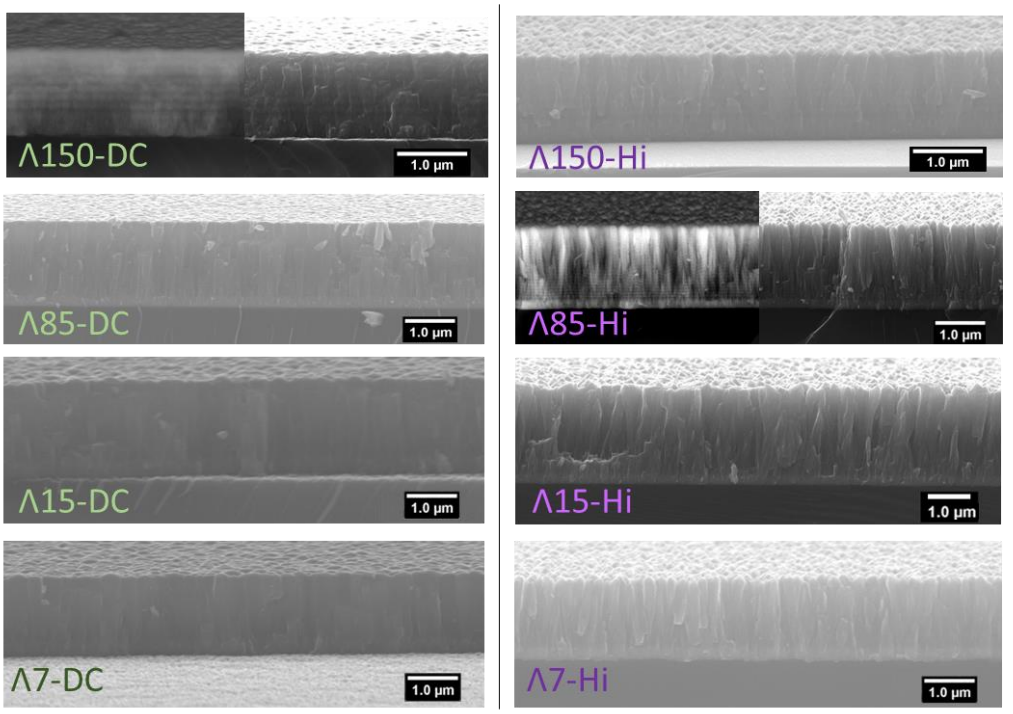

Figure 6.19: Cross-section SEM images of the coatings deposited by both using a DC and Hi bias mode.

In Figure 6.19, the cross-section SEM images of the coatings are shown. For some coatings, the backscattered electron (BSE) SEM images are also shown. Within the BSE images, the composition and distribution of the layers can be observed for the samples with Λ ≥ 85 nm. The lighter colored layers correspond to CrN and the darker ones to TiN. All the samples deposited by using a DC bias, show a very compact, featureless structure. However, for the samples deposited by using a HiPIMS bias, the coatings show a completely different trend. All the coatings appear to be highly oriented in the form of columns. That is mainly due to differences in energies delivered into the growing film by bombarding ions. When a bias voltage is applied to the substrates, it induces ion bombardment which enhances the adatoms' mobility and promotes densification of the films [180,324,325]. In this case, the energy transferred to the adatoms by applying a DC voltage, is high enough to allow them to diffuse among the columns in the structure and fill in the vacancies, thus creating more compact structures. Coatings with similar structure to those obtained using a HiPIMS bias have been

reported by several authors when using a floating bias or very low voltage values which do not transfer enough energy to the adatoms to allow coating densification [321,324,326,327].

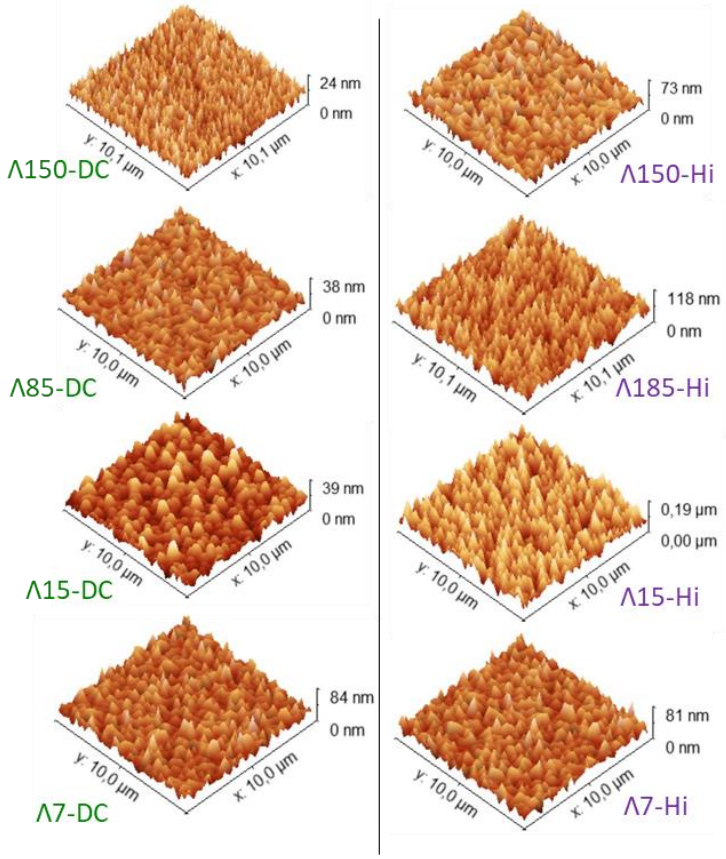

Figure 6.20: AFM images of the coatings deposited by DC and Hi bias.

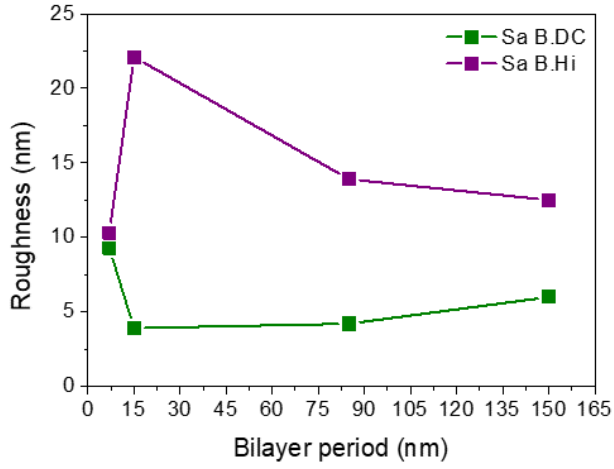

Figure 6.21: Sa values in nm obtained from the AFM images as function of the bilayer period.

Figure 6.20 shows the AFM topography images obtained for all the coatings (scanning area = 10x10 μm). The values of the Sa obtained from the AFM images are represented in Figure 6.21. The columnar growth of the samples deposited by using a HiPIMS bias resulted in an increase in the surface roughness which is in good agreement with the results obtained by SEM images. The increase in the roughness value can also be observed in the aspect of the coated disk steels. While all samples deposited with a DC bias have a shiny appearance similar to the initial appearance of the substrate, samples deposited with a HiPIMS bias appear to be more matt with less vivid colours.

Figure 6.22 shows the GI-XRD diffractograms measured at a constant grazing incident angle of 1º for all the coatings. The analysis of the diffractograms allowed the identification of the following crystalline phases: fcc-TiN (ICDD card nº 38-1420) and fcc-CrN (ICDD card nº 11-0065). Separate TiN and CrN phases are observed in the diffractograms from the coatings with $\Lambda \geq 85$ nm, suggesting semi-coherent or incoherent interfaces. However, upon reduction of Λ, the peaks of CrN and TiN approach each other, which indicates a change in the structure of the coatings showing potential coherent stress due to the low lattice parameter mismatch of around 2 % between the TiN and CrN, thus pointing to the formation of a single-phase solid solution when the Λ is small enough. The presence of satellite peaks around the respective main peak indicates the formation of a superlattice structure in the sample with $\Lambda = 15$ nm. These peak shift as a function of the bilayer period can be observed regardless of the bias mode used. Nevertheless, two main differences can be observed in the XRDs as function of the bias mode applied during the deposition of the coatings. The first one is the position of the peaks with respect to the standard patterns, and the second one is the difference in the preferential crystalline growth direction of the coatings.

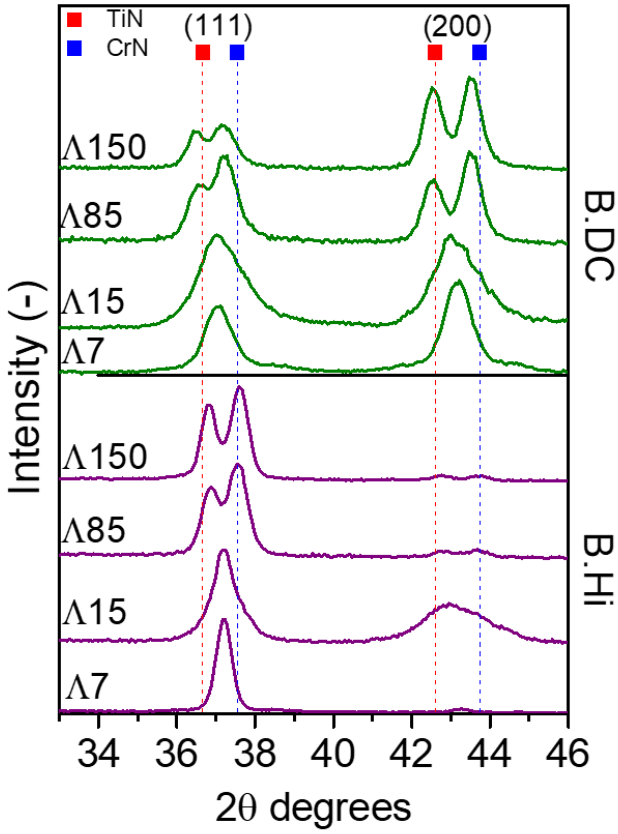

Figure 6.22: X-Ray diffractograms measured in GI-XRD at 1º.

The XRD peak positions of the coatings deposited by using a DC bias are shifted towards lower 2θ angles as compared to the standard patterns. This can be explained by the presence of compressive residual stress of the coatings as discussed in the following section.

Crystalline growth is observed in two different crystallographic planes: (111) and (200). For the coatings deposited with a DC bias, a mixture of crystalline growth is clear in both directions; (111) and (200). In contrast, for the samples deposited with B.Hi, a strong texture is observed in the (111) direction regardless of the bilayer period. The development of preferred orientation is usually explained by thermodynamic and kinetic factors. Planes (111) and (200) have the lowest strain energy and lowest surface energy in NaCl-type FCC nitrides, respectively [184]. The (111) orientation is preferred for coatings formed at low substrate bias as it can accommodate the most atoms per unit area at low energy sites. However, the increase in substrate bias increases the mobility of adatoms and thus promotes a closed packed structure in near thermodynamic equilibrium conditions. Since (200) is the

lowest surface energy plane, it is expected to be the preferred orientation when the bias is increased [326]. From a kinetic aspect, (111) direction has the fastest growing planes and the densest arrays of columns, so it is the most suffered from collision cascades. When coatings are grown in relatively high-ion-energy conditions, their textures tend to evolve toward the (200) direction [324,325]. In this study, the substrate bias voltage is not changed but the way of application. When the bias is applied in DC mode, all the coatings are grown in a most preferred (200) orientation which is the preferential one when coatings are grown with higher ion/atom ratios. With the results obtained, it can be concluded that the energy transferred to the adatoms when the bias is applied in HiPIMS mode is not sufficient and therefore most of the crystalline growth is observed in the (111) direction. These results are in good agreement with the ones obtained by SEM images in which these coatings also show a denser structure.

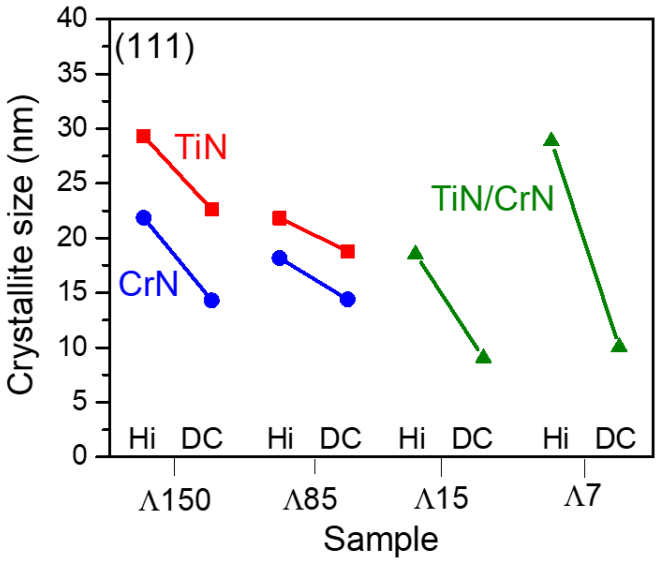

Figure 6.23: Crystallite size calculated from the XRD measurements.

The crystalline size calculated by Rietveld refinement for the (111) direction can be observed in Figure 6.23. A clear reduction of the crystallite size is observed for the samples deposited by DC bias. The decrease in the crystallite size with the increasing effective bias for the DC-biased samples, can be explained by the larger defects generated because of the enhanced ion bombardment and resputtering effect, which will increase the number of preferential nucleation sites and lead to a decrease of the crystallite size [328,329].

6.3.1.2. Mechanical characterization

Figure 6.24 shows the results of the residual stress as determined by the $\sin^2\psi$ method from the (111) diffraction peak [217]. Similar to the previous trends observed, significant transitions occurred between different substrate biases. Residual stress levels in

coatings deposited under low and high voltages are clearly different. The residual stress calculated for the HiPIMS-biased samples is slightly tensile, between -0.2 and 0.8 GPa, while for the DC-biased samples is clearly compressive with values ranging from -2.1 and -3.1 GPa. These compressive stress for the samples deposited by using a DC bias was also observed in the XRD measurements with peak position displacements towards lower diffraction angles compared with a standard reference [217]. The increase of the intrinsic stress with increasing energy of bombarding ions for the DC-biased samples can be due to the peening effect. Therefore, at higher energies, ions can penetrate deeper into the coatings inducing more irregular incorporation of atoms/ions into the crystalline lattice which raises the intrinsic stress of the coatings [330,331]. Very high compressive stress levels can lead to the formation of buckles and film delamination, which is detrimental for the application of the coatings in cutting operations. However, a small amount of compressive residual stress might improve the coating's performance by boosting its hardness, adhesion, and fatigue life [312–314].

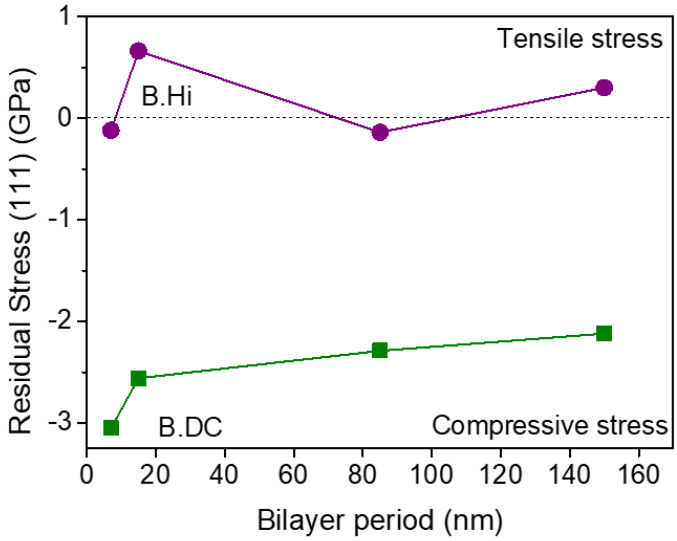

Figure 6.24: Calculated residual stress of the coatings.

Hardness (H) and Young's modulus (E) of the coatings were measured by nanoindentation and the values are presented in Figure 6.25. H and E values obtained for the samples deposited by using a DC bias are much higher to the values obtained for the HiPIMS biased coatings. The increase in the hardness can be attributed to the film densification, texture, residual stress, and grain size. The more compact and featureless structures obtained with a DC bias leads to an increase in the mechanical properties of the coatings. Also, the change in the preferential growth direction of these coatings have a direct effect on the hardness of the coatings. According to Schmidt factor the (200) is harder than the (111) direction. Furthermore, the (111) plane is denser than (200), and the dislocations glide more easily in denser planes [182,332]. So, dislocation will glide easily on (111) which makes plastic

deformation easier which decreases the hardness for the HiPIMS biased coatings. In addition, the decrease in the crystallite size for the DC-biased coatings can influence the hardness of the films because of the Hall-Petch effect by hindering the dislocation movements at the grain boundaries [126,127]. The effect of the bilayer period in the mechanical properties of these coatings was explained in detail in the previous section. However, it is observed that the multilayer coatings with lower bilayer periods deposited with DC bias have greater values of H and E than the respective TiN and CrN monolayers. Especially, the coatings with $\Lambda \leq 15$ nm in which a superlattice structure was confirmed by XRD measurements.

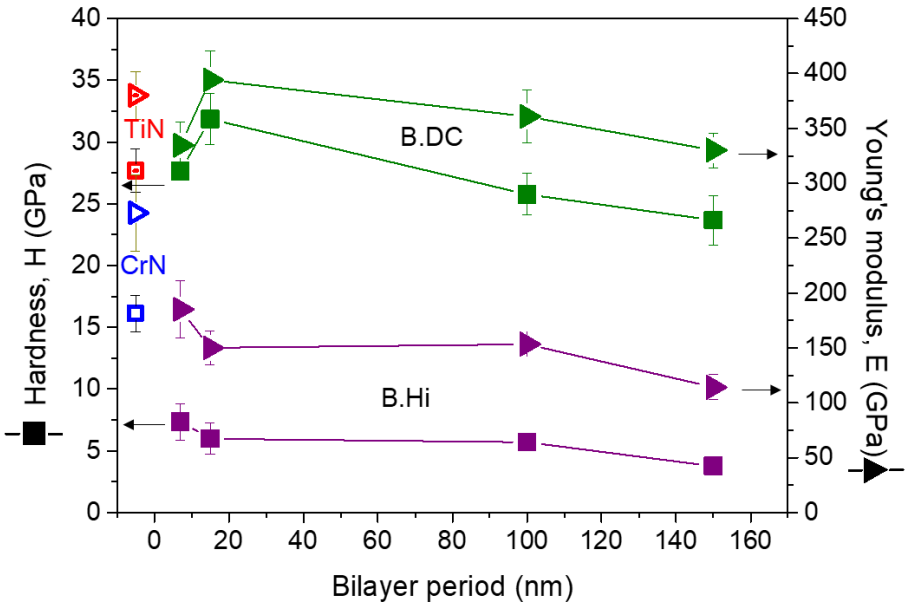

Figure 6.25: Hardness (H) and Young Modulus (E) obtained for the coatings.

6.3.2. Effect of the synchronization of the BIAS

In the previous section, the effect of the bias application mode (either in continuous or pulsed form) on the properties of the coatings was studied. The best results in terms of microstructure and mechanical properties were obtained for the samples deposited by using a DC Bias, especially for the sample with a bilayer period of 15 nm. However, some studies suggest that the properties of the coatings deposited by HiPIMS technique are improved by using a HiPIMS bias but shifted with respect to the pulse applied to the deposition cathode in the region where the plasma is metal-ion rich. Thus, to study the effect of the synchronization of the bias pulse with respect to the cathode pulse, a sequentially bias pulse delay was performed during the deposition stage of that coating. An schematic view of the pulse delay can be observed in Figure 6.26.

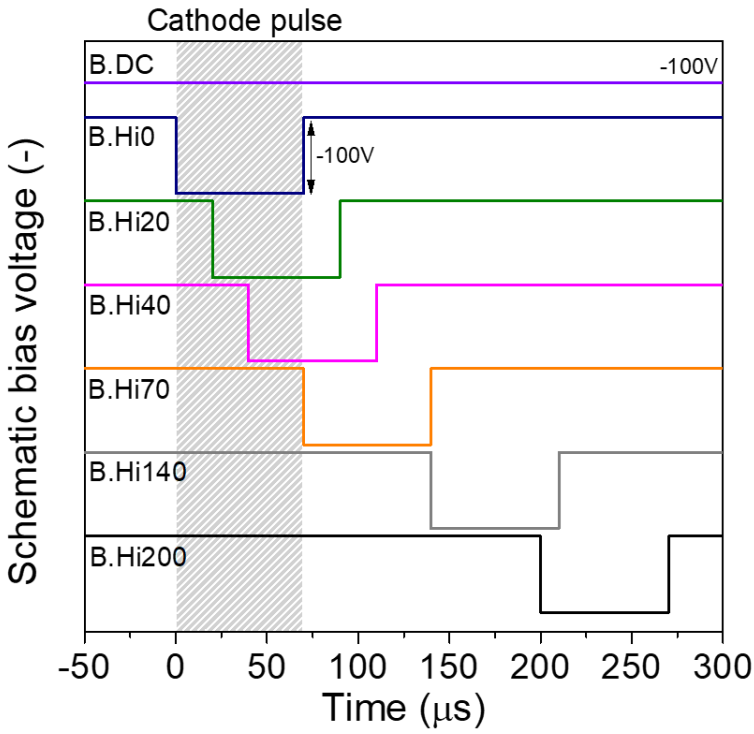

Figure 6.26: Schematic view of bias pulse with respect the cathode pulse used in the coating's deposition step.

While the continuous substrate bias remains active during the entire coating step, the pulsed substrate bias is applied with a duty cycle, which can be synchronized to the duty cycle of the HiPIMS cathode pulses or alternatively, the pulse-on-time of the substrate bias can be chosen applying an offset with regard to the pulse of the HiPIMS cathode.

Introducing a delay between the onset of the HiPIMS pulse and the bias pulse will influence the metal-ion and process-gas-ion dominated bombardment situation during film growth. The typical time-evolution of dominating ions during a HiPIMS pulse is headed by energetic process gas-ions, normally Ar+ ions, which is then followed by metal ions (very often the doubly-charged metal ions lead the singly-charged metal ions). Consequently, by using a delay it is possible to tune the influx of high-energetic process-gas and metal ions (singly- and doubly-charged) reaching the substrate [97,333].

6.3.2.1. Elemental composition and microstructural characterization

The chemical composition of all the coatings was determined by GD-OES technique. Results from the coatings obtained by using a DC bias, a synchronized pulse bias and a bias pulse delay of 70 µs with respect to the cathode pulse are given as an example in Figure 6.27. These results are significant for all the samples. No remarkable differences can be observed as function of the bias delay time. The multilayer structure cannot be observed in the elemental lines due to the small bilayer period of approximately 15 nm for all the coatings. The irregular crater geometry created during the test may result in a mixing of consecutive layers especially when the coatings are in the nanometer range, applicable for these coatings.

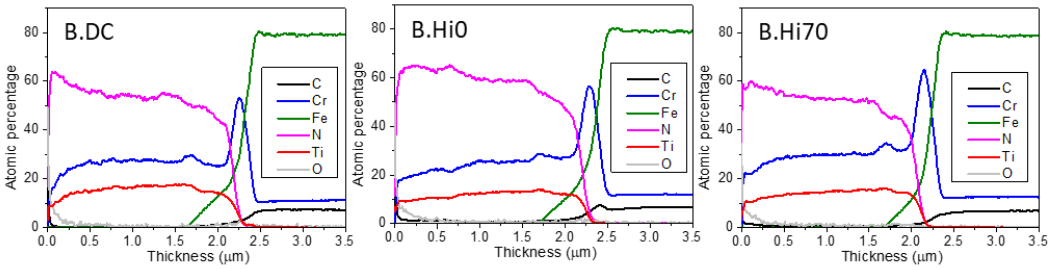

Figure 6.27: GD-OES results obtained for 3 coatings.

Figure 6.28 depicts the SEM cross-section images of the coatings and the topography images (scanning area = 10x10 µm) obtained by AFM. The roughness values of the coatings obtained from the AFM images can be found in Figure 6.29. Although all the coatings have a multilayer structure, the resolution of the equipment is not enough to observe the composition of the individual layers either by secondary electrons or backscattered electrons. However, a Cr anchor layer of about 200 nm can be observed, which is well known for enhancing the adhesion of the coating to the substrate [334].

In terms of the structure of the coatings, the main difference that can be observed in the SEM cross-sectional images is the presence of highly oriented columns with trigonal-shaped facets surface for all the coatings deposited by using a HiPIMS bias, regardless of the delay time of the bias pulse, in contrast to the very dense and compact structure observed for the DC-biased coating. Although columns can be observed in all the coatings deposited by bias HiPIMS, some minor differences can be observed between them. Among them, the coating with the most distinct structure is B.Hi20 which has a feather-like architecture with higher intercolumnar space. This kind of structure is reported to be an indirect indication of the (111) preferred orientation of the coating [335]. it can be seen that initially small grains grow near the substrate and become larger towards the surface, which is indicative of competitive growth (zone T in Ref. [105]) and explains the prevalence of the (111) orientation, the kinetically favoured orientation with the highest growth rate under these conditions [325].

Greczynski *et. al.* reported that the plasma is maintained primarily by Ar^+ and N_2^+ gas ions. After a delay time of 20 µs, N^+ ions start to originate and after 30-40 µs, gas-ion intensities begin to decrease. At that time, metal-ion such as Ti^+ and Cr^+ ions, start to originate and are predominant in the region between 40 – 100 µs. After that time, the Ar^+ ion intensity dominates again [333]. According to those studies, coating B.Hi20 was deposited in a gas-ion rich environment which goes in detriment of the properties of the coating, thus maximizing a predominant (111) texture with trigonal-shaped facets. Sample deposited with a delay of 40 µs of bias pulse delay is in between the gas-ion and metal-ion rich regions, and the structure is not as columnar as for the B.Hi20 coating. A small densification with lower intercolumnar space is observed for the sample B.Hi70 in which the plasma was supposed to be dense in metal-ions which is in good agreement with the results obtained by Greczynski et.al. [336]. Samples B.Hi140 and B.Hi200 were both again deposited in the gas-ion rich region, showing more columnar trend. However, among all the coatings, the best structure regarding the density and compacity was obtained by using a direct current bias.

AFM images that can be observed in Figure 6.28 and roughness values shown in Figure 6.29 match completely with the cross-sectional SEM images. Columnarity of the coatings results in an increase of the surface roughness, especially for the sample B.Hi20 where the roughness reaches a maximum value of 15.5 nm^2. The two coatings (B.Hi20 and B.Hi200) deposited in the most gas-ion rich region are the ones which also show higher roughness values. The lowest roughness value is obtained for the DC-biased coating which also showed the densest structure.

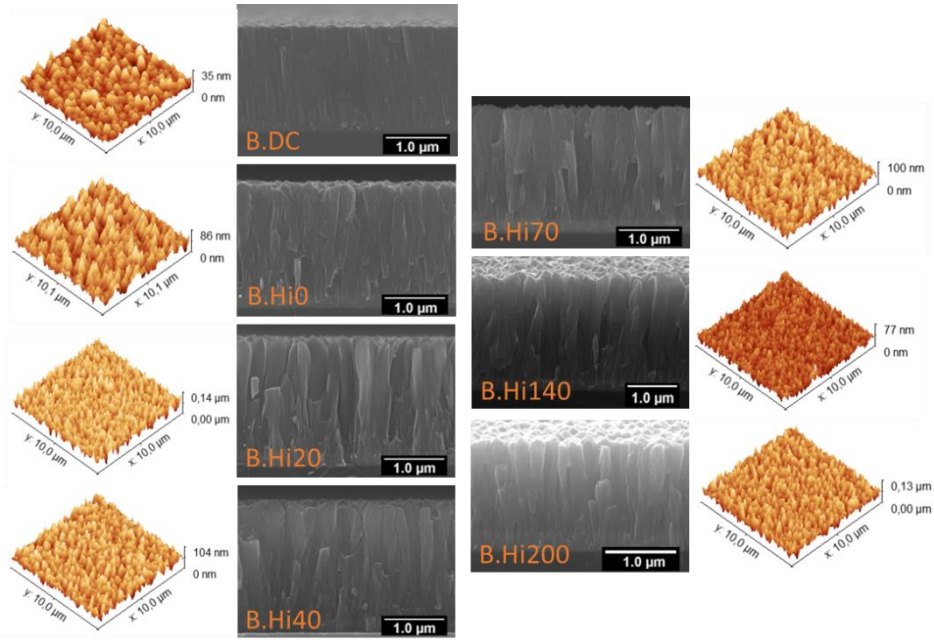

Figure 6.28: SEM and AFM images obtained for the coatings with different bias delay times.

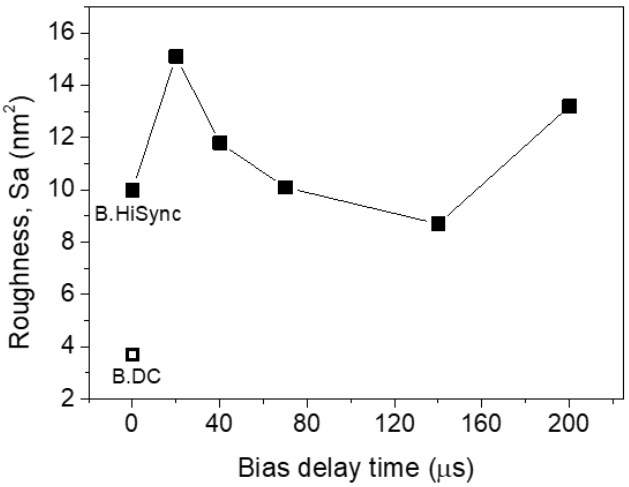

Figure 6.29: Roughness values obtained for the coatings as function of the bias delay time.

Figure 6.30 shows the GI-XRD measurements obtained for the coatings with a fixed grazing incident angle of 1º used to maximize the signals from the coating and avoid the ones from the substrate. From the analysis of the diffractograms it is expected to identify the following crystalline phases: fcc-TiN (ICDD card nº 38-1420) and fcc-CrN (ICDD card nº 11-0065). However, due to the small bilayer period of approximately 15 nm for all of these coatings, peaks corresponding to the single crystalline phases cannot be observed. These have completely converged into a single peak leading the formation of a single-phase solid solution. This process has been explained in detail in the previous sections. Satellite peaks around the main one can also be observed arising to the formation of a superlattice structure for all the coatings.

The texture of the coatings is in good agreement with the SEM results obtained. Samples deposited with low concentrations of metal ions in the plasma (B.Hi20 and B.Hi200) show a higher crystalline growth in the (111) direction, especially for sample B.Hi20. As the amount of metal ions in the plasma increases, more crystalline growth occurs in the (200) direction, which is the hardest plane and the most thermodynamically stable one [324,337]. Those samples correspond to the B.Hi0 and B.Hi70, respectively, which also showed a slightly denser structure in SEM cross-section images.

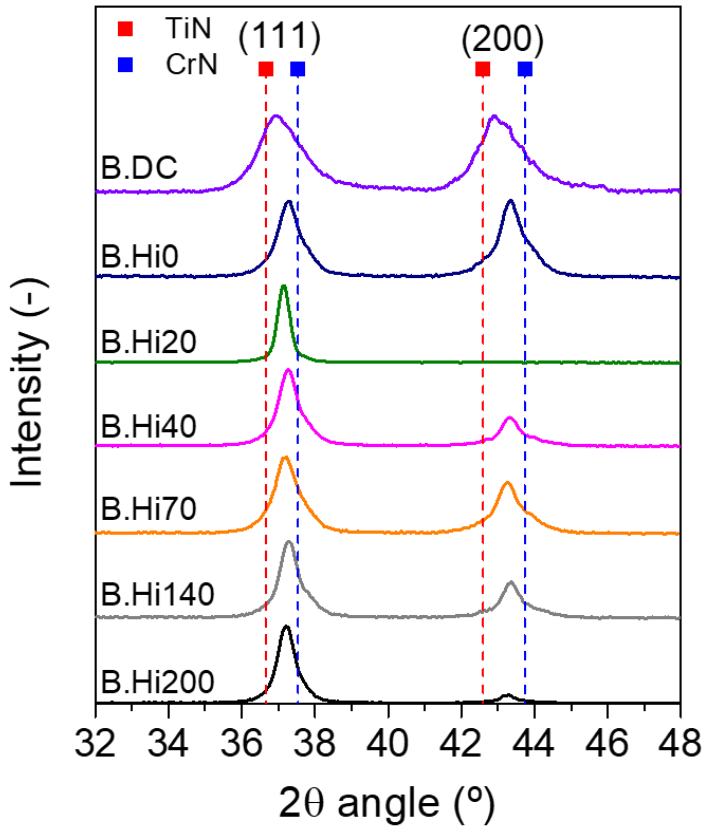

Figure 6.30: GI-XRD measurements of the coatings

The crystallite size calculated by Rietveld refinement for all the coatings can be observed in Figure 6.31. No differences in the crystallite size can be observed as function of the crystalline growth direction. The lowest crystallite size is obtained for the coatings deposited by DC bias which also showed a denser structure, smooth surface and preferential crystalline growth in the (200) direction. Among all the coatings deposited by HiPIMS bias, B.Hi0 and B.Hi70 coatings present smaller crystallite sizes as compared to the others. The decrease in the crystallite size can be explained by larger defects generated because of the enhanced ion bombardment and resputtering effect produced mainly be metal ions, which will increase the number of preferential nucleation sites and lead to a decrease of the crystallite size [328,329]. In contrary, the largest crystallite size can be obtained for the B.Hi20 coating which presented a more open feather-like structure with a total texture in the (111) direction. The increase in the crystallite size in the (111) direction has previously been reported by several authors [316,325,338].

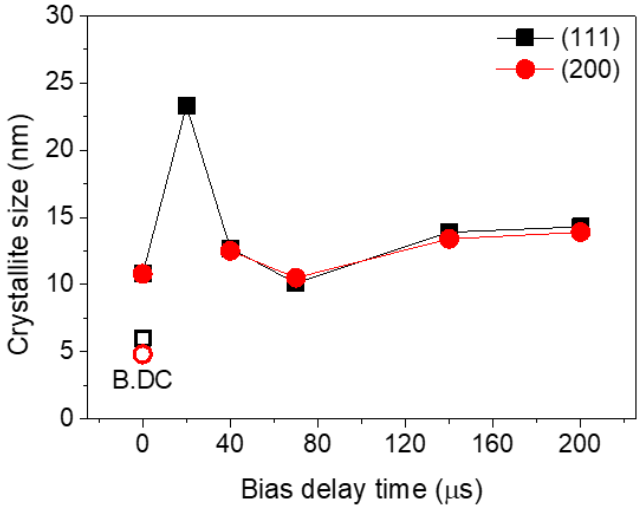

Figure 6.31: Crystallite size calculated from the XRD measurements as function of the bias delay time.

6.3.2.2. Mechanical characterization

Figure 6.32 shows the results of the residual stress as determined by the $\sin^2\psi$ method from the (111) diffraction peak [217]. For most of the coatings, the residual stress observed is compressive except for the coatings deposited with a bias pulse synchronized with the cathode pulse which turns to be tensile. The displacements of the peaks with respect to the standard pattern observed in the diffractograms are in good agreement with the calculated residual stresses. While a compressive stress is observed with peak positions displacements towards lower angles, tensile stress displacements tend to higher angles [217]. The highest residual stress value is observed for the DC-biased coating probably due to the peening effect. In which at higher energies, ions can penetrate deeper into the coatings inducing more irregular incorporation of atoms/ions into the crystalline lattice [330,331]. No clear trend in the residual stress can be observed as function of the bias delay time used.

The hardness (H) and reduced Young's modulus (Er) obtained by nanoindentation technique are shown in Figure 6.33. For all the coatings deposited by HiPIMS bias, the values obtained are in the range between 13 and 5.5 GPa. Among them, coatings which show the highest hardness value are B.Hi0 and B.Hi70. These two samples were deposited in a metal-ion rich plasma and showed an increase in the coating density in the SEM images even presenting a columnar structure, and consequently, a lower roughness value. The smaller crystallite size and a remarkable crystalline growth in the (200) orientation also contribute to the hardness increase [339]. The maximum hardness value of almost 33 GPa was obtained for the DC-biased sample, which is in good agreement with the previous results shown.

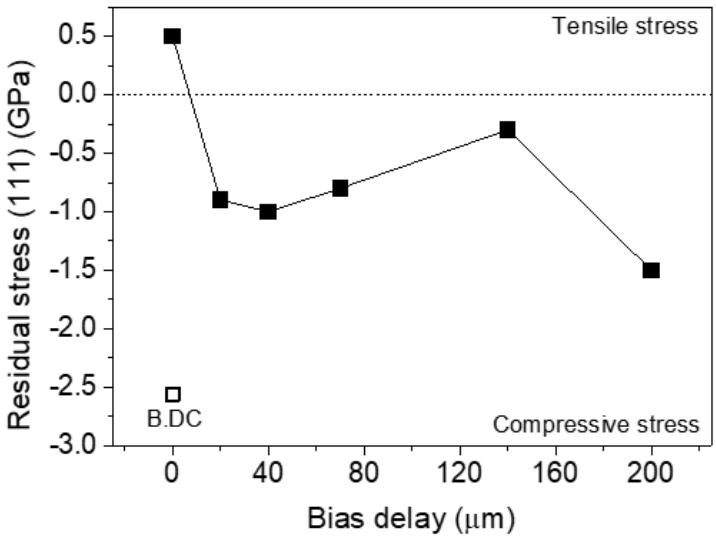

Figure 6.32: Residual stress of the coatings.

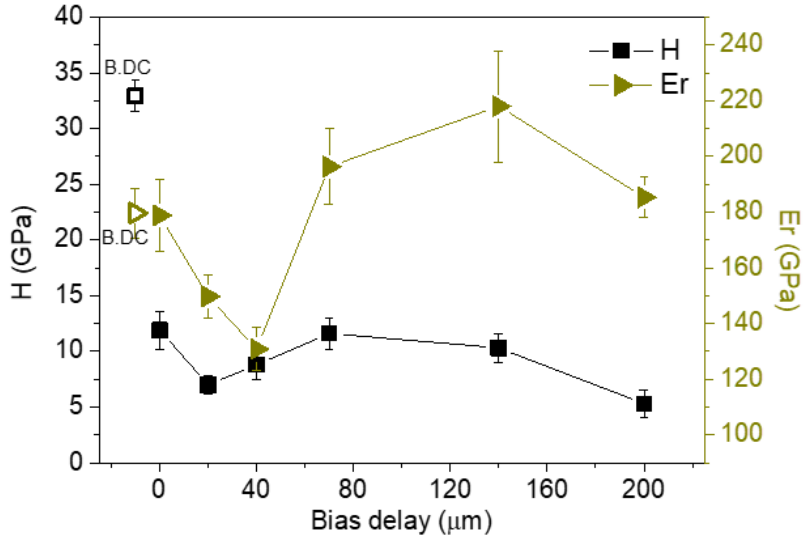

Figure 6.33: Hardness and reduced Young's modulus obtained for all the coatings.

In Figure 6.34, results of the scratch tests performed on coatings B.DC, H.Hi0 and B.Hi70 are shown. These three coatings were selected for having the best microstructural and mechanical properties among all of them. The first critical load (Lc_1) corresponds to the first cohesive failure observed in the coating, usually perpendicular cracks on the borders of the track; the second critical load (Lc_2) is registered when the first adhesive failure is

appreciated, i.e., chipping on the edges of the track; and the third critical load (Lc_3) corresponds to the total delamination of the coating due to wear. Lc_2 is commonly considered a sign of the coating adhesion's failure [340]. Lc_1 could not be identified for any of the samples. The values obtained of Lc_2 and Lc_3 for the different coatings are as follow: For B.DC, 15 ± 1 N and 88 ± 7 N, for B.Hi0, 7 ± 1 N and 95 ± 2 N and for B.Hi70, 45 ± 5 N and 93 ± 5N. According to Bull's studies, residual stress in coatings has a very significant impact on its fracture mode and also, an increase in the residual stress leads to a decrease in the adhesion strength of the coatings to the substrate [214,215].

For coatings B.DC and B.Hi70, which showed compressive residual stress, the main fracture mechanism observed along the scratch test is spallation. However, coating B.Hi70 also show some plastic deformation on the edges of the scratch due to the low hardness values obtained. The highest compressive residual stress value for B.DC leads to a decrease in the Lc_2 value as described in the literature [153]. In contrast, for sample B.Hi0, which showed residual tensile stress, low hardness value, only plastic deformation is observed from the beginning to the end of the scratch test. For all the coatings, the determined Lc_3 values is very high, with values around 92 N. These could be obtained thanks to the Cr interlayer which was deposited with the same conditions for all the samples [341].

Lower coating adhesion values were obtained by Ou *et.al.* for TiN/CrN multilayer coatings deposited by pulsed DCMS [281], by Atmani *et. al.* for TiN/CrN multilayer coatings deposited by PVD-DC system [342] and by Tillman *et.al*. for TiAlN coatings deposited by DCMS and HiPIMS [343].

Although it has been reported in the literature that the properties of coatings can be improved by using a pulsed bias, in our case, the most effective way to transfer energy to the growing coating is by applying a continuous bias [75,344]. It has to be pointed out that all of the coatings studied in this thesis were deposited by using an industrial-scale reactor which has much more variables than the laboratory-scale PVD systems.

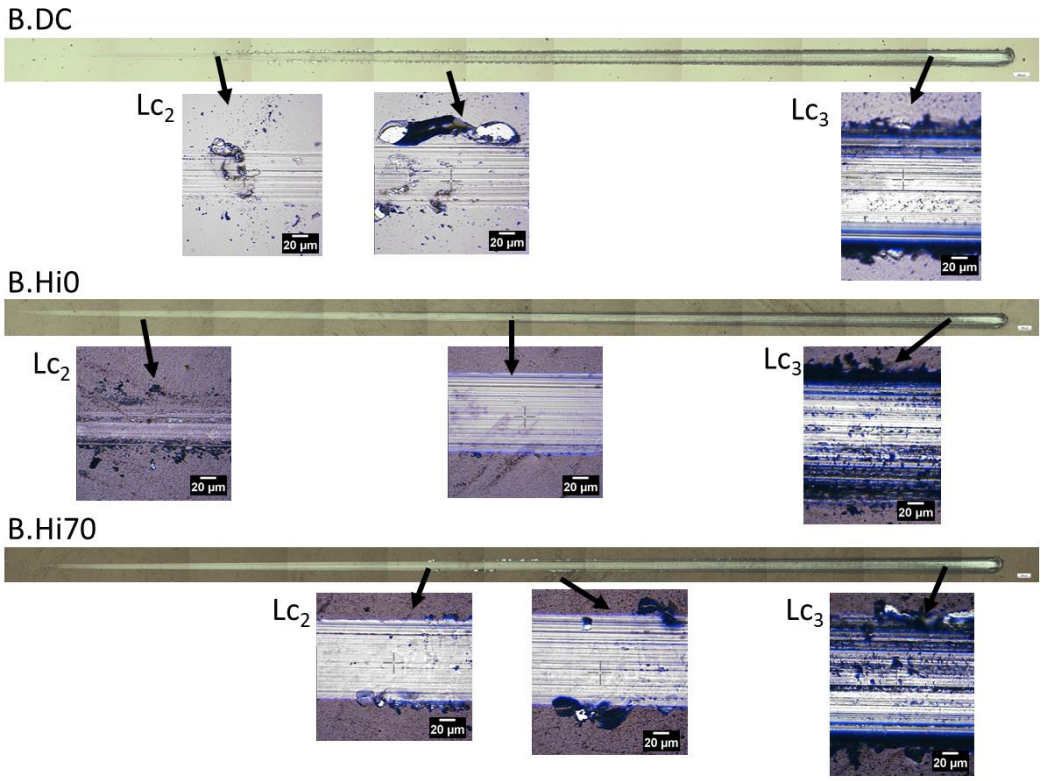

Figure 6.34: Scratch tests results for samples B.DC, B,Hi0 and B.Hi70.

6.4. Conclusions

TiN/CrN multilayer coatings have been successfully deposited using the reactive HiPIMS technique with an industrial-scale deposition system.

In the analysis of the deposition time (i.e., bilayer period), the deposition time of the respective sublayers was adjusted in such a way to get bilayer periods between 460 and 7 nm. All coatings present a compact, featureless structure with roughness values between 5 and 10 nm. X-ray diffraction showed separate crystalline phases of TiN and CrN for the samples with bilayer periods > 85 nm. However, as the bilayer period decreases, the TiN and CrN peaks overlap, showing epitaxial crystalline growth that was then confirmed by HR-STEM measurements. The presence of satellite peaks around the principal peak in the X-ray diffractogram confirms a superlattice structure comprising TiN and CrN sublayers formed for the sample with a bilayer period of 15 nm. Residual stress values are around -2.2 GPa for the samples. The optimum mechanical properties are obtained for the superlattice structure with a bilayer period of 15 nm showing a hardness of 32 GPa.

Regarding the influence of the bias application mode, all the DC-biased coatings present a denser, featureless structure with lower roughness values as compared to the HiPIMS-biased coatings. The growth of the coatings under high ion-energy conditions promotes the crystalline growth in the (200) direction and decreases the crystallite sizes as observed in the XRD measurements. All the residual stresses calculated for the DC-biased coatings show compressive stress values around -2 GPa, in contrast to the HiPIMS-biased samples which show non or positive tensile stress values. Coatings deposited with B.DC show hardness and young's modulus values up to 4 times higher than for samples deposited with B.Hi, with a maximum value of 32 GPa obtained for the sample with Λ 15 nm.

From the study of the synchronization of the bias with respect to the HiPIMS cathode pulse, all the B.Hi coatings present a columnar structure regardless of the pulse delay time. However, coatings deposited under the metal-ion rich region (B.Hi0 and B.Hi70) show slightly denser structures with higher crystalline growth in the (200) direction. These two coatings also show a small increase in the H and Er values as compared to the rest of the HiPIMS-biased samples. The coatings show good-substrate adhesion in the scratch test measurements. However, the increase in the compressive stress value is revealed with a decrease in the Lc_2 value for the B.DC coating, with a main fracture mechanism of spallation. Lower values of hardness and residual stress lead to a plastic deformation of the coating during the scratch test. The best properties regarding the microstructure and mechanical properties of the coatings are obtained when using a DC bias. With a constant polarization of the substrate, more energy is transferred to the adatoms, its mobility is increased, and the properties obtained for the coatings are improved.

CHAPTER 7

TiN/CrN, TiSiN/CrN and NbN/CrN multilayer coatings

The results of this chapter gave place to some scientific communications:

Contributions to communications:

1. Junior Euromat 2022 Coimbra, Portugal. "*TiN/CrN, TiSiN/CrN and NbN/CrN multilayer coatings deposited in an industrial-scale HiPIMS system*". **N. Sala**, M. R. de Figueiredo, R. Franz, C. Kainz, C. Colominas, M. D. Abad. Poster presentation. 19-22 of July 2022.
2. 18th International Conference on Plasma Surface Engineering (PSE 2022). Trade Fair Erfurt, Germany. "*TiN/CrN, TiSiN/CrN and NbN/CrN multilayers prepared by HiPIMS*". M. D. Abad, **N. Sala**, M. R. de Figueiredo, R. Franz, C. Kainz, C. Colominas Oral presentation. 12-15 September 2022.

Contributions to publications:

1. Part of this chapter will be submitted to Surface&Coatings Technology journal.

7. TiN/CrN, TiSiN/CrN and NbN/CrN multilayer coatings

Metal transition nitrides such as TiN, NbN and CrN have been extensively studied in the last years and are well known for their high hardness, good thermal stability and good wear resistance [82,345–347]. Therefore, they are widely used to solve industrial problems. To improve the performance of the coatings in respect to the traditional monolithic ones, new coatings have been developed, such as bilayer [348], gradient [349] and multilayer structures [286].

TiN/CrN has attracted especial interest for their microstructure, good mechanical and tribological properties as explained in the previous chapter. However, the influence of incorporating Si in TiN coatings has been less reported but has special interest regarding the excellent mechanical properties that can be obtained with the formation of a nanostructure comprising TiN grains embedded in an amorphous Si_3N_4 matrix [350,351]. Some multilayer coatings have been developed combining TiSiN with another metal nitride compound coatings but still not with CrN [352,353]. Regarding the use of NbN/CrN coatings, they have been deposited by several techniques and have been widely used for high temperature application and as a tribocorrosion resistance coatings, but have not been studied in depth by HiPIMS technique [354–356].

In this study, different TiN/CrN, TiSiN/CrN and NbN/CrN multilayer coatings were deposited by HiPIMS technique in an industrial-scale reactor with different bilayer periods with best deposition conditions found during the development of this thesis. The chemical composition, crystalline phases and mechanical properties were investigated and compared as a function of the bilayer period and the different composition for the three sets of samples.

7.1. Coating deposition parameters

TiN/CrN, TiSiN/CrN and NbN/CrN coatings have been deposited using an industrial-scale CemeCon CC800/9 ML magnetron sputtering reactor in reactive HiPIMS mode. For each set of coatings, two metallic targets were used to deposit the coatings. One titanium and one chromium target from CemeCon (99.95% purity) were used to deposit the TiN/CrN multilayer coatings on single-crystalline silicon wafers (100) and mirror-polished cold-worked 1.2379 steel. One $Ti_{74}Si_{26}$ and one Cr targets were used for depositing the TiSIN/CrN multilayer coatings while a Nb and a Cr target were used for the NbN/CrN multilayer coatings. Argon was used for plasma formation and nitrogen was used as a reactive gas at 170 sccm. Background pressure was 3×10^{-3} Pa, whereas the working pressure amounted to 0.65 Pa. The sputtering powers were 4 kW and 4.2 kW for the titanium and chromium targets, respectively. The HiPIMS pulse parameters were: a duty cycle of 5.6 %, a pulse duration of 70 μs, and a repetition frequency of 800 Hz for Ti, $Ti_{74}Si_{26}$ and Nb; a duty cycle of 2.5 %, a

pulse duration of 50 µs, and a repetition frequency of 500 Hz for Cr. A DC substrate bias of -100 V was applied during the entire deposition processes with an applied table rotation speed of 3 rpm. The multilayer structure was obtained by switching on/off sequentially each pair of targets and the different Λ were obtained by changing the deposition time of each TiN/TiSiN/NbN as well as CrN single layer. Three different multilayered coatings were deposited for each composition with different Λ and number of single layers in order to obtain thicknesses between 1.4 and 3.1 µm. All coatings comprise a chromium base layer, followed by a CrN layer and subsequently alternating layers of TiN/TiSiN/NbN and CrN. On top, a thin TiN/TiSiN/NbN top layer was deposited. Single layer TiN, TiSiN, NbN and CrN coatings were deposited as a reference using the same deposition parameters. The specific details of the deposition process for each coating are summarized in Table 7-1.

Table 7-1: Summary of the sputtering conditions and properties of the coatings.

Sample	Sputtering time (s)				Nº sublayers	Λ (nm)	Thickness (µm)	Chemical composition (at. %)					Ra (nm)
	Cr	Ti	$Ti_{76}Si_{24}$	Nb				Cr	Ti	Si	Nb	N	
TΛ85	200	600	-	-	50	85	2.3	26	18			56	4.2
TΛ15	50	150	-	-	176	15	2.2	28	18			54	3.9
TΛ7	20	60	-	-	320	7	2.0	27	18			55	9.3
SΛ85	200	-	600	-	50	85	2.4	26	15	3		55	2.2
SΛ20	50	-	150	-	176	20	2.1	26	15	3		55	4.9
SΛ5	20	-	60	-	320	5	1.5	25	15	4		56	4.3
NΛ125	200	-	-	600	50	125	3.1	25			30	44	2.5
NΛ30	50	-	-	150	176	30	3.0	25			27	47	4.1
NΛ10	20	-	-	60	320	10	2.3	22			29	49	3.2

7.2. Results and discussion

7.2.1. Elemental composition

A schematic view of the coatings is represented in Figure 7.1. For each set of compositions, three different coatings with different Λ were deposited. More detailed information about the coatings can be found in Table 7-1.

The chemical composition of the multilayers was determined by EPMA and is summarized in Table 7-1. No pronounced influence of Λ on the composition is apparent. The N content of about 50 at. % indicates stoichiometric sublayers. The O content was below 1 at. % for all coatings. Regarding the metal ratio Cr/(Cr+Ti), a value of about 0.6 was observed for the TiN/CrN and TiSiN/CrN coatings regardless of the variation in Λ. A possible explanation for this value is the presence of the Cr base layer contribution to the measured composition. For the NbN/CrN coatings, the metal ratio Cr/(Cr+Nb) value is 0.45. The difference in the metal ratio can be attributed to a higher sputtering rate of Nb compared of those of the Ti and TiSi.

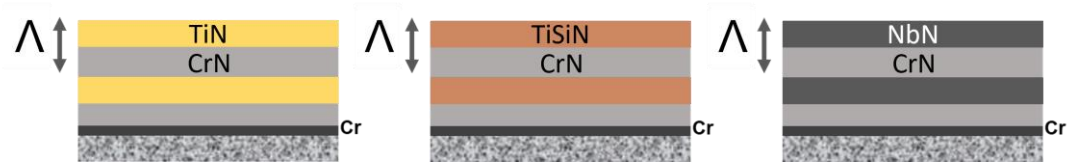

Figure 7.1: Schematic view of the depostied coatings

The disposition of the sublayers was also observed by GDOES technique, and the results are shown in Figure 7.2. For all the coatings with Λ between 85-125 nm it is possible to observe the sublayers with different composition, as well as the Cr anchoring layer. This indicates a well-formed and coherent structure. The loss of resolution with depth has been previously reported and can be attributed mostly to the surface roughening produced by the ion bombardment and a subsequent change in the crater geometry resulting in a mixing of consecutive layers especially when they are in the nanometre range [298,299].

For coatings with Λ of 15-30 nm and below, the sublayers are too thin to be distinguishable with this technique. Even though the coatings have a multilayer structure, during the GDOES process a mixture of consecutive layers are sputtered at the same time resulting in a flat line in the atomic composition. Results are not shown for coatings with Λ 5-10 nm.

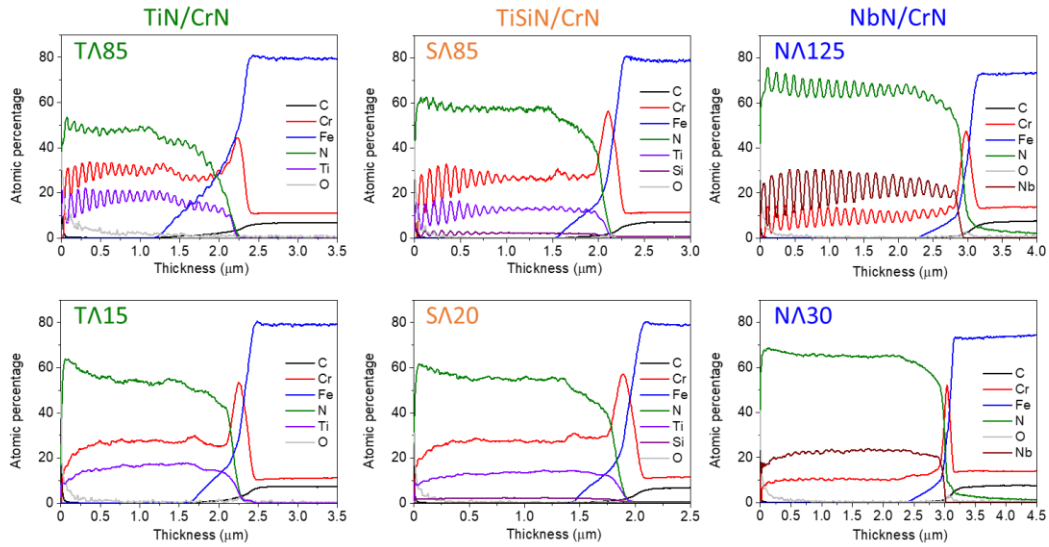

Figure 7.2: GD-OES results obtained for some coatings.

7.2.2. Microstructural characterization

In Figure 7.3, the cross-section SEM images of the coatings can be observed. In all of them, an anchoring layer based of Cr (~200 nm) can be easily observed. For the coatings with Λ 85-125 nm it is also possible to observe the distribution of the sublayers of different composition. If continuously decreasing Λ the resolution of the technique is not enough to observe the different sublayers. All the coatings appear to be smooth and compact although some fine columns are observed regardless of the Λ. Especially in case of the coatings with a bilayer period of 85 nm it appears that the TiSiN/CrN coatings have a smoother microstructure as compared to the TiN/CrN and NbN/CrN coatings. This grain refinement due to the addition of Si in the TiN coatings have been previously reported by other authors [107,228].

These NbN/CrN coatings are also less columnar than some reported in literature for the same deposition technique [138].

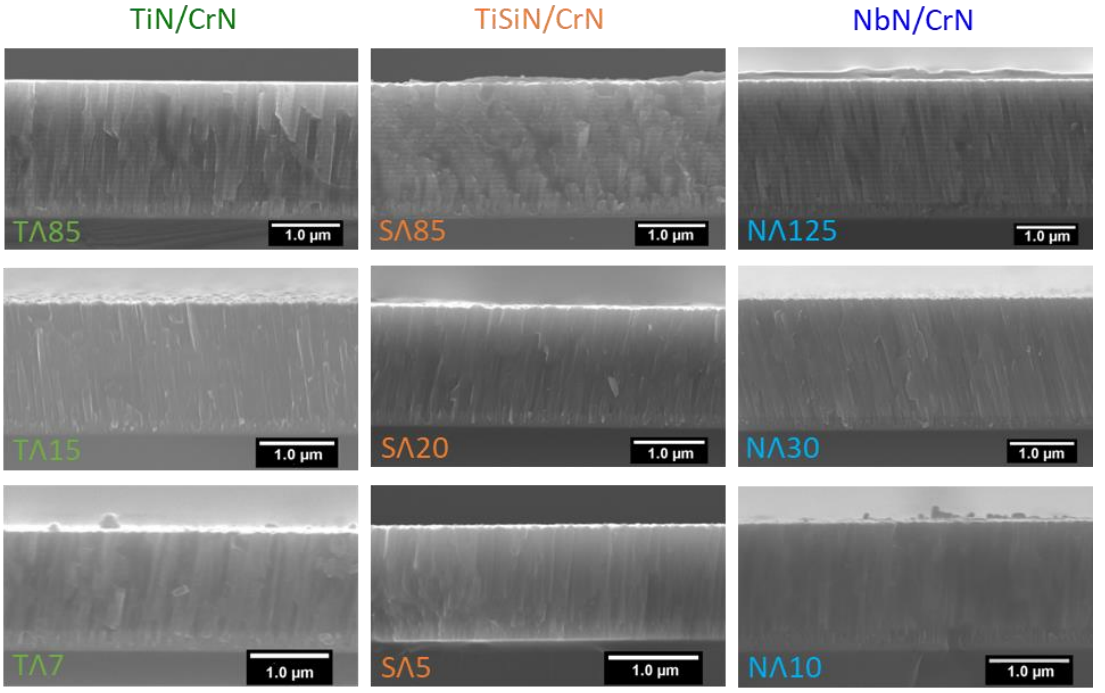

Figure 7.3: SEM cross-section images of the deposited coatings.

The AFM top surface images (scanning area = 10 × 10 µm^2) are shown in Figure 7.4. The roughness values (Sa) can be found in Table 7-1. All the values are in the range of nanometres indicating very smooth and flat surfaces as also clear in SEM images. No clear trend is observed neither in the bilayer period nor in the composition of the coatings.

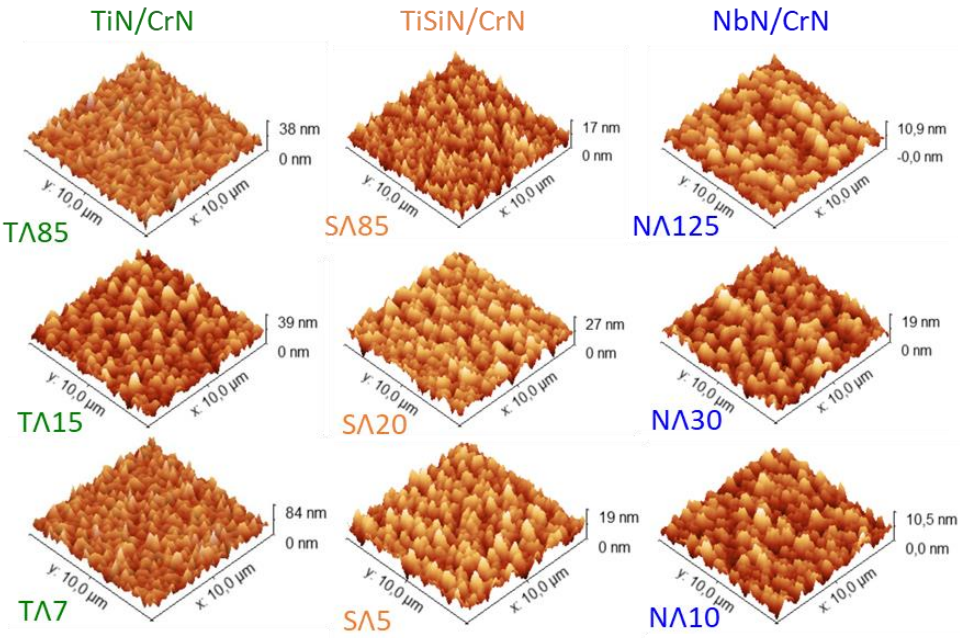

Figure 7.4: AFM topography images of the coatings.

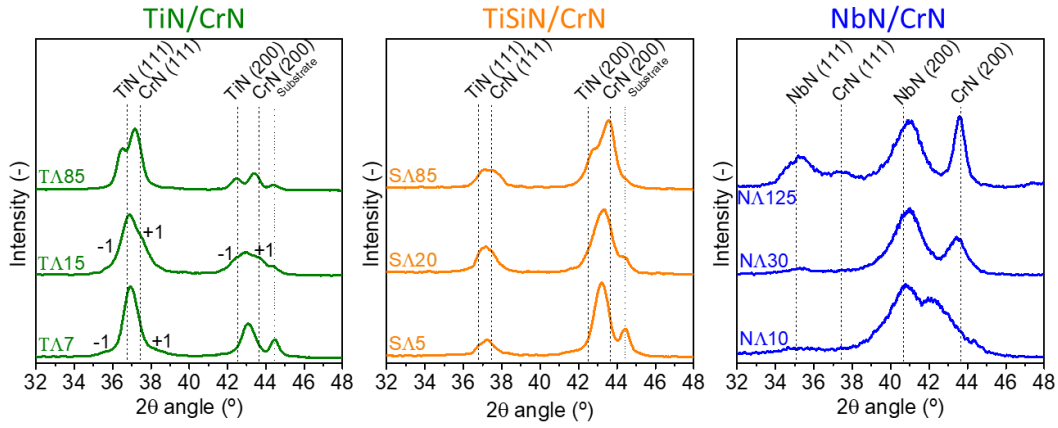

Figure 7.5: GI-XRD measurements of the coatings.

Figure 7.5 depicts the results obtained from the XRD measurements measured in grazing incidence angle at 1º. The analysis of the diffractograms allowed the identification of the following phases: fcc-TiN (ICDD 38-1420), fcc-CrN (ICDD 11-0065) and the substrate for the TiN/CrN and TiSiN/CrN multilayer coatings, and fcc-NbN (ICDD 65-0436), fcc-CrN and the substrate for the NbN/CrN multilayer coatings. Separate TiN, NbN and CrN phases are evident from the XRD for larger bilayer periods suggesting semi-coherent or incoherent interfaces. However, as the bilayer period decreases, the reflections of the single crystalline phases approach each other, which would indicate a change in the structure of the coatings

showing potential coherent stress towards the formation of a single-phase solid solution, especially for the TiN/CrN coatings where the lattice parameter mismatch is around 2 % [357]. The convolution of the peaks due to the small parameter mismatch between TiN and CrN results in a mutual diffraction interference between them. [358,359]. The presence of satellite peaks around the respective main peak in the TiN/CrN coatings confirms a superlattice structure for Λ of 15 and 7 nm.

This same trend can be observed also for the TiSiN/CrN and NbN/CrN coatings although the satellite peaks cannot be easily distinguished, probably due to a different parameter mismatch between the monolayers. For the TiSiN/CrN coatings, the value is between 1-2 %, while for the NbN/CrN is around 5-6 % [360,361].

TiSiN crystalline phases cannot be detected from the XRD analysis indicating the presence of Si in either forming a solid solution interstitially or substituting Ti atom in the crystalline lattice, and/or an amorphous SiNx phase [362–365]. The shifted position of the peaks towards larger angles would indicate that Si is substituting Ti atoms in the lattice, since the crystalline radius of Si is smaller than Ti, there is a modification of the cell parameter towards larger angles and therefore smaller interplanar distance. According to some studies, with the amount of Si present in these samples, amorphous SiNx phases should not form. With these results it is considered that these amorphous phases are not formed and that Si is substituted to the crystal lattice. This is discussed later in the TEM-EELS section.

The TiN, NbN and CrN crystallite size was calculated from the (111) and (200) reflections using Rietveld refinement. For all the coatings, the crystallite size is in the range of nanometers (10-20 nm) as expected from the broadening of the peaks observed in the XRD measurements. Special attention was given to the samples with larger bilayer periods in which it is possible de deconvolute the peaks to obtain the contribution of each of the crystalline phases. The value of the crystalline size of the TiN phase calculated for the TiN/CrN and TiSiN/CrN coatings are 20 nm and 14 nm respectively. This decrease in the crystallite size could be also attributed to a decrease in the cell parameter due to the Si incorporation in the TiN crystalline phase which would be in good agreements with the other XRD results obtained [366].

Crystalline growth is observed in two different crystallographic planes: (111) and (200). For the TiN/CrN coatings, a strong texture is observed in the (111) direction regardless of the bilayer period. However, the incorporation of the Si in the coating induces a change in the texture to a (200) preferred orientation. This same effect was previously reported by other authors [358,367–369] but it is normally not discussed. For the NbN/CrN coatings, all of them have a (200) preferred orientation although the decrease of the bilayer period induces a change to a more pronounced (200) crystalline growth, being the coating with the smallest Λ completely textured in the (200) direction. Similar behavior has been previously reported by

Araujo *et. al.* for NbN/CrN multilayer coatings deposited by cathodic arc technique [370] and by Purandare *et. al.* for NbN/CrN coatings deposited by HiPIMS technique [371].

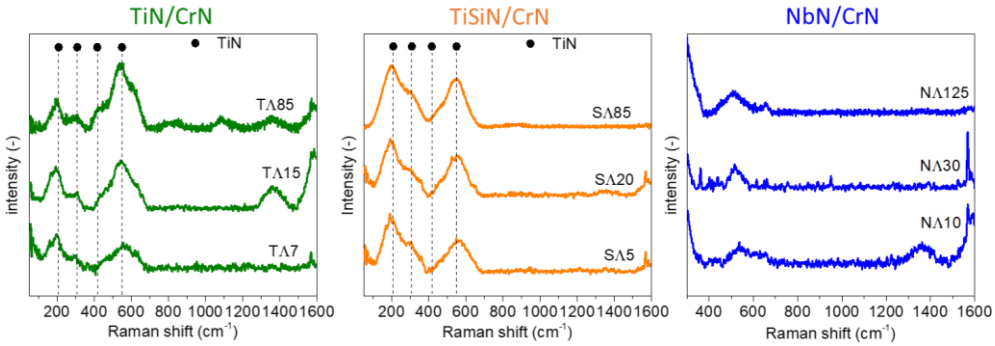

Figure 7.6: Raman spectra measured of the coatings.

Figure 7.6 shows the Raman spectra of the as deposited coatings. All of the spectra were measured at 532 nm and under identical conditions to allow direct comparison of their intensities. Different bands can be observed at 210, 309, 417 and 544 cm^{-1} for the TiN coating. The first two at lower-frequency scattering can be attributed to acoustic phonons, while the ones at high-frequencies are due to optical phonons of the defect-induced first-order Raman scattering [372–374]. However, really weak Raman bands can be observed for the CrN coatings. There is no influence on the raman signal intensity with the reducing bilayer period for the coatings. For the TiN/CrN and TiSiN/CrN coatings, some extra bands appear around 1400-1600 cm^{-1} for the bilayer period of 15 nm that can stem from the superlattice structure. This same effect can be observed for the NbN/CrN coatings with a Λ of 10 nm. One possible explanation for the appearance of this bands could arise from the difference in the nanostructure specially when a superlattice is formed and the grain size is small enough, but it is still to be defined. These results are in good agreement with the ones obtained in the XRD measurements for the formation of superlattice structures for the samples with Λ 15 nm [342,357,374].

HRTEM and EELS studies were necessary to examine the nanostructure of the TiSiN/CrN coatings and to determine how Si is incorporated into them.

- **SΛ5 coating**

In Figure 7.7a, the structure of the coating can be observed. The growth of the coating is in the form of nanocolumns of approximately 35 nm thick. These columns reach between 65 and 130 nm on the surface of the coating.

Similar to the results obtained for the TiN/CrN samples, double periodicity is also observed in the coatings due to the 3-fold rotation used for the deposition of the coating

(Figure 7.7b). When taking a closer look at the coating, it is clear that the black regions are not a single compound but a region in which the bilayer period is smaller. The thickness of the individual layers was obtained by the HAADF profiles such as the one shown in Figure 7.7c. The bilayer period obtained is not constant throughout the hole coating. TiSiN (dark) layers have a thickness of about 2.5 nm, and CrN (bright) layers of ca. 4 nm. This makes a bilayer period of ca. 6.5 nm. However, every 44 nm, a thinner TiSiN – CrN – TiSiN layers are observed. In those regions, the thickness of the TiSiN layers is 2 nm and the CrN layer is 2.5 nm which makes a bilayer period of 4.5 nm.

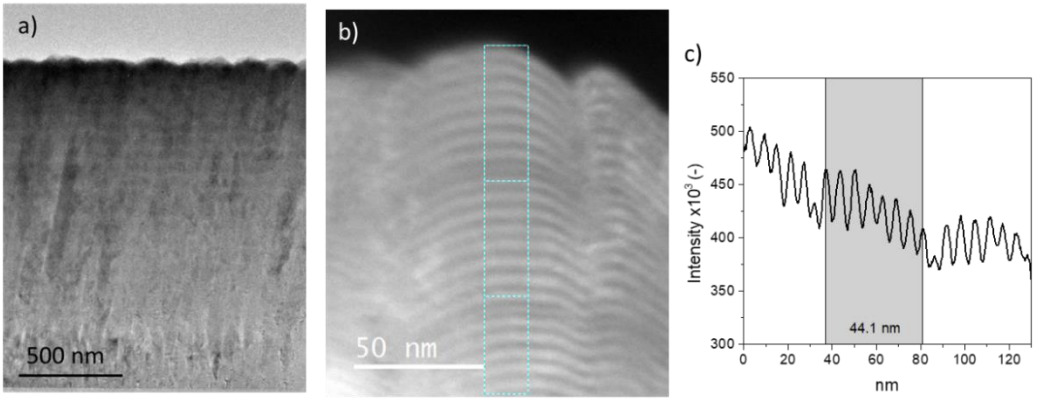

Figure 7.7: a) TEM image of the coating SΛ5, b) HAADF-STEM or Z-contrast image of a higher magnification area zoom-in a and c) HAADF intensity profile in the indicated region.

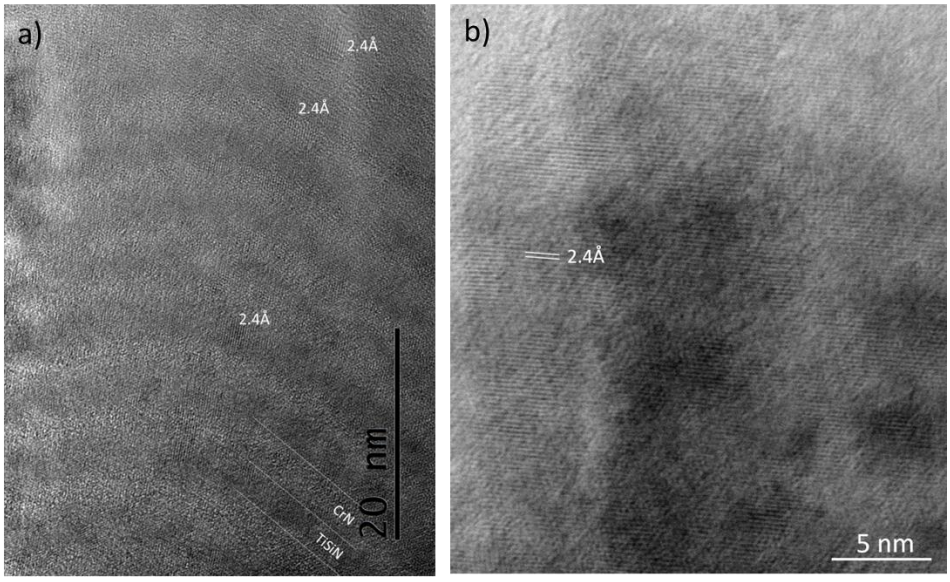

Figure 7.8: a) and b) HRTEM images

Figure 7.8 a) and b) shows representative HRTEM images from one of the columns of the coating. A coherent crystalline growth of the TiSiN and CrN planes can be observed, although same amorphous small areas are notice along the layers in comparison with TiN/CrN system where the epitaxial growth along the layers was more evident (see Figure 6.10). This epitaxial growth can be explained in terms of energy as for the TiN/CrN coatings.

The measured interplanar spacing in the HREM images is 2.4 Å. This is in good agreement with the XRD results for crystalline growth in the (111) plane.

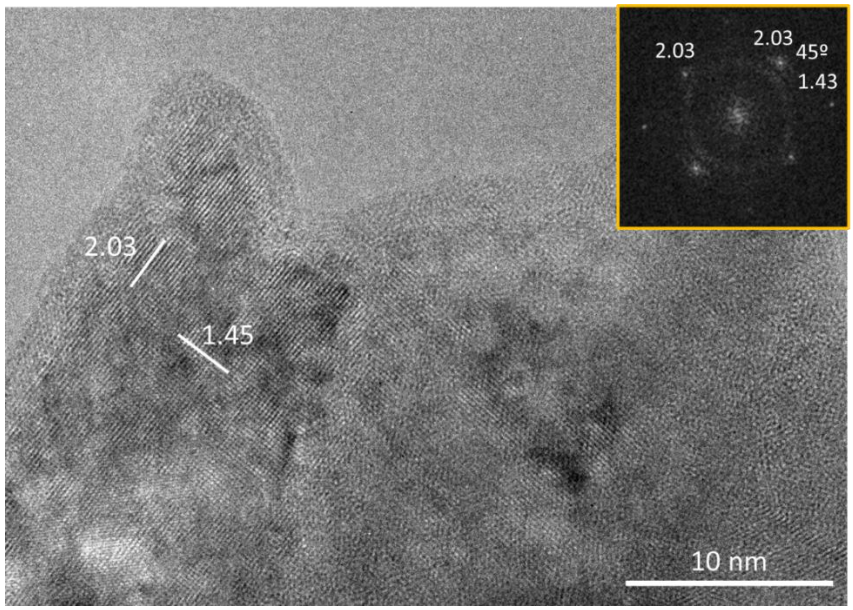

Figure 7.9: HRTEM image. DDP pattern is shown as an insert.

Figure 7.9 shows an HRTEM image in a much thinner region with its corresponding DDP pattern as an insert. Crystalline growth is found in two different planes with different interplanar spacing which may correspond to the growth in the 200 and 220 directions as in good agreement with the values calculated by Rietveld adjustment by XRD. Some amorphous character could be inferred from the diffuse halo observed in the DDP insert.

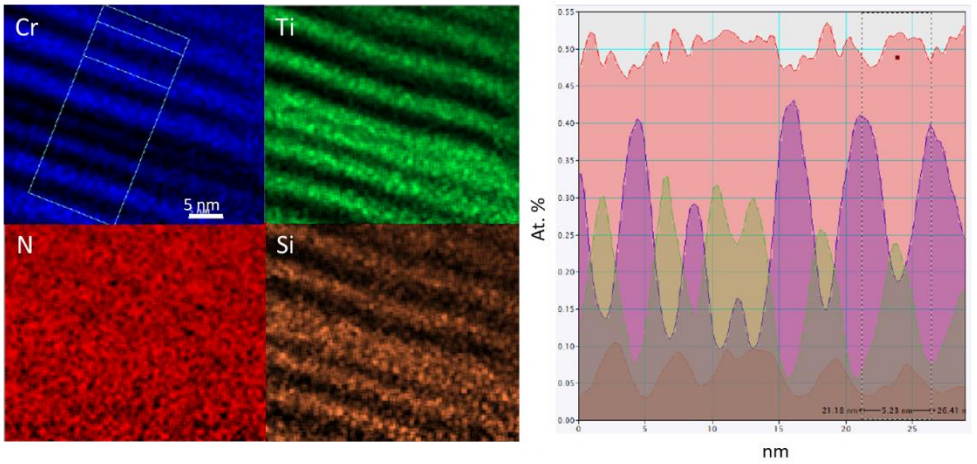

Figure 7.10: HAADF-EDS profiles obtained for the SΛ5 coating.

From the HAADF-EDS profiles shown in Figure 7.10, a clear alternation between CrN and TiSiN layers can be observed. The composition of the sample obtained by integrated EDS profiles, in at. % is: 50 N, 28 Cr, 18 Ti and 4 Si, respectively. These results are in good agreement with the composition obtained by EPMA. By this analysis technique, the formation of a ternary and/or quaternary compound (TiSiCrN) in interfaces regions of less than 1nm cannot be discarded.

- **SΛ20 coating**

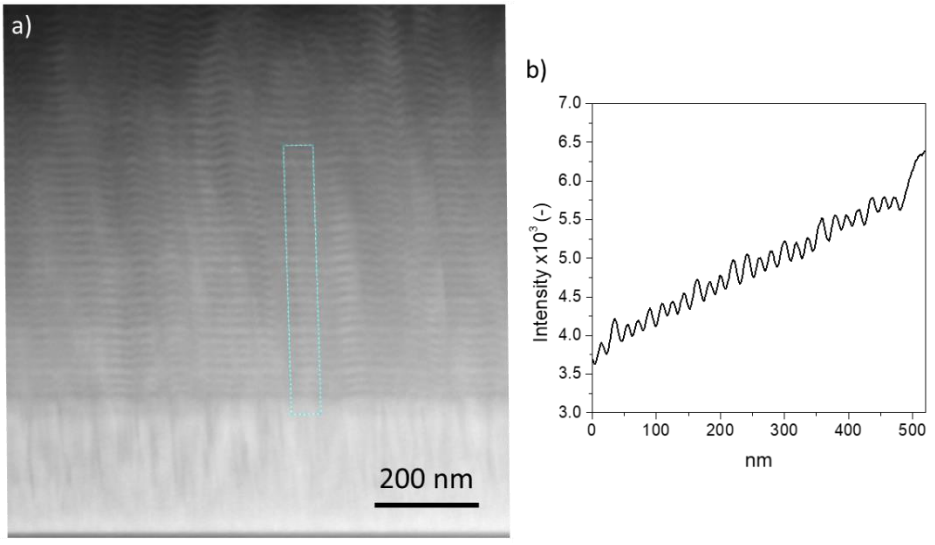

Figure 7.11: a) HAADF-STEM image of SΛ20 coating. b) HAADF intensity profile in the indicated region.

In Figure 7.11a a HAADF-STEM image for the SΛ20 coating can be observed. For this sample, a double periodicity is not observed. However, different CrN layer thicknesses are observed throughout the coating structure. As can be measured in the HAADF intensity profile in Figure 7.11b, every two periods, the CrN layer changes from 12.5 to 9.5 nm while the TiN layers keep a constant thickness in between 7-8 nm. The total bilayer period obtained for that coating in around 20 nm.

In Figure 7.12, HRTEM images of the sample are shown. Figure 7.12a shows a region of the coating in which the TiSiN and CrN layers can be clearly observed. The interplanar spacing calculated directly in the image is 2.4 Å, which corresponds to the crystal growth in the (111) plane. In the DDP insert, some diffuse halos indicating amorphous regions could indicate a nanocomposite structure formation. In Figure 7.12b, a coherent crystalline plane growth can be observed for the TiSiN and CrN planes although this growth is interrupted by some small amorphous areas.

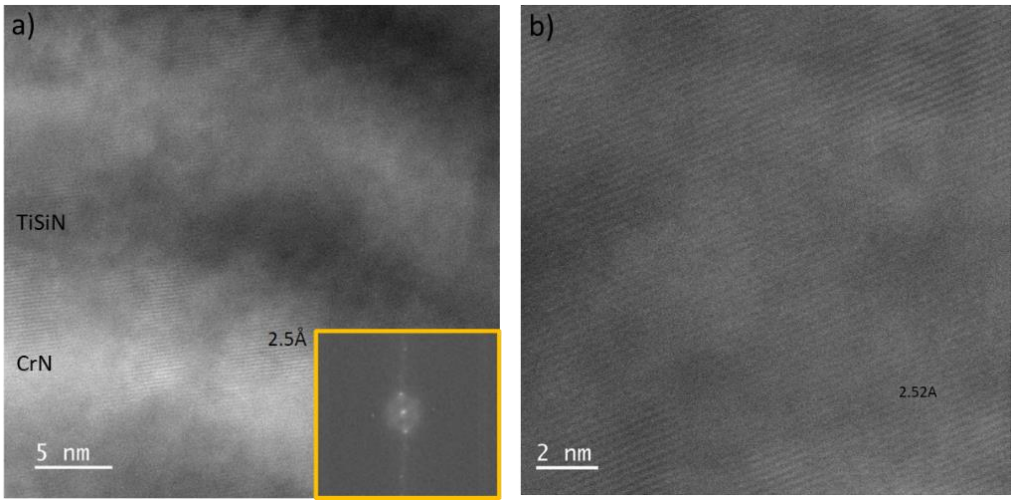

Figure 7.12: a and b, HRTEM image of the SΛ20 coating. Al DDP pattern is shown as an insert in a.

The composition for the SΛ20 sample was measured by nanoprobe-EDS (Figure 7.13) and by nanoprobe- EELS (Figure 7.14) analysis. As can be appreciated in the elemental's maps of the Figure 7.13 there is an alternation of the TiSiN and CrN layers. The thickness of the bilayer period is approximately 20 nm which is consistent with the results obtained from the HAADF intensity profiles. The presence of two thicker CrN layers between two thinner CrN layers can also be observed.

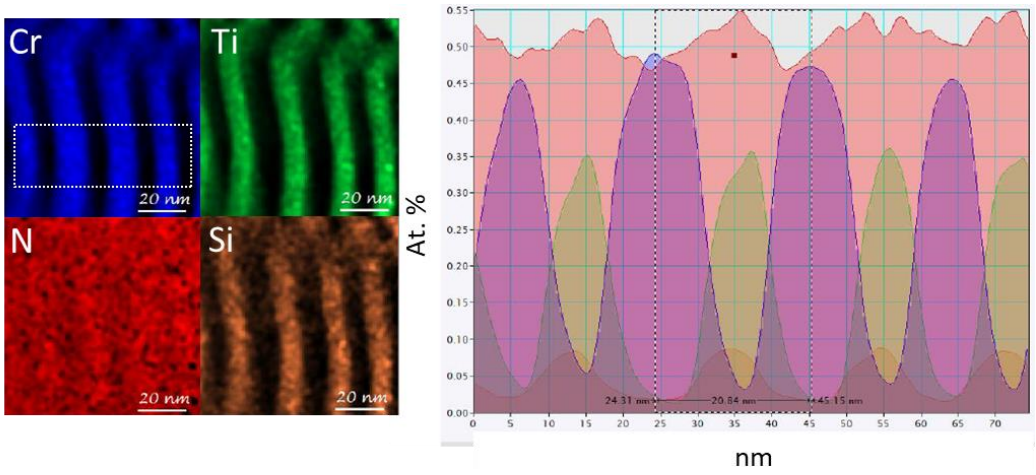

Figure 7.13: HAADF-EDS profiles obtained for the SΛ25 coating.

This sample has been studied deeply by EELS. The N-*K* edge and Ti, Cri and Si-$L_{2,3}$ edges were used to get elemental maps as in the areas in Figure 7.13. The compositional profile obtained by EELS could be used to measure the bilayer periods (around 20 nm). While the Cr at.% reaches 0 in the TiSiN zones, Ti does not quite reach 0 in the CrN zones, which could indicate diffusion of Ti through the nanolayers. The amount of Si obtained in the coating is about 4%, in good agreement with the values obtained by EPMA.

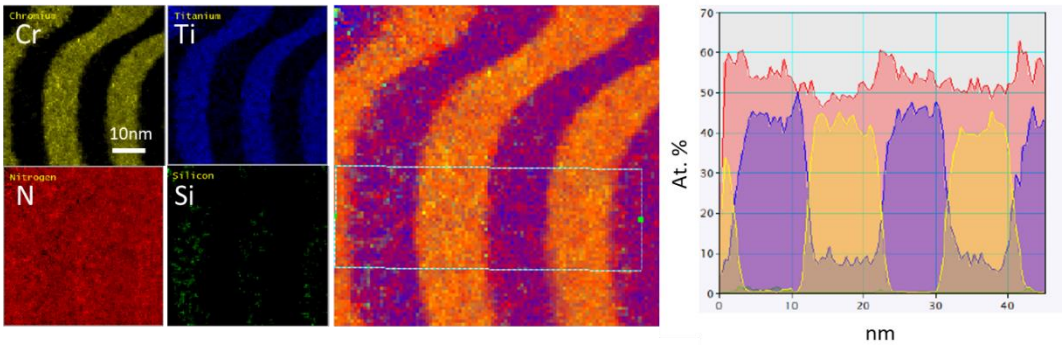

Figure 7.14: Coating composition obtained by EELS technique.

- **SΛ85 coating**

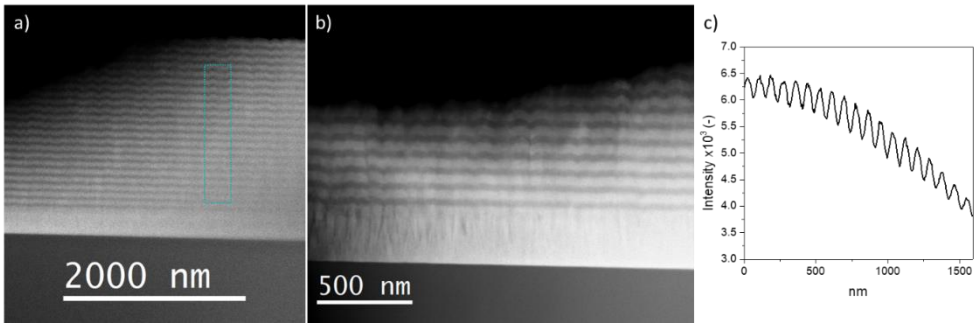

Figure 7.15: a) TEM image of the coating SΛ85, b) HAADF-STEM image of a higher magnification area zoom-in a and c) HAADF intensity profile in the indicated region.

In Figure 7.15, some TEM images of the coating SΛ85 are shown. For this sample, neither a double periodicity nor a difference in the CrN layers thicknesses is observed. The bilayer period obtained is around 85 nm, which corresponds to a 48-50 nm CrN layer plus a 35 nm TiN layer.

- **Chemical bonding of the TiSiN/CrN and TiN/CrN multilayer coatings (Samples SΛ5, SΛ20 and TΛ7)**

The TiSiN/CrN and TiN/CrN have been studied in parallel by EELS in order to understand how the silicon is incorporated in the coating structure. Figure 7.16 shows the EELS spectra of the individual TiN, TiSiN and CrN layers of the SΛ5 and TΛ7 multilayer coatings. The N-*K* and $L_{2,3}$ edges of Ti and Cr were identified according to literature [375,376].

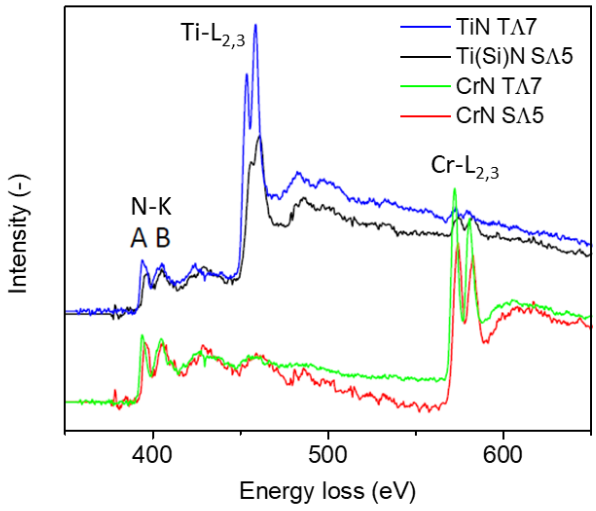

Figure 7.16: EELS measurement from the central region of the CrN and TiN layers of the SΛ5 and TΛ7 coatings.

When Si is introduced into TiN in the SΛ5 coating, there is a decrease in the intensity of the A peak at the N-*K* edge and Ti-$L_{2,3}$ edge, indicating that Si is substitutionally replacing Ti in the TiN crystalline cell. Also, an amorphization of the Ti(Si)N phase is observed with the broadening of the N-*K* and $L_{2,3}$ edge of the titanium. This behaviour has been previously reported for different coating systems such as CrAlYN coatings [311,377].

In the TiN (TΛ7) and TiSiN (SΛ5) layers, Cr does not disappear completely, indicating Cr interdiffusion in the thin Ti(Si)N layers. However, no Ti is observed in the Cr layers. In the thicker TiSiN layers of the SΛ20 coating, practically no Cr is observed in the TiN layers (Figure 7.17). The increase in the TiSiN thickness layers limits the mixing of species as already reported by Araujo *et. al.* [378].

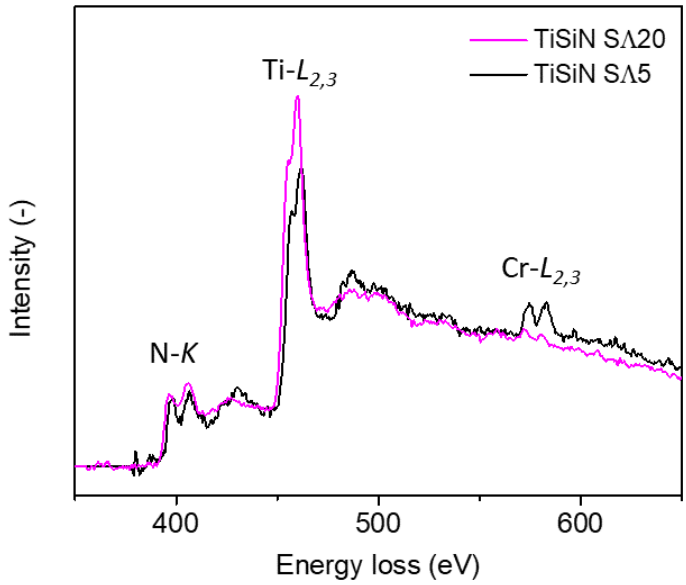

Figure 7.17: EELS measurement from the central region of the TiSiN layer of the SΛ5 and SΛ20 coatings.

The Si-*K* edge was also studied for the SΛ20 coating. (Figure 7.18). Neither the shape of peaks A and B, nor the ratio of intensities indicate the segregation of the thermodynamically stable amorphous Si_3N_4 phase within the TiN matrix [379,380]. It is then confirmed that the amorphous phases observed by TEM actually correspond to TiN structures with substitutional Si incorporation. The thin layers, the deposition technique and the presence of many interlayers may affect this segregation as the structure does not eventually relax.

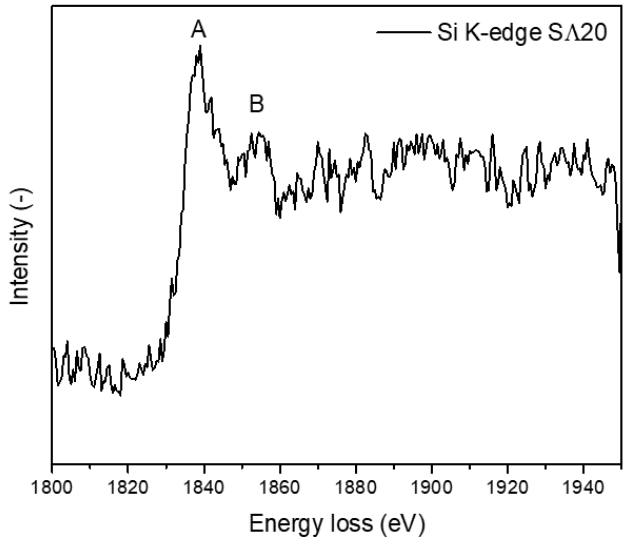

Figure 7.18: EELS Si-K edge for SΛ20 coating.

7.2.3. Mechanical properties

Figure 7.19 shows the results of the residual stress as determined by the $\sin^2\psi$ method from the (111) peak [217]. Samples were tilted in the range between 0 and 0.9 $\sin^2\psi$. Increasing the tilt angle induces a shift of the peak position to higher 2θ angles, which indicates compressive residual stress in the coatings. The residual stress values in the (111) direction are from higher to lower: TiN/CrN > NbN/CrN > TiSiN/CrN. Some studies suggest that the (111) crystallographic plane is associated with a higher residual stress value than the (200) direction [182,319]. Thus, TiN/CrN coatings that are highly textured in the (111) direction have higher stress values than the other coatings. The reduction of Λ has no significant influence on the residual stress of the coatings. The residual stress values obtained for the multilayer coatings of about -2.5 GPa are between the values obtained for the single layered TiN and CrN coatings with -3.6 and -1.1 GPa, respectively (results not shown).

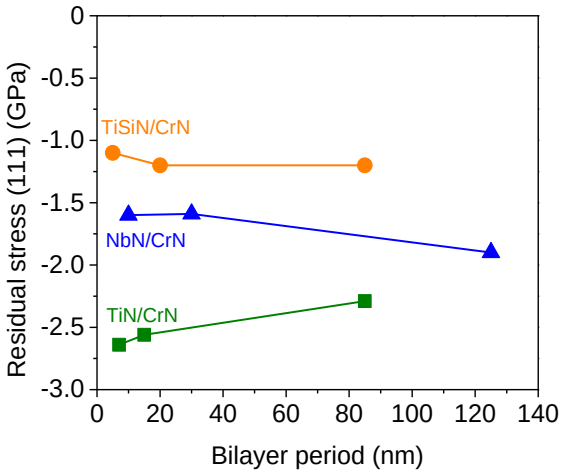

Figure 7.19: Residual stress calculated from the (111) crystalline plane of the coatings.

To evaluate the mechanical properties of the coatings, the hardness (H) and Young's modulus (E) was determined using nanoindentation; the results are shown in Figure 7.20. Data derived from these results can be also found in Figure 7.21.

For the TiN/CrN coatings, H and E vary from 25.8-32.1 GPa and 334-394 GPa, respectively. For the TiSiN/CrN coatings, H and E vary from 22.3-28.5 GPa and 316-342 GPa, respectively and for the NbN/CrN coatings, H and E vary from 25.5-30.3 GPa and 310-351 GPa, respectively. The mechanical properties of the multilayer coatings are better than those of the respective monolayers in the case of the TiN/CrN and NbN/CrN multilayers. This increase in hardness and Young's modulus for the multilayer systems with respect to the single layered ones is mainly associated with the hindering of dislocation movements arising from the lattice mismatch at the interfaces and due to the Hall-Petch effect [124,126,127,318]. TiSiN/CrN coatings are well known for the formation of nanocomposite based on SiNx phases in the structure that rises the hardness values up to 40-50 GPa. [107,351]. It is not possible to obtain such high hardness in the multilayer coatings studied as no SiNx nanocomposite-based structures were formed.

For each set of samples, the maximum hardness value was observed for the sample with a bilayer period of approximately 20 nm which according to the XRD results corresponds to the formation of a superlattice structure. The highest values of 32.1 GPa for TiN/CrN coating, 28.5 GPa for the TiSiN/CrN and 30.3 GPa for NbN/CrN are also in good agreement with the residual stress values obtained.

H/E and H^3/E^2 values can be used to estimate the material elastic strain to failure and the material resistance to plastic deformation, respectively. Higher values of these parameters indicate better properties [284,319]. These values follow the same trend that the values

obtained for the H and E, being higher for the multilayer coatings with a bilayer period of around 20 nm. The values for the sample TΛ15 are lower than expected but still have better mechanical properties than those of the monolayers. The improvement of H/E and H^3/E^2 can be related to a more effective blocking of dislocation movements, well-defined interfaces, optimization of the bilayer period, and denser microstructures [281,291].

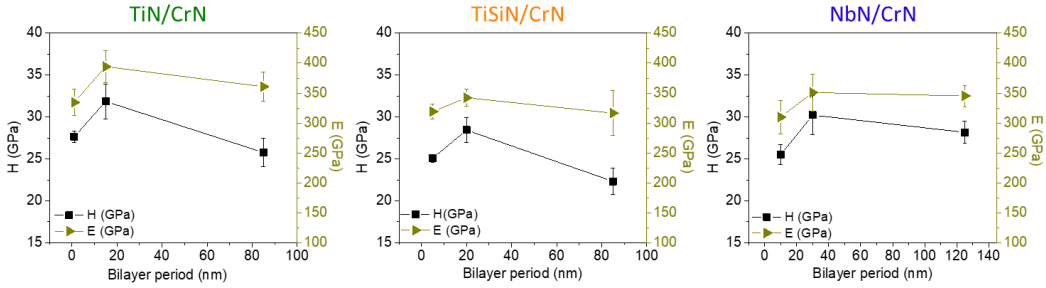

Figure 7.20: Hardness (H) and Young Modulus (E) vs. the bilayer period of the coatings.

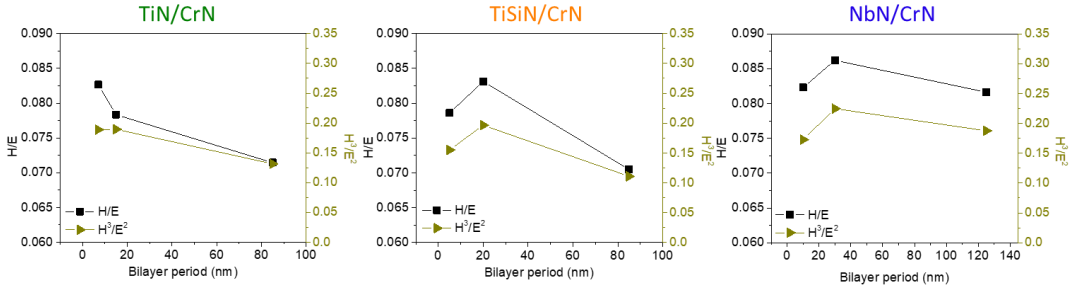

Figure 7.21: H/E and H^3/H^2 ratios of the coatings.

7.2.4. Tribological properties

According to the mechanical properties discussed in the previous section, the best coatings for tribological applications should be the ones having higher hardness and H/E and H^3/H^2 ratios. Among all the coatings of study, the ones showing better properties are TΛ15, SΛ20 and NΛ30. Although tribological analyses were carried out from room temperature and up to 500°C for all coatings, results are only shown for the selected samples. In order to prove the thermal stability of the coatings, tests were carried out at room temperature after the high temperature tests. The same tests with the same conditions were performed on steel substrates to allow comparison of the results.

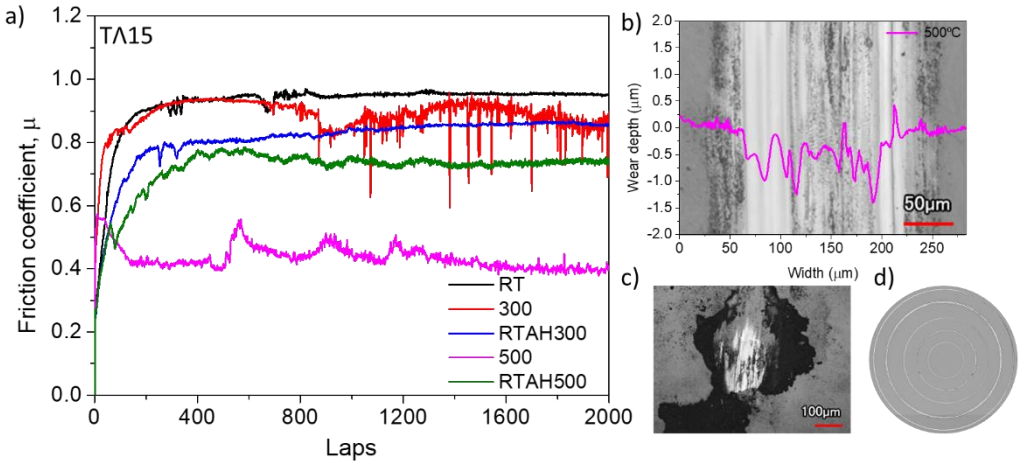

Figure 7.22: Tribological results for sample TΛ15. a) COF as a function of number of laps. b) Laser image of the wear track and surface profile after the ball-on-disk test. c) Laser image of the wear scar on ball counterpart for the test at 500ºC. d) Stitched image of the whole sample after the tribological tests. The wear tracks from the centre outwards are RT, 300ºC, RTAH300, 500ºC and RTAH500.

In Figure 7.22, Figure 7.25a and Table 7-2, results obtained for the TΛ15 sample are shown.

Figure 7.22a depicts the friction coefficients (COF) monitored during the tests. At room temperature they are stable in the studied range showing a value around 0.8. When testing at high temperatures some fluctuations are observed, probably because of the presence of debris formed during the test, as can be seen in the ball counterpart laser image in Figure 7.22c for the 500ºC test. The COF of 0.45 for the 500ºC test is much lower than the obtained for the rest of the tests. Figure 7.22b shows the track derived from the test and the corresponding profile. A non-uniform wear of the coating surface is observed, which leads to a smaller contact surface between the ball and the coating and therefore decreases the COF. Figure 7.22d shows all the tracks of the tribological tests. The order of the tests from the centre outwards are RT, 300ºC, RT after heating at 300ºC, 500ºC and RT after heating at 500ºC. For all tests a uniform wear of the coating is observed. The substrate is not reached in any of the cases as can be seen in the depth of the track in Figure 7.25a. The calculated wear rates for both the ball and the track increase with increasing temperature. Even so, all the values obtained for the coated sample are lower than the ones of the substrate (Table 7-2), affirming the protective capacity of the coating. Neither the tribological behaviour of the coating nor the appearance are changed after heating the sample which would indicate a good thermal stability of the samples.

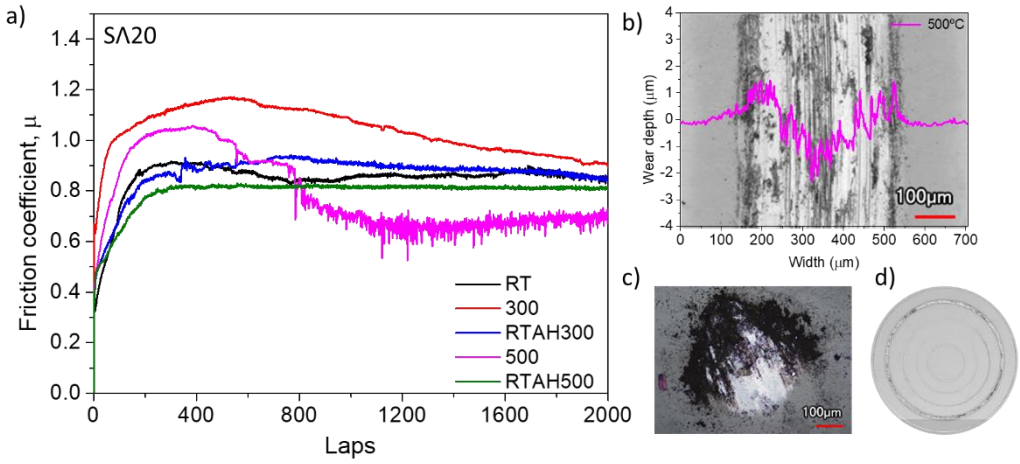

Figure 7.23: Tribological results for sample SΛ20. a) COF as a function of number of laps. b) Laser image of the wear track and surface profile after the ball-on-disk test. c) Laser image of the wear scar on ball counterpart for the test at 500ºC. d) Stitched image of the whole sample after the tribological tests. The wear tracks from the centre outwards are RT, 300ºC, RTAH300, 500ºC and RTAH500.

In Figure 7.23, Figure 7.25b and Table 7-2, results obtained for the SΛ20 sample are shown. Figure 7.23a depicts the friction coefficients (COF) monitored during the tests. All the tests performed at RT show stable COFs around 0.8. At 300ºC, after an increase of the COF, this is stabilized and decreases until it reaches the same value for the tests at RT. At 500ºC some cracking, and breakage of the coating is observed, which destabilises the COF due to the formation of debris and coating particles that remain adhered to the ball and on the disc. This can be observed in the depth profile in the wear track and the ball counterpart in Figure 7.23b-c. The wear track at 500ºC in Figure 7.23d also shows discontinuous and non-uniform scar confirming this coating delamination and bad adhesion to the substrate. The COF for the test at 300ºC is much more stable than for the sample TΛ15 which would indicate better thermal properties with the addition of Si in the coating as previously reported by other authors [366,381]. Calculated wear rates that can be found in Figure 7.25b are in good agreement with the results of the COF explained before for this coating. Wear rates for the ball and the disk are almost equal at RT and 300ºC whereas at 500ºC a reasonable increase is observed. However, all the values recorded are better than the ones from the substrate even at 500ºC in where the substrate is exposed.

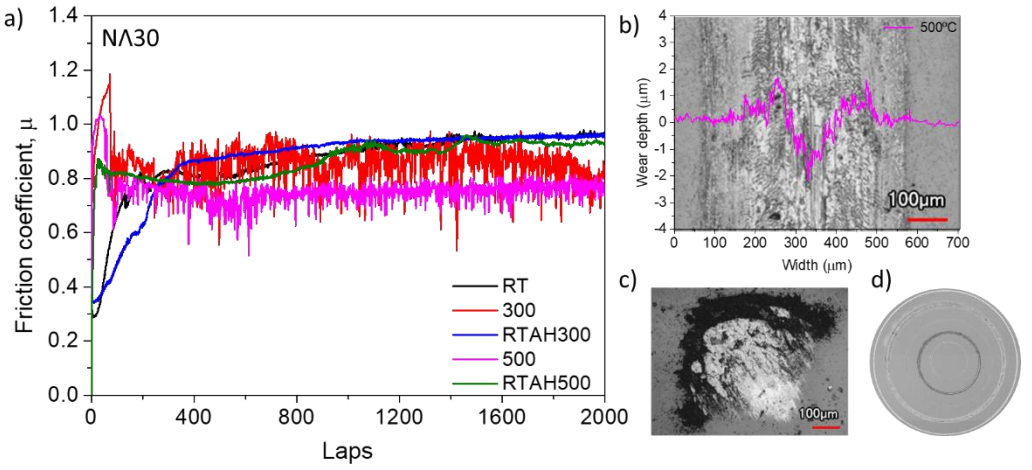

Figure 7.24: Tribological results for sample NΛ30. a) COF as a function of number of laps. b) Laser image of the wear track and surface profile after the ball-on-disk test. c) Laser image of the wear scar on ball counterpart for the test at 500ºC. d) Stitched image of the whole sample after the tribological tests. The wear tracks from the centre outwards are RT, 300ºC, RTAH300, 500ºC and RTAH500.

In Figure 7.24, Figure 7.25c and Table 7-2, results recorded for the NΛ30 sample are shown. Figure 7.24a displays representative friction curves for the tribological tests at different temperatures. All the tests performed at RT exhibit stable values of COF of around 0.8. In the high temperature tests delamination of the coating occurs denoting poor adhesion to the substrate after just a few laps. In the laser image and profile of the wear track at 500ºC Figure 7.24b) two distinguished regions can be observed. The first one in the external part of the wear track in where the ball slit on top of the coatings instead of wearing it. In the central part of the track, delamination of the coating occurred reaching the substrate. Figure 7.24d also shows this layer delamination for the high temperature tests in the form of discontinuities in the track. Despite the coating delamination in the region of the tribological test, the rest of the coating remains unaltered as proved for the tribological tests after heating up the sample. Even if high temperature wear rate values are given for the tests at high temperature, they cannot be reliable due to the coating delamination (Figure 7.25c). These values are still not as high as compared with the ones for just the unprotected substrate.

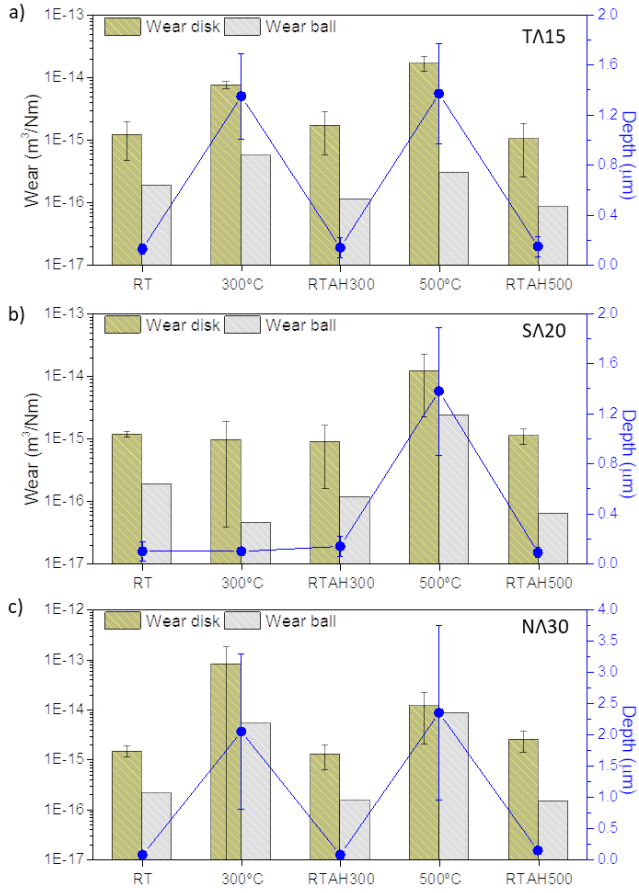

Figure 7.25: Calculated wear of the disk and the ball and the mean depth of the track as function of the temperature of the tribological tests. Results obtained for the TΛ15 (a), SΛ20 (b) and NΛ30 (c) coatings are shown.

Table 7-2: Values of the wear rate (ball and disk), COF and wear depth for the substrate, TΛ15, SΛ20 and NΛ30 coatings. Standard deviations are shown in the corresponding figures.

	Substrate				TΛ15				SΛ20				NΛ30			
	Wear (m^3/Nm)		COF	Depth (µm)	Wear (m^3/Nm)		COF	Depth (µm)	Wear (m^3/Nm)		COF	Depth (µm)	Wear (m^3/Nm)		COF	Depth (µm)
	Disk	Ball			Disk	Ball			Disk	Ball			Disk	Ball		
RT	$3.5x10^{-14}$	$1.9x10^{-15}$	1.05	1.55	$1.2x10^{-15}$	$1.9x10^{-16}$	0.92	0.13	$1.2x10^{-15}$	$1.9x10^{-16}$	0.85	0.10	$1.5x10^{-15}$	$2.1x10^{-16}$	0.86	0.08
300	$2.9x10^{-13}$	$1.2x10^{-14}$	0.80	5.23	$7.6x10^{-15}$	$5.7x10^{-16}$	0.88	1.35	$9.6x10^{-16}$	$4.5x10^{-17}$	1.04	0.12	$8.1x10^{-14}$	$5.3x10^{-15}$	0.85	2.05
RTAH300	$6.7x10^{-14}$	$1.9x10^{-14}$	1.00	2.21	$1.7x10^{-15}$	$1.1x10^{-16}$	0.81	0.14	$8.9x10^{-16}$	$1.2x10^{-16}$	0.87	0.14	$1.3x10^{-15}$	$1.5x10^{-16}$	0.87	0.08
500	$6.7x10^{-14}$	$2.1x10^{-13}$	0.77	7.3	$1.7x10^{-14}$	$3.0x10^{-16}$	0.43	1.37	$1.2x10^{-14}$	$2.4x10^{-15}$	0.78	1.38	$1.2x10^{-14}$	$8.7x10^{-15}$	0.75	2.35
RTAH500	$1.1x10^{-13}$	$3.4x10^{-15}$	0.98	2.7	$1.0x10^{-15}$	$8.6x10^{-17}$	0.71	0.15	$1.1x10^{-15}$	$6,4x10^{-17}$	0.79	0.09	$2.5x10^{-15}$	$1.5x10^{-16}$	0.86	0.15

7.3. Conclusions

TiN/CrN, TiSiN/CrN and NbN/CrN multilayer coatings with controlled bilayer periods between 125 and 5 nm have been successfully deposited using the HiPIMS technique in an industrial-scale deposition system. All coatings present a very smooth and compact structure in SEM images. XRD showed separate crystalline phases for the samples with high bilayer periods. However, as the bilayer period decreases, the crystalline peaks overlap, which would suggest epitaxial growth of the two crystalline phases. A superlattice structure is confirmed by satellite peaks around the main one by XRD analysis for TiN/CrN coatings with $\Lambda \leq 15$ nm. From the analysis of the TiSiN/CrN coatings by TEM and EELS, it could be deduced that Si is substitutionally incorporated into the TiN crystalline lattice without segregation of amorphous SiN_X phases. However, an epitaxial growth interrupted by more amorphous zones is observed, especially for the samples with smaller bilayer period.

All the coatings showed residual compressive stress varying between -1.1 and -2.6 GPa. TiN/CrN > NbN/CrN > TiSiN/CrN. High hardness values were recorded for all the coatings. For the TiN/CrN system, the highest value was 32 GPa while for TiSiN/CrN it was 28 GPa and for NbN/CrN it was 30 GPa. In all three systems, the highest hardness values were recorded for the sample with a Λ15 nm, which also exhibited a superlattice structure in the XRD analysis. All the coatings showed great substrate protection in the tribological tests, especially at room temperature.

CHAPTER 8

SUMMARY AND CONCLUSIONS

8. Summary and conclusions

Coatings consisting solely of one compound, commonly known as pure single-layer coatings, are extensively used in diverse engineering sectors. However, concerns about their performance limitations persist. Offering only a singular set of properties, they may lack the versatility needed to meet specific performance requirements. One major disadvantage of single-layer coatings is often their inability to withstand the severe conditions encountered in diverse industrial processes. As manufacturing methods grow increasingly complex due to the introduction of new materials, there's a pressing need to develop coatings capable of enduring these challenging conditions, such as nanocomposites or multi-layered coatings.

Nanostructured coatings, characterised by their fine-grained microstructure and tailored composition gradients, offer a paradigm shift in the enhancement of surface functionalities. Among the most advanced techniques, HiPIMS stands out as a crucial deposition method. HiPIMS takes advantage of high-power pulsed plasma to achieve superior control of growth kinetics, microstructure and coating composition. However, the migration of this technique from controlled laboratory environments to industrial-scale reactors presents a dynamic frontier in coatings manufacturing, which warrants further investigation.

This PhD thesis conducts a thorough investigation into nanostructured coatings, utilizing HiPIMS in an industrial-scale reactor. It delves into the complex relationship between process parameters, the evolution of microstructure, and the emergent material properties.

The most significant outcomes for each of these systems can be summarized below.

For the TiB_2/TiBC coatings, it was found that the C incorporation in the coating structure changes the fracture mechanism, increases the mechanical properties, and improves the adhesion to the substrate. Thus, a first insight into the potential of nanostructure modification was revealed.

Aiming to enhance the coatings' tribological properties and guided by earlier findings on the behavior of HiPIMS deposition parameters, a new system based on Nb-doped DLC coatings was developed. In this case, the influence of deposition parameters as well as carbon incorporation were compared between traditional DC-MS and the newest HiPIMS technique.

HiPIMS-deposited NbC/a-C(:H) coatings developed a considerably much more columnar structure in comparison with the dense and well-packed DC-MS coatings even having higher amount of a-C(:H) content. This didn't significantly improve mechanical or thermal properties. Both DC-MS and HiPIMS coatings exhibited protective tribological behavior with over 50 at.% carbon, emphasizing the need for compactness in film structure to enhance mechanical strength and oxidation resistance in Nb–C coatings. Using HiPIMS technology does not necessarily improve the film microstructure and functionality. Rather, the

plasma conditions must be optimized to select an appropriate ion bombardment (type, energy, and flux) to guarantee film densification.

After facing obstacles in depositing dense and non-columnar DLC composites in HiPIMS industrial-scale reactors, the emphasis was redirected towards nanostructured multilayer hard coatings. Given the need to fine-tune the HiPIMS parameters for achieving coatings with superior microstructural and mechanical qualities, the decision was made to opt for a simpler and more traditional systems like TiN and CrN, which have been thoroughly studied using arc-PVD and various other methods. Once the HiPIMS deposition parameters of these single-layer coatings were preliminary investigated, multilayer TiN/CrN HiPIMS systems were developed. The primary focus of the study was to determine how varying the bilayer period affects the properties of the nano/multilayered coatings, as well as to assess the influence of the bias potential applied during the HiPIMS deposition on the coatings' final properties.

The deposition time of individual layers was modified to yield bilayer periods ranging from 460 nm down to 7 nm. Coatings exhibited compact, smooth structures with low roughness values. X-ray diffraction showed separate TiN and CrN crystalline phases for coatings with $\Lambda \geq 85$ nm; as it decreased, epitaxial growth was confirmed. A superlattice structure comprising TiN and CrN sublayers was clear in for Λ15 coating. This sample also showed the highest hardness values of 32 GPa due to phenomena occurring in the nanoscale range.

Regarding bias application, DC-biased TiN/CrN coatings had denser, smoother structures compared to HiPIMS-biased ones. High ion-energy conditions promoted crystalline growth and reduced crystallite sizes. XRD revealed epitaxial growth as bilayer period decreased, with satellite peaks confirming a superlattice structure at a bilayer period of 15 nm. DC-biased coatings showed compressive stress, while HiPIMS-biased ones exhibited non or positive tensile stress. DC-biased coatings outperformed in hardness and young's modulus, reaching up to 32 GPa.

Synchronization of bias with HiPIMS cathode pulses resulted in columnar structures for all HiPIMS-biased coatings, with slightly denser structures for coatings deposited under the metal-ion rich region. Overall, DC bias led to enhanced coating properties due to increased adatom mobility and energy transfer to the coatings.

In the concluding chapter, the optimal HiPIMS deposition conditions identified over the course of this research were employed to create nano/multilayer coatings of varying chemical compositions. NbN/CrN coatings were selected for having great industrial potential in high-temperature sheet metal forming applications. TiSiN/CrN were selected to be an upgrade of the TiN/CrN coatings for the possibility of forming a complex nanocomposite and

multilayer coating by SiNx segregation phase into the TiN matrix in every single TiSiN single-layer of the multilayer coating.

Results show that all the multilayer coatings exhibited smooth and compact structures. XRD showed separate crystalline phases at high bilayer periods but overlapping peaks at lower periods, suggesting epitaxial growth and formation of superlattice structures. TEM and EELS analysis of TiSiN/CrN coatings revealed Si incorporation into the TiN lattice without SiN_X phase segregation, although epitaxial growth was interrupted by amorphous zones, especially at smaller bilayer periods. High hardness values around 30 GPa were obtained for all the coatings, showing a maximum at $\Lambda \sim 15$ nm.

In conclusion, this extensive research explored two distinct HiPIMS nanostructured coating systems deposited in industrial-scale reactors: one involving carbon introduction into DLC-like coatings, suited for low friction and low wear in tribological applications, and the other centred on multilayer hard ceramic coatings, where properties were significantly enhanced compared to monolayers. These findings contribute valuable insights into the potential and challenges of HiPIMS technology in industrial reactors tailoring advanced coatings to meet diverse industrial requirements.

Future work

The HiPIMS deposition parameters for NbC/a-C(:H) coatings should be optimised in order to get denser and more compact structures and thus improve their properties. A first approach could be carried out by applying the bias voltage in a continuous mode.

Nanostructured coatings developed in this thesis using HiPIMS technology could improve machining and manufacturing processes in different ways. TiN/CrN, TiSiN/CrN and NbN/CrN HiPIMS-deposited coatings are significantly hard and wear-resistant, which could lead to increased tool life and reduced downtime for maintenance. This could result, for example, in a tool life up to 5 times longer than conventional coatings in machining hardened steel, according to similar reported results. Industrial tests with a proper experimental design would be necessary to confirm the potential benefits of the developed coatings. The smooth surface finish obtained for the coatings in this work could also make them suitable for the protection of moulds and dies.

On the other hand, HiPIMS-deposited NbC/a-C(:H) DLC coatings have significant low coefficients of friction that could reduce friction and wear between moving parts, which can also lead to improved performance and reduced maintenance costs. Again, industrial field tests would be required to evaluate real implementation of the coatings.

All in all, despite the promising results obtained for the multilayer coatings developed during this thesis, the potential performance of some of them should be tested in real working conditions before these coatings can be commercialised.

Plasma diagnostics could aid in the development of new coatings. Knowing the species present in the plasma during the deposition stage of the coatings is of great importance to achieve coatings with the desired properties.

9. References

[1] J. Romano, L. Ladani, M. Sadowski, Thermal Modeling of Laser Based Additive Manufacturing Processes within Common Materials, Procedia Manuf. 1 (2015) 238–250. https://doi.org/10.1016/j.promfg.2015.09.012.

[2] I. Baran, K. Cinar, N. Ersoy, R. Akkerman, J.H. Hattel, A Review on the Mechanical Modeling of Composite Manufacturing Processes, Arch. Comput. Methods Eng. 24 (2017) 365–395. https://doi.org/10.1007/s11831-016-9167-2.

[3] R. Dach, J.J. Song, F. Roschangar, W. Samstag, C.H. Senanayake, The eight criteria defining a good chemical manufacturing process, Org. Process Res. Dev. 16 (2012) 1697–1706. https://doi.org/10.1021/op300144g.

[4] S. Heidrich, A. Richmann, P. Schmitz, E. Willenborg, K. Wissenbach, P. Loosen, R. Poprawe, Optics manufacturing by laser radiation, Opt. Lasers Eng. 59 (2014) 34–40. https://doi.org/10.1016/j.optlaseng.2014.03.001.

[5] T. Grünberg, A review of improvement methods in manufacturing operations, Work Study. 52 (2003) 89–93. https://doi.org/10.1108/00438020310462890.

[6] A. Giret, D. Trentesaux, V. Prabhu, Sustainability in manufacturing operations scheduling: A state of the art review, J. Manuf. Syst. 37 (2015) 126–140. https://doi.org/10.1016/j.jmsy.2015.08.002.

[7] D.A. Kunz, J. Schmid, P. Feicht, J. Erath, A. Fery, J. Breu, Clay-Based Nanocomposite Coating for Flexible Optoelectronics Applying Commercial Polymers, ACS Nano. 7 (2013) 4275–4280. https://doi.org/10.1021/nn400713e.

[8] N. Ledermann, J. Baborowski, P. Muralt, N. Xantopoulos, J.-M. Tellenbach, Sputtered silicon carbide thin films as protective coating for MEMS applications, Surf. Coatings Technol. 125 (2000) 246–250. https://doi.org/https://doi.org/10.1016/S0257-8972(99)00568-X.

[9] T. Hantschel, A. Schulze, U. Celano, A. Moussa, K. Arstila, P. Eyben, B. Majeed, D.S. Tezcan, T. Werner, W. Vandervorst, TiN scanning probes for electrical profiling of nanoelectronics device structures, Microelectron. Eng. 97 (2012) 255–258. https://doi.org/https://doi.org/10.1016/j.mee.2012.04.026.

[10] R. Braak, U. May, L. Onuseit, G. Repphun, M. Guenther, C. Schmid, K. Durst, Accelerated thermal degradation of DLC-coatings via growth defects, Surf. Coatings Technol. 349 (2018) 272–278. https://doi.org/https://doi.org/10.1016/j.surfcoat.2018.05.063.

[11] M. He, C. Yeo, Evaluation of thermal degradation of DLC film using a novel Raman spectroscopy technique, Coatings. 8 (2018) 1–10. https://doi.org/10.3390/coatings8040143.

[12] Y. Wang, Application of ceramic thermal spray coatings for molten metal handling tools and moulds, Surf. Eng. 15 (1999) 205–209. https://doi.org/10.1179/026708499101516524.

[13] O. Knotek, F. Löffler, B. Bosserhoff, PVD coatings for diecasting moulds, Surf. Coatings Technol. 62 (1993) 630–634. https://doi.org/https://doi.org/10.1016/0257-8972(93)90310-K.

[14] M. Holtzer, A. Bobrowski, D. Drożyński, J. Mocek, Selection of Protective Coatings of Moulds for Castings of High-Manganese Cast Steel in Dependence of the Applied Moulding Sand Kind, Arch. Metall. Mater. 58 (2013) 853–857. https://doi.org/10.2478/amm-2013-0086.

[15] P. Steyer, S. Anderbouhr, P. Jacquot, Effect of Ni Interlayer on Corrosion Behaviour of Crn Pvd Coating Deposited onto Plastic Mould Steels, Surf. Eng. 17 (2001) 327–331. https://doi.org/10.1179/026708401101517962.

[16] B. Navinšek, P. Panjan, I. Milošev, Industrial applications of CrN (PVD) coatings, deposited at high and low temperatures, Surf. Coatings Technol. 97 (1997) 182–191. https://doi.org/https://doi.org/10.1016/S0257-8972(97)00393-9.

[17] M.A. Alipovna, K.A. Karaulovich, P.A. Vladimirovich, A.Z. Zhanuzakovich, K.B. Bolatovna, W. Wieleba, T. Leśniewski, N. Bakhytuly, The study of the tribological properties under high contact pressure conditions of TiN, TiC and TiCN coatings deposited by the magnetron sputtering method on the AISI 304 stainless steel substrate, Mater. Sci. 41 (2023) 1–14. https://doi.org/doi:10.2478/msp-2022-0055.

[18] M. Pfeifer, Manufacturing Process Considerations, Mater. Enabled Des. (2009) 115–160. https://doi.org/10.1016/b978-0-7506-8287-9.00005-7.

[19] A.L.O. Zaid, Blanking and piercing theory, applications and recent experimental results, IOP Conf. Ser. Mater. Sci. Eng. 60 (2014). https://doi.org/10.1088/1757-899X/60/1/012065.

[20] C.F. Noble, P.L.B. Oxley, Crack formation in blanking and piercing, Int. J. Prod. Res. 2 (1963) 265–274. https://doi.org/10.1080/00207546308947830.

[21] M. Murakawa, M. Suzuki, T. Shionome, F. Komuro, A. Harai, A. Matsumoto, N. Koga, Precision piercing and blanking of ultrahigh-strength steel sheets, Procedia Eng. 81 (2014) 1114–1120. https://doi.org/10.1016/j.proeng.2014.10.219.

[22] O.M. Ikumapayi, E.T. Akinlabi, N. Madushele, S.O. Fatoba, A brief overview of bending operation in sheet metal forming, Lect. Notes Mech. Eng. (2020) 149–159. https://doi.org/10.1007/978-981-15-5753-8_14/COVER.

[23] S.B. Chikalthankar, G.D. Belurkar, V.M. Nandedkar, Factors Affecting on Springback in Sheet Metal Bending : A Review, Int. J. Eng. Adv. Technol. 3 (2014) 247–251.

[24] H. Karbasian, A.E. Tekkaya, A review on hot stamping, J. Mater. Process. Technol. 210 (2010) 2103–2118. https://doi.org/10.1016/j.jmatprotec.2010.07.019.

[25] Y. Lim, R. Venugopal, A.G. Ulsoy, Process Control for Sheet-Metal Stamping, Springer London, London, 2014. https://doi.org/10.1007/978-1-4471-6284-1.

[26] J. A. Schey, Tribology in Metalworking: Friction, lubrication and wear, 1983. https://www.worldcat.org/es/title/tribology-in-metalworking-friction-lubrication-and-wear/oclc/472157575 (accessed October 11, 2022).

[27] S.Y. Luo, Effect of the geometry and the surface treatment of punching tools on the tool life and wear conditions in the piercing of thick steel plate, J. Mater. Process. Technol. 88 (1999) 122–133. https://doi.org/10.1016/S0924-0136(98)00375-6.

[28] P. Tröber, H.A. Weiss, T. Kopp, R. Golle, W. Volk, On the correlation between thermoelectricity and adhesive tool wear during blanking of aluminum sheets, Int. J. Mach. Tools Manuf. 118–119 (2017) 91–97. https://doi.org/10.1016/j.ijmachtools.2017.03.005.

[29] J.J. Hernández, P. Franco, M. Estrems, F. Faura, Modelling and experimental analysis of the effects of tool wear on form errors in stainless steel blanking, J. Mater. Process. Technol. 180 (2006) 143–150. https://doi.org/10.1016/j.jmatprotec.2006.05.015.

[30] M. Lindgren, U. Bexell, L. Wikström, Roll forming of partially heated cold rolled stainless steel, J. Mater. Process. Technol. 209 (2009) 3117–3124. https://doi.org/10.1016/j.jmatprotec.2008.07.041.

[31] K. Mori, P.F. Bariani, B.A. Behrens, A. Brosius, S. Bruschi, T. Maeno, M. Merklein, J. Yanagimoto, Hot stamping of ultra-high strength steel parts, CIRP Ann. - Manuf. Technol. 66 (2017) 755–777. https://doi.org/10.1016/j.cirp.2017.05.007.

[32] H. Hoffmann, H. So, H. Steinbeiss, Design of hot stamping tools with cooling system, CIRP Ann. - Manuf. Technol. 56 (2007) 269–272. https://doi.org/10.1016/j.cirp.2007.05.062.

[33] M. Ohring, Materials Processing and Forming Operations, Eng. Mater. Sci. (1995) 371–IX. https://doi.org/10.1016/b978-012524995-9/50032-5.

[34] K. Olsson, S.S. Steel, P.J. Sperle, S. Consulting, New Advanced Ultra-High Strength, (2006) 46–49.

[35] N. Bay, D.D. Olsson, J.L. Andreasen, Lubricant test methods for sheet metal forming, Tribol. Int. 41 (2008) 844–853. https://doi.org/10.1016/j.triboint.2007.11.017.

[36] R. Sousa, Incremental Sheet Forming Technologies, Ref. Modul. Mater. Sci. Mater. Eng. 1 (2016) 1–10. https://doi.org/10.1016/b978-0-12-803581-8.04055-8.

[37] N. Bay, A. Azushima, P. Groche, I. Ishibashi, M. Merklein, M. Morishita, T. Nakamura, S. Schmid, M. Yoshida, Environmentally benign tribo-systems for metal forming, CIRP Ann. - Manuf. Technol. 59 (2010) 760–780. https://doi.org/10.1016/j.cirp.2010.05.007.

[38] C. Escher, T. Henke, New Trends in Thin Coatings for Sheet-Metal Forming Tools, 6th Int. Tool. Conferece - Vol. II. (2002) 771–784.

[39] B. Podgornik, V. Leskovšek, Wear mechanisms and surface engineering of forming tools, Mater. Tehnol. 49 (2015) 313–324. https://doi.org/10.17222/mit.2015.005.

[40] B. Podgornik, B. Zajec, N. Bay, J. Vižintin, Application of hard coatings for blanking and piercing tools, Wear. 270 (2011) 850–856. https://doi.org/10.1016/j.wear.2011.02.013.

[41] E. Lugscheider, K. Bobzin, C. Pinero, F. Klocke, T. Massmann, Development of a superlattice (Ti,Hf,Cr)N coating for cold metal forming applications, Surf. Coatings Technol. 177–178 (2004) 616–622. https://doi.org/10.1016/S0257-8972(03)00935-6.

[42] F. Sergejev, P. Peetsalu, A. Sivitski, M. Saarna, E. Adoberg, Surface fatigue and wear of PVD coated punches during fine blanking operation, Eng. Fail. Anal. 18 (2011) 1689–1697. https://doi.org/10.1016/j.engfailanal.2011.02.011.

[43] J. Daniel, R. Žemlička, J. Grossman, A. Lümkemann, P. Tapp, C. Galamand, T. Fořt, Comparison of lifetime of the PVD coatings in laboratory dynamic impact test and industrial fine blanking process, Materials (Basel). 13 (2020) 1–11. https://doi.org/10.3390/ma13092154.

[44] S. Ebnesajjad, PART II 7 Injection Molding, Melt Process. Fluoroplastics. (2003) 151–193.

[45] J.P. Greene, Injection Molding, in: Automot. Plast. Compos., William Andrew

Publishing, 2021: pp. 241–254. https://doi.org/10.1016/B978-0-12-818008-2.00019-2.

[46] M.P. Groover, Fundamentals of modern manufacturing Materials, Processes and Systems, 2010.

[47] D.V. Rosato, Marlene G. Rosato, Injection Molding Handbook , 3rd ed., 2000. https://books.google.es/books?hl=es&lr=&id=4VHxBwAAQBAJ&oi=fnd&pg=PR29&dq=related:iWpxiJL_9oQJ:scholar.google.com/&ots=5JxWbnsx6K&sig=sEJ_dsNuBXLHWQ9CbGiCjoOD3eU&redir_esc=y#v=onepage&q&f=false (accessed October 11, 2022).

[48] J. Bergstrom, F. Thuvander, P. Devos, C. Boher, Wear of die materials in full scale plastic injection moulding of glass fibre reinforced polycarbonate, Wear. 250 (2001) 1511–1521. https://doi.org/10.1016/S0043-1648(01)00787-6.

[49] J. Samei, H. Asgari, C. Pelligra, M. Sanjari, S. Salavati, A. Shahriari, M. Amirmaleki, M. Jahanbakht, A. Hadadzadeh, B.S. Amirkhiz, M. Mohammadi, A hybrid additively manufactured martensitic-maraging stainless steel with superior strength and corrosion resistance for plastic injection molding dies, Addit. Manuf. 45 (2021) 102068. https://doi.org/10.1016/j.addma.2021.102068.

[50] M.C. Carrupt, A.P. Piedade, Modification of the Cavity of Plastic Injection Molds : A Brief Review of Materials and Influence on the Cooling Rates, (2021).

[51] T. Sasaki, N. Koga, K. Shirai, Y. Kobayashi, A. Toyoshima, An experimental study on ejection forces of injection molding, 24 (2000) 270–273.

[52] F.J.G. Silva, R.P. Martinho, R.J.D. Alexandre, A.P.M. Baptista, Increasing the wear resistance of molds for injection of glass fiber reinforced plastics, Wear. 271 (2011) 2494–2499. https://doi.org/10.1016/j.wear.2011.01.074.

[53] L. Cunha, M. Andritschky, K. Pischow, Z. Wang, A. Zarychta, A.S. Miranda, A.M. Cunha, Performance of chromium nitride and titanium nitride coatings during plastic injection moulding, 153 (2002) 160–165.

[54] A. Aytaç, U. Malayoğlu, Comparison of PVD and JVD / DVD Thin Film Coatings by Physical Vapor Deposition Methods and a Conceptual, Academic and Theoretical Analysis on Industrial Applications of DVD Coating Technology, J. Def. Sci. 17 (2018).

[55] P. Mathew, J. George, T.S. Mathews, P.J. Kurian, Experimental verification of modified Paschen's law in DC glow discharge argon plasma, AIP Adv. 9 (2019). https://doi.org/10.1063/1.5086246.

[56] C. Torres, G. Reyes, F. Castillo, H. Martínez, Paschen law for argon glow discharge, J. Phys. Conf. Ser. 370 (2012) 3–7. https://doi.org/10.1088/1742-6596/370/1/012067.

[57] P.S. Sidky, M.G. Hocking, Review of inorganic coatings and coating processes for reducing wear and corrosion, Br. Corros. J. 34 (1999) 171–183. https://doi.org/10.1179/000705999101500815.

[58] D.M. Mattox, Physical Sputtering and Sputter Deposition (Sputtering), 2010. https://doi.org/10.1016/b978-0-8155-2037-5.00007-1.

[59] A. Baptista, F. Silva, J. Porteiro, J. Míguez, G. Pinto, Sputtering physical vapour deposition (PVD) coatings: A critical review on process improvement andmarket trend demands, Coatings. 8 (2018). https://doi.org/10.3390/COATINGS8110402.

[60] ALCA technology, Magnetron Sputtering: Types of coating processes and

Advantages, (n.d.). https://www.alcatechnology.com/en/blog/magnetron-sputtering/ (accessed October 4, 2022).

[61] K. Wasa, I. Kanno, H. Kotera, Handbook of Sputter Deposition Technology: Fundamentals and Applications for Functional Thin Films, Nano-Materials and MEMS: Second Edition, Elsevier Inc., 2012. https://doi.org/10.1016/C2010-0-67037-4.

[62] FHR Thin film Technology, Magnetron sputtering & magnetron sputtering deposition | FHR Thin film technology, (n.d.). https://www.fhr.biz/en/thin-film-technology/sputtering-technology/magnetron-sputtering/ (accessed October 4, 2022).

[63] D. Depla, S. Mahieu, J.E. Greene, Sputter Deposition Processes, Third Edit, Elsevier Ltd., 2009. https://doi.org/10.1016/B978-0-8155-2031-3.00005-3.

[64] D.A. Glocker, S. Ismat Shah, Handbook of thin film process technology: 98/1 reactive sputtering, Handb. Thin Film Process Technol. 98/1 React. Sputtering. (2018) 1–90. https://doi.org/10.1201/9781351072786.

[65] C. Christou, Z.H. Barber, Ionization of sputtered material in a planar magnetron discharge, J. Vac. Sci. Technol. A Vacuum, Surfaces, Film. 18 (2000) 2897–2907. https://doi.org/10.1116/1.1312370.

[66] Y. Lifshitz, S.R. Kasi, J.W. Rabalais, Snbplantation Model for Film Growth From Hyperthermal Species: Application to Diamond, Phys. Rev. Lett. 62 (1989) 1290–1293.

[67] G.C.A.M. Janssen, J.D. Kamminga, Stress in hard metal films, Appl. Phys. Lett. 85 (2004) 3086–3088. https://doi.org/10.1063/1.1807016.

[68] C.A. Davis, A simple model for the formation of compressive stress in thin films by ion bombardment, Thin Solid Films. 226 (1993) 30–34. https://doi.org/10.1016/0040-6090(93)90201-Y.

[69] S. Berg, T. Nyberg, T. Kubart, Modelling of Reactive Sputtering Processes, Springer Ser. Mater. Sci. 109 (2008) 131–152. https://doi.org/10.1007/978-3-540-76664-3_4.

[70] D.M. Mattox, The Low Pressure Plasma Processing Environment, 2010. https://doi.org/10.1016/b978-0-8155-2037-5.00005-8.

[71] H. Hotop, 11. Detection of Metastable Atoms and Molecules, Exp. Methods Phys. Sci. 29 (1996) 191–215. https://doi.org/10.1016/S0076-695X(08)60793-0.

[72] S. Berg, T. Nyberg, Fundamental understanding and modeling of reactive sputtering processes, Thin Solid Films. 476 (2005) 215–230. https://doi.org/10.1016/j.tsf.2004.10.051.

[73] D. Depla, R. De Gryse, Target poisoning during reactive magnetron sputtering: Part I: The influence of ion implantation, Surf. Coatings Technol. 183 (2004) 184–189. https://doi.org/10.1016/j.surfcoat.2003.10.006.

[74] A. Anders, Tutorial: Reactive high power impulse magnetron sputtering (R-HiPIMS), J. Appl. Phys. 121 (2017). https://doi.org/10.1063/1.4978350.

[75] L. Zauner, P. Ertelthaler, T. Wojcik, H. Bolvardi, S. Kolozsvári, P.H. Mayrhofer, H. Riedl, Reactive HiPIMS deposition of Ti-Al-N: Influence of the deposition parameters on the cubic to hexagonal phase transition, Surf. Coatings Technol. 382 (2020) 125007. https://doi.org/10.1016/j.surfcoat.2019.125007.

[76] M. Fakete, P. Bernaátová, P. Klein, J. Hnilica, P. Vasina, Evolution of discharge

parameters and sputtered species ionization in reactive HiPIMS with oxygen, nitrogen and acetylene, Plasma Sources Sci. Technol. 28 (2019) 11–25. https://doi.org/https://doi.org/10.1088/1361-6595/ab0363.

[77] J.T. Gudmundsson, N. Brenning, D. Lundin, U. Helmersson, High power impulse magnetron sputtering discharge, J. Vac. Sci. Technol. A. 30 (2012) 030801. https://doi.org/10.1116/1.3691832.

[78] M. Hala, J. Capek, O. Zabeida, J.E. Klemberg-Sapieha, L. Martinu, Hysteresis-free deposition of niobium oxide films by HiPIMS using different pulse management strategies, J. Phys. D. Appl. Phys. 45 (2012). https://doi.org/10.1088/0022-3727/45/5/055204.

[79] K. Sarakinos, J. Alami, C. Klever, M. Wuttig, Process stabilization and enhancement of deposition rate during reactive high power pulsed magnetron sputtering of zirconium oxide, Surf. Coatings Technol. 202 (2008) 5033–5035. https://doi.org/10.1016/j.surfcoat.2008.05.009.

[80] K. Sarakinos, J. Alami, S. Konstantinidis, High power pulsed magnetron sputtering: A review on scientific and engineering state of the art, Surf. Coatings Technol. 204 (2010) 1661–1684. https://doi.org/10.1016/j.surfcoat.2009.11.013.

[81] D. Depla, R. De Gryse, Cross section for removing chemisorbed oxygen from an aluminum target by sputtering, J. Vac. Sci. Technol. A Vacuum, Surfaces, Film. 20 (2002) 521–525. https://doi.org/10.1116/1.1451254.

[82] A.P. Ehiasarian, A. Vetushka, Y.A. Gonzalvo, G. Sfrn, L. Székely, P.B. Barna, Influence of high power impulse magnetron sputtering plasma ionization on the microstructure of TiN thin films, J. Appl. Phys. 109 (2011) 104314. https://doi.org/10.1063/1.3579443.

[83] F. Ferreira, J.C. Oliveira, A. Cavaleiro, CrN thin films deposited by HiPIMS in DOMS mode, Surf. Coatings Technol. 291 (2016) 365–375. https://doi.org/10.1016/j.surfcoat.2016.02.064.

[84] J. Weichart, M. Lechthaler, Titanium aluminum nitride sputtered by HIPIMS, IOP Conf. Ser. Mater. Sci. Eng. 39 (2012). https://doi.org/10.1088/1757-899X/39/1/012001.

[85] M. Colasuonno, T.C.C. Rojas, A. Patelli, S. Dominguez-Meister, M. Bazzan, J.C.C. Sánchez-López, S. Dominguez-Meister, T.C.C. Rojas, M. Colasuonno, M. Bazzan, A. Patelli, Tribological properties of TiC/a-C:H nanocomposite coatings prepared via HiPIMS, Appl. Surf. Sci. 440 (2018) 458–466. https://doi.org/10.1016/j.apsusc.2018.01.135.

[86] G. Gassner, P.H. Mayrhofer, J. Patscheider, C. Mitterer, Thermal stability of nanocomposite CrC/a-C:H thin films, Thin Solid Films. 515 (2007) 5411–5417. https://doi.org/10.1016/j.tsf.2006.12.149.

[87] A. Anders, High power impulse magnetron sputtering and related discharges: Scalable plasma sources for plasma-based ion implantation and deposition, Surf. Coatings Technol. 204 (2010) 2864–2868. https://doi.org/10.1016/j.surfcoat.2010.01.047.

[88] J. Bohlmark, J. Alami, C. Christou, A.P. Ehiasarian, U. Helmersson, Ionization of sputtered metals in high power pulsed magnetron sputtering, J. Vac. Sci. Technol. A Vacuum, Surfaces, Film. 23 (2005) 18–22. https://doi.org/10.1116/1.1818135.

[89] K. Macák, V. Kouznetsov, J. Schneider, U. Helmersson, I. Petrov, Ionized sputter

deposition using an extremely high plasma density pulsed magnetron discharge, J. Vac. Sci. Technol. A Vacuum, Surfaces, Film. 18 (2000) 1533–1537. https://doi.org/10.1116/1.582380.

[90] A. Hecimovic, A.P. Ehiasarian, Spatial and temporal evolution of ion energies in high power impulse magnetron sputtering plasma discharge, J. Appl. Phys. 108 (2010) 3–11. https://doi.org/10.1063/1.3486018.

[91] A. Anders, A review comparing cathodic arcs and high power impulse magnetron sputtering (HiPIMS), Surf. Coatings Technol. 257 (2014) 308–325. https://doi.org/10.1016/j.surfcoat.2014.08.043.

[92] V. Kouznetsov, K. Macák, J.M. Schneider, U. Helmersson, I. Petrov, A novel pulsed magnetron sputter technique utilizing very high target power densities, Surf. Coatings Technol. 122 (1999) 290–293. https://doi.org/10.1016/S0257-8972(99)00292-3.

[93] U. Helmersson, M. Lattemann, J. Bohlmark, A.P. Ehiasarian, J.T. Gudmundsson, Ionized physical vapor deposition (IPVD): A review of technology and applications, Thin Solid Films. 513 (2006) 1–24. https://doi.org/10.1016/j.tsf.2006.03.033.

[94] D.J. Christie, Target material pathways model for high power pulsed magnetron sputtering, J. Vac. Sci. Technol. A Vacuum, Surfaces, Film. 23 (2005) 330–335. https://doi.org/10.1116/1.1865133.

[95] J. Bohlmark, M. Östbye, M. Lattemann, H. Ljungcrantz, T. Rosell, U. Helmersson, Guiding the deposition flux in an ionized magnetron discharge, Thin Solid Films. 515 (2006) 1928–1931. https://doi.org/10.1016/j.tsf.2006.07.183.

[96] J. Emmerlich, S. Mráz, R. Snyders, K. Jiang, J.M. Schneider, The physical reason for the apparently low deposition rate during high-power pulsed magnetron sputtering, Vacuum. 82 (2008) 867–870. https://doi.org/10.1016/j.vacuum.2007.10.011.

[97] G. Greczynski, J. Lu, M.P. Johansson, J. Jensen, I. Petrov, J.E. Greene, L. Hultman, Role of Ti n+ and Al n+ ion irradiation (n=1, 2) during Ti 1-xAl xN alloy film growth in a hybrid HIPIMS/magnetron mode, Surf. Coatings Technol. 206 (2012) 4202–4211. https://doi.org/10.1016/j.surfcoat.2012.04.024.

[98] M. Harsdorff, Heterogeneous nucleation and growth of thin films, Thin Solid Films. 90 (1982) 1–14. https://doi.org/10.1016/0040-6090(82)90061-X.

[99] P.B. Barna, M. Adamik, Fundamental structure forming phenomena of polycrystalline films and the structure zone models, Thin Solid Films. 317 (1998) 27–33. https://doi.org/10.1016/S0040-6090(97)00503-8.

[100] Norbert Kaiser, Review of the fundamentals of thin-film growth, Appl. Opt. 41 (2002) 3053–3060. http://linkinghub.elsevier.com/retrieve/pii/B9780408013505500088.

[101] I. Markov, R. Kaischew, Influence of the supersaturation on the mode of thin film growth, Krist. Und Tech. 11 (1976) 685–697. https://doi.org/10.1002/crat.19760110702.

[102] J.A. Thornton, Influence of Apparatus Geometry and Deposition Conditions on the Structure and Topography of Thick Sputtered Coatings., J Vac Sci Technol. 11 (1974) 666–670. https://doi.org/10.1116/1.1312732.

[103] D.M. Mattox, Handbook of Physical Vapor Deposition (PVD) Processing, Elsevier Inc., 2010.

[104] A.K. Krella, Degradation of protective PVD coatings, in: Handb. Mater. Fail. Anal. with Case Stud. from Chem. Concr. Power Ind., Elsevier Ltd., 2016: pp. 411–440. https://doi.org/10.1016/B978-0-08-100116-5.00016-8.

[105] A. Anders, A structure zone diagram including plasma-based deposition and ion etching, Thin Solid Films. 518 (2010) 4087–4090. https://doi.org/10.1016/j.tsf.2009.10.145.

[106] D. Manova, J.W. Gerlach, S. Mändl, Thin film deposition using energetic ions, Materials (Basel). 3 (2010) 4109–4141. https://doi.org/10.3390/ma3084109.

[107] Y. Moritz, C. Kainz, M. Tkadletz, C. Czettl, M. Pohler, N. Schalk, Microstructure and mechanical properties of arc evaporated Ti(Al,Si)N coatings, Surf. Coatings Technol. 421 (2021) 127461. https://doi.org/10.1016/j.surfcoat.2021.127461.

[108] J.C. Sánchez-López, D. Martínez-Martínez, M.D. Abad, A. Fernández, Metal carbide/amorphous C-based nanocomposite coatings for tribological applications, Surf. Coatings Technol. 204 (2009) 947–954. https://doi.org/10.1016/j.surfcoat.2009.05.038.

[109] H. Randhawa, Hard coatings for decorative applications, Surf. Coatings Technol. 36 (1988) 829–836.

[110] H. Caliskan, P. Panjan, C. Kurbanoglu, Hard Coatings on Cutting Tools and Surface Finish, Elsevier Ltd., 2017. https://doi.org/10.1016/B978-0-12-803581-8.09178-5.

[111] R. Dumpala, M. Chandran, M.S. Ramachandra Rao, Engineered CVD Diamond Coatings for Machining and Tribological Applications, Jom. 67 (2015) 1565–1577. https://doi.org/10.1007/s11837-015-1428-2.

[112] A. Wang, D.C. Sun, C. Stark, J.H. Dumbleton, Wear mechanisms of UHMWPE in total joint replacements, Wear. 181–183 (1995) 241–249. https://doi.org/10.1016/0043-1648(94)07027-X.

[113] N. Nedfors, A. Mockute, J. Palisaitis, P.O.Å. Persson, L.Å. Näslund, J. Rosen, Influence of pulse frequency and bias on microstructure and mechanical properties of TiB2 coatings deposited by high power impulse magnetron sputtering, Surf. Coatings Technol. 304 (2016) 203–210. https://doi.org/10.1016/j.surfcoat.2016.06.086.

[114] F.J.G. Silva, R.C.B. Casais, R.P. Martinho, A.P.M. Baptista, Mechanical and tribological characterization of TiB2 thin films, J. Nanosci. Nanotechnol. 12 (2012) 9187–9194. https://doi.org/10.1166/jnn.2012.6759.

[115] N. Sala, M.D. Abad, J.C. Sánchez-López, M. Cruz, J. Caro, C. Colominas, Tribological performance of Nb-C thin films prepared by DC and HiPIMS, Mater. Lett. 277 (2020) 128334. https://doi.org/10.1016/j.matlet.2020.128334.

[116] N. Gupta, S.K. Singh, S.M. Pandey, Tribological characterisation of thermal sprayed CrC alloyed coating–A review, Adv. Mater. Process. Technol. 00 (2020) 1–24. https://doi.org/10.1080/2374068X.2020.1793262.

[117] M.A. Baker, R. Gilmore, C. Lenardi, P.N. Gibson, W. Gissler, Microstructure and mechanical properties of multilayer TiB_2/C and co-sputtered TiB_2-C coatings for cutting tools, Vacuum. 53 (1999) 113–116. https://doi.org/10.1016/S0042-207X(98)00404-7.

[118] L. Wang, J. Jin, C. Zhu, G. Li, X. Kuang, K. Huang, Effects of HiPIMS pulse-length on plasma discharge and on the properties of WC-DLC coatings, Appl. Surf. Sci. 487 (2019) 526–538. https://doi.org/10.1016/j.apsusc.2019.05.046.

[119] J. Lin, X. Zhang, F. Ge, F. Huang, Thick CrN/AlN superlattice coatings deposited by hot filament assisted HiPIMS for solid particle erosion and high temperature wear resistance, Surf. Coatings Technol. 377 (2019) 124922. https://doi.org/10.1016/j.surfcoat.2019.124922.

[120] J.S. Koehler, Attempt to Design a Strong Solid, Phys. Rev. B. 2 (1970) 547–551. https://doi.org/10.1103/physrevb.2.547.

[121] R.W. Springer, D.S. Catlett, Structure and mechanical properties of Al/AlxOy vacuum-deposited laminates, Thin Solid Films. 54 (1978) 197–205. https://doi.org/10.1016/0040-6090(78)90199-2.

[122] S.L. Lehoczky, Strength enhancement in thin-layered Al-Cu laminates, J. Appl. Phys. 49 (1978) 5479–5485. https://doi.org/10.1063/1.324518.

[123] P.M. Anderson, C. Li, Hall-Petch relations for multilayered materials, Nanostructured Mater. 5 (1995) 349–362. https://doi.org/10.1016/0965-9773(95)00250-I.

[124] R. Hahn, M. Bartosik, R. Soler, C. Kirchlechner, G. Dehm, P.H. Mayrhofer, Superlattice effect for enhanced fracture toughness of hard coatings, Scr. Mater. 124 (2016) 67–70. https://doi.org/10.1016/j.scriptamat.2016.06.030.

[125] Y.Y. Chang, D.Y. Wang, C.Y. Hung, Structural and mechanical properties of nanolayered TiAlN/CrN coatings synthesized by a cathodic arc deposition process, Surf. Coatings Technol. 200 (2005) 1702–1708. https://doi.org/10.1016/j.surfcoat.2005.08.088.

[126] N.J. Petch, The orientation relationships between cementite and α-iron, Acta Crystallogr. 6 (1953) 96–96. https://doi.org/10.1107/s0365110x53000260.

[127] E. O. Hall, The deformation and ageing of mild steel: III discussion of results, Proc. Phys. Soc. Sect. B. 64 (1951) 747–753. http://iopscience.iop.org/0370-1301/64/9/303.

[128] H. Holleck, V. Schier, Multilayer PVD coatings for wear protection, Surf. Coatings Technol. 76–77 (1995) 328–336. https://doi.org/10.1016/0257-8972(95)02555-3.

[129] P. Wiecinski, J. Smolik, H. Garbacz, J. Bonarski, A. Mazurkiewicz, K.J. Kurzydłowski, Microstructure and properties of metal/ceramic and ceramic/ceramic multilayer coatings on titanium alloy Ti6Al4V, Surf. Coatings Technol. 309 (2017) 709–718. https://doi.org/10.1016/j.surfcoat.2016.11.003.

[130] L. Bathini, M.J.N.V. Prasad, N.P. Wasekar, Compositionally modulated Ni-W multilayer coatings: A facile approach to enhance the tribological performance, Tribol. Int. 179 (2023) 108145. https://doi.org/https://doi.org/10.1016/j.triboint.2022.108145.

[131] M. Anand, G. Burmistroviene, I. Tudela, R. Verbickas, G. Lowman, Y. Zhang, Tribological evaluation of soft metallic multilayer coatings for wear applications based on a multiple pass scratch test method, Wear. 388–389 (2017) 39–46. https://doi.org/10.1016/j.wear.2017.01.119.

[132] S. Shetty, M.M. Jaffer Sadiq, D.K. Bhat, A.C. Hegde, Development of multilayer Sn-Ni alloy coating by pulsed sonoelectrolysis for enhanced corrosion protection, RSC Adv. 6 (2016) 77465–77473. https://doi.org/10.1039/c6ra13302a.

[133] M.R. Stoudt, R.E. Ricker, R.C. Cammarata, The influence of a multilayered metallic coating on fatigue crack nucleation, Int. J. Fatigue. 23 (2001) 215–223. https://doi.org/10.1016/s0142-1123(01)00153-0.

[134] K.L. Hwu, B. Derby, Fracture of metal/ceramic laminates - II. Crack growth resistance and toughness, Acta Mater. 47 (1999) 545–563. https://doi.org/10.1016/S1359-6454(98)00358-9.

[135] P. Wieciński, J. Smolik, H. Garbacz, K.J. Kurzydłowski, Failure and deformation mechanisms during indentation in nanostructured Cr/CrN multilayer coatings, Surf. Coatings Technol. 240 (2014) 23–31. https://doi.org/10.1016/j.surfcoat.2013.12.006.

[136] Y.H. Cheng, T. Browne, B. Heckerman, C. Bowman, V. Gorokhovsky, E.I. Meletis, Mechanical and tribological properties of TiN/Ti multilayer coating, Surf. Coatings Technol. 205 (2010) 146–151. https://doi.org/10.1016/j.surfcoat.2010.06.023.

[137] Q. Jin, H. Wang, G. Li, J. Zhang, J. Liu, Microstructures and Mechanical Properties of TiN/CrN Multilayer Films, Rare Met. Mater. Eng. 46 (2017) 2857–2862. https://doi.org/10.1016/s1875-5372(18)30020-1.

[138] B. Biswas, Y. Purandare, I. Khan, P.E. Hovsepian, Effect of substrate bias voltage on defect generation and their influence on corrosion and tribological properties of HIPIMS deposited CrN/NbN coatings, Surf. Coatings Technol. 344 (2018) 383–393. https://doi.org/10.1016/j.surfcoat.2018.03.009.

[139] F. Frank, C. Kainz, M. Tkadletz, C. Czettl, M. Pohler, N. Schalk, Microstructural and micro-mechanical investigation of cathodic arc evaporated ZrN/TiN multilayer coatings with varying bilayer thickness, Surf. Coatings Technol. 432 (2022) 128070. https://doi.org/10.1016/j.surfcoat.2021.128070.

[140] C. Calebrese, L. Hui, L. Schadler, J. Nelson, A Review on the Importance of Nanocomposite Processing to Enhance Electrical Insulation, IEEE Trans. Dielectr. Electr. Insul. - IEEE TRANS DIELECT ELECTR. 18 (2011) 938–945. https://doi.org/10.1109/TDEI.2011.5976079.

[141] A. Iqbal, A. Saeed, A. Ul-Hamid, A review featuring the fundamentals and advancements of polymer/CNT nanocomposite application in aerospace industry, Polym. Bull. 78 (2021) 539–557. https://doi.org/10.1007/s00289-019-03096-0.

[142] V.K. Thakur, M.R. Kessler, Self-healing polymer nanocomposite materials: A review, Polymer (Guildf). 69 (2015) 369–383. https://doi.org/https://doi.org/10.1016/j.polymer.2015.04.086.

[143] I. Siró, D. Plackett, Microfibrillated cellulose and new nanocomposite materials: a review, Cellulose. 17 (2010) 459–494. https://doi.org/10.1007/s10570-010-9405-y.

[144] G.M. Chow, R.L. Holtz, A. Pattnaik, A.S. Edelstein, T.E. Schlesinger, R.C. Cammarata, Alternative approach to nanocomposite synthesis by sputtering, Appl. Phys. Lett. 56 (1990) 1853–1855. https://doi.org/10.1063/1.103067.

[145] K. Ohtsuka, J. Koga, M. Tsunoda, M. Suda, M. Ono, Epitaxial Growth of Nickel(II) Hydroxide on layer Silicate and Derived Nickel-(Layer Silicate) Nanocomposite, J. Am. Ceram. Soc. 73 (1990) 1719–1725. https://doi.org/10.1111/j.1151-2916.1990.tb09819.x.

[146] C.P. Barker, K.H. Kochem, K.M. Revell, R.S.A. Kelly, J.P.S. Badyal, The interfacial chemistry of metallized, oxide coated, and nanocomposite coated polymer films, Thin Solid Films. 257 (1995) 77–82. https://doi.org/10.1016/0040-6090(94)06349-4.

[147] J. Musil, Hard and superhard nanocomposite coatings, Surf. Coatings Technol. 125 (2000) 322–330. https://doi.org/10.1016/S0257-8972(99)00586-1.

[148] A.A. Voevodin, J.P. O'Neill, J.S. Zabinski, Nanocomposite tribological coatings for aerospace applications, Surf. Coatings Technol. 116–119 (1999) 36–45. https://doi.org/10.1016/S0257-8972(99)00228-5.

[149] L. Settineri, M.G. Faga, G. Gautier, M. Perucca, Evaluation of wear resistance of AlSiTiN and AlSiCrN nanocomposite coatings for cutting tools, CIRP Ann. - Manuf. Technol. 57 (2008) 575–578. https://doi.org/10.1016/j.cirp.2008.03.103.

[150] A.M. Kamalan Kirubaharan, P. Kuppusami, Corrosion behavior of ceramic nanocomposite coatings at nanoscale, Elsevier Inc., 2020. https://doi.org/10.1016/b978-0-12-819359-4.00016-7.

[151] S. Zhang, D. Sun, Y. Fu, H. Du, Recent advances of superhard nanocomposite coatings: A review, Surf. Coatings Technol. 167 (2003) 113–119. https://doi.org/10.1016/S0257-8972(02)00903-9.

[152] J. Musil, J. Vlček, Magnetron sputtering of hard nanocomposite coatings and their properties, Surf. Coatings Technol. 142–144 (2001) 557–566. https://doi.org/10.1016/S0257-8972(01)01139-2.

[153] B.D. Beake, V.M. Vishnyakov, R. Valizadeh, J.S. Colligon, Influence of mechanical properties on the nanoscratch behaviour of hard nanocomposite TiN/Si3N4 coatings on Si, J. Phys. D. Appl. Phys. 39 (2006) 1392–1397. https://doi.org/10.1088/0022-3727/39/7/009.

[154] S. Vepřek, S. Reiprich, L. Shizhi, Superhard nanocrystalline composite materials: The TiN/Si3N4 system, Appl. Phys. Lett. 2640 (1995) 2640. https://doi.org/10.1063/1.113110.

[155] I. Saladukhin, G. Abadias, V. Uglov, S. Zlotski, A.J. Van Vuuren, J.H.O. Connell, ZrN / SiN x , CrN / SiN x and AlN / SiN x Multilayered Films Deposited by Magnetron Sputtering Technique, (2020).

[156] Y. He, X. Wang, T. Guo, K. Gao, X. Pang, Effect of interface on oxidation behavior and tribological properties of CrAlN/SiNx multilayer films, Ceram. Int. (2022). https://doi.org/10.1016/J.CERAMINT.2022.09.118.

[157] P. Souček, J. Daniel, J. Hnilica, Superhard nanocomposite nc-TiC/a-C:H coatings: The effect of HiPIMS on coating microstructure and mechanical properties, Surf. Coatings Technol. 311 (2017) 257–267. https://doi.org/10.1016/j.surfcoat.2017.01.021.

[158] F. Zhao, H. Li, L. Ji, Y. Wang, H. Zhou, J. Chen, Ti-DLC films with superior friction performance, Diam. Relat. Mater. 19 (2010) 342–349. https://doi.org/10.1016/j.diamond.2010.01.008.

[159] S. El Mrabet, M.D. Abad, J.C. Sánchez-López, Identification of the wear mechanism on WC/C nanostructured coatings, Surf. Coatings Technol. 206 (2011) 1913–1920. https://doi.org/10.1016/j.surfcoat.2011.07.059.

[160] M.D. Abad, R. Sanjinés, J.L. Endrino, R. Gago, J. Andersson, J.C. Sánchez-Lõpez, Identification of ternary phases in TiBC/a-C nanocomposite thin films: Influence on the electrical and optical properties, Plasma Process. Polym. 8 (2011) 579–588. https://doi.org/10.1002/ppap.201000182.

[161] M.D. Abad, J.C. Sánchez-López, M. Brizuela, A. García-Luis, D. V. Shtansky, Influence of carbon chemical bonding on the tribological behavior of sputtered nanocomposite TiBC/a-C coatings, Thin Solid Films. 518 (2010) 5546–5552.

https://doi.org/10.1016/j.tsf.2010.04.038.

[162] N. Nedfors, O. Tengstrand, E. Lewin, A. Furlan, P. Eklund, L. Hultman, U. Jansson, Structural, mechanical and electrical-contact properties of nanocrystalline-NbC/amorphous-C coatings deposited by magnetron sputtering, Surf. Coatings Technol. 206 (2011) 354–359. https://doi.org/10.1016/j.surfcoat.2011.07.021.

[163] W. Schintlmeister, W. Wallgram, J. Kanz, K. Gigl, Cutting tool materials coated by chemical vapour deposition, Wear. 100 (1984) 153–169. https://doi.org/10.1016/0043-1648(84)90011-5.

[164] S.H. Wan, Solid Lubricant: Soft Metal, Encycl. Tribol. (2013) 3152–3159. https://doi.org/10.1007/978-0-387-92897-5_1231.

[165] F.P. Bowden, D. Tabor, The Friction and Lubrication of Solids, Volume 1, (2001) 374. https://books.google.com/books/about/The_Friction_and_Lubrication_of_Solids.html?hl=es&id=OQ7FCKNixK0C (accessed September 30, 2022).

[166] V.N. Aderikha, A.P. Krasnov, Solid Lubricants, Polymer-Based Self-Lubricating Materials, Encycl. Tribol. (2013) 3186–3193. https://doi.org/10.1007/978-0-387-92897-5_1232.

[167] C. Donnet, A. Erdemir, Friction Mechanisms and Fundamental Aspects in Solid Lubricant Coatings, Mater. Surf. Process. by Dir. Energy Tech. (2006) 573–593. https://doi.org/10.1016/B978-008044496-3/50018-6.

[168] A.C. Ferrari, J. Robertson, Interpretation of Raman spectra of disordrred and amorphous carbon, Phys. Rev. B. 61 (2000) 14 295. https://doi.org/10.1103/PhysRevB.61.14095.

[169] J. Robertson, Hard amorphous (diamond-like) carbons, Prog. Solid State Chem. 21 (1991) 199–333. https://doi.org/10.1016/0079-6786(91)90002-H.

[170] C. Donnet, A. Erdemir, Tribology of Diamond-Like Carbon Films, 2008. https://doi.org/10.1007/978-0-387-49891-1.

[171] G.M. Pharr, D.L. Callahan, S.D. McAdams, T.Y. Tsui, S. Anders, A. Anders, J.W. Ager, I.G. Brown, C.S. Bhatia, S.R.P. Silva, J. Robertson, Hardness, elastic modulus, and structure of very hard carbon films produced by cathodic-arc deposition with substrate pulse biasing, Appl. Phys. Lett. 779 (1995) 779. https://doi.org/10.1063/1.116530.

[172] D. Martínez-Martínez, C. López-Cartes, A. Fernández, J.C. Sánchez-López, Influence of the microstructure on the mechanical and tribological behavior of TiC/a-C nanocomposite coatings, Thin Solid Films. 517 (2009) 1662–1671. https://doi.org/10.1016/j.tsf.2008.09.091.

[173] C. Pusch, H. Hoche, C. Berger, R. Riedel, E. Ionescu, A. Klein, Influence of the PVD sputtering method on structural characteristics of SiCN-coatings - Comparison of RF, DC and HiPIMS sputtering and target configurations, Surf. Coatings Technol. 205 (2011) S119–S123. https://doi.org/10.1016/j.surfcoat.2011.04.095.

[174] Q. Luo, S. Yang, K.E. Cooke, Hybrid HIPIMS and DC magnetron sputtering deposition of TiN coatings: Deposition rate, structure and tribological properties, Surf. Coatings Technol. 236 (2013) 13–21. https://doi.org/10.1016/j.surfcoat.2013.07.003.

[175] M.R. Alhafian, J.B. Chemin, Y. Fleming, L. Bourgeois, M. Penoy, R. Useldinger, F. Soldera, F. Mücklich, P. Choquet, Comparison on the structural, mechanical and tribological properties of TiAlN coatings deposited by HiPIMS and Cathodic Arc

Evaporation, Surf. Coatings Technol. 423 (2021) 127529. https://doi.org/10.1016/j.surfcoat.2021.127529.

[176] E. Lewin, D. Loch, A. Montagne, A.P. Ehiasarian, J. Patscheider, Comparison of Al-Si-N nanocomposite coatings deposited by HIPIMS and DC magnetron sputtering, Surf. Coatings Technol. 232 (2013) 680–689. https://doi.org/10.1016/j.surfcoat.2013.06.076.

[177] J. Vetter, J. Müller, G. Erkens, Domino platform: PVD coaters for arc evaporation and high current pulsed magnetron sputtering, IOP Conf. Ser. Mater. Sci. Eng. 39 (2012). https://doi.org/10.1088/1757-899X/39/1/012004.

[178] C. Gautier, H. Moussaoui, F. Elstner, J. Machet, Comparative study of mechanical and structural properties of CrN films deposited by d.c. magnetron sputtering and vacuum arc evaporation, Surf. Coatings Technol. 86–87 (1996) 254–262. https://doi.org/10.1016/S0257-8972(96)02951-9.

[179] M. Bielawski, D. Seo, Residual stress development in UMS TiN coatings, Surf. Coatings Technol. 200 (2005) 1476–1482. https://doi.org/10.1016/j.surfcoat.2005.08.049.

[180] T. Hurkmans, D.B. Lewis, H. Paritong, J.S. Brooks, W.D. Münz, Influence of ion bombardment on structure and properties of unbalanced magnetron grown CrNx coatings, Surf. Coatings Technol. 114 (1999) 52–59. https://doi.org/10.1016/S0257-8972(99)00031-6.

[181] W.K. Grant, C. Loomis, J.J. Moore, D.L. Olson, B. Mishra, A.J. Perry, Characterization of hard chromium nitride coatings deposited by cathodic arc vapor deposition, Surf. Coatings Technol. 86–87 (1996) 788–796. https://doi.org/10.1016/S0257-8972(96)03071-X.

[182] M. Ahlgren, H. Blomqvist, Influence of bias variation on residual stress and texture in TiAlN PVD coatings, Surf. Coatings Technol. 200 (2005) 157–160. https://doi.org/10.1016/j.surfcoat.2005.02.078.

[183] U. Helmersson, B.O. Johansson, J. -E. Sundgren, H.T.G. Hentzell, P. Billgren, Adhesion of titanium nitride coatings on high-speed steels, J. Vac. Sci. Technol. A Vacuum, Surfaces, Film. 3 (1985) 308–315. https://doi.org/10.1116/1.573256.

[184] L. Joshua Pelleg, L.Z. Zevin, S. Lungo, N. Croitoru, Reactive-sputter-deposited TiN films on glass substrates, Thin Solid Films. 197 (1991) 117–128. https://doi.org/10.1016/0040-6090(91)90225-M.

[185] AZoM, D2 Tool Steel - High - Carbon , High - Chromium , Cold - Work Steel (UNS T30402), (2012) 2–4.

[186] Atlas Specialty Metals, Stainless Steel - Grade 420 (UNS S42000), 420 (2001) 1–10. https://www.azom.com/article.aspx?ArticleID=972.

[187] J. Paulitsch, M. Schenkel, T. Zufraß, P.H. Mayrhofer, W.D. Münz, Structure and properties of high power impulse magnetron sputtering and DC magnetron sputtering CrN and TiN films deposited in an industrial scale unit, Thin Solid Films. 518 (2010) 5558–5564. https://doi.org/10.1016/j.tsf.2010.05.062.

[188] R. Benavides, V; Restrepo, E; Rodríguez, Diseño Y Construccion De Un Calotest Utilizado Para Medir Espesores, Sci. Tech. 1 (2004) 269–272.

[189] T.D.T. Oyedotun, X-ray fluorescence (XRF) in the investigation of the composition of

earth materials: a review and an overview, Geol. Ecol. Landscapes. 2 (2018) 148–154. https://doi.org/10.1080/24749508.2018.1452459.

[190] Bruker, ¿Cómo funciona XRF? | Bruker, (n.d.). https://www.bruker.com/es/products-and-solutions/elemental-analyzers/xrf-spectrometers/how-does-xrf-work.html (accessed September 21, 2022).

[191] X. Llovet, Microscopy | Electron probe microanalysis, Encycl. Anal. Sci. 7 (2019) 30–38. https://doi.org/10.1016/B978-0-12-409547-2.14369-0.

[192] A.B. Martín-Rojo, M. González, F.L. Tabarés, Glow Discharge Emission Spectrometry (GDOES): Introducción Teórica, Aspectos Generales y Aplicabilidad en el Marco del Programa Technofusion, Ciemat. (2013) 4–15. http://www-fusion.ciemat.es/InternalReport/IR1273.pdf.

[193] Spectruma Analytik GMBH, GDOES Theory - Spectruma Website, (n.d.). https://www.spectruma.de/en/gdoes-theory.html (accessed September 21, 2022).

[194] D.R. Pendse, A.K. Chin, Cathodoluminescence and Transmission Cathodoluminescence, Encycl. Mater. Sci. Technol. (2001) 1–7. https://doi.org/10.1016/B0-08-043152-6/00190-X.

[195] W. Zhou, R. Apkarian, Z.L. Wang, D. Joy, Fundamentals of scanning electron microscopy (SEM), in: Scanning Microsc. Nanotechnol. Tech. Appl., 2007: pp. 1–40. https://doi.org/10.1007/978-0-387-39620-0_1.

[196] L. Kohl, R. H., Transmission Electron Microscopy: Physics of Image Formation, Springer, 2008. https://doi.org/10.1007/978-0-387-40093-8.

[197] D. Shindo, T. Oikawa, Energy Dispersive X-ray Spectroscopy, in: Anal. Electron Microsc. Mater. Sci., Springer Japan, Tokyo, 2002: pp. 81–102. https://doi.org/10.1007/978-4-431-66988-3_4.

[198] R.F. Egerton, An Introduction to EELS, in: R.F. Egerton (Ed.), Electron Energy-Loss Spectrosc. Electron Microsc., Springer US, Boston, MA, 2011: pp. 1–28. https://doi.org/10.1007/978-1-4419-9583-4_1.

[199] V.J. Keast, Application of EELS in materials science, Mater. Charact. 73 (2012) 1–7. https://doi.org/10.1016/j.matchar.2012.07.013.

[200] J. Silcox, Core-loss EELS, Curr. Opin. Solid State Mater. Sci. 3 (1998) 336–342. https://doi.org/10.1016/S1359-0286(98)80042-9.

[201] Y. Seo, W. Jhe, Atomic force microscopy and spectroscopy, Reports Prog. Phys. 71 (2008). https://doi.org/10.1088/0034-4885/71/1/016101.

[202] S. Sinha Ray, Techniques for characterizing the structure and properties of polymer nanocomposites, in: Environ. Friendly Polym. Nanocomposites, 2013: pp. 74–88. https://doi.org/10.1533/9780857097828.1.74.

[203] J. Epp, X-Ray Diffraction (XRD) Techniques for Materials Characterization, in: Mater. Charact. Using Nondestruct. Eval. Methods, Elsevier Ltd, 2016: pp. 81–124. https://doi.org/10.1016/B978-0-08-100040-3.00004-3.

[204] S. Zhang, X.L. Bui, J. Jiang, X. Li, Microstructure and tribological properties of magnetron sputtered nc-TiC/ a-C nanocomposite, Surf. Coatings Technol. 198 (2005) 206–211. https://doi.org/10.1016/j.surfcoat.2004.10.041.

[205] T.F. Zhang, B. Gan, S. mo Park, Q.M. Wang, K.H. Kim, Influence of negative bias

voltage and deposition temperature on microstructure and properties of superhard TiB2 coatings deposited by high power impulse magnetron sputtering, Surf. Coatings Technol. 253 (2014) 115–122. https://doi.org/10.1016/j.surfcoat.2014.05.023.

[206] D. Simeone, G. Baldinozzi, D. Gosset, S. Le Caer, J.F. Bérar, Grazing incidence X-ray diffraction for the study of polycrystalline layers, Thin Solid Films. 530 (2013) 9–13. https://doi.org/10.1016/j.tsf.2012.07.068.

[207] P. van der Heide, X-ray Photoelectron Spectroscopy: An introduction to Principles and Practices, John Wiley and Sons, 2011. https://doi.org/10.1002/9781118162897.

[208] J.S. Lupoi, E. Gjersing, M.F. Davis, Evaluating lignocellulosic biomass, its derivatives, and downstream products with Raman spectroscopy, Front. Bioeng. Biotechnol. 3 (2015) 1–18. https://doi.org/10.3389/fbioe.2015.00050.

[209] J.R. Ferraro, K. Nakamoto, C.W. Brown, Introductory Raman spectroscopy, Academic Press, 2003.

[210] N. Vidakis, A. Antoniadis, N. Bilalis, The VDI 3198 indentation test evaluation of a reliable qualitative control for layered compounds, J. Mater. Process. Technol. 143–144 (2003) 481–485. https://doi.org/10.1016/S0924-0136(03)00300-5.

[211] S. Mato, J.C. Sánchez-López, J. Barriga, F.J. Pérez, G. Alcalá, Insights into the role of the layer architecture of Cr–Ti–N based coatings in long-term high temperature oxidation experiments in steam atmosphere, Ceram. Int. 47 (2020) 4257–4266. https://doi.org/10.1016/j.ceramint.2020.10.003.

[212] E.. Bull, S J ; Berasategui, An overview of the potential of quantitativa coating adhesion measurements by scratch testing, Tribol. Int. 39 (2006) 136–165.

[213] K. Lukaszkowicz, A. Kriz, J. Sondor, Structure and adhesion of thin coatings deposited by PVD technology on the X6CrNiMoTi17-12-2 and X40CrMoV5-1 steel substrates, Arch. Mater. Sci. Eng. 51 (2011) 40–47.

[214] S.J. Bull, Failure mode maps in the thin film scratch adhesion test, Tribol. Int. 30 (1997) 491–498. https://doi.org/10.1016/S0301-679X(97)00012-1.

[215] S.J.Bull, Failure modes in scratch adhesion testing, Surf. Coatings Technol. 50 (1991) 25–32.

[216] Q. Luo, S. Yang, Uncertainty of the X-ray diffraction (XRD) sin 2 Ψtechnique in measuring residual stresses of physical vapor deposition (pvd) hard coatings, Coatings. 7 (2017). https://doi.org/10.3390/coatings7080128.

[217] Q. Luo, A.H. Jones, High-precision determination of residual stress of polycrystalline coatings using optimised XRD-sin2ψ technique, Surf. Coatings Technol. 205 (2010) 1403–1408. https://doi.org/10.1016/j.surfcoat.2010.07.108.

[218] A. Ashyralyev, Determination of Residual Stresses by X-ray Diffraction, AIP Conf. Proc. 1309 (2010) 66–84. https://doi.org/10.1063/1.3525214.

[219] W. Sekkal, A. Zaoui, S. Schmauder, Nanoindentation study of the superlattice hardening effect at TiC(110)/NbC(110) interfaces, Appl. Phys. Lett. 86 (2005) 1–3. https://doi.org/10.1063/1.1897432.

[220] P.-L. Larssont, A.E. Giannakopoulos, E. Soderlund, D.J. Rowcliffe, R. Vestergaard, Analysis of Berkovich Indentation, Int. J. Solid Struct. 33 (1996) 221–248.

[221] W.C. Oliver, G.M. Pharr, An improved technique for determining hardness and elastic

modulus using load and displacement sensing indentation experiments, J. Mater. Res. 7 (1992) 1564–1583.

[222] D.A. Rigney, J.P. Hirth, Plastic deformation and sliding friction of metals, Wear. 53 (1979) 345–370. https://doi.org/10.1016/0043-1648(79)90087-5.

[223] G. Costagliola, F. Bosia, N.M. Pugno, Static and dynamic friction of hierarchical surfaces, Phys. Rev. E. 94 (2016) 1–10. https://doi.org/10.1103/PhysRevE.94.063003.

[224] K. Kato, Wear in relation to friction - A review, Wear. 241 (2000) 151–157. https://doi.org/10.1016/S0043-1648(00)00382-3.

[225] J. Robertson, Diamond-like carbon, Pure Appl. Chem. 66 (1994) 1789–1796. https://doi.org/10.1351/pac199466091789.

[226] M. Mikula, B. Grančič, V. Buršíková, A. Csuba, M. Držík, Š. Kavecký, A. Plecenik, P. Kúš, Mechanical properties of superhard TiB_2 coatings prepared by DC magnetron sputtering, Vacuum. 82 (2007) 278–281. https://doi.org/10.1016/j.vacuum.2007.07.036.

[227] O. Knotek, F. Jungblut, R. Breidenbach, Magnetron-sputtered superhard coatings within the system TiBCN, Vacuum. 41 (1990) 2184–2186. https://doi.org/10.1016/0042-207X(90)94220-K.

[228] Q. Ma, L. Li, Y. Xu, X. Ma, Y. Xu, H. Liu, Effect of Ti content on the microstructure and mechanical properties of TiAlSiN nanocomposite coatings, Int. J. Refract. Met. Hard Mater. 59 (2016) 114–120. https://doi.org/10.1016/j.ijrmhm.2016.06.005.

[229] B. Basu, G.B. Raju, A.K. Suri, Processing and properties of monolithic TiB_2 based materials, Int. Mater. Rev. 51 (2006) 352–374. https://doi.org/10.1179/174328006X102529.

[230] B. Grančič, M. Mikula, L. Hrubá, M. Gregor, M. Štefečka, A. Csuba, E. Dobročka, A. Plecenik, P. Kúš, The influence of deposition parameters on TiB_2 thin films prepared by DC magnetron sputtering, Vacuum. 80 (2005) 174–177. https://doi.org/10.1016/j.vacuum.2005.08.013.

[231] N. Panich, Y. Sun, Mechanical properties of TiB2-based nanostructured coatings, Surf. Coatings Technol. 198 (2005) 14–19. https://doi.org/10.1016/j.surfcoat.2004.10.096.

[232] M. Saeedi Heydari, H.R. Baharvandi, Comparing the effects of different sintering methods for ceramics on the physical and mechanical properties of B4C-TiB2 nanocomposites, Int. J. Refract. Met. Hard Mater. 51 (2015) 224–232. https://doi.org/10.1016/j.ijrmhm.2015.04.003.

[233] M.D. Abad, D. Cáceres, Y.S. Pogozhev, D. V. Shtansky, J.C. Sánchez-López, Bonding structure and mechanical properties of Ti-B-C coatings, Plasma Process. Polym. 6 (2009) 107–112. https://doi.org/10.1002/ppap.200930403.

[234] J.C. Sánchez-López, M.D. Abad, A. Justo, R. Gago, J.L. Endrino, A. García-Luis, M. Brizuela, Phase composition and tribomechanical properties of Ti-B-C nanocomposite coatings prepared by magnetron sputtering, J. Phys. D. Appl. Phys. 45 (2012) 375401. https://doi.org/10.1088/0022-3727/45/37/375401.

[235] L. Jaworska, M. Karolus, S. Cygan, J. Morgiel, J. Cyboroń, J. Laszkiewicz Łukasik, P. Putyra, Influence of pulsed current during high pressure sintering on crystallite size

and phase composition of diamond with Ti–B bonding phase, Int. J. Refract. Met. Hard Mater. 70 (2018) 101–106. https://doi.org/10.1016/j.ijrmhm.2017.09.011.

[236] B. Kurt, L. Özdoğan, B. Güney, Ö.S. Bölükbaşı, A. Günen, Characterization and wear behavior of TiBC coatings formed by thermo-reactive diffusion technique on AISI D6 steel, Surf. Coatings Technol. 385 (2020) 125332. https://doi.org/10.1016/j.surfcoat.2020.125332.

[237] W. Dai, X. Gao, X. Li, Q. Wang, Influence of carbon incorporation on microstructure and properties of titanium diboride coatings deposited by combining ion beam with magnetron sputtering, Ceram. Int. 45 (2019) 22498–22505. https://doi.org/10.1016/j.ceramint.2019.07.273.

[238] H.Y. Zhai, H.M. Christen, C. Cantoni, A. Goyal, D.H. Lowndes, H.Y. Zhai, H.M. Christen, C. Cantoni, Epitaxial titanium diboride films grown by pulsed-laser deposition, 1963 (2002) 1–4. https://doi.org/10.1063/1.1461869.

[239] J.T. Ok, I.W. Park, J.J. Moore, M.C. Kang, K.H. Kim, Syntheses and mechanical properties of Ti-B-C coatings by a plasma-enhanced chemical vapor deposition, Surf. Coatings Technol. 200 (2005) 1418–1423. https://doi.org/10.1016/j.surfcoat.2005.08.078.

[240] J. Lauridsen, N. Nedfors, U. Jansson, J. Jensen, P. Eklund, L. Hultman, Ti-B-C nanocomposite coatings deposited by magnetron sputtering, Appl. Surf. Sci. 258 (2012) 9907–9912. https://doi.org/10.1016/j.apsusc.2012.06.049.

[241] J.C. Qian, Z.F. Zhou, W.J. Zhang, K.Y. Li, I. Bello, L. Martinu, J.E. Klemberg-Sapieha, Microstructure and tribo-mechanical properties of Ti-B-C nanocomposite films prepared by magnetron sputtering, Surf. Coatings Technol. 270 (2015) 290–298. https://doi.org/10.1016/j.surfcoat.2015.02.043.

[242] E. Contreras, Y. Galindez, M.A. Gómez, Microstructure, mechanical and tribological properties of TiBC coatings by DC magnetron sputtering onto AISI M2 steel using independent TiB2 and graphite targets, Surf. Coatings Technol. 350 (2018) 298–306. https://doi.org/10.1016/j.surfcoat.2018.05.079.

[243] M.A. Baker, Advanced characterisation of nanocomposite coatings, Surf. Coatings Technol. 201 (2007) 6105–6111. https://doi.org/10.1016/j.surfcoat.2006.08.118.

[244] J. Pelleg, G. Sade, M. Sinder, D. Mogilyanski, Compositional and structural changes in TiB2 films induced by bias, in situ and post-deposition annealing, respectively, Phys. B Condens. Matter. 381 (2006) 118–127. https://doi.org/10.1016/j.physb.2005.12.260.

[245] J.A. García, P.J. Rivero, E. Barba, I. Fernández, J.A. Santiago, J.F. Palacio, G.G. Fuente, R.J. Rodríguez, A comparative study in the tribological behavior of DLC coatings deposited by HiPIMS technology with positive pulses, Metals (Basel). 10 (2020). https://doi.org/10.3390/met10020174.

[246] S. Schmidt, T. Hänninen, J. Wissting, L. Hultman, N. Goebbels, A. Santana, M. Tobler, H. Högberg, SiNx coatings deposited by reactive high power impulse magnetron sputtering: Process parameters influencing the residual coating stress, J. Appl. Phys. 121 (2017). https://doi.org/10.1063/1.4977812.

[247] J. Musil, Hard nanocomposite coatings: Thermal stability, oxidation resistance and toughness, Surf. Coatings Technol. 207 (2012) 50–65. https://doi.org/10.1016/j.surfcoat.2012.05.073.

[248] C. Casiraghi, A.C. Ferrari, J. Robertson, Raman spectroscopy of hydrogenated amorphous carbons, Phys. Rev. B - Condens. Matter Mater. Phys. 72 (2005) 1–14. https://doi.org/10.1103/PhysRevB.72.085401.

[249] A.C. Ferrari, J. Robertson, Interpretation of Raman spectra of disordered and amorphous carbon, Phys. Rev. Bical Rev. 61 (1999). https://doi.org/10.1063/1.2219983.

[250] J. Robertson, Properties of diamond-like carbon, Surf. Coatings Technol. 50 (1992) 185–203. https://doi.org/10.1016/0257-8972(92)90001-Q.

[251] S. Zhang, H. Xie, X. Zeng, P. Hing, Residual stress characterization of diamond-like carbon coatings by an X-ray diffraction method, Surf. Coatings Technol. 122 (1999) 219–224. https://doi.org/10.1016/S0257-8972(99)00298-4.

[252] C.. N. Zoita, L. Braic, A. Kiss, M. Braic, Characterization of NbC coatings deposited by magnetron sputtering method, Surf. Coatings Technol. 204 (2010) 2002–2005. https://doi.org/10.1016/j.surfcoat.2009.08.050.

[253] X. Sui, J. Liu, S. Zhang, J. Yang, J. Hao, Microstructure, mechanical and tribological characterization of CrN/DLC/Cr-DLC multilayer coating with improved adhesive wear resistance, Appl. Surf. Sci. 439 (2018) 24–32. https://doi.org/10.1016/j.apsusc.2017.12.266.

[254] K. Nygren, M. Samuelsson, A. Flink, H. Ljungcrantz, Å. Kassman Rudolphi, U. Jansson, Growth and characterization of chromium carbide films deposited by high rate reactive magnetron sputtering for electrical contact applications, Surf. Coatings Technol. 260 (2014) 326–334. https://doi.org/10.1016/j.surfcoat.2014.06.069.

[255] M. Cuppari, S. Santos, Physical Properties of the NbC Carbide, Metals (Basel). 6 (2016) 250. https://doi.org/10.3390/met6100250.

[256] T. Amriou, B. Bouhafs, H. Aourag, B. Khelifa, S. Bresson, C. Mathieu, FP-LAPW investigations of electronic structure and bonding mechanism of NbC and NbN compounds, Phys. B Condens. Matter. 325 (2003) 46–56. https://doi.org/10.1016/S0921-4526(02)01429-1.

[257] L. Yate, L. Emerson Coy, G. Wang, M. Beltrán, Tailoring mechanical properties and electrical conductivity of flexible niobium carbide nanocomposite thin films, RSC Adv. 4 (2014) 61355–61362. https://doi.org/10.1039/c4ra11292j.

[258] B. Sustarsic, M. Jenko, M. Godec, L. Kosec, Microstructural investigation of NbC-doped vacuum-sintered tool-steel-based composites, User Model. User-Adapt. Interact. 71 (2003) 77–82. https://doi.org/10.1016/S0042-207X(02)00717-0.

[259] M. Braic, V. Braic, M. Balaceanu, A. Vladescu, C.N. Zoita, I. Titorencu, V. Jinga, F. Miculescu, Preparation and characterization of biocompatible Nb-C coatings, Thin Solid Films. 519 (2011) 4064–4068. https://doi.org/10.1016/j.tsf.2011.01.193.

[260] L. Yate, L.E. Coy, D. Gregurec, W. Aperador, S.E. Moya, G. Wang, Nb-C nanocomposite films with enhanced biocompatibility and mechanical properties for hard-tissue implant applications, ACS Appl. Mater. Interfaces. 7 (2015) 6351–6358. https://doi.org/10.1021/acsami.5b01193.

[261] A. Bendavid, P.J. Martin, T.J. Kinder, E.W. Preston, The deposition of NbN and NbC thin films by filtered vacuum cathodic arc deposition, Surf. Coatings Technol. 163–164 (2003) 347–352. https://doi.org/10.1016/S0257-8972(02)00623-0.

[262] Y.Y. Chang, D.Y. Wang, W. Te Wu, Tribological enhancement of CrN coatings by niobium and carbon ion implantation, Surf. Coatings Technol. 177–178 (2004) 441–446. https://doi.org/10.1016/j.surfcoat.2003.09.022.

[263] K. Zhang, S.X. Du, P. Ren, C.Q. Hu, W.T. Zheng, M. Wen, Preparation and Microstructure, Mechanical, Tribological Properties of Niobium Carbide Films, Mater. Sci. Forum. 898 (2017) 1498–1504. https://doi.org/10.4028/www.scientific.net/msf.898.1498.

[264] K. Zhang, M. Wen, G. Cheng, X. Li, Reactive magnetron sputtering deposition and characterization of niobium carbide films, Vacuum. 99 (2014) 233–241. https://doi.org/10.1016/j.vacuum.2013.06.012.

[265] K. Zhang, M. Wen, Q.N. Meng, C.Q. Hu, X. Li, C. Liu, W.T. Zheng, Effects of substrate bias voltage on the microstructure, mechanical properties and tribological behavior of reactive sputtered niobium carbide films, Surf. Coatings Technol. 212 (2012) 185–191. https://doi.org/10.1016/j.surfcoat.2012.09.046.

[266] N. Nedfors, O. Tengstrand, A. Flink, A.M. Andersson, P. Eklund, L. Hultman, U. Jansson, Reactive sputtering of NbCx-based nanocomposite coatings: An up-scaling study, Surf. Coatings Technol. 253 (2014) 100–108. https://doi.org/10.1016/j.surfcoat.2014.05.021.

[267] P. Kumar, M. Gupta, D.M. Phase, J. Stahn, Influence of oxygen on growth of carbon thin films, AIP Conf. Proc. 1942 (2018). https://doi.org/10.1063/1.5028913.

[268] M. Samuelsson, D. Lundin, K. Sarakinos, F. Björefors, B. Wälivaara, H. Ljungcrantz, U. Helmersson, Influence of ionization degree on film properties when using high power impulse magnetron sputtering, J. Vac. Sci. Technol. A Vacuum, Surfaces, Film. 30 (2012) 031507. https://doi.org/10.1116/1.3700227.

[269] L. Tang, C. Gao, J. Huang, H. Zhang, W. Chang, Dry sliding friction and wear behaviour of hardened AISI D2 tool steel with different hardness levels, Tribol. Int. 66 (2013) 165–173. https://doi.org/10.1016/j.triboint.2013.05.006.

[270] A.A. McConnell, J.S. Anderson, C.N.R. Rao, Raman spectra of niobium oxides, Spectrochim. Acta Part A Mol. Spectrosc. 32 (1976) 1067–1076. https://doi.org/10.1016/0584-8539(76)80291-7.

[271] T. Vitu, A. Escudeiro, T. Polcar, A. Cavaleiro, Sliding properties of Zr-DLC coatings: The effect of tribolayer formation, Surf. Coatings Technol. 258 (2014) 734–745. https://doi.org/10.1016/j.surfcoat.2014.08.003.

[272] B. Gunawardana, N. Singhal, P. Swedlund, Degradation of Chlorinated Phenols by Zero Valent Iron and Bimetals of Iron: A Review, Environ. Eng. Res. 16 (2011) 187–203. https://doi.org/10.4491/eer.2011.16.4.187.

[273] C. Cao, D. Ford, S. Bishnoi, T. Proslier, B. Albee, E. Hommerding, A. Korczakowski, L. Cooley, G. Ciovati, J.F. Zasadzinski, Detection of surface carbon and hydrocarbons in hot spot regions of niobium superconducting rf cavities by Raman spectroscopy, Phys. Rev. Spec. Top. - Accel. Beams. 16 (2013). https://doi.org/10.1103/PhysRevSTAB.16.064701.

[274] H.T. Kreissl, M.M.J. Li, Y.K. Peng, K. Nakagawa, T.J.N. Hooper, J. V. Hanna, A. Shepherd, T.S. Wu, Y.L. Soo, S.C.E. Tsang, Structural Studies of Bulk to Nanosize Niobium Oxides with Correlation to Their Acidity, J. Am. Chem. Soc. 139 (2017) 12670–12680. https://doi.org/10.1021/jacs.7b06856.

[275] S. Periasamy, S. Venkidusamy, R. Venkatesan, J. Mayandi, J. Pearce, J.H. Selj, R. Veerabahu, Micro-Raman Scattering of Nanoscale Silicon in Amorphous and Porous Silicon, Zeitschrift Fur Phys. Chemie. 231 (2017) 1585–1598. https://doi.org/10.1515/zpch-2016-0961.

[276] J. Aziz, H. Kim, S. Rehman, M.F. Khan, D.K. Kim, Chemical nature of electrode and the switching response of RF-sputtered NBOX films, Nanomaterials. 10 (2020) 1–11. https://doi.org/10.3390/nano10112164.

[277] L. Pan, Y. Wang, X.J. Wang, H.Y. Qu, J.P. Zhao, Y. Li, A. Gavrilyuk, Hydrogen photochromism in Nb2O5 powders, Phys. Chem. Chem. Phys. 16 (2014) 20828–20833. https://doi.org/10.1039/c4cp02834a.

[278] M.D.M.D. Abad, S.C.S.C. Veldhuis, J.L.J.L. Endrino, B.D.B.D. Beake, A. García-Luis, M. Brizuela, J.C. Sánchez-López, Mechanical and phase stability of TiBC coatings up to 1000 °C, J. Vac. Sci. Technol. A Vacuum, Surfaces, Film. 32 (2014) 021508. https://doi.org/10.1116/1.4861365.

[279] S. El Mrabet, M.D. Abad, C. López-Cartes, D. Martínez-Martínez, J.C.J.C. Sánchez-López, Thermal evolution of WC/C nanostructured coatings by raman and in situ XRD analysis, Plasma Process. Polym. 6 (2009) 444–449. https://doi.org/10.1002/ppap.200931004.

[280] X. Chu, S.A. Barnett, Model of superlattice yield stress and hardness enhancements, J. Appl. Phys. 77 (1995) 4403–4411. https://doi.org/10.1063/1.359467.

[281] Y.X. Ou, J. Lin, H.L. Che, W.D. Sproul, J.J. Moore, M.K. Lei, Mechanical and tribological properties of CrN/TiN multilayer coatings deposited by pulsed dc magnetron sputtering, Surf. Coatings Technol. 276 (2015) 152–159. https://doi.org/10.1016/j.surfcoat.2015.06.064.

[282] Y.X. Ou, J. Lin, S. Tong, H.L. Che, W.D. Sproul, M.K. Lei, Wear and corrosion resistance of CrN/TiN superlattice coatings deposited by a combined deep oscillation magnetron sputtering and pulsed dc magnetron sputtering, Appl. Surf. Sci. 351 (2015) 332–343. https://doi.org/10.1016/j.apsusc.2015.05.110.

[283] Y.X. Ou, H.Q. Wang, B. Liao, M.K. Lei, X.P. Ouyang, Tribological behaviors in air and seawater of CrN/TiN superlattice coatings irradiated by high-intensity pulsed ion beam, Ceram. Int. 45 (2019) 24405–24412. https://doi.org/10.1016/j.ceramint.2019.08.162.

[284] Y.X. Ou, J. Lin, S. Tong, W.D. Sproul, M.K. Lei, Structure, adhesion and corrosion behavior of CrN/TiN superlattice coatings deposited by the combined deep oscillation magnetron sputtering and pulsed dc magnetron sputtering, Surf. Coatings Technol. 293 (2016) 21–27. https://doi.org/10.1016/j.surfcoat.2015.10.009.

[285] P. Yashar, S.A. Barnett, J. Rechner, W.D. Sproul, Structure and mechanical properties of polycrystalline CrN / TiN superlattices, J. Vac. Sci. Technol. A. 2913 (1998). https://doi.org/10.1116/1.581439.

[286] A. Azizpour, R. Hahn, F.F. Klimashin, T. Wojcik, E. Poursaeidi, P.H. Mayrhofer, Deformation and cracking mechanism in CrN/TiN multilayer coatings, Coatings. 9 (2019) 9–17. https://doi.org/10.3390/coatings9060351.

[287] H.C. Barshilia, K.S. Rajam, Deposition of TiN/CrN hard superlattices by reactive d.c. magnetron sputtering, Bull. Mater. Sci. 26 (2003) 233–237. https://doi.org/10.1007/BF02707797.

[288] H.C. Barshilia, N. Selvakumar, K.S. Rajam, K. Gopinadhan, S. Chaudhary, Investigation of interface properties of sputter deposited TiN/CrN superlattices by low angle x-ray reflectivity, J. Phys. D. Appl. Phys. 41 (2008). https://doi.org/10.1088/0022-3727/41/20/205409.

[289] J. Paulitsch, C. Maringer, P.H. Mayrhofer, Low friction CrN MPP/TiN DCMS multilayer coatings, Tribol. Lett. 46 (2012) 87–93. https://doi.org/10.1007/s11249-012-9922-y.

[290] J. Paulitsch, M. Schenkel, A. Schintlmeister, H. Hutter, P.H. Mayrhofer, Low friction CrN/TiN multilayer coatings prepared by a hybrid high power impulse magnetron sputtering/DC magnetron sputtering deposition technique, Thin Solid Films. 518 (2010) 5553–5557. https://doi.org/10.1016/j.tsf.2010.05.061.

[291] J. Paulitsch, P.H. Mayrhofer, W.D. Münz, M. Schenkel, Structure and mechanical properties of CrN/TiN multilayer coatings prepared by a combined HIPIMS/UBMS deposition technique, Thin Solid Films. 517 (2008) 1239–1244. https://doi.org/10.1016/j.tsf.2008.06.080.

[292] M. Nordin, M. Larsson, S. Hogmark, Mechanical and tribological properties of multilayered PVD TiN/CrN, Wear. 232 (1999) 221–225. https://doi.org/10.1016/S0043-1648(99)00149-0.

[293] M. Nordin, M. Larsson, Deposition and characterisation of multilayered PVD TiN/CrN coatings on cemented carbide, Surf. Coatings Technol. 116–119 (1999) 108–115. https://doi.org/10.1016/S0257-8972(99)00263-7.

[294] S. Rabadzhiyska, L. Kolaklieva, V. Chitanov, T. Cholakova, R. Kakanakov, N. Dimcheva, K. Balashev, Mechanical, wear and corrosion behavior of CrN/TiN multilayer coatings deposited by low temperature unbalanced magnetron sputtering for biomedical applications, Mater. Today Proc. 5 (2018) 16012–16021. https://doi.org/10.1016/j.matpr.2018.05.046.

[295] J.W. Du, L. Chen, J. Chen, Y. Du, Mechanical properties, thermal stability and oxidation resistance of TiN/CrN multilayer coatings, Vacuum. 179 (2020) 109468. https://doi.org/10.1016/j.vacuum.2020.109468.

[296] M.D. Huang, Y. Liu, F.Y. Meng, L.N. Tong, P. Li, Thick CrN/TiN multilayers deposited by arc ion plating, Vacuum. 89 (2013) 101–104. https://doi.org/10.1016/j.vacuum.2011.12.004.

[297] L. Major, W. Tirry, G. Van Tendeloo, Microstructure and defect characterization at interfaces in TiN/CrN multilayer coatings, Surf. Coatings Technol. 202 (2008) 6075–6080. https://doi.org/10.1016/j.surfcoat.2008.07.005.

[298] R. Escobar Galindo, R. Gago, D. Duday, C. Palacio, Towards nanometric resolution in multilayer depth profiling: A comparative study of RBS, SIMS, XPS and GDOES, Anal. Bioanal. Chem. 396 (2010) 2725–2740. https://doi.org/10.1007/s00216-009-3339-y.

[299] R. Escobar Galindo, J.M. Albella, Modelling of Glow Discharge Optical Emission Spectroscopy depth profiles of metal (Cr,Ti) multilayer coatings, Spectrochim. Acta - Part B At. Spectrosc. 63 (2008) 422–430. https://doi.org/10.1016/j.sab.2007.12.006.

[300] N. Matsunami, Y. Yamamura, Y. Ltikawa, N. Itoh, Y. Kazumata, S. Miyagawa, K. Morita, R. Shimizu, H. Tawara, Energy Dependence of Sputtering Yields of Monatomic Solids, At. Data Nucl. Data Tables. 31 (1984) 1–80.

[301] T. Young, An essay on the cohesion of fluids, Phil. Trans. R. Soc. 95 (1804) 65–87. https://doi.org/https://doi.org/10.1098/rstl.1805.0005.

[302] D. Blanco, J.L. Viesca, M.T. Mallada, B. Ramajo, R. González, A.H. Battez, Wettability and corrosion of [NTf_2] anion-based ionic liquids on steel and PVD (TiN, CrN, ZrN) coatings, Surf. Coatings Technol. 302 (2016) 13–21. https://doi.org/10.1016/j.surfcoat.2016.05.051.

[303] P.A. Dearnley, Low friction surfaces for plastic injection moulding dies - An experimental case study, Wear. 225–229 (1999) 1109–1113. https://doi.org/10.1016/S0043-1648(98)00417-7.

[304] Z.A. Fazel, H. Elmkhah, A. Fattah-Alhosseini, K. Babaei, M. Meghdari, Comparing electrochemical behavior of applied CrN/TiN nanoscale multilayer and TiN single-layer coatings deposited by CAE-PVD method, J. Asian Ceram. Soc. 8 (2020) 510–518. https://doi.org/10.1080/21870764.2020.1756065.

[305] B. Lu, N. Li, Versatile aluminum alloy surface with various wettability, Appl. Surf. Sci. 326 (2015) 168–173. https://doi.org/10.1016/j.apsusc.2014.11.138.

[306] A. de Leon, R.C. Advincula, Conducting Polymers with Superhydrophobic Effects as Anticorrosion Coating, Elsevier Inc., 2015. https://doi.org/10.1016/B978-0-12-411467-8.00011-8.

[307] M. Stueber, H. Holleck, H. Leiste, K. Seemann, S. Ulrich, C. Ziebert, Concepts for the design of advanced nanoscale PVD multilayer protective thin films, J. Alloys Compd. 483 (2009) 321–333. https://doi.org/10.1016/j.jallcom.2008.08.133.

[308] J.W. Du, L. Chen, J. Chen, Y. Du, Mechanical properties, thermal stability and oxidation resistance of TiN/CrN multilayer coatings, Vacuum. 179 (2020). https://doi.org/10.1016/j.vacuum.2020.109468.

[309] M. Panjan, S. Šturm, P. Panjan, M. Čekada, TEM investigation of TiAlN/CrN multilayer coatings prepared by magnetron sputtering, Surf. Coatings Technol. 202 (2007) 815–819. https://doi.org/10.1016/j.surfcoat.2007.05.084.

[310] M. Panjan, M. Čekada, P. Panjan, A. Zalar, T. Peterman, Sputtering simulation of multilayer coatings in industrial PVD system with three-fold rotation, Vacuum. 82 (2007) 158–161. https://doi.org/10.1016/j.vacuum.2007.07.053.

[311] I.M. Ross, W.M. Rainforth, C.R. Seabourne, A.J. Scott, P. Wang, B.G. Mendis, A.L. Bleloch, C. Reinhard, P.E. Hovsepian, Electron energy loss spectroscopy of nano-scale CrAlYN/CrN-CrAlY(O)N/Cr(O)N multilayer coatings deposited by unbalanced magnetron sputtering, Thin Solid Films. 518 (2010) 5121–5127. https://doi.org/10.1016/j.tsf.2010.03.012.

[312] G. Montay, A. Cherouat, A. Nussair, J. Lu, Residual stresses in coating technology, J. Mater. Sci. Technol. 20 (2004) 81–84.

[313] G. Abadias, E. Chason, J. Keckes, M. Sebastiani, G.B. Thompson, E. Barthel, G.L. Doll, C.E. Murray, C.H. Stoessel, L. Martinu, Review Article: Stress in thin films and coatings: Current status, challenges, and prospects, J. Vac. Sci. Technol. A Vacuum, Surfaces, Film. 36 (2018) 020801. https://doi.org/10.1116/1.5011790.

[314] S.J. Bull, D.S. Rickerby, The inter-relationship between coating microstructure and the tribological performance of PVD coatings, Tribol. Ser. 17 (1990) 337–349. https://doi.org/10.1016/s0167-8922(08)70273-6.

[315] G. Li, J. Sun, Y. Xu, Y. Xu, J. Gu, L. Wang, K. Huang, K. Liu, L. Li, Microstructure, mechanical properties, and cutting performance of TiAlSiN multilayer coatings prepared by HiPIMS, Surf. Coatings Technol. 353 (2018) 274–281. https://doi.org/10.1016/j.surfcoat.2018.06.017.

[316] K. Aouadi, C. Nouveau, A. Besnard, B. Tlili, A. Montagne, M. Chafra, The Effect of Bilayer Periods and Their Thickness in Magnetron Sputtering Protective Multilayer Coatings for Tribological Applications, J. Mater. Eng. Perform. 30 (2021) 2526–2535. https://doi.org/10.1007/s11665-021-05587-6.

[317] W. Tillmann, D. Kokalj, D. Stangier, Q. Fu, F.E. Kruis, L. Kesper, U. Berges, C. Westphal, On the synthesis and structural evolution of artificial CrN/TiN nanocomposites, Appl. Surf. Sci. 535 (2021) 147736. https://doi.org/10.1016/j.apsusc.2020.147736.

[318] U. Helmersson, S. Todorova, S.A. Barnett, J.E. Sundgren, L.C. Markert, J.E. Greene, Growth of single-crystal TiN/VN strained-layer superlattices with extremely high mechanical hardness, J. Appl. Phys. 62 (1987) 481–484. https://doi.org/10.1063/1.339770.

[319] R. Akhter, Z. Zhou, Z. Xie, P. Munroe, Influence of substrate bias on the scratch, wear and indentation response of TiSiN nanocomposite coatings, Surf. Coatings Technol. 425 (2021) 127687. https://doi.org/10.1016/j.surfcoat.2021.127687.

[320] Z. Hubička, J.T. Gudmundsson, P. Larsson, D. Lundin, Hardware and power management for high power impulse magnetron sputtering, 2019. https://doi.org/10.1016/B978-0-12-812454-3.00007-3.

[321] D. Bhaduri, A. Ghosh, S. Gangopadhyay, S. Paul, Effect of target frequency, bias voltage and bias frequency on microstructure and mechanical properties of pulsed DC CFUBM sputtered TiN coating, Surf. Coatings Technol. 204 (2010) 3684–3697. https://doi.org/10.1016/j.surfcoat.2010.04.047.

[322] S. Guruvenket, G. Mohan Rao, Effect of ion bombardment and substrate orientation on structure and properties of titanium nitride films deposited by unbalanced magnetron sputtering, J. Vac. Sci. Technol. A Vacuum, Surfaces, Film. 20 (2002) 678–682. https://doi.org/10.1116/1.1460888.

[323] Y. Zhu, M. Dong, J. Li, L. Wang, Wear failure mechanism of TiSiN coating at elevated temperatures, Appl. Surf. Sci. 487 (2019) 349–355. https://doi.org/10.1016/j.apsusc.2019.05.120.

[324] Z. Wang, D. Zhang, P. Ke, X. Liu, A. Wang, Influence of Substrate Negative Bias on Structure and Properties of TiN Coatings Prepared by Hybrid HIPIMS Method, J. Mater. Sci. Technol. 31 (2015) 37–42. https://doi.org/10.1016/j.jmst.2014.06.002.

[325] W.J. Shen, M.H. Tsai, Y.S. Chang, J.W. Yeh, Effects of substrate bias on the structure and mechanical properties of (Al 1.5CrNb 0.5Si 0.5Ti)N x coatings, Thin Solid Films. 520 (2012) 6183–6188. https://doi.org/10.1016/j.tsf.2012.06.002.

[326] P.K. Huang, J.W. Yeh, Effects of substrate bias on structure and mechanical properties of (AlCrNbSiTiV)N coatings, J. Phys. D. Appl. Phys. 42 (2009). https://doi.org/10.1088/0022-3727/42/11/115401.

[327] T. Kubart, A. Aijaz, J. Andersson, F. Ferreira, J.C. Oliveira, A. Sobetkii, A.C. Parau, C. Vitelaru, High power impulse magnetron sputtering of diamond-like carbon coatings, J. Vac. Sci. Technol. A. 38 (2020) 043408. https://doi.org/10.1116/6.0000070.

[328] G. Hakansson, T.F. Group, D. Mcintyre, J.E. Greene, Microstrucure and physical properties of polycrystalline metastable Ti0.5Al0.5N alloys grown by D.C. magnetron sputter deposition, Thin Solid Films. 153 (1987) 55–65.

[329] J.-W. Lee, S.-K. Tien, Y.-C. Kuo, The effects of pulse frequency and substrate bias to the mechanical properties of CrN coatings deposited by pulsed DC magnetron sputtering, Thin Solid Films. 494 (2006) 161–167. https://doi.org/10.1016/j.tsf.2005.07.190.

[330] G. Carter, Peening in ion-assisted thin-film deposition: A generalized model, J. Phys. D. Appl. Phys. 27 (1994) 1046–1055. https://doi.org/10.1088/0022-3727/27/5/024.

[331] S. Vales, P.R.T. Avila, A. Rosenkranz, R. Droppa, F. Soldera, J. Garcia, F. Alvarez, H. Pinto, Effect of ion peening and pulsed plasma nitriding on the structural properties of TiN coatings sputtered onto 100Cr6 steel, Mater. Chem. Phys. 235 (2019) 121723. https://doi.org/10.1016/j.matchemphys.2019.121723.

[332] Traugott Fischer, Materials Science for Engineering Students, 2009.

[333] G. Greczynski, J. Lu, J. Jensen, S. Bolz, W. Kölker, C. Schiffers, O. Lemmer, J.E. Greene, L. Hultman, A review of metal-ion-flux-controlled growth of metastable TiAlN by HIPIMS/DCMS co-sputtering, Surf. Coatings Technol. 257 (2014) 15–25. https://doi.org/10.1016/j.surfcoat.2014.01.055.

[334] Y.Y. Chang, Y.J. Yang, S.Y. Weng, Effect of interlayer design on the mechanical properties of AlTiCrN and multilayered AlTiCrN/TiSiN hard coatings, Surf. Coatings Technol. 389 (2020) 125637. https://doi.org/10.1016/j.surfcoat.2020.125637.

[335] H.S. Park, D.H. Jung, H.D. Na, J.H. Joo, J.J. Lee, The properties of (Ti,Al) N coatings deposited by inductively coupled plasma assisted d.c. magnetron sputtering, Surf. Coatings Technol. 142–144 (2001) 999–1004. https://doi.org/10.1016/S0257-8972(01)01217-8.

[336] G. Greczynski, J. Lu, J. Jensen, I. Petrov, J.E. Greene, S. Bolz, W. Kölker, C. Schiffers, O. Lemmer, L. Hultman, Strain-free, single-phase metastable Ti0.38Al0.62N alloys with high hardness: Metal-ion energy vs. momentum effects during film growth by hybrid high-power pulsed/dc magnetron cosputtering, Thin Solid Films. 556 (2014) 87–98. https://doi.org/10.1016/j.tsf.2014.01.017.

[337] A. Ghailane, H. Larhlimi, Y. Tamraoui, M. Makha, The effect of magnetic field configuration on structural and mechanical properties of TiN coatings deposited by HiPIMS and dcMS, Surf. Coat. Technol. 404 (2020) 126572. https://doi.org/10.1016/j.surfcoat.2020.126572.

[338] C.L. Chang, C.Y. Lin, F.C. Yang, J.F. Tang, The effect of match between high power impulse and bias voltage: Tin coating deposited by high power impulse magnetron sputtering, Coatings. 11 (2021). https://doi.org/10.3390/coatings11070822.

[339] Z.B. Qi, P. Sun, F.P. Zhu, Z.C. Wang, D.L. Peng, C.H. Wu, The inverse Hall-Petch effect in nanocrystalline ZrN coatings, Surf. Coatings Technol. 205 (2011) 3692–3697. https://doi.org/10.1016/j.surfcoat.2011.01.021.

[340] W. Chen, J. Zheng, Y. Lin, S. Kwon, S. Zhang, Comparison of AlCrN and AlCrTiSiN coatings deposited on the surface of plasma nitrocarburized high carbon steels, Appl. Surf. Sci. 332 (2015) 525–532. https://doi.org/10.1016/j.apsusc.2015.01.212.

[341] S. PalDey, S.C. Deevi, Single layer and multilayer wear resistant coatings of (Ti,Al)N:

A review, Mater. Sci. Eng. A. 342 (2003) 58–79. https://doi.org/10.1016/S0921-5093(02)00259-9.

[342] T.D. Atmani, M. Gaceb, H. Aknouche, C. Nouveau, M.S. Bouamrene, Parametric study of the mechanical properties of nanocrystalline TiN/CrN multilayer coatings with a special focus on the effect of coating thickness and substrate roughness, Surfaces and Interfaces. 23 (2021) 101001. https://doi.org/10.1016/j.surfin.2021.101001.

[343] W. Tillmann, D. Grisales, D. Stangier, I. Ben Jebara, H. Kang, Influence of the etching processes on the adhesion of TiAlN coatings deposited by DCMS, HiPIMS and hybrid techniques on heat treated AISI H11, Surf. Coatings Technol. 378 (2019) 125075. https://doi.org/10.1016/j.surfcoat.2019.125075.

[344] Š. Batková, J. Čapek, J. Rezek, R. Čerstvý, P. Zeman, Effect of positive pulse voltage in bipolar reactive HiPIMS on crystal structure , microstructure and mechanical properties of CrN films, Surf. Coat. Technol. 393 (2020) 125773. https://doi.org/10.1016/j.surfcoat.2020.125773.

[345] N. Cansever, Properties of niobium nitride coatings deposited by cathodic arc physical vapor deposition, Thin Solid Films. 515 (2007) 3670–3674. https://doi.org/10.1016/j.tsf.2006.10.133.

[346] Y.G. Li, H. Yuan, Z.T. Jiang, N. Pan, M.K. Lei, Phase composition and mechanical properties of homostructure NbN nanocomposite coatings deposited by modulated pulsed power magnetron sputtering, Surf. Coatings Technol. 385 (2020). https://doi.org/10.1016/j.surfcoat.2020.125387.

[347] M.C.R. Guimarães, B.C.N.M. De Castilhoa, C. Cunha, W.R. Correr, P. Mordente, F. Alvarez, H.C. Pinto, On the effect of aluminum on the microstructure and mechanical properties of CrN coatings deposited by HiPIMS, Mater. Res. 21 (2018) 1–6. https://doi.org/10.1590/1980-5373-MR-2017-0848.

[348] R. Li, Y. Cai, K. Wippermann, W. Lehnert, Bilayer CrN/Cr coating-modified 316L stainless steel bipolar plates for high temperature polymer electrolyte fuel cells, J. Power Sources. 434 (2019) 1–7. https://doi.org/10.1016/j.jpowsour.2019.226718.

[349] N. Sala, M.D. Abad, J.C. Sánchez-López, J. Caro, C. Colominas, Nb–C thin films prepared by DC-MS and HiPIMS: Synthesis, structure, and tribomechanical properties, Surf. Coatings Technol. 422 (2021). https://doi.org/10.1016/j.surfcoat.2021.127569.

[350] S. Peng, J. Xu, Z. Li, S. Jiang, P. Munroe, Z.H. Xie, H. Lu, A reactive-sputter-deposited TiSiN nanocomposite coating for the protection of metallic bipolar plates in proton exchange membrane fuel cells, Ceram. Int. 46 (2020) 2743–2757. https://doi.org/10.1016/j.ceramint.2019.09.263.

[351] R. Akhter, Z. Zhou, Z. Xie, P. Munroe, TiN versus TiSiN coatings in indentation, scratch and wear setting, Appl. Surf. Sci. 563 (2021) 150356. https://doi.org/10.1016/j.apsusc.2021.150356.

[352] Y.H. Peng, L. Chen, Y.X. Xu, C. Hu, Y. Du, Interface enhanced mechanical and thermal properties of TiSiN/TiAlN multilayers, J. Alloys Compd. 861 (2021). https://doi.org/10.1016/j.jallcom.2020.158571.

[353] W. Chen, A. Yan, C. Wang, Y. Deng, D.C. Chen, H. Xiao, D. Zhang, X. Meng, Microstructures and mechanical properties of AlCrN/TiSiN nanomultilayer coatings consisting of fcc single-phase solid solution, Appl. Surf. Sci. 509 (2020) 145303.

https://doi.org/10.1016/j.apsusc.2020.145303.

[354] P.E. Hovsepian, A.P. Ehiasarian, Y.P. Purandare, B. Biswas, F.J. Pérez, M.I. Lasanta, M.T. De Miguel, A. Illana, M. Juez-Lorenzo, R. Muelas, A. Agüero, Performance of HIPIMS deposited CrN/NbN nanostructured coatings exposed to 650 °c in pure steam environment, Mater. Chem. Phys. 179 (2016) 110–119. https://doi.org/10.1016/j.matchemphys.2016.05.017.

[355] Y.P. Purandare, G.L. Robinson, A.P. Ehiasarian, P.E. Hovsepian, Investigation of High Power Impulse Magnetron Sputtering deposited nanoscale CrN/NbN multilayer coating for tribocorrosion resistance, Wear. 452–453 (2020) 203312. https://doi.org/10.1016/j.wear.2020.203312.

[356] C. Reinhard, A.P. Ehiasarian, P.E. Hovsepian, CrN/NbN superlattice structured coatings with enhanced corrosion resistance achieved by high power impulse magnetron sputtering interface pre-treatment, Thin Solid Films. 515 (2007) 3685–3692. https://doi.org/10.1016/j.tsf.2006.11.014.

[357] Q. Yang, C. He, L.R. Zhao, J.P. Immarigeon, Preferred orientation and hardness enhancement of TiN/CrN superlattice coatings deposited by reactive magnetron sputtering, Scr. Mater. 46 (2002) 293–297. https://doi.org/10.1016/S1359-6462(01)01241-6.

[358] S.M. Yang, Y.Y. Chang, D.Y. Lin, D.Y. Wang, W. Wu, Microstructure characterization of multilayered TiSiN/CrN thin films, J. Nanosci. Nanotechnol. 8 (2008) 2688–2692. https://doi.org/10.1166/jnn.2008.592.

[359] H.C. Barshilia, A. Jain, K.S. Rajam, Structure, hardness and thermal stability of nanolayered TiN/CrN multilayer coatings, Vacuum. 72 (2003) 241–248. https://doi.org/10.1016/j.vacuum.2003.08.003.

[360] A. Wagner, D. Holec, P.H. Mayrhofer, M. Bartosik, Enhanced fracture toughness in ceramic superlattice thin films: On the role of coherency stresses and misfit dislocations, Mater. Des. 202 (2021) 109517. https://doi.org/10.1016/j.matdes.2021.109517.

[361] D.D. Kumar, N. Kumar, S. Kalaiselvam, S. Dash, R. Jayavel, Wear resistant super-hard multilayer transition metal-nitride coatings, Surfaces and Interfaces. 7 (2017) 74–82. https://doi.org/10.1016/j.surfin.2017.03.001.

[362] J. Patscheider, Nanocomposite hard coatings for wear protection, System. (2003) 180–183.

[363] M. Sperr, Z.L. Zhang, Y.P. Ivanov, P.H. Mayrhofer, M. Bartosik, Correlating elemental distribution with mechanical properties of TiN/SiNx nanocomposite coatings, Scr. Mater. 170 (2019) 20–23. https://doi.org/10.1016/j.scriptamat.2019.05.020.

[364] Y.H. Cheng, T. Browne, B. Heckerman, E.I. Meletis, Mechanical and tribological properties of nanocomposite TiSiN coatings, Surf. Coatings Technol. 204 (2010) 2123–2129. https://doi.org/10.1016/j.surfcoat.2009.11.034.

[365] F.F. Komarov, S. V. Konstantinov, A.D. Pogrebnjak, V. V. Pilko, C. Kozak, M. Opielak, Formation and characterization of nanostructured composite coatings based on the TiN phase, Acta Phys. Pol. A. 125 (2014) 1292–1295. https://doi.org/10.12693/APhysPolA.125.1292.

[366] F. Pei, Y.X. Xu, L. Chen, Y. Du, H.K. Zou, Structure, mechanical properties and

thermal stability of Ti1-xSixN coatings, Ceram. Int. 44 (2018) 15503–15508. https://doi.org/10.1016/j.ceramint.2018.05.210.

[367] S.M. Yang, Y.Y. Chang, D.Y. Lin, D.Y. Wang, W. Wu, Mechanical and tribological properties of multilayered TiSiN/CrN coatings synthesized by a cathodic arc deposition process, Surf. Coatings Technol. 202 (2008) 2176–2181. https://doi.org/10.1016/j.surfcoat.2007.09.004.

[368] A. Flink, T. Larsson, J. Sjölén, L. Karlsson, L. Hultman, Influence of Si on the microstructure of arc evaporated (Ti,Si)N thin films; evidence for cubic solid solutions and their thermal stability, Surf. Coatings Technol. 200 (2005) 1535–1542. https://doi.org/10.1016/j.surfcoat.2005.08.096.

[369] W. Li, P. Liu, X. Zhu, K. Zhang, F. Ma, X. Liu, X. Chen, D. He, Si content dependent microstructure and mechanical properties of CrN/TiSiN nanomultilayered films, Mater. Sci. Eng. A. 610 (2014) 28–32. https://doi.org/10.1016/j.msea.2014.05.030.

[370] J.A. Araujo, G.M. Araujo, R.M. Souza, A.P. Tschiptschin, Effect of periodicity on hardness and scratch resistance of CrN/NbN nanoscale multilayer coating deposited by cathodic arc technique, Wear. 330–331 (2015) 469–477. https://doi.org/10.1016/j.wear.2015.01.051.

[371] Y.P. Purandare, A.P. Ehiasarian, P.E. Hovsepian, Deposition of nanoscale multilayer CrN/NbN physical vapor deposition coatings by high power impulse magnetron sputtering, J. Vac. Sci. Technol. A Vacuum, Surfaces, Film. 26 (2008) 288–296. https://doi.org/10.1116/1.2839855.

[372] W. Spengler, R. Kaiser, A.N. Christensen, G. Müller-Vogt, Raman scattering, superconductivity, and phonon density of states of stoichiometric and nonstoichiometric TiN, Phys. Rev. B. 17 (1978) 1095–1101. https://doi.org/10.1103/PhysRevB.17.1095.

[373] M. Bernarda, A. Deneuville, O. Thomas, P. Gergaudb, P. Sandstrom, J. Birch, Raman spectra of TiN / AlN superlattices, Thin Solid Films. 380 (2000) 252–255.

[374] H.C. Barshilia, K.S. Rajam, A Raman-scattering study on the interface structure of nanolayered TiAlN/TiN and TiN/NbN multilayer thin films grown by reactive dc magnetron sputtering, J. Appl. Phys. 98 (2005) 014311. https://doi.org/10.1063/1.1946193.

[375] P. Yashar, X. Chu, S.A. Barnett, J. Rechner, Y.Y. Wang, M.S. Wong, W.D. Sproul, Stabilization of cubic CrN0.6 in CrN0.6/TiN superlattices, Appl. Phys. Lett. 72 (1998) 987–989. https://doi.org/10.1063/1.120621.

[376] Y. Kihn, C. Mirguet, L. Calmels, EELS studies of Ti-bearing materials and ab initio calculations, J. Electron Spectros. Relat. Phenomena. 143 (2005) 117–127. https://doi.org/10.1016/j.elspec.2004.02.170.

[377] T.C. Rojas, S. Domínguez-Meister, M. Brizuela, A. García-Luis, A. Fernández, J.C. Sánchez-López, A nanoscale characterization with electron microscopy of multilayered CrAlYN coatings: A singular functional nanostructure, Microsc. Microanal. 20 (2014) 14–24. https://doi.org/10.1017/S1431927613013962.

[378] J.A. Araujo, R.A.R. Giorjão, J. Bettini, R.M. Souza, A.P. Tschiptschin, Modeling intrinsic residual stresses built-up during growth of nanostructured multilayer NbN/CrN coatings, Surf. Coatings Technol. 308 (2016) 264–272. https://doi.org/10.1016/j.surfcoat.2016.07.108.

[379] K. Kanda, S. Suzuki, M. Niibe, T. Hasegawa, T. Suzuki, H. Saitoh, Local structure analysis on Si-containing DLC films based on the measurement of C K-Edge and Si K-Edge X-ray absorption spectra, Coatings. 10 (2020). https://doi.org/10.3390/coatings10040330.

[380] Y.K. Chang, H.H. Hsieh, W.F. Pong, M.H. Tsai, T.E. Dann, F.Z. Chien, P.K. Tseng, L.C. Chen, S.L. Wei, K.H. Chen, J.J. Wu, Y.F. Chen, X-ray absorption of Si-C-N thin films: A comparison between crystalline and amorphous phases, J. Appl. Phys. 86 (1999) 5609–5613. https://doi.org/10.1063/1.371568.

[381] L. García-González, J. Morales-Hernández, F.J. Espinoza-Beltrán, J. Muñoz-Saldaña, T. Scholz, G.A. Schneider, Thermal Stability, Structure and Mechanical Properties of TiSiN Coatings Prepared by Reactive DC Magnetron Co-Sputtering, Mater. Sci. Forum. 509 (2006) 93–98. https://doi.org/10.4028/www.scientific.net/msf.509.93.

List of figure captions

List of table captions

List of scientific contributions

Contributions to scientific publications

1. **N. Sala**, M.D. Abad, J.C. Sánchez-López, F. Crugeira, A. Ramos-masana, C. Colominas, **Influence of the carbon incorporation on the mechanical properties of TiB_2 thin films prepared by HiPIMS**, Int. J. Refract. Met. Hard Mater. 107 (2022). https://doi.org/10.1016/j.ijrmhm.2022.105884.

2. **N. Sala**, M.D. Abad, J.C. Sánchez-López, M. Cruz, J. Caro, C. Colominas, **Tribological performance of Nb-C thin films prepared by DC and HiPIMS**, Mater. Lett. 277 (2020) 128334. https://doi.org/10.1016/j.matlet.2020.128334.

3. **N. Sala**, M.D. Abad, J.C. Sánchez-López, J. Caro, C. Colominas, **Nb–C thin films prepared by DC-MS and HiPIMS: Synthesis, structure, and tribomechanical properties**, Surf. Coatings Technol. 422 (2021). https://doi.org/10.1016/j.surfcoat.2021.127569.

Contributions to scientific communications

1. Advances in Surfaces, Interfaces and Interphases Conference, online conference. "*Influence of the carbon incorporation on the mechanical properties of TiB_2 thin films prepared by HiPIMS*". **N. Sala**, M.D. Abad, J.C. Sánchez-López, F. Crugeira, A. Ramos-Masana, C. Colominas. Poster presentation. 15-18 May 2022.

2. I Jornada de doctorands IQS. Barcelona, Spain. "*Characterization of niobium carbide films deposited by two different techniques: DC and HiPIMS*". **N. Sala**, C. Colominas, M.D. Abad. Poster presentation. 16-17 May 2019.

3. 11a trobada de joves investigadors de la Societat catalana de química. Vilanova i la Geltru, Spain "*Recobriments ceràmics nanoestructurats preparats per plasma d'alta energía*". **N. Sala**, C. Colominas, M.D. Abad. Oral presentation. 28-30 January 2020.

4. ICMCTF 2021. Online conference. *"Nb-C Thin Films Prepared by DC-MS and HiPIMS: Synthesis, Structure and Tribo-mechanical Properties"*. **N. Sala**, M.D. Abad, J.C. Sánchez-López, J. Caro, C. Colominas. Poster presentation. 26-30 April 2021.

5. ÖGV Seminar 2021. Vienna, Austria. "*Ceramic nanostructured coatings prepared by high energy plasma Technology"*. **N. Sala**, M.D. Abad, C. Colominas, J.C. Sánchez-López. Oral presentation. 24th September 2021.

6. 11a trobada de joves investigadors de la Societat catalana de química. Vilanova i la Geltru, Spain "*Recobriments ceràmics nanoestructurats preparats per plasma d'alta energía*". **N. Sala**, C. Colominas, M.D. Abad. Oral presentation. 28-30 January 2020.
7. ÖGV Seminar 2021. Vienna, Austria. "*Ceramic nanostructured coatings prepared by high energy plasma Technology"*. **N. Sala**, M.D. Abad, C. Colominas, J.C. Sánchez-López. Oral presentation. 24th September 2021.
8. Advances in Surfaces, Interfaces and Interphases Conference, online conference. "*Microstructure and mechanical properties of TiN/CrN multilayer coatings deposited in an industrial scale HiPIMS system*". **N. Sala**, M.D. Abad, M. R. de Figueiredo, R. Franz, C. Kainz, C. Colominas. Poster presentation. 15-18 May 2022.
9. Junior Euromat 2022 Coimbra, Portugal. "*TiN/CrN, TiSiN/CrN and NbN/CrN multilayer coatings deposited in an industrial-scale HiPIMS system*". **N. Sala**, M. R. de Figueiredo, R. Franz, C. Kainz, C. Colominas, M. D. Abad. Poster presentation. 19-22 of July 2022.
10. 18th International Conference on Plasma Surface Engineering (PSE 2022). Trade Fair Erfurt, Germany. "*TiN/CrN, TiSiN/CrN and NbN/CrN multilayers prepared by HiPIMS*". M. D. Abad, **N. Sala**, M. R. de Figueiredo, R. Franz, C. Kainz, C. Colominas Oral presentation. 12-15 September 2022.